FACULTY OF APPLIED SCIENCES

Department of Chemical Engineering – Nanomaterials, Catalysis, Electrochemistry

Co-Supervised Thesis

Presented by

Marlène Huguette TSAFFO MBOGNOU

To obtain the title of

Doctor of Philosophy in Engineering Sciences

PHYSICO-CHEMICAL AND MINERALOGICAL CHARACTERISATION OF CLAY MATERIAL FROM THE BAKOTCHA LOCALITY: APPLICATION TO WASTEWATER TREATMENT

Supervisor: Prof. Stéphanie Lambert

Co-supervisor: Dr. Julien Mahy

Joint supervisor: Prof. Emmanuel Djoufac Woumfo

Novembre 2025

DEDICATIONS

I dedicate this work

To my parents,

Mr and Mrs, MBOGNOU Joseph Richard and LAFFO Marie Noelle

ACKNOWLEDGEMENTS

This study was conducted at the Nanomaterials, Catalysis, Electrochemistry (NCE) Research Unit of the Department of Chemical Engineering at the University of Liège and at the Laboratory of Physicochemistry of Mineral Materials ($LPCM_2$) at the University of Yaoundé I.

This thesis is part of a joint supervision agreement between the University of Liège and the University of Yaoundé I. This thesis was made possible thanks to the 2022-2027 five-year development cooperation program of ARES, ULiège ARES/Pacodel, and a contribution from the laboratory's funds.

At the end of these four years of research, I would like to express my sincere gratitude to the many people who have participated, directly or indirectly, in the development of this thesis.

I want to take this opportunity to express my heartfelt gratitude to Stephanie Lambert, Professor, Director of the Chemical Engineering Research Unit, for the opportunity and honour she has given me by welcoming me into her research unit. I would also like to express my deep appreciation for the interest she has consistently shown in my thesis work and for her invaluable support, advice, explanations, and comments on the results obtained, as well as for all the time she has devoted to proofreading the thesis and the publications that have resulted from it. I would also like to thank Prof. Emmanuel Djoufac Woumfo, co-supervisor of this thesis, for his guidance since my final year project and for the time he devoted to supervising the proofreading of the thesis and scientific articles. I also thank him for his trust and advice.

My sincere thanks also go to Prof. Benoit Heinrichs for his guidance and the enriching discussions we had during our laboratory meetings while I was conducting my research.

I would particularly like to thank Dr. Julien Mahy for his help, availability, and support. His wise advice and knowledge enabled me to move forward during the most difficult moments. I am very grateful to him for the help he gave me during certain experiments, for his explanations when interpreting the results, and for his corrections when drafting publications.

I would also like to thank Prof. Nathalie Fagel, head of the Clay, Geochemistry and Sedimentary Environment Research Unit (AGEs), for her help in conducting certain characterizations and analyzing their results, as well as for proofreading certain publications.

I would also like to thank Dr. Ernestine Mimba Mumbfu, my colleague, for the many scientific discussions throughout my thesis, her constant good humor, and her constant support. I would also like to thank Dr. Christelle Alié, Mr. Pierre Ngue Song, Mr. Joachim Caucheteux, and Mr. Antoine Farcy for their good humor, advice, and contributions during our laboratory meetings.

I would like to thank Dr. Alexandre Léonard for his help and support in carrying out certain characterizations.

I am very grateful to Dr. Steven Njonte Wouamba from the Laboratory of Chemistry of Natural Substances of Plant and Fungal Origin at the Ecole Normale Supérieure de Yaoundé for facilitating the analyses during my research.

My sincere thanks go to the coordinator of the 2022-2027 five-year development cooperation program of ARES, ULiège, and Pacodel for allowing me to carry out this research through a doctoral scholarship at the University of Liège.

I would also like to thank my thesis committee and the members of the jury for agreeing to evaluate this work.

I would also like to express my sincere gratitude to all the members of the Department of Chemical Engineering of the Faculty of Applied Sciences at the University of Liège, particularly Martine Lovato, Cédric Calberg, and Jérémy Greens, for their kindness and support.

I would like to warmly thank my friends and colleagues, in particular Linda Zangho, Dr. Gaelle Assomo, Dr. Nasser Nducol, Dr. Achille Kakeu, Phebe Teh, Dr. Donald Fossi, and Arline Sonita, for their encouragement over the years.

I would also like to thank Dr Patrick Fotsing and Dr Patrick Tsopbou from the Physico-Chemistry of Mineral Materials Laboratory for our daily discussions on clay minerals and their applications. I would like to give special thanks to Mandjewil Albert and Ngoungouré Fatimatou for the good times we shared.

I am very grateful to my parents, my siblings, and my in-laws for supporting me throughout my academic career and for believing in me. I want to express my heartfelt thanks to my twin sister, Dr Florette Fobasso, and her husband for their motivation, advice, and support during the writing of this thesis.

I would like to express my gratitude to Raoul Lowe, Dr. Idriss Nguefeu, Miyo Franck, Laeticia Laha, Arlette Yon, and their families for everything they have done for me during my stay in Liège.

I would like to express my gratitude to my friends and colleagues at the Institute for Geological and Mining Research (IRGM) who, throughout these years, have supported and encouraged me, and I hope that they find the fulfilment of their expectations here.

To my wonderful husband, Adrien Emeric, and my son Raphael Adriel, your faith in me has carried me through the toughest moments. Thank you for your love, sacrifices, and constant reassurance. This thesis is as much yours as it is mine.

My sincere thanks to all those who, directly or indirectly, contributed to the development of this thesis. Glory be to the Lord, the God of Hosts, for all He has done for me during this journey. Praise, honor, and worship belong to Him.

M. H. TSAFFO MBOGNOU

ABSTRACT

In the two first parts of this study, raw clays extracted from Bana, in western Cameroon, were modified with semiconductors (TiO_2 and ZnO) to improve their pollution control properties by adding photocatalytic properties. Cu^{2+}, Na^{+} and Zn^{2+} ions were added to the clay by ion exchange to increase the specific surface area, and to modify the charge of the clay surface. The results obtained from X-ray diffraction show that the clay belonged to the smectite family and was composed of different crystalline phases. The presence of TiO_2 and ZnO was confirmed by the detection of anatase and wurtzite, respectively. The composite clays showed increased specific surface areas. The pollutant removal properties of the samples were evaluated using different model pollutants: fluorescein (FL), *p*-nitrophenol (PNP), malachite green (MG) and diamond bright violet (DBV). It was demonstrated the possibility of obtaining highly effective hybrid materials for the removal of pollutants from water using inexpensive natural clay modified with a small amount of photocatalytic material (approximately 30% by weight of TiO_2 or ZnO).

The third step consisted of modifying the clay material with two silanes, tetramethoxysilane (TMOS) and [3-(2-aminoethyl)aminopropyl]trimethoxysilane (EDAS), to increase its adsorption properties. The modified clay is intended for use as an effective adsorbent for the removal of organic pollutants from water. Three clay/TMOS samples and two clay/EDAS samples with different [silane]/[clay] ratios were produced and characterized. Their adsorption properties were evaluated on three model organic pollutants (i.e., FL, MG, and DBV). The two types of clays modified with TMOS and TEOS, respectively, exhibit different adsorption behaviors for the three pollutants.

In the final part of this study, the growing presence of pharmaceuticals in wastewater, such as ibuprofen, which raises serious environmental and public health concerns, was demonstrated. Some photocatalytic ZnO and TiO_2-doped natural Cameroonian clays were used to ensure effective degradation of ibuprofen and bacterial inhibition under UV light (365 nm). Characterization confirmed the successful dispersion of semiconductors on the clay matrix. Under UV irradiation, the composites achieved significant degradation efficiencies, with mineralization monitored by total organic carbon (TOC), and antibacterial tests revealed notable inhibition against *Shigella spp*., supporting the dual functionality of the materials.

RESUME

Dans les deux premières parties de cette étude, des argiles brutes extraites de Bana, dans l'ouest du Cameroun, ont été modifiées avec des semi-conducteurs (TiO_2 et ZnO) afin d'améliorer leurs propriétés de contrôle de la pollution en leur ajoutant des propriétés photocatalytiques. Des ions Cu^{2+}, Na^{+} et Zn^{2+} ont également été ajoutés à l'argile par échange d'ions afin d'augmenter la surface spécifique et de modifier la charge de la surface de l'argile. Les résultats obtenus par diffraction des rayons X montrent que l'argile appartient à la famille des smectites et qu'elle est composée de différentes phases cristallines. De plus, la présence de TiO_2 et de ZnO a été confirmée par la détection d'anatase et de wurtzite, respectivement. En outre, les argiles composites ont montré une augmentation de leur surface spécifique. Enfin, les propriétés d'élimination des polluants des échantillons ont été évaluées à l'aide de différents polluants modèles : fluorescéine (FL), *p*-nitrophénol (PNP), vert de malachite (MG) et violet brillant diamant (DBV). Il a été démontré qu'il était possible d'obtenir des matériaux hybrides très efficaces pour l'élimination des polluants de l'eau en utilisant de l'argile naturelle peu coûteuse modifiée avec une petite quantité de matériau photocatalytique (environ 30 % en poids de TiO_2 ou de ZnO).

La troisième étape de cette thèse consistait à modifier l'argile à l'aide de deux silanes, le tétraméthoxysilane (TMOS) et le [3-(2-aminoéthyl)aminopropyl]triméthoxysilane (EDAS), afin d'augmenter ses propriétés d'adsorption. L'argile modifiée est destinée à être utilisée comme adsorbant efficace pour éliminer les polluants organiques de l'eau. Trois échantillons d'argile/TMOS et deux échantillons d'argile/EDAS avec différents rapports [silane]/[argile] ont été produits et caractérisés. Leurs propriétés d'adsorption ont été évaluées sur trois polluants organiques modèles (à savoir FL, MG et DBV). Les deux types d'argiles modifiées respectivement avec du TMOS et du TEOS présentent deux comportements d'adsorption différents pour les trois polluants.

Dans la dernière partie de cette étude, la présence croissante de produits pharmaceutiques dans les eaux usées, tels que l'ibuprofène, qui soulève de graves préoccupations pour l'environnement et la santé publique, a été démontrée. Dans cette étude, des argiles naturelles camerounaises dopées au ZnO et au TiO_2 ont été utilisées pour assurer une dégradation efficace de l'ibuprofène et une inhibition bactérienne sous lumière UV (365 nm). La caractérisation a confirmé la dispersion réussie des semi-conducteurs sur la matrice argileuse. Sous irradiation UV, les composites ont atteint des efficacités de dégradation significatives, la minéralisation étant contrôlée par le carbone organique total (COT), et les tests antibactériens ont révélé une inhibition notable contre Shigella spp., confirmant la double fonctionnalité des matériaux.

Table of contents

CHAPTER I: General Introduction

1.1. Wastewater problems in Cameroon

The drinking water supply is essential to the population's socio-economic and environmental development. The international community is concerned about this issue, which is included in the sixth sustainable development goal (United Nations Regional Information Centre) [1]. Drinking water must comply with the drinking water quality standards set by the World Health Organization. Reasonable minimum requirements are established for safe practices to safeguard consumers' health. Wastewater management in Cameroon presents several challenges that directly impact public health, the environment, and socio-economic development. Most towns in Cameroon lack adequate wastewater treatment systems. Existing infrastructure is often aging and poorly maintained, leading to frequent overflows. Untreated wastewater is generally discharged into nearby rivers or streams, contaminating sources of drinking water and aquatic ecosystems. This pollution exposes people to health risks such as cholera, waterborne diseases, diarrhea, and parasitic infections. For example, in the case of the Cité-Verte wastewater treatment plant in Yaoundé (the capital of Cameroon), which is designed to treat wastewater with an estimated pollutant load of 5.000 population equivalents, the daily flow of wastewater to be treated is 805 m^3/day. This water, which generally has a very high pollutant load (bacteria and organic compounds), is discharged into the shallows, where some residents use it for various purposes, such as watering vegetable crops and washing clothes and vehicles. So, the Cité-Verte wastewater treatment plant is capable of eliminating certain pollutants (Chemical Oxygen Demand (COD), the five-day Biochemical oxygen demand (BOD_5), suspended solids in water (SS)) present in wastewater.

In most wastewater treatment plants (WWTPs) in Cameroon, only conventional plant-filter systems are used. These biological treatments are unable to treat complex substances, and they are insufficient for the complete elimination of pharmaceutical and bacteriological substances received by these WWTPs. It is therefore important to direct our research efforts towards the development of ternary or finition treatments, which would degrade these micropollutants and bacteria. However, some micropollutants, because of their persistence, toxicity, their very low concentration (µg/L to ng/L) in the environment, and their bioaccumulation, are a paramount public health concern throughout the world [2]. It is, therefore, crucial to focus on their fate and removal processes by conventional facilities, which can remove traditional pollutants (concentration mg/L). According to the Growth and Employment Strategy Paper [3], 86.2% of large towns in Cameroon are equipped with drinking water supply systems. However, only 25%

of households have permanent access to it [4]. In 2018, the Ministry of Water and Energy launched various projects aimed at strengthening the drinking water production system in urban areas. These projects included the implementation of a drinking water supply project for the city of Yaoundé and the surrounding area, aimed at increasing production by 300.000 m^3 per day. However, despite these initiatives, access to drinking water in urban areas still seems limited, and residents of outlying districts have very little access to it. As water is rarely supplied by the public network in these areas, other sources such as wells and springs are often used for domestic work, cooking, personal hygiene, and even direct consumption. This leads to dangers to the health of residents. Indeed, the compliance of this water with the requirements of the Cameroonian standard has to be taken into account. According to Nzouebet *et al.* [5], 3% of households in Yaoundé do not have a toilet and defecate outside. National Institute of Statistics - Federal Institute for Geosciences and Natural Resources (INS-BGR)[6] shows that around 52% of households drain toilet water into septic tanks, while 34% pour it into a hole. In addition, up to 15% use the gutters that serve the neighborhoods to evacuate their household wastewater. If inadequately managed, this waste could represent a major source of contamination for the water table.

Due to their numerous applications, natural clay minerals are currently the focus of various research investigations. This is supported by their strong sorption qualities, ion exchange potential, and natural abundance on the majority of the world's continents at a moderate cost [7] [8]. This is explained in Section 1.2 for the case of Cameroon, because of its position and the diversity of its basement rocks. Adsorption was observed to be advantageous over other wastewater treatment methods in terms of initial price, simple in design, easy to use, and not sensitive to harmful substances [9] [10]. This is widely used to eliminate complex contaminants from wastewater like dyes. The precautionary principle applied to persistent micropollutants inherently relies on powerful and unselective methods to address this problem. As it shall be shown in Section 1.3, under certain conditions, the adsorption reaction of a solute can be carried out in several successive elementary stages, each of which can influence the overall phenomenon.

In Section 1.4, advanced oxidation processes (AOPs) are emerging as promising technologies in the field of wastewater depollution. Heterogeneous photocatalysis appears to be a highly effective and economical alternative that can destroy micropollutants while leading to complete mineralization [7]. In this work, the challenge is to resolve issues relating to wastewater quality after treatment and propose its safe reuse to deal with the scarcity of water resources, which is a real problem in all regions of Cameroon.

1.2. Use of natural clays for the adsorption of micropollutants

The breakdown of rock minerals produces some clays. Understanding clays' chemical composition and mineral morphology is necessary for their use in industrial applications. Cameroon has an abundance of clay deposits [11-15]. The majority of these studies examined the origins of minerals present in clay deposits. More particularly, some research has been conducted on the clay deposit from Akilbenza, a location in Cameroon's Eastern Region. This clay mineral has a significant potential to remove both organic and inorganic contaminants, including heavy metals, because of its intriguing physico-chemical properties (lamellar structure and surface qualities).

1.2.1. The composition of phyllosilicates

Clays are a family of phyllosilicate minerals. Their structure is based on a two-dimensional silicate sheet formed by the stacking of tetrahedral and octahedral layers (Figure 1.1). O^- ions occupy the vertices of the tetrahedral layer, while those of the octahedral layer are occupied by OH^- ions [16].

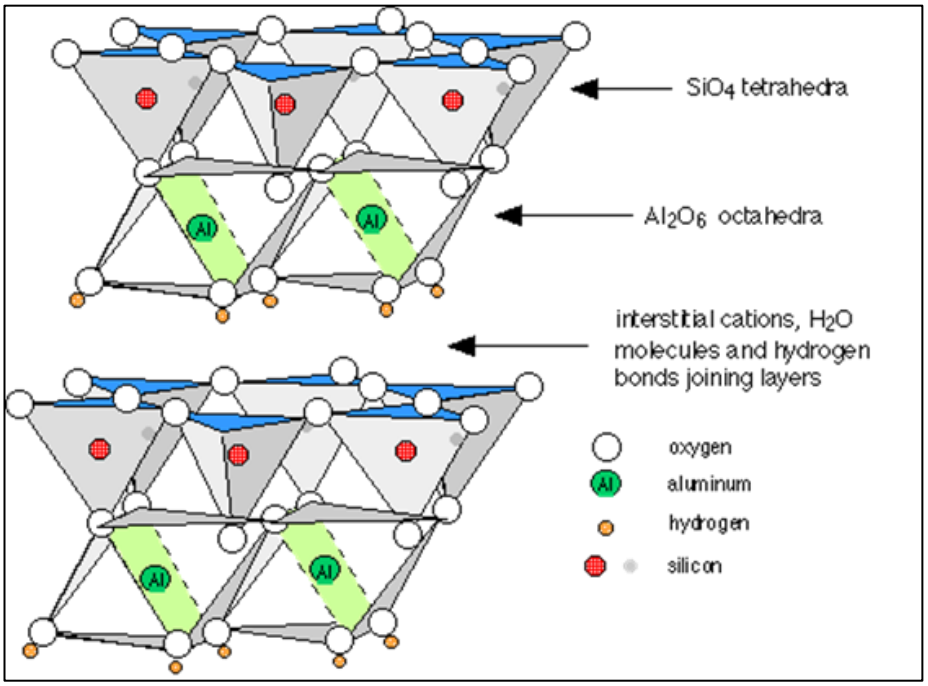

Figure 1.1: Representation of tetrahedra (a) and octahedra (b) layers [16].

The layer, the primary particle, and the aggregate are the three structural components that can be used to characterize clay mineral systems. The layer is made up of two or three tetrahedral or octahedral layers that are bonded together with strong connections. These layers can be assimilated to a plate or disc with a thickness of roughly 1 nm and are comparatively flexible and malleable (Figure 1.2). The area between these layers, named as the interlayer space, can be empty or contain hydrated alkaline and alkaline earth cations. The lateral diameters of these

layers range from 1 to 1000 nm. The physico-chemical and mineralogical properties of the clay fraction are influenced by the composition of this layer.

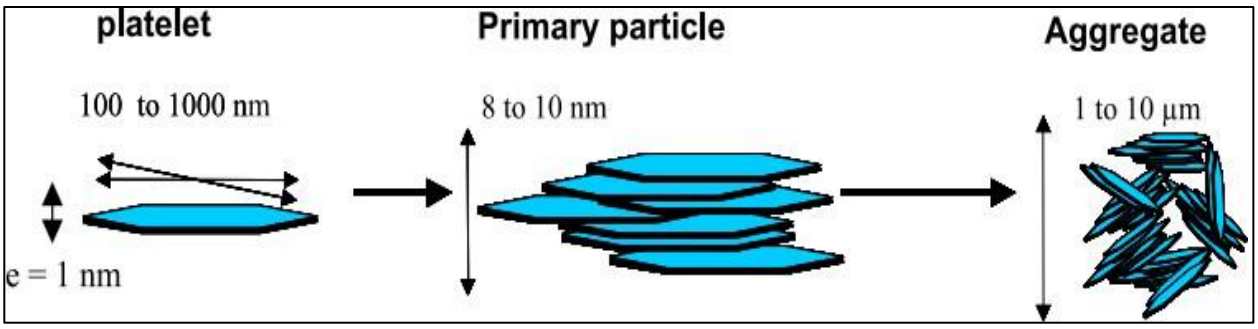

Figure 1.2: Multiscale Structure of a Clay Mineral [17].

The International Association for the Study of Clays (AIPEA) [18] established a classification of clay minerals based on three criteria: the type of sheet, the overall charge of the sheet, and the nature of the interfoliar cations.

1.2.2. Types of sheet

Based on the number and arrangement of tetrahedral (silica) and octahedral (alumina-magnesia) sheets, phyllosilicates can be classified into three different groups (Figure 1.3):

a) Minerals with classification T:O or sheet 1:1: a tetrahedral layer (T) and an octahedral layer (O) make up the sheet. It is about 7 Å thick. Kaolinite is an illustration of this (Figure 1.3 (1.1)).

b) Minerals with a T:O:T or sheet 2:1 composition: the sheet is made up of two tetrahedral layers (T), with an octahedral layer (O) sandwiched between them. It is approximately 10 Å thick (Figure 1.3 (2.1)). The talc, smectite, vermiculite, illite, and mica groups belong to this family.

c) Minerals 2:1:1 samples composed of alternating T-O-T sheets with an octahedral layer (O) between them, making it an interfoliar. The chlorite group corresponds to this type (Figure 1.3 (2.1.1)).

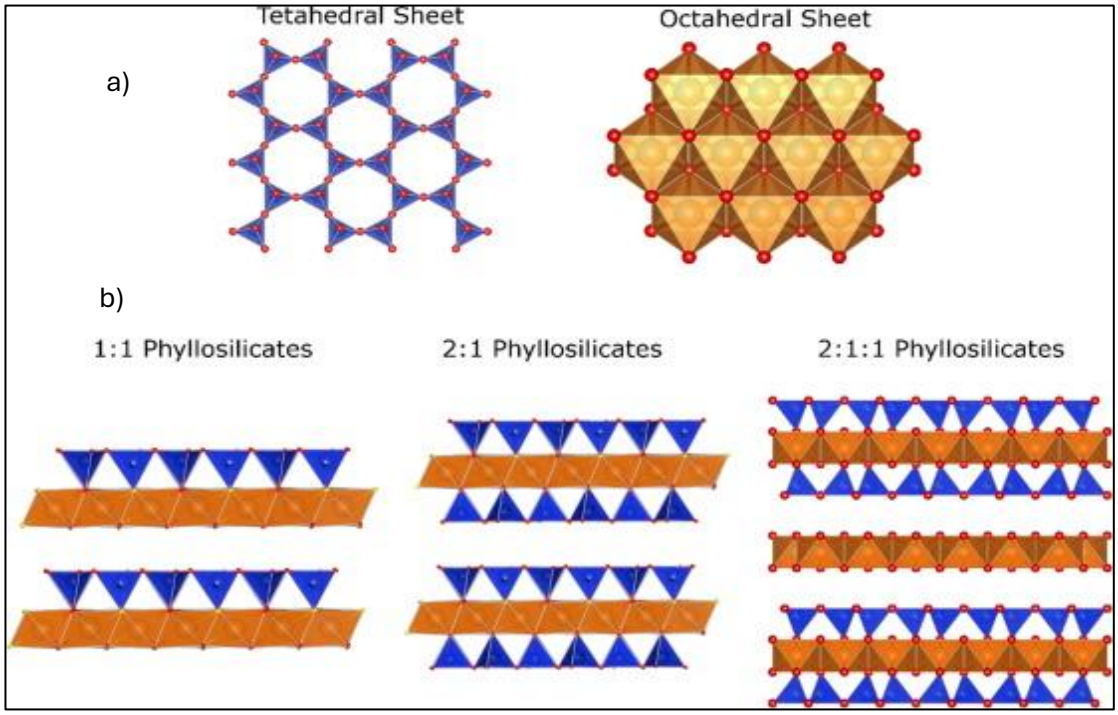

Figure 1.3: (a) Graphical representation of the tetrahedral and octahedral sheets in phyllosilicates and (b) phyllosilicates classification in function of the number of tetrahedral and octahedral sheets (down) [19].

A discontinuity in their octahedral layer gives palygorskite and sepiolite, fibrous clay minerals, a lath-like morphology instead of continuous sheets, setting them apart from 2:1 type minerals. They belong to a distinct family of minerals because of this structural feature. The crystal structures of sepiolite and palygorskite (also called attapulgite) are made up of 2:1 (t:o:t, tetrahedral:octahedral:tetrahedral) pseudo-leaflets with particular inversions of the tetrahedral sheets. Water molecules and exchangeable cations are stored in channels or tunnels created by this inversion. Figure 1.4 presents the arrangement of octahedral and tetrahedral layers in phyllosilicates [20].

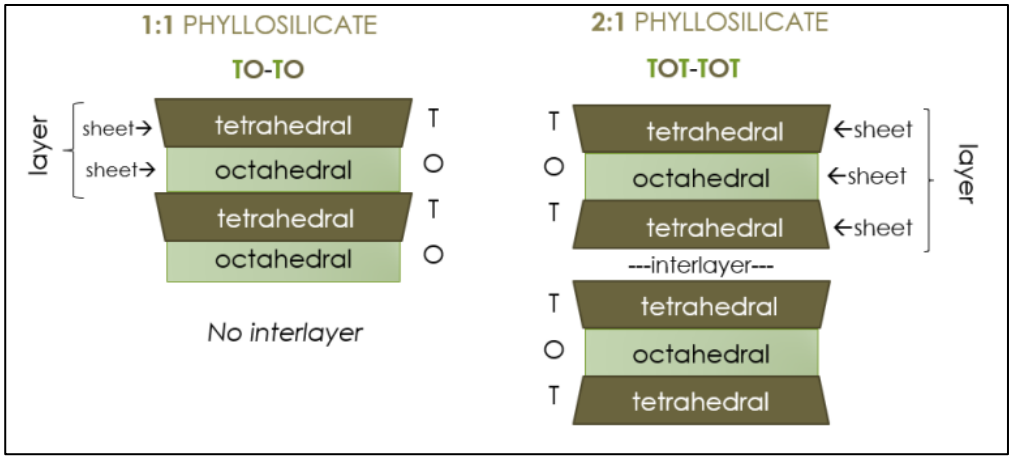

Figure 1.4: Arrangement of octahedral and tetrahedral layers in phyllosilicates [20].

1.2.3. Overall charge of the sheet of phyllosilicates

A charge deficit is observed in tetrahedral layers (Si^{4+} ions replaced by Al^{3+}, Fe^{3+} ions) and/or octahedral layers (Al^{3+} ions replaced by Mg^{2+}, Fe^{2+} ions or Mg^{2+} ions replaced by Li^{+} ions) due to isomorphic substitutions. A classification of phyllosilicates has been proposed by McKenzie [21] and Brindley [22], and is based on the value of the permanent charge of the sheet obtained by these ion substitutions (Table 1.1). The alkali or alkaline-earth cations in the interfoliar spaces compensate for the lack of charge in the clay mineral sheets.

Table 1.1: Classification of 1:1 and 2:1 phyllosilicates according to charge [21].

Layer	Interlayer	Layer charge	Species	Formula
1:1	None or H_2O only	≈ 0	Kaolinite	$Al_4\,Si_4O_{10}(OH)_8$
			Krysotile	$Mg_6\,Si_4O_{10}(OH)_8$
2:1	None	≈ 0	Pyrophyllite	$Al_4\,Si_8O_{20}(OH)_4$
			Talc	$Mg_6\,Si_8O_{20}(OH)_4$
	Hydrated exchangeable cations	0.4 - 1.2	Montmorillonite	$M^{n+}_{x/n}[Al_{4-x}Mg_x][Si_8]O_{20}(OH)_4.nH_2O$
			Beidellite	$M^{n+}_{x/n}[Al_4][Si_{8-x}Al_x]O_{20}(OH)_4.nH_2O$
			Nontronite	$M^{n+}_{x/n}[Fe_4][Si_{8-x}Al_x]O_{20}(OH)_4.nH_2O$
		1.2 - 1.8	Saponite	$M^{n+}_{x/n}[Mg_6][Si_{8-x}Al_x]O_{20}(OH)_4.nH_2O$
			(F-)hectorite	$M^{n+}_{x/n}[Mg_{6-x}Li_x][Si_8]O_{20}(OH,F)_4.nH_2O$
			Vermiculite	$[Mg,Ca]^{2+}_{x/2}[Al_{4-x}Mg_x][Si_8]O_{20}(OH)_4.8H_2O$
			Vermiculite	$[Mg,Ca]^{2+}_{x/2}[Mg_6][Si_{8-X}Al_x]O_{20}(OH)_4.nH_2O$
	Non-hydrated cations	1.0 2.0	Paragonite	$Na_2[Al_4][Si_6Al_2]O_{20}(OH)_4$
			Phlogopite	$F_2[Mg,Fe]_6[Si_6Al_2]O_{20}(OH,F)_4$

1.2.4. Classification of phyllosilicates based on the nature of the interlayer cation

Phyllosilicates or sheet silicates can be classified based on the nature of the interlayer cations present between the silicate layers [20]. There are:

- Monovalent cations: micas and vermiculites ;
- Divalent cations: chlorites and smectites ;

- Trivalent cations: kaolinites and illites ;
- Varied cations: talc and serpentine.

This classification highlights the importance of interlayer cations in determining the properties and behavior of phyllosilicate minerals. Each category exhibits distinct characteristics influenced by the type and arrangement of these cations. An example of the classification of phyllosilicates based on the nature of the interlayer cation can be illustrated using smectite group clays (Table 1.2).

Table 1.2: Smectite group – classified by interlayer cation type [20].

Mineral Name	Interlayer Cation	Description
Na-montmorillonite	Na^{+}	Expands readily in water; commonly used in drilling muds.
Ca-montmorillonite	Ca^{2+}	Less swelling than Na-montmorillonite; more stable in freshwater.
Fe-montmorillonite (nontronite)	Fe^{3+} or Fe^{2+}	Iron-rich variety; often greenish in color.
Mg-smectite (saponite)	Mg^{2+}	Often associated with basaltic rocks, relatively high cation exchange capacity.

The interlayer cation in phyllosilicates like smectites can vary (e.g., Na^{+}, Ca^{2+}, Mg^{2+}), and this affects properties like swelling behavior, cation exchange capacity, and stability. This variation forms the basis for subclassifying them. Smectites, which include for example bentonite, nontronite, saponite, montmorillonite, are phyllosilicates of type 2:1. Smectites have a general structure of:

$(Ca, Na, H)_{0.33}(Al, Mg, Fe)_2(Si, Al)_4O_{10}(OH)_2.nH_2O$

where $(Ca, Na, H)_{0.33}$: exchangeable interlayer cations that balance the negative charge resulting from layer substitutions. They might vary in quantity and be hydrated ;

where $(Al, Mg, Fe)_2$: octahedral sheet (O-sheet) cations.

If Al → dioctahedral smectite, such as montmorillonite, predominates.

If mostly Mg/Fe → trioctahedral smectite,such as saponite, predominates.

where $(Si, Al)_4O_{10}$: T-sheets, or tetrahedral sheets, are primarily composed of SiO_4 tetrahedra, with the possibility of Al replacement.

where $(OH)_2$: octahedral sheet's hydroxyl groups.

The variable amount of interlayer water, or nH_2O, is what causes smectite to expand [23].

Because of this potential for swelling, smectites are referred to as swelling clays, and their interlayer spacing can range from 10 Å to 21 Å. These clays have a large, persistent, negative, and pH-independent charge due to isomorphic replacements at the interlayer region. Clays have a high capacity for exchanging cations. The action of water can cause soils with high smectite concentrations to increase in volume by 30%. These minerals' exceptional plastic, colloidal, swelling, and physico-chemical properties enable their use in a variety of fields, including medicine, drilling fluids, water treatment, ceramics, papermaking, and dyes [23].

Cation exchange capacity (CEC) is the proportion of smectites that absorb cationic species from solution. Polymeric hydroxides of aluminum, iron, chromium, zinc, and titanium can be intercalated into smectites for cation exchange. These 'pillar clays' present high values of specific surface area and porosity, a high acidity, and catalytic properties when heated. Similarly, cationic organic molecules (such as aliphatic and aromatic amines, pyridines, and methylene blue) can substitute exchangeable inorganic cations in the interlayer space, while polar non-ionic organic molecules can substitute water adsorbed on the external surfaces. In this family, bentonite and montmorillonite are the most prevalent clay minerals.

1.2.5. Montmorillonite

Within the sheets, certain Al^{3+} cations are replaced by Mg^{2+} ions. There is a lack of charge in the sheet, and compensating cations must be added to the structure to obtain a neutral compound. Na^+ and Ca^{2+} ions are the most common compensating cations in natural montmorillonite. When montmorillonite is exposed to water, it swells, which means that this mineral absorbs water in the space between the sheets, known as the interfoliar space, as well as in any other accessible porosity. When water is present, the cations are hydrated. This alters the electrical forces and leads to a distance between the sheets, resulting in swelling. The impact of the hydration state of the clay on the swelling of the structure can be understood qualitatively by taking into account the electrostatic forces between the interfoliar cation and the surface [24]. When water molecules interfere with electrostatic interactions, these forces decrease. The concepts of clay hydration and swelling can therefore be associated with electrostatic interactions.

The theoretical structural formula for montmorillonite is as follows (Figure 1.5):

$Na_{0,26}\ Ca_{0,02}\ K_{0,20}[Al_{2,48}\ Mg_{0,40}\ Fe_{0,34}\ Ti_{0,02}]Si_{8,48}\ O_{20}(OH)_4$

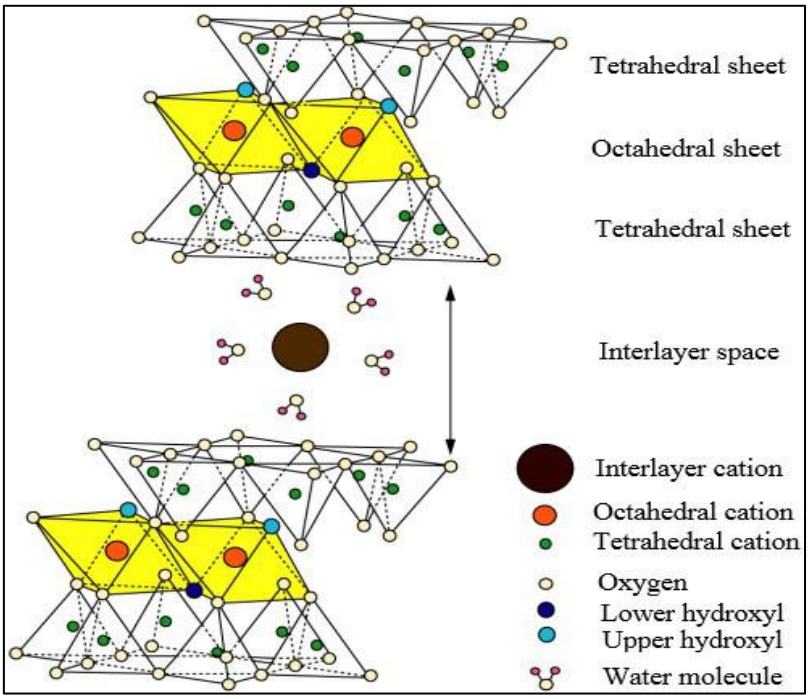

Figure 1.5: Schematic representation of the montmorillonite structure [24].

The technological uses of montmorillonite are mainly related to reactions taking place in the interlayer spaces. The 2:1 negative charge is balanced by the elements Na^+, K^+, Ca^{2+}, and Mg^{2+}, which are usually hydrated and exchangeable. The water molecules are adsorbed at the surfaces of layers and in the spaces between layers [25].

Hydrophilic surfaces immersed in water have a strong attraction to the water molecules in the vicinity, resulting in the formation of ordered boundary layers on the surfaces. This phenomenon is termed hydration, and the layer is termed the hydration layer. Three modes of hydration are generally identified (recognized as pH-dependent) :

- Hydration of the primary clay mineral particles between the different layers;
- Continuous hydration due to unlimited adsorption of water on internal and external surfaces;
- Capillary condensation of free water in the mesopores.

The hydration layer on a hydrophilic surface is schematically depicted in Figure 1.6. Compared to bulk water, the water in hydration layers is denser and more viscous. Hydration layers have been discovered to be essential in a wide range of scientific and technical domains [26].

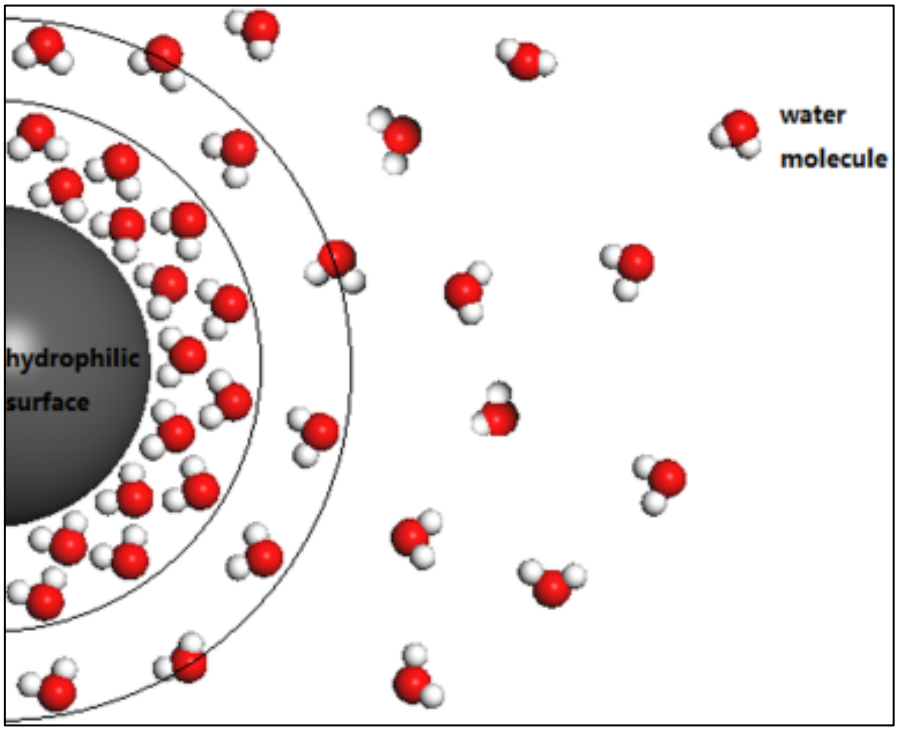

Figure 1.6: Schematic view of hydration layer on hydrophilic surface. Water molecules in the small concentric circles can be attracted to the vicinity of a hydrophilic surface to form ordered layers [26].

The main components of interlayer hydration include:

(i) hydration of interlayer cations,

(ii) interactions between clay surfaces and water molecules and interlayer cations.

Interlayer hydration complexes can be distinguished from smectites, which are the result of the intercalation of a variable number of water layers. This number varies from zero to three, corresponding to the creation of hydrates in layers of zero, one, two or three.

The interlayer hydration of smectites is influenced by several factors:

(i) the hydration energy of the interlayer cation;

(ii) the polarization of water molecules by interlayer cations;

(iii) variations in electrostatic surface potentials due to variations in the location of the layer's charge;

(iv) water activity.

In the interlayer space, it is possible to create two types of hydration complexes: "inner sphere" and "outer sphere" complexes. In the first situation, the cation is directly attached to the clay

surface on the one hand and to a certain number of water molecules on the other, whereas in the outer sphere hydration complexes, the interlayer cation is surrounded by water molecules.

1.2.6. Origin of hydration layers on clay mineral surfaces

There is a fundamental difference between the 1:1 and the 2:1 layers (Figure 1.7). The 2:1 layer is bounded on both sides by basal oxygen planes, whereas the 1:1 layer has basal oxygens on one surface and hydroxyls on the other surface. The interlayer bonding for the 1:1 layer silicates, whether dioctahedral or trioctahedral, is by hydrogen bonds from one hydroxyl surface to the adjacent oxygen surface of the neighboring 1:1 layer. Although they are long hydrogen bonds, there are many of them, and the contribution to the interlayer bonding is strong. The 2:1 layer is more complex because it is possible to have a net layer charge as a result of isomorphous substitution. Al for Si in the tetrahedral sheet and Mg for Al in the octahedral sheet are most common. Such a situation would be unstable due to the electrostatic repulsion between all the layers, so the charge must be balanced by an extra positive charge [26].

Hydrogen bonds make up the majority of the unsaturated bonds visible on the basal surface of 1:1 clay minerals like kaolinite and serpentine. Illite, smectite, and vermiculite are examples of 2:1 clay minerals with a high degree of isomorphous substitution, where the unsaturated bonds are mostly ionic bonds brought by the silica tetrahedron anions on the electronegative layer-charged siloxane surface. Also, as in talc and pyrophyllite, the exposed unsaturated bonds are basically van der Waals bonds resulting from the neutral siloxane surface. Among all these unsaturated bonds, the hydrogen bonds and ionic bonds are relatively strong, whereas van der Waals bonds are very weak. So in aqueous solution, to compensate for the unsaturated bonds, the surfaces with the unsaturated hydrogen bonds and ionic bonds are capable of having strong interactions with water molecules and hydrated cations, and strong hydration layers can easily form on these types of clay mineral surfaces [26].

1.3. Adsorption of molecules at the surface of materials

The adsorption phenomenon of molecules at the surface of solid materials is currently one of the most crucial separation methods. It is commonly used to purify gases and liquids in various environmental and pharmaceutical sectors [27]. There are two distinct types of adsorption mechanisms: physical and chemical. Nonspecific or electrostatic forces between substances in solution and the surface of the solid are responsible for physical adsorption (or physisorption). The former are interactions with Van Der Waals forces, while the latter are interactions between permanent or induced dipoles and hydrogen bonds. Covalent or electrostatic chemical bonds

between the adsorbate and the adsorbent are called chemical adsorption (or chemisorption). As a general rule, chemisorption is irreversible and causes a transformation of the adsorbed molecules (exchange of matter). In comparison, physisorption is faster and partially reversible.

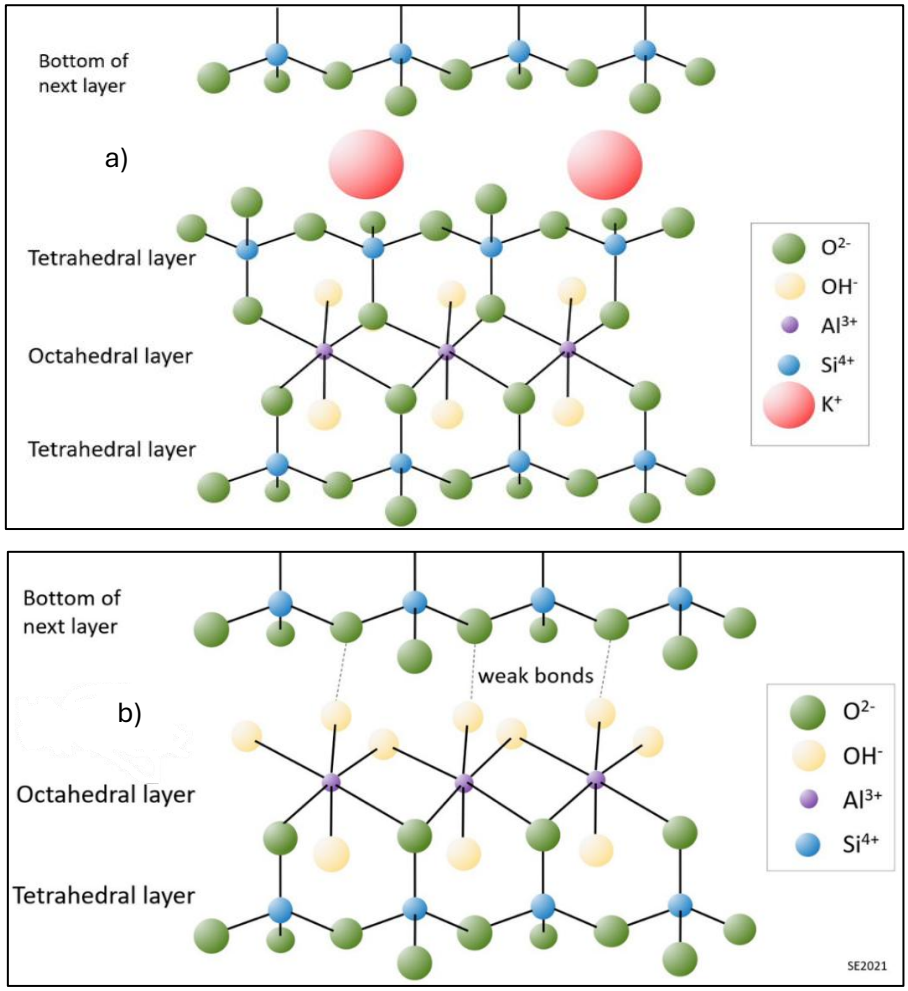

Figure 1.7: Layered structures composed of silicon tetrahedron and aluminum octahedron sheets. (a) smectite, which belongs to the 2:1 clay mineral with isomorphous substitution. There are exchangeable cations in the interlayer space. (b) kaolinite, which belongs to the 1:1 clay mineral. There are no exchangeable cations in the interlayer space [26].

Under certain conditions, the adsorption reaction of a solute can be carried out in several successive elementary stages, each of which can influence the overall phenomenon. Let's take the example of adsorption on a porous adsorbent. In this situation, solute adsorption takes place in 4 main stages [28] :

- the movement of the molecule towards the outer surface of the adsorbent. It results from a mechanism of molecular diffusion.
- The movement of the molecule from the outside of the adsorbent towards the inside of the pores;

- the adsorption of the molecule at the surface of the adsorbent or inside the pores of the adsorbent. This step is often extremely rapid and has no impact on the overall process.
- the movement of the adsorbed molecules from the surface of areas where the concentration of the adsorbed phase is high to regions where the concentration is low. This phase is known as internal diffusion in the solid.

1.3.1. Adsorption isotherm

Any adsorption system's isotherm is an equation which relates the amount of adsorbate on the adsorbent surface and the adsorbent's concentration or partial pressure at constant temperature [29]. Mostly used adsorption isotherm models for contaminants removal are the Langmuir isotherm and the Freundlich isotherm, which are used to gain extensive knowledge on the relationships between the adsorbent surface and the adsorbate [30].

For Langmuir adsorption, the adsorbent's surface is homogeneous, meaning almost all binding sites are equal. Adsorbed molecules don't come into contact with each other. And there is the formation of a monolayer of adsorbed molecules. The Langmuir isotherm is given as [31] [32]:

$$\frac{C_e}{q_e} = \frac{1}{q_{max}K_L} + \frac{C_e}{q_{max}} \tag{1.1}$$

where C_e is the concentration of the adsorbate at equilibrium (mg/L), q_e and q_{max} are the amount of adsorbed molecules at the surface at any time and at the end of the adsorption process (maximum adsorption capacity) (mg/g), and K_L is the Langmuir constant (L/mg). When C_e/q_e is plotted against C_e, a straight line with a slope of $1/q_{max}$ and an intercept of $1/K_L\ q_{max}$, is obtained.

The Freundlich model is based on the following key assumptions: the surface of the adsorbent is heterogeneous, and the adsorption sites have a non-uniform energy distribution. It is an empirical model that generally applies to low concentrations and suggests that adsorption can be single-layer or multi-layer. The mathematical expression of the Freundlich isotherm is [33] [34]:

$$ln(q_e) = ln(K_F) + \frac{1}{n}\ ln(C_e) \tag{1.2}$$

where K_F is the Freundlich constant or adsorption capacity (L/mg), n represents the extent of heterogeneity in the surface and defines how the adsorbate is distributed on the adsorbent surface. As ln q_e is plotted against ln C_e, a straight line with a slope of 1/n and an intercept of ln K_F emerges.

1.3.2. Parameters affecting the adsorption process

Main parameters which influence the mechanism of adsorption include: i) specific surface area of adsorbent ; (ii) adsorbate's nature ; (iii) initial concentration of adsorbate ; (iv) pH of the solution ; (v) temperature ; (vi) pressure, and (vii) contact time [35].

Specific surface area of adsorbent: Adsorption is a surface phenomenon, so it is directly proportional to the specific surface area of the adsorbent, which may be known as the total free surface area available for adsorption. So it is more interesting to use very porous adsorbents, giving a larger quantity of surface per unit mass of this adsorbent [35].

Adsorbate's nature: the adsorbate solubility plays a very important role in the progression of the adsorption mechanism, and also the rate of adsorption. If the adsorbate is completely soluble in the solvent, then the affinity of the solute with the solvent is high [37]. Therefore, it is possible to suggest an inversely proportional relationship between the degree of adsorption and its solute solubility [38].

Initial concentration of adsorbate: the initial concentration of the adsorbate in the solution creates the driving force (concentration gradient) for mass transfer between the solution and the adsorbent [39]. The impact of the initial concentration of adsorbate on the adsorption rate and uptake capacity is that at lower concentration, the ratio of the number of solute molecules to the adsorbate surface is low, and after some time, the adsorption process becomes independent of the initial concentration of the solute [40]. At high concentrations, however, the ratio becomes high, i.e., the unused adsorption sites for adsorbate decrease, and the adsorption uptake capacity depends on the initial concentration [35].

pH of the solution: the solution's pH affects the degree of adsorption. H^+ or OH^- ions present in the solution are adsorbed at the surface of the adsorbent, thereby influencing the adsorption process, resulting in a shift in the kinetics of the adsorption reaction and in the properties of equilibrium [41] [42]. For example, at low pH, the number of adsorbed H^+ ions at the surface of the adsorbent increases. So the surface of the adsorbent becomes positively charged. Since the adsorbent surface is positively charged at low pH, an attractive electrostatic force forms between these positive charges and the negative charge molecules in the solute, resulting in a full sorption process.

Contact time: In particular, the adsorption efficiency improves with increased contact time. The amount of adsorbate adsorbed on the adsorbent surface increases rapidly at the initial stage, and then at a certain stage, this adsorption rate slows down a bearing [43].

Clays have been studied extensively for their ability to adsorb several types of pollutants, particularly micropollutants like dyes, heavy metals, pesticides, and medicines. They are especially efficient adsorbents because of their high specific surface area, cation exchange capacity, and surface charge properties [44]. For example, the alkaline activation of bentonite increases the distance between the leaves, increasing the specific surface area. Another way to modify clay is to intercalate between sheets, large single or mixed metal polycations. This method results in microporous materials with a rigid structure for large interfoliar spacing, and a very stable thermal structure. Luo *et al.* [40] have modified montmorillonites using a gemini surfactant. A gemini surfactant consists of two conventional surfactant molecules chemically bonded together by a spacer. Methyl orange is adsorbed by this modified clay with a capacity that can reach more than 200 mg/g. According to Ren *et al.*[42], Montmorillonite modified with Fe polycation and cetyltrimethylammonium bromide (CTMAB) was used to remove As(V) and As(III) ions from waste waters. Different authors have suggested the use of modified clay to remove other anions such as fluorides, perchlorates, chromates, nitrates, phosphates, etc. [45] [46]. Kaolinite, a 1:1 alumino-silicate clay, adsorbs cationic dyes like methylene blue through electrostatic interactions. The dye molecules, being positively charged, are attracted to the negatively charged surface sites of kaolinite. The presence of electrolytes can enhance this adsorption by increasing the ionic strength of the solution, which reduces the repulsion between dye molecules and the clay surface [46]. Montmorillonite, a smectite clay, exhibits high cation exchange capacity and surface area, facilitating the adsorption of anionic pharmaceuticals like diclofenac. At pH levels above the pKa of diclofenac (approximately 4.5), the drug exists predominantly in its anionic form, which can interact with the positively charged sites on the clay surface. Antonio Gil *et al.* [47] show that pillared clays, such as Al-pillared montmorillonite, have enhanced interlayer spaces due to the introduction of metal oxide pillars. This increased porosity allows for the adsorption of larger organic molecules like bisphenol A (BPA) through π-π interactions and hydrogen bonding.

Thibault *et al.* [48] examined the adsorption of tramadol and doxepin, two pharmaceutical micropollutants, onto sodium-exchanged smectite clay. The results indicated that the adsorption was primarily driven by electrostatic interactions, with the drugs intercalating into the clay's interlayer space in a monolayer arrangement. The study also observed that additional doxepin molecules could adsorb via weak molecular interactions, especially at lower temperatures.

Yan *et al*. [49] investigated the use of calcium-montmorillonite for removing tetracycline, a type of antibiotic micropollutant, from water. The study found that under optimized conditions, over 90% of tetracycline was removed, with a maximum adsorption capacity of 526 mg/g. The

adsorption process was influenced by various factors, including pH, adsorption duration, concentration, and co-cations (Na^+ and Ca^{2+}), with the Langmuir model providing the best description of the monolayer adsorption process. These investigations demonstrate the ability of clay minerals to absorb a range of micropollutants. Clays can be made more effective for particular contaminants by altering them to increase their hydrophobicity or interlayer spacing. It is essential to understand how clays and micropollutants interact to create effective and long-lasting remediation techniques.

1.4. Overview of advanced oxidation processes and their principles

Organic micropollutants can be oxidized into harmless substances like carbon dioxide and water by different "advanced oxidation processes (AOPs)". Khan *et al.* [50] list six different AOPs: photolysis, photochemical processes, photocatalysis, cavitation, and electrochemical processes.

1.4.1. Photolysis

Photolysis is the process of generating radicals by the direct action of energetic light on water. Generally, VUV (vacuum ultraviolet) light is used for standalone photolysis. This causes water to undergo two main reactions [51]: homolysis and ionization (Equations 1.3 and 1.4).

$$H_2O \rightarrow OH^{\cdot} + H^{\cdot} \quad (1.3)$$

$$H_2O \rightarrow H^+ + e^- + OH^{\cdot} \quad (1.4)$$

The quantum yield of this process is close to 1 for hydroxyl radical production for the range of light wavelengths proposed. However, it suffers from a few disadvantages.

Photolysis is dependent on the absorption of light by water. It can be calculated using Beer's law (Equation 1.5).

$$A=\alpha_\lambda\, l \quad (1.5)$$

where A is the absorbance, α_λ is the absorption coefficient (m^{-1}), where the index λ represents the wavelength of light used (nm), and l is the path length (m). For water, α_λ is very high in the far UV (orders of magnitude: 107 m^{-1} at λ = 140 nm; 100 m^{-1} at λ = 180 nm). Thus, photolysis in water using that type of light has a very short range under the surface. In industrial applications, degradation of pollutants would only be made possible by secondary oxidative species rather than $OH^{\cdot}$ radical itself, which cannot diffuse far from its place of creation due to its very short lifetime. Furthermore, this type of light will produce ozone when it travels through

O_2 (Equations 1.6 and 1.7). Ozone is toxic to human health, and its release in the environment is forbidden. Conversely, it can have a beneficial impact on AOPs as it is a powerful oxidizer.

$$O_2 \xrightarrow{h\upsilon} 2O^{\cdot} \tag{1.6}$$

$$O^{\cdot} + O_2 \rightarrow O_3 \tag{1.7}$$

1.4.2. Photochemical processes

These processes consist of using the previously described types of light with one or several chemicals to produce reactive radicals. The two most common chemicals are hydrogen peroxide (H_2O_2) and ozone (O_3). UVA, UVB, and UVC lights can create $OH^{\cdot}$ radicals from H_2O_2. This renders these processes as potent as VUV photolysis, with the advantage that there is no significant surface effect due to the penetration of light. However, the chemicals have a cost, and process limitations are associated with them. In the case of ozone, commercial generators rely on 185-nm lamps or on the corona discharge technology, where arcs of electricity are generated in air at high voltage. These technologies have relatively high capital costs, but moderate operating costs. H_2O_2 decomposes well when exposed to UV, with quantum yields Φ equal to 0.5 if λ = 254 nm, and 0.3 if λ = 313 nm [52]. In this system, H_2O_2 is usually directly injected as a concentrated liquid. It can generate high amounts of heat and gas at the place of injection, especially if the target water still contains lots of dissolved matter. Indeed, the products of H_2O_2 decomposition are dioxygen and water. In particular, iron ions can act as a Fenton catalyst and accelerate this process significantly. This must be taken into account when designing such systems.

1.4.3. Photocatalysis

Photocatalysts are semiconductors. When those are exposed to a suitable type of light, an electron is promoted from the valence band (VB) to the conduction band (CB). Overcoming the band gap energetic barrier, or simply ”band gap”, the electron leaves a positive hole in the VB and forms what is commonly called an ”electron-hole pair” (e^-h^+ pair) (Equation 1.8) [53] [54].

$$e^-(VB) \overset{h\upsilon}{\leftrightarrows} e^-(CB) + h^+(VB) \tag{1.8}$$

Once again, this process can generate $OH^{\cdot}$ and O_2^- radicals in the presence of water.

Photocatalysts can be used either as a powder, a slurry [55], or in the form of thin layers. The two former options come with the problem of the photocatalyst retrieval from the process, although they permit a higher flexibility in terms of concentration. Thin layers are mechanically stable and can typically be used for a large number of cycles [51]. Nonetheless, scaling processes from laboratory to industrial scale can be a problem for two reasons: (i) the deposition

method used at lab-scale is often not suitable for industrial-scale reactors, and (ii) the inherent lower surface-to-volume ratio in the industrial process inevitably decreases the efficiency of photocatalysis.

Titanium dioxide (TiO_2) and zinc oxide (ZnO) have been widely used as photocatalysts to break down extremely toxic and non-biodegradable pollutants, as well as to inactivate pathogenic bacteria, in both air and water [51-55].

As the band gap of TiO_2 or ZnO puts it very close to being sensitive to visible light ($E_{gap} \approx 3.2$ eV or $\lambda = 388$ nm), a lot of efforts are made to lower the band gap's value. Doping TiO_2 or ZnO with various species is a solution to shift their absorption range from UV light to visible light. One advantage of using visible light is related to the energy sources used in those systems: indeed, visible LEDs (light-emitting diodes) are much more efficient in the visible range than LEDs or traditional lamps emitting in the UV range; the sun can also be considered as a potential light source, as it emits mainly in the visible range.

Using visible light also implies a higher safety and an easier process to put in place. The corresponding drawback is the loss of the possible synergy between photocatalysis and photolysis. TiO_2 also presents the advantage of being cheap. Also, no chemical is put directly in contact with water.

1.4.4. Cavitation

Cavitation is, in essence, the same phenomenon that is responsible, e.g., for damaged parts in hydrodynamic systems. When it is intentional, it is based on the use of ultrasounds in water [56]. The acoustic waves create zones of high and low pressure alternatively. When the pressure is at its low point, gas can no longer be dissolved in water, so it forms tiny bubbles instead. After its formation, a given bubble will continue to grow until it reaches an unstable size. Cavitation then occurs: the bubble collapses in an adiabatic manner. The temperature and pressure can reach thousands of kelvins and thousands of bars, which is sufficient to create radicals according to Equations 1.9 and 1.10.

$$H_2O \xrightarrow{))))} H^{\cdot} + OH^{\cdot} \quad (1.9)$$

$$H^{\cdot} + O_2 \rightarrow HO_2^{\cdot} \quad (1.10)$$

"))))" represents cavitation."

Cavitation shares the advantage of the absence of chemicals with photocatalysis. It is reported to be less expensive when used in conjunction with other AOPs [52].

1.4.5. Electrochemical AOPs

These AOPs are quite numerous Nidheesh *et al.* [58]. Two main techniques will be discussed here: anodic production of $OH^{\cdot}$ radicals and cathodic in-situ production of H_2O_2. In a simple electrochemical system consisting of water, a cathode, and an anode, electrolysis of water can take place following the two semi-equations (1.11).

$$4H^+ + 4e^- \rightarrow 2H_2 \qquad E_0 = 0.00\ V$$

$$2H_2O \rightarrow O_2 + 4H^+ + 4e^- \qquad E_0 = 1.23\ V \tag{1.11}$$

The standard redox potentials, E_0 (V), must be corrected if we work in non-standard conditions, *i.e.*, if $[H_3O^+] \neq 1$ M. The potentials at pH = 7 can be readily calculated using the Nernst equation:

$$E = E_0 - \frac{RT}{nF} ln \frac{a_{Red,i}}{a_{Ox,i}} \tag{1.12}$$

where R is the universal gas constant (8.314 J/mol/K), T is the temperature (K), n is the number of electrons exchanged, F is the Faraday constant (96485 C/mol), a is the chemical activity, and the indices Red,i and Ox,i designate respectively the reduced and oxidized forms involved in the semi-reaction. When applied to the two semi-reactions at pH = 7, the values of the potential become, respectively, at 298 K (Equation 1.13):

$$E_{cathode}(V) = -0.41 - 0.0128 \times ln\ a_{H2}$$

$$E_{anode}(V) = 0.82 + 0.0257 \times ln\ a_{O2} \tag{1.13}$$

Now, it is possible to have different reactions at both the anode and the cathode by choosing the adequate oxidoreduction potentials. At the anode, the possible oxidation states of H_2O's oxygen atom have been determined by Wood (Figure 1.8) [57].

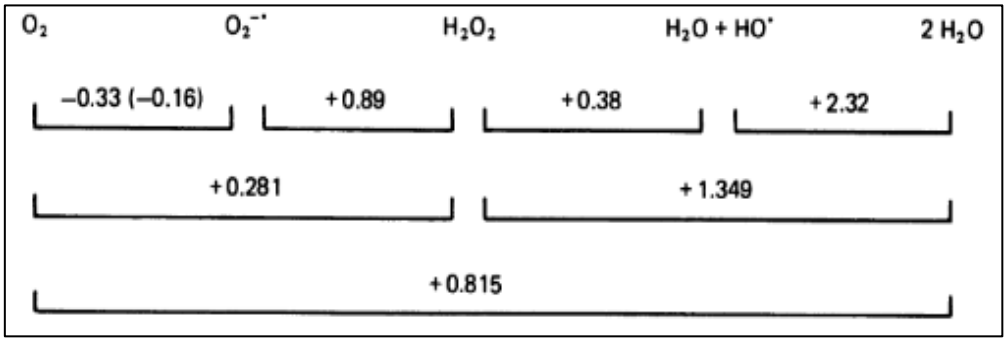

Figure 1.8: Potential diagram for oxygen at pH = 7 [57].

Certain anodes exhibit properties that make them produce $OH^{\cdot}$ radicals instead of dioxygen, despite the unfavorable oxidation potential. This is the case of boron-doped diamond thin film

anodes [58]. Thanks to their large overpotential for O_2 production, the main reaction has been proven through current-potential curves to be Equation 1.14.

$$H_2O \rightarrow OH^{\cdot} + H^+ + e^- \quad (1.14)$$

It must be noted that H_2O_2 naturally accumulates in such systems because of hydroxyl radicals reacting with each other. The radicals, initially sorbed on the anode, can also lead to the production of oxygen gas or react directly with pollutants in water [58]. In the case of metal oxide anodes, oxygen atoms can also be chemisorbed at the anode, contributing to the oxidative environment at its surface. These anodes have been proven to be efficient at removing micropollutants such as dyes, thanks to the hydroxyl radical. In their paper, Beck *et al.* [59] show that a Si/BDD anode can decrease the total organic carbon (TOC) of a phenol solution with an initial concentration equal to 1400 mg/L to a negligible level using a charge of about 20 Ah/L instead of at least 50 Ah/L for conventional electrodes. More recently, Monteil *et al.* [61] completely mineralized a 30 mg/L solution of hydrochlorothiazide in 15 min only, using the same type of anode. This system is often combined with cathodic production of H_2O_2, which promotes both an oxidative medium in water and a higher concentration of hydroxyl radicals.

This is done by reduction of dissolved oxygen (Equation 1.15):

$$O_2 + 2H^+ + 2e^- \rightarrow H_2O_2 \quad (1.15)$$

Usually, carbon-based materials are used for such cathodes [57]. Graphite is usually suitable for such a system because of its high porosity, which induces enhanced sorption of oxygen gas. They also have low catalytic activity for hydrogen peroxide decomposition [57].

1.4.6. Combination of AOPs

The whole is often greater than the sum of its parts: this holds for some combinations of AOPs. For example, Bedolla-Guzman *et al.* [62] eliminated the reactive yellow 160 (a type of azo dye) efficiently when using a combination of $OH^{\cdot}$ radicals generated by a BDD anode, UVA, and Fenton reagents. Refinery wastewater was treated by a combination of UVC and H_2O_2 in the presence of a catalyst promoting its decomposition [63].

Various materials or processes are combined with AOPs, too, such as activated carbon and simulated solar light with ozone [64], or membrane contactors with O_3/H_2O_2 [65].

Several studies have investigated the use of heterogeneous photocatalysis as an advanced oxidation method for treating contaminated water and removing bio-recalcitrant pollutants such as dyes, drugs, and pesticides.

The degradation of niflumic acid (NIF) was investigated by Madjene *et al.* (2017) using a novel solar photocatalytic reactor on immobilized ZnO. They examined the residence time distribution (RSD) and the efficiency of the reactor in removing NIF. They also studied the consequences of the photocatalytic degradation process caused by the different operating conditions. The reactor was developed to guarantee its energy autonomy by using solar energy, which is free, inexhaustible, and environmentally friendly.

The photodegradation of 2-chlorophenol in the presence of ZnO was examined by Ba-Abbad *et al.* (2016). They analyzed the three main components: radiation intensity, calcination temperature, and solution pH, to assess their impacts on photocatalytic efficiency. The process was optimized using the Response Surface Method (RSM) using the D-optimal design. According to the ANOVA analysis, solar intensity and calcination temperature were identified as two important factors. The ideal conditions included a light intensity of 19.8 W/m^2, a calcination temperature of 404 °C, and a pH of 6. The maximum degradation was equal to 90.5%, which corresponded perfectly to the actual experimental value of 93.5%. The experimental results were closely related to the D-optimal design fit, with a correlation coefficient of 0.9847. 2-Chlorophenol was converted to acetic acid, a non-toxic compound, according to the results of gas chromatography-mass spectrometry (GC-MS) analyses.

According to Khan *et al.* (2016), photocatalytic treatment of textile industry wastewater was investigated using TiO_2 and ZnO in the presence and absence of H_2O_2, under UV artificial radiation, and at various pH values. Both catalysts proved exceptionally effective in treating textile waste. After 150 min of solar irradiation, a maximum decolorization efficiency of 95% was achieved for TiO_2 and 64% for ZnO at 37 °C and pH 9. The results showed that TiO_2 is more effective than ZnO for the photocatalytic degradation of textile effluents. This research shows that textile wastewater reacts differently to catalysts than synthetic dye solutions.

ZnO and lanthanum-doped ZnO nanoparticles were fabricated by Shakir *et al.* (2016) using the freeze-combustion method for paracetamol photodegradation applications. Various spectroscopic and other techniques were used to analyze the resulting nanoparticles, revealing the presence of lanthanum ions. After doping, the photocatalytic activity of ZnO was enhanced by a spectral shift towards the visible region.

Rossetto *et al.* (2010) used four types of bentonite and a diatomite from Argentina as supports for commercial TiO_2 P_{25} (Degussa AG Evonik). The materials were characterized by XRD, SEM, FT-IR, elemental analysis and diffuse reflectance spectroscopy. The specific surface area measured by the BET method was equal to 76, 46, 80, and 31 m^2/g for the four bentonites and 153 m^2/g for the diatomite. SEM images revealed agglomerates, probably due to the presence

of TiO_2 on the surface. All these materials showed photocatalytic activity for the elimination of methylene blue. Impregnated bentonites were more effective than TiO_2 alone, probably due to the distribution of the latter and better accessibility.

Still, to this day, few took notice of that admonition, as shown by the large number of publications focusing on the degradation of one or a few micropollutants, often at lab scale.

1.5.Structure of the thesis

The goal of the thesis is to highlight the value of composite clays in the removal of contaminants in wastewater. Advanced oxidation processes such as heterogeneous photocatalysis and adsorption are used. These methods present a chance to purify water using natural clay materials with minor adjustments.

The thesis first focuses on the mineralogy and physico-chemical characterization of adequate materials; then, it concentrates on their practical application at a large scale. This work is divided into five chapters.

- In Chapter I, a general introduction is developed, which means the context in which this work is set is reviewed. The problem of micropollutants in Cameroon is described. The clay materials used in the thesis are explained. A potential solution lies in radicals, some very powerful chemical species: their chemistry is thus described. Then, state-of-the-art water treatment is summarized, and potential future solutions, called advanced oxidation processes, are explored. As these methods often require advanced materials to be produced, some synthesis methods are also described.
- In Chapter II, the synthesis of mixed materials based on clay-TiO_2 or clay-ZnO, which combines adsorption and photocatalysis, is presented. Fluorescein (FL) and *p*-nitrophenol (PNP), two dye and pesticide-type pollutants, respectively, are investigated. The adsorption and photocatalytic activity of the pure and combined materials are ascertained, together with their physico-chemical characteristics. By producing mixed materials, a material that is already found in Cameroon can be used, and a tiny percentage (less than 30%) of photocatalysts can be added to improve the clay's ability to remove pollutants. The efficiency of the process and the cost can be studied and compared to other known methods.

  Chapter published in: Natural clay modified with ZnO/TiO_2 to enhance pollutant removal from water, Julien G. Mahy, Marlène Huguette Tsaffo Mbognou, Clara Léonard, Nathalie Fagel, Emmanuel Djoufac Woumfo and Stéphanie D. Lambert, Catalysts 2022, 12, 148.

- In Chapter III, the goal is to produce hybrid materials made of good adsorbent materials (clay) and efficient photocatalyst (ZnO) at a low price. The objective is to create a hybrid material that can use either photocatalysis or adsorption to clean up water. To do this, Cameroonian natural clay extract will be utilised, along with modifications made through the ion exchange procedure to improve its adsorption capabilities. To maintain the low cost of these materials, the amount of ZnO added to clay is restricted to 30 weight percent and is created using a green sol-gel process. To ascertain their composition and morphology, the hybrid materials are characterized along with the matching pure clay and pure ZnO samples. Then, the pollutant removal property of these samples is evaluated on model water polluted with three different molecules: the p-nitrophenol (PNP), the malachite green (MG) and the Diamant brilliant violet (DBV).

  Chapter published in: Hybrid clay-based materials for organic dyes and pesticides elimination in water: Marlène Huguette Tsaffo Mbognou, Stéphanie D. Lambert, Joachim Caucheteux, Antoine Farcy, Christelle Alié, Nathalie Fagel, Emmanuel Djoufac Woumfo, Julien G. Mahy: Journal of Sol-Gel Science and Technology, 14 (2024) 100183. doi.org/10.1007/s10971-022-06005-6.
- Chapter IV investigates the potential of using natural Cameroonian clays as a raw material for the grafting of silanol groups, such as [3-(2-aminoethylamino)propyl] trimethoxysilane (EDAS) or tetramethoxysilane (TMOS), using a simple and well-controlled sol-gel process. The resultant nanocomposite materials are assessed as adsorbents for dyes found in water contaminated by the textile industry, including fluorescein, malachite green, and brilliant purple diamond. Raw clays from the Bakotcha region of West Cameroon are used in the studies. Several physicochemical methods were employed to assess the functionalization process.

  Chapter published in: Silane-modified clay for enhanced dye pollution adsorption in water. Marlène Huguette Tsaffo Mbognou, Stéphanie D. Lambert, Ernestine Mimba Mumbfu, Joachim Caucheteux, Antoine Farcy, Nathalie Fagel, Emmanuel Djoufac Woumfo, Julien G. Mahy; Results in Surfaces and Interfaces 14 (2024) 100183.
- Chapter V analyzes the photocatalytic degradation of Ibuprofen from clay materials doped to photocatalysts (ZnO and TiO_2) on both sides, to evaluate the antimicrobial and antishigellose activities of doped clay as an important factor in the elimination of bacteria responsible for water diseases in our cities.

  Chapter published in: Dual-function cameroonian clay-supported ZnO and TiO_2 photocatalysts for ibuprofen mineralization and bacteria inactivation. Marlène Huguette Tsaffo Mbognou, Stéphanie D. Lambert, Antoine Farcy, Hela Rekik, Steven

Wouamba, Emmanuel Djoufac Woumfo, Julien G. Mahy; Next Materials 9 (2025) 101290.

Finally, conclusions and perspectives are drawn to highlight the obtained results through this research.

Bibliography

[1] Cameroon National Contribution Report (2015). Third United Nations Conference on Housing and Sustainable Urban Development (Habitat III), p. 47, [online] www.habitat3.org/wp-content/uploads/Cameroon-Rapport-national-Habitat-III-Version fev16.pdf.Accessed 06/08/2024.

[2] WHO (2004). Guidelines for drinking-water quality, volume 1, recommendations (3rd edn). WHO, Geneva, Switzerland, p. 110.

[3] INS-BGR (Institut National de la Statistique-Institut Fédérale des Géosciences et des Ressources Naturelles) (2013). Étude pilote sur la pollution des eaux de surface et souterraines à Yaoundé et impact sur la santé des populations riveraines (EPESS). Technical report of the BMZ project PN 2002.3510.1 BGR 05-2203-54, p. 194. Yaoundé, Hanover, Bonn.

[4] Bernard Tassongwa, Francois Eba, Dayirou Njoya , Jacqueline Numbem Tchakounte , Narcisse Jeudong , Charles Nkoumbou, Daniel Njopwouo, 2017. Physico-chemistry and geochemistry of Balengou clay deposit (West Cameroon) with inference to an argillic hydrothermal alteration. http://dx.doi.org/10.1016/j.crte.2017.06.002

[5] Wilfried Arsène Letah Nzouebet, Ebenezer Soh Kengne , Guy Valerie Djumyom Wafo, Chistian Wanda, Andrea Rechenburg And Ives Magloire Kengne Noumsi, 2019. Assessment of the faecal sludge management practices in households of a sub-Saharan Africa urban area and the health risks associated: the case study of Yaoundé, Cameroon. http://www.ifgdg.org

[6] INS-BGR (Institut National de la Statistique-Institut Fédérale des Géosciences et des Ressources Naturelles) (2013). Étude pilote sur la pollution des eaux de surface et souterraines à Yaoundé et impact sur la santé des populations riveraines (EPESS). Technical report of the BMZ project PN 2002.3510.1 BGR 05-2203-54, p. 194. Yaoundé, Hanover, Bonn

[7] Mahy, Julien, et al. (2020). "Activation Treatments and SiO_2/Pd Modification of Sol-Gel TiO_2 Photocatalysts for Enhanced Photoactivity under UV Radiation". Catalysts, vol. 10, no. 10, p. 1184. DOI.org (Crossref), doi:10.3390/catal10101184

[8] Diane Armelle Moussima Yaka, Ange Alex Tiemeni, Bertrand Zing Zing, Thérèse Line Laure Jokam Nenkam, Amina Aboubakar, Aline Beatrice Nzeket, Brice Hermann Fokouong Tcholong Et Yvette Clarisse Mfopou Mewouo (2020) DOI : https://doi.org/10.4314/ijbcs.v14i5.32

[9] Rajeev Kumar · M. A. Laskar · I. F. Hewaidy · M. A. Barakat, 2018: Modified Adsorbents for Removal of Heavy Metals from Aqueous Environment: A Reviewhttps://doi.org/10.1007/s41748-018-0085-3

[10] Mohd. Rafatullah, Othman Sulaiman, Rokiah Hashim, Anees Ahmad, 2010: Adsorption of methylene blue on low-cost adsorbents: A review doi:10.1016/j.jhazmat.2009.12.047

[11] A. Njoya *et al.*, « Genesis of Mayouom kaolin deposit (western Cameroon) », *Applied Clay Science*, vol. 32, nº 1-2, p. 125-140, avr. 2006, doi: 10.1016/j.clay.2005.11.005.

[12] E. D. Woumfo, P. Djomgoue, P. A. Tamfuh, D. Bitom, F. Figueras, et D. Njopwouo, « Clays from the Bafang region (West Cameroon): Properties and potential application as decolorizing agent of river water », *Applied Clay Science*, vol. 50, nº 3, p. 322-329, nov. 2010, doi: 10.1016/j.clay.2010.08.017.

[13] J. R. Mache *et al.*, « Smectite clay from the Sabga deposit (Cameroon): mineralogical and physicochemical properties », *Clay miner.*, vol. 48, nº 3, p. 499-512, juin 2013, doi: 10.1180/claymin.2013.048.3.07.

[14] S. Fadil-Djenabou, P.-D. Ndjigui, et J. A. Mbey, « Mineralogical and physicochemical characterization of Ngaye alluvial clays (Northern Cameroon) and assessment of its suitability in ceramic production », *Journal of Asian Ceramic Societies*, vol. 3, nº 1, p. 50-58, mars 2015, doi: 10.1016/j.jascer.2014.10.008.

[15] D. Tsozué, A. Nzeukou, et P. Azinwi, « Genesis and classification of soils developed on gabbro in the high reliefs of Maroua region, North Cameroon », *EURASIAN JOURNAL OF SOIL SCIENCE (EJSS)*, vol. 6, nº 2, p. 168-168, janv. 2017, doi: 10.18393/ejss.286631.

[16] M. F. Brigatti, E. Galan, et B. K. G. Theng, « Chapter 2 Structures and Mineralogy of Clay Minerals », in *Developments in Clay Science*, vol. 1, Elsevier, 2006, p. 19-86. doi: 10.1016/S1572-4352(05)01002-0.

[17] L. Le Pluart, J. Duchet, H. Sautereau, P. Halley, et J.-F. Gerard, « Rheological properties of organoclay suspensions in epoxy network precursors », *Applied Clay Science*, vol. 25, nº 3-4, p. 207-219, juin 2004, doi: 10.1016/j.clay.2003.11.004.

[18] F. Bergaya et G. Lagaly, « Chapter 1 General Introduction: Clays, Clay Minerals, and Clay Science », in *Developments in Clay Science*, vol. 1, Elsevier, 2006, p. 1-18. doi: 10.1016/S1572-4352(05)01001-9.

[19] E. Pavón et M. D. Alba, « Swelling layered minerals applications: A solid state NMR overview », *Progress in Nuclear Magnetic Resonance Spectroscopy*, vol. 124-125, p. 99-128, juin 2021, doi: 10.1016/j.pnmrs.2021.04.001.

[20] B. Tassongwa *et al.*, « Physico-chemistry and geochemistry of Balengou clay deposit (West Cameroon) with inference to an argillic hydrothermal alteration », *Comptes Rendus. Géoscience*, vol. 349, nº 5, p. 212-222, août 2017, doi: 10.1016/j.crte.2017.06.002.

[21] G. D. MCKENZIE & R. O. UTGARD. *Man and His Physical Environment* (2nd edition). Readings in Environmental Geology, x+388 pp. Contains 48 selected articles. Burgess, Minneapolis, (Eds) 1975.

[22] BRINDLEY G. W. Discussions and recommendations concerning the nomenclature of clay minerals and related phyllosilicates. Materials Research Laboratory, and Department of Geochemistry and Mineralogy, The Pennsylvania State University

[23] L. Bouna, « Fonctionnalisation des minéraux argileux d'origine marocaine par TiO_2 en vue de l'élimination par photocatalyse de micropolluants organiques des milieux aqueux ».

[24] B. Fatiha et K. Hussein, « Effet Du Pontage Et Dopage Sur La Degradation De Certains Colorants Synthetiques », 2014.

[25] R. L. Anderson, I. Ratcliffe, H. C. Greenwell, P. A. Williams, S. Cliffe, et P. V. Coveney, « Clay swelling — A challenge in the oilfield », *Earth-Science Reviews*, vol. 98, nº 3-4, p. 201-216, févr. 2010, doi: 10.1016/j.earscirev.2009.11.003.

[26] F. Min, C. Peng, et S. Song, « Hydration Layers on Clay Mineral Surfaces in Aqueous Solutions: a Review/Warstwy Uwodnione Na Powierzchni Minerałów Ilastych W Roztworach Wodnych: Przegląd », *Archives of Mining Sciences*, vol. 59, nº 2, p. 489-500, juin 2014, doi: 10.2478/amsc-2014-0035.

[27] B. S. Rathi, P. S. Kumar, et P.-L. Show, « A review on effective removal of emerging contaminants from aquatic systems: Current trends and scope for further research », *Journal of Hazardous Materials*, vol. 409, p. 124413, mai 2021, doi: 10.1016/j.jhazmat.2020.124413.

[28] A. Cheknane, « Optimal design of electrode grids dimensions for ITO-free organic photovoltaic devices », *Progress in Photovoltaics*, vol. 19, nº 2, p. 155-159, mars 2011, doi: 10.1002/pip.1000.

[29] G. Limousin, J.-P. Gaudet, L. Charlet, S. Szenknect, V. Barthès, et M. Krimissa, « Sorption isotherms: A review on physical bases, modeling and measurement », *Applied Geochemistry*, vol. 22, nº 2, p. 249-275, févr. 2007, doi: 10.1016/j.apgeochem.2006.09.010.

[30] M. A. Al-Ghouti et D. A. Da'ana, « Guidelines for the use and interpretation of adsorption isotherm models: A review », *Journal of Hazardous Materials*, vol. 393, p. 122383, juill. 2020, doi: 10.1016/j.jhazmat.2020.122383.

[31] N. Ayawei, A. N. Ebelegi, et D. Wankasi, « Modelling and Interpretation of Adsorption Isotherms », *Journal of Chemistry*, vol. 2017, p. 1-11, 2017, doi: 10.1155/2017/3039817.

[32] S. Bendjabeur, R. Zouaghi, B. Zouchoune, et T. Sehili, « DFT and TD-DFT insights, photolysis and photocatalysis investigation of three dyes with similar structure under UV irradiation with and without TiO2 as a catalyst: Effect of adsorption, pH and light intensity », *Spectrochimica Acta Part A: Molecular and Biomolecular Spectroscopy*, vol. 190, p. 494-505, févr. 2018, doi: 10.1016/j.saa.2017.09.045.

[33] M. Suganya, S. Kavitha, B. Mythili Gnanamangai, et P. Ponmurugan, « Phytofabrication of silver nanoparticles using *Bacopa monnieri* leaf extract and its antibacterial activity as well as oxidative stress-induced apoptosis of lung cancer », *IET nanobiotechnol.*, vol. 12, n° 3, p. 318-324, avr. 2018, doi: 10.1049/iet-nbt.2017.0146.

[34] G. S. Kumar, « Enhancing water use efficiency and water productivity of maize-onion cropping system », *International Journal of Farm Sciences*, vol. 12, n° 1, p. 84-87, 2022, doi: 10.5958/2250-0499.2022.00019.2.

[35] V. Tharaneedhar, P. Senthil Kumar, A. Saravanan, C. Ravikumar, et V. Jaikumar, « Prediction and interpretation of adsorption parameters for the sequestration of methylene blue dye from aqueous solution using microwave assisted corncob activated carbon », *Sustainable Materials and Technologies*, vol. 11, p. 1-11, avr. 2017, doi: 10.1016/j.susmat.2016.11.001.

[36] K. Y. Foo et B. H. Hameed, « Insights into the modeling of adsorption isotherm systems », *Chemical Engineering Journal*, vol. 156, n° 1, p. 2-10, janv. 2010, doi: 10.1016/j.cej.2009.09.013.

[37] K. S. Padmavathy, G. Madhu, et P. V. Haseena, « A study on Effects of pH, Adsorbent Dosage, Time, Initial Concentration and Adsorption Isotherm Study for the Removal of Hexavalent Chromium (Cr (VI)) from Wastewater by Magnetite Nanoparticles », *Procedia Technology*, vol. 24, p. 585-594, 2016, doi: 10.1016/j.protcy.2016.05.127.

[38] P. Senthil Kumar, K. Kirthika, « Equilibrium and kinetic study of adsorption of nickel from aqueous solution onto bael tree leaf powder », J*ournal of Engineering Science and Technology* Vol. 4, No. 4 (2009) 351 - 363.

[39] C. Senthamarai *et al.*, « Adsorption behavior of methylene blue dye onto surface modified *Strychnos potatorum* seeds », *Env Prog and Sustain Energy*, vol. 32, nº 3, p. 624-632, oct. 2013, doi: 10.1002/ep.11673.

[40] A. Ely, « Synthèse et propriétés de biosorbants à base d'argiles encapsulées dans des alginates : application au traitement des eaux », Université de Limoges, Faculté des Sciences et Techniques, Thèse 2010.

[41] Z. Luo, M. Gao, Y. Ye, et S. Yang, « Modification of reduced-charge montmorillonites by a series of Gemini surfactants: Characterization and application in methyl orange removal », *Applied Surface Science*, vol. 324, p. 807-816, janv. 2015, doi: 10.1016/j.apsusc.2014.11.043.

[42] B. S. Sekhon, « Gemini (dimeric) surfactants: The two-faced molecules », *Reson*, vol. 9, nº 3, p. 42-49, mars 2004, doi: 10.1007/BF02834987.

[43] X. Ren *et al.*, « Adsorption of arsenic on modified montmorillonite », *Applied Clay Science*, vol. 97-98, p. 17-23, août 2014, doi: 10.1016/j.clay.2014.05.028.

[44] T. Bajda et Z. Kłapyta, « Adsorption of chromate from aqueous solutions by HDTMA-modified clinoptilolite, glauconite and montmorillonite », *Applied Clay Science*, vol. 86, p. 169-173, déc. 2013, doi: 10.1016/j.clay.2013.10.005.

[45] K. Reitzel, S. Lotter, M. Dubke, S. Egemose, H. S. Jensen, et F. Ø. Andersen, « Effects of Phoslock® treatment and chironomids on the exchange of nutrients between sediment and water », *Hydrobiologia*, vol. 703, nº 1, p. 189-202, févr. 2013, doi: 10.1007/s10750-012-1358-8.

[46] J. P. Richards, « Discussion of Sun *et al* . (2011): 'The genetic association of adakites and Cu–Au ore deposits' », *International Geology Review*, vol. 54, nº 3, p. 368-369, févr. 2012, doi: 10.1080/00206814.2011.580612.

[47] K. Mukherjee, A. Kedia, K. Jagajjanani Rao, S. Dhir, et S. Paria, « Adsorption enhancement of methylene blue dye at kaolinite clay–water interface influenced by electrolyte solutions », *RSC Adv.*, vol. 5, nº 39, p. 30654-30659, 2015, doi: 10.1039/C5RA03534A.

[48] A. Gil et M. A. Vicente, « Progress and perspectives on pillared clays applied in energetic and environmental remediation processes », *Current Opinion in Green and Sustainable Chemistry*, vol. 21, p. 56-63, févr. 2020, doi: 10.1016/j.cogsc.2019.12.004.

[49] T. Thiebault, R. Guégan, et M. Boussafir, « Adsorption mechanisms of emerging micro-pollutants with a clay mineral: Case of tramadol and doxepine pharmaceutical products »,

Journal of Colloid and Interface Science, vol. 453, p. 1-8, sept. 2015, doi: 10.1016/j.jcis.2015.04.029.

[50] Y. Shi, X. Wang, C. Feng, et S. Yang, « Nano-clay montmorillonite removes tetracycline in water: Factors and adsorption mechanism in aquatic environments », *iScience*, vol. 27, nº 2, p. 108952, févr. 2024, doi: 10.1016/j.isci.2024.108952.

[51] S. Khan, M. Sayed, M. Sohail, L. A. Shah, et M. A. Raja, « Advanced Oxidation and Reduction Processes », in *Advances in Water Purification Techniques*, Elsevier, 2019, p. 135-164. doi: 10.1016/B978-0-12-814790-0.00006-5.

[52] M. Gonzalez, E. Oliveros, M. Worner, et A. Braun, « Vacuum-ultraviolet photolysis of aqueous reaction systems », *Journal of Photochemistry and Photobiology C: Photochemistry Reviews*, vol. 5, nº 3, p. 225-246, déc. 2004, doi: 10.1016/j.jphotochemrev.2004.10.002.

[53] C. Wolfs, « Advanced oxidation processes for persistent micropollutant elimination in wastewater intended for surface release » University of Liège, 2024.

[54] M. A. Rauf et S. S. Ashraf, « Fundamental principles and application of heterogeneous photocatalytic degradation of dyes in solution », *Chemical Engineering Journal*, vol. 151, nº 1-3, p. 10-18, août 2009, doi: 10.1016/j.cej.2009.02.026.

[55] M. A. Sousa, C. Gonçalves, V. J. P. Vilar, R. A. R. Boaventura, et M. F. Alpendurada, « Suspended TiO_2-assisted photocatalytic degradation of emerging contaminants in a municipal WWTP effluent using a solar pilot plant with CPCs », *Chemical Engineering Journal*, vol. 198-199, p. 301-309, août 2012, doi: 10.1016/j.cej.2012.05.060.

[56] G. Balasubramanian, D. Dionysiou, M. Suidan, I. Baudin, et J. Laine, « Evaluating the activities of immobilized TiO_2 powder films for the photocatalytic degradation of organic contaminants in water », *Applied Catalysis B: Environmental*, vol. 47, nº 2, p. 73-84, janv. 2004, doi: 10.1016/j.apcatb.2003.04.002.

[57] K. Yasui, « Fundamentals of Acoustic Cavitation and Sonochemistry », in *Theoretical and Experimental Sonochemistry Involving Inorganic Systems*, Pankaj et M. Ashokkumar, Éd., Dordrecht: Springer Netherlands, 2010, p. 1-29. doi: 10.1007/978-90-481-3887-6_1.

[58] P. V. Nidheesh, M. Zhou, et M. A. Oturan, « An overview on the removal of synthetic dyes from water by electrochemical advanced oxidation processes », *Chemosphere*, vol. 197, p. 210-227, avr. 2018, doi: 10.1016/j.chemosphere.2017.12.195.

[59] P. M. Wood, « The potential diagram for oxygen at pH 7 », *Biochemical Journal*, vol. 253, nº 1, p. 287-289, juill. 1988, doi: 10.1042/bj2530287.

[60] F. Beck, W. Kaiser, et H. Krohn, « Boron doped diamond (BDD)-layers on titanium substrates as electrodes in applied electrochemistry », *Electrochimica Acta*, vol. 45, n° 28, p. 4691-4695, oct. 2000, doi: 10.1016/S0013-4686(00)00621-6.

[61] H. Monteil, N. Oturan, Y. Péchaud, et M. A. Oturan, « Efficient removal of diuretic hydrochlorothiazide from water by electro-Fenton process using BDD anode: a kinetic and degradation pathway study », *Environ. Chem.*, vol. 16, n° 8, p. 613, 2019, doi: 10.1071/EN19121.

[62] A. Bedolla-Guzman, I. Sirés, A. Thiam, J. M. Peralta-Hernández, S. Gutiérrez-Granados, et E. Brillas, « Application of anodic oxidation, electro-Fenton and UVA photoelectro-Fenton to decolorize and mineralize acidic solutions of Reactive Yellow 160 azo dye », *Electrochimica Acta*, vol. 206, p. 307-316, juill. 2016, doi: 10.1016/j.electacta.2016.04.166.

[63] Z. Rajah, M. Guiza, R. R. Solís, F. J. Rivas, et A. Ouederni, « Catalytic and photocatalytic ozonation with activated carbon as technologies in the removal of aqueous micropollutants », *Journal of Photochemistry and Photobiology A: Chemistry*, vol. 382, p. 111961, sept. 2019, doi: 10.1016/j.jphotochem.2019.111961.

[64] J. J. Rueda-Márquez, I. Levchuk, I. Salcedo, A. Acevedo-Merino, et M. A. Manzano, « Post-treatment of refinery wastewater effluent using a combination of AOPs (H_2O_2 photolysis and catalytic wet peroxide oxidation) for possible water reuse. Comparison of low and medium pressure lamp performance », *Water Research*, vol. 91, p. 86-96, mars 2016, doi: 10.1016/j.watres.2015.12.051.

[65] T. Merle, W. Pronk, et U. von Gunten, « MEMBRO$_3$ X, a Novel Combination of a Membrane Contactor with Advanced Oxidation (O_3 /H_2O_2) for Simultaneous Micropollutant Abatement and Bromate Minimization », *Environ. Sci. Technol. Lett.*, vol. 4, n° 5, p. 180-185, mai 2017, doi: 10.1021/acs.estlett.7b00061.

[66] F. Madjene and N. Yeddou Mezenner. "Design and optimization of a new photocatalytic reactor with immobilized ZnO for water purification," Separation Science and Technology, 2018 vol. 53, no. 2, pp. 364-373.

[67] M.M. Ba-Abbad, M.S. Takriff, A.A.H. Kadhum, A.B. Mohamad, A. Benamor, and A.W. Mohammad. "Solar photocatalytic degradation of 2-chlorophenol with ZnO nanoparticles: optimization with D-optimal design and study of intermediate mechanisms," Environmental Science and Pollution Research, 2017, vol. 24, no 3, p. 2804-2819.

[68] W.Z. Khan, I. Najeeb, and I. Ishtiaque. "Photocatalytic Degradation of a Real Textile Wastewater using Titanium Dioxide, Zinc Oxide and Hydrogen Peroxide," The International Journal Of Engineering And Science, 2016, vol. 5, no. 7, pp. 61-70.

[69] M. Shakir, M. Faraz, Mohd., A. Sherwani, and S.I. Al-Resayes. "Photocatalytic degradation of the drug Paracetamol using Lanthanum doped ZnO nanoparticles and their invitro cytotoxicity assay," Journal of Luminescence, 2016 vol. 176, p. 159-167

[70] E. Rossetto, D.I. Petkowicz, J.H.Z. Dos Santos, S.B.C. Pergher, and F.G. Penha. "Bentonites impregnated with TiO_2 for photodegradation of methylene blue", Applied Clay Science, 2010 vol. 48, no. 4, pp. 602-606.

[71] V. Augugliaro, M. Litter, L. Palmisano, et J. Soria, « The combination of heterogeneous photocatalysis with chemical and physical operations: A tool for improving the photoprocess performance », *Journal of Photochemistry and Photobiology C: Photochemistry Reviews*, vol. 7, nº 4, p. 127-144, déc. 2006, doi: 10.1016/j.jphotochemrev.2006.12.001.

CHAPITRE II: Natural Clay modified with ZnO/TiO_2 to enhance pollutant removal in Water

In this chapter, natural clays (montmorillonite) from Cameroon were modified with two semiconductors (namely TiO_2 and ZnO) known as photocatalysts.

The main questions explored in this chapter are: (i) Can Cu^{2+} ions added by ionic exchange increase the specific surface area of clays? (ii) Can doping clay materials with photocatalyst increase their depollution properties? (iii) What is the efficiency of raw clay and doped clay samples?

To answer these questions, all doped clay samples have been characterized and tested under UV and visible light.

This chapter is published through the following reference: Natural clay modified with ZnO/TiO_2 to enhance pollutant removal from water, Julien G. Mahy, Marlène Huguette Tsaffo Mbognou, Clara Léonard, Nathalie Fagel, Emmanuel Djoufac Woumfo, and Stéphanie D. Lambert, Catalysts 2022, 12, 148. https://doi.org/10.3390/catal12020148.

2.1. Introduction

The population growth, intensive industrialization, and agricultural practices that occurred in recent decades have led to an increase in environmental pollution, which is now considered a global crisis [1]. This scourge has its origins in the constant improvement in the standard of living and the strong demands of consumers. In Cameroon, for example, many cotton, pharmaceutical, fertilizer, tanning, and pesticide manufacturing industries release pollutants such as dyes, pesticides, or bacteria into the environment, leading to disturbances of aquatic fauna and constituting a risk for human health [2]. Faced with this alarming situation, the global water demand, the most vital natural resource, is increasing [3], and at the same time, the quality of freshwater sources is declining due to the presence of emerging contaminants. Most of these contaminants escape conventional wastewater treatment offered by wastewater treatment plants. The presence of these emerging pollutants in the environment is a matter of concern for most environmental agencies in developing countries [4]. This water should be treated as part of the recycling of wastewater that can be used by low-income populations for watering vegetable crops and washing cars and clothes, to allow these populations to have a profitable and healthy economic activity.

To limit the arrival of these various types of refractory contaminants into the environment, effective and ecological treatment strategies have been developed, such as the use of local clays widely available in Cameroon from kaolinites, andosols, illites, and smectites [5], and globally, the use of adsorption as an efficient process to remove pollutants [6]. Clays have been the subject of different characterizations and applications [7].

For nearly three decades, numerous research studies have been conducted on clay materials from Cameroon and their applications [8]. Advanced oxidation processes (AOPs) have been applied in several sectors for the treatment of surface and groundwaters [9,10] and for the elimination of odors and volatile organic compounds [11], as well as for water discoloration, the degradation of phytosanitary and pharmaceutical products [12], the production of molecules such as H_2 [13], and water disinfection [14]. AOPs can be used either as an oxidative pretreatment leading to easily biodegradable compounds or as a tertiary treatment method for removing or completely mineralizing residual pollutants [15]. This process is based on the generation of radical species that can degrade organic pollutants thanks to the use of photocatalyst material activated by UV radiation [16]. The most-used UV-sensitive photocatalysts are TiO_2 and ZnO [17–19]. Different composites of photocatalysts have already been developed for pollutant removal [20–24].

In this work, a combination of adsorption and photocatalysis through the synthesis of mixed materials based on smectite-TiO_2 or smectite-ZnO is presented. Two types of pollutants are explored, one dye and one pesticide-type pollutant: fluorescein (FL) and p-nitrophenol (PNP), respectively. The physico-chemical properties of the pure and mixed materials are determined, as well as their adsorption and photocatalytic activities. The production of mixed materials allows the use of a material already present in Cameroon and the addition of a small fraction (< 30 wt%) of photocatalysts to increase the pollutant removal efficiency of the clay. The efficiency of the process and the cost can be studied and compared to other known methods.

The advantages of using semiconductor-modified clay materials for pollutant removal in water in developing countries are numerous: (i) the materials are composed primarily of natural material (the clay) directly located in the country where the pollution will be treated; (ii) the semiconductor material loading stays low (< 30 wt %), reducing the cost of production; (iii) ZnO and TiO_2 are the most common semiconductor materials and can be produced with green synthesis with low use of organic reagents; (iv) the composite material presents both high adsorption capacity and photocatalytic properties, increasing its depollution properties compared to bare materials; and (v) the process for the production of the composite materials is simple.

2.2. Materials and Methods

2.2.1. Description of the Clay and Modification with Cu^{2+} Ions

2.2.1.1. Presentation of the Clay

The clay material was collected from a homogeneous site yellowish dyke of about 0.5 m in width and about 13 m in height, within the granitic rock outcropping about 1 km south. Clays are actually exploited by the local population for therapy and consumption. The UTM coordinates of the sampling were north 506008.3” and east 1017028.0”, at an altitude of 1423 m. These coordinates corresponded to Mont Batcha, commonly called Bakotcha, in the district of Bana (West Cameroon). This region has an equatorial climate, characterized by average annual rainfall of 1300–2500 mm and a mean annual temperature of 21,23 °C [25]. The vegetation is a highly anthropogenized post-forestry savannah with remains of a persisting semi-deciduous forest in areas of difficult accessibility [26]. The dominant soil types are red ferralitic soils, associated with brunified and hydromorphic soils [27]. The sampled clay was air-dried in the laboratory to a constant weight before grinding and sieving in a 160 µm diameter sieve.

2.2.1.2. Modification of Clay with Ions Cu^{2+} or InterfoliarCation Exchange

This treatment does not destroy the structure of the clay material, and it allows the insertion of ions. We used the following reagents: copper (II) sulfate pentahydrate (> 98.0 % from LabChem, Gauteng, South Africa), barium sulfate (99 %, pure, from Laboratoriumdiscounter), clay powder (> 160 µm), and distilled water.

To produce a homogeneous cation exchange, 50 g of clay was mixed under stirring in 0.1 M of $CuSO_4$ solution for 4 h. After a 2 h rest, the supernatant was poured, and the agitation was repeated with a new solution of 0.1 M of $CuSO_4$. This operation was repeated twice, and excess Cu^{2+} and $SO4^{2-}$ ions were washed with distilled water until the Barium test (precipitation test) became negative. Barium test is a qualitative chemical test that determines whether sulfate ions (SO_4^{2-}) are present in a solution. It's a traditional test for inorganic analysis [28]. The principle is based on the production of a white precipitate of barium sulfate ($BaSO_4$) when a solution containing sulfate ions is treated with a solution of a barium salt (often barium chloride, $BaCl_2$). Because barium sulfate is insoluble in both water and acids, this reaction takes place. The procedure consists of filling a clean test tube with roughly 2 mL of the test fluid. A few drops of barium chloride solution ($BaCl_2$) should be added. It was checked if a white precipitate forms. The homoionic Cu^{2+} clay material was then oven-dried at 110 °C overnight.

2.2.2. Synthesis of Pure TiO_2 and ZnO Photocatalysts

2.2.2.1. ZnO Sample

Pure zinc oxide powders were synthesized by the sol-gel method following Benhebal *et al.* [29,30]. The reagents were zinc acetate dihydrate (98%), oxalic acid dihydrate (99%), and absolute ethanol (ACS grade). They were obtained from Biochem, Chemopharma (Cosne-Cours-sur-Loire, France). The reagents are present in an analytical grade and are used directly as purchased.

Zinc acetate dihydrate (10.98 g) was treated with ethanol (300 mL) at 60 °C. The salt was completely dissolved in about 30 minutes. Oxalic acid dihydrate (12.6 g) was dissolved in ethanol (200 mL) at 60 °C for 30 min. The oxalic acid solution was added slowly, under stirring, to the hot ethanolic zinc solution, and the mixture was stirred for 90 min at 50 °C.

The resulting gel was placed in an oven at 80 °C for 24 h. The sample was calcined at 500 °C for 3 h. The color of the pure ZnO powder was white.

2.2.2.2. TiO_2 Sample

Pure titanium oxide powders were synthesized by the sol-gel method of Mahy *et al.* [31].

The reagents used were titanium (IV) tetraisopropoxide (TTIP > 97%, Sigma-Aldrich, St. Louis, MO, USA), nitric acid (HNO_3, 65 %, Merck, Darmstadt, Germany), isopropanol (IsoP, 99.5%, Acros, Hull, Belgium), and distilled water. Nitric acid HNO_3 (65%, Merck) was used to acidify 250 mL of distilled water to pH 1. Then, 15 mL of TTIP was added to 15 mL of isopropanol (IsoP), and the mixture was stirred for 30 min at room temperature. The resulting solution of TTIP + IsoP mixture was added to acidified water under controlled stirring. The liquid was left under stirring for 4 h at 80 °C. The obtained sol had a clear blue color. Then, the sol was dried for 10 h under an ambient air flow to obtain a xerogel. The powders were dried at 100 °C for 1 h, and a pure TiO_2 powder of yellowish-white color was obtained [31].

2.2.3. Synthesis of Hybrid Clay/Photocatalyst Materials

2.2.3.1. Clay/ZnO Material

For the preparation of modified clays with ZnO, the procedure was similar to that for pure ZnO material. However, when the oxalic acid solution was added slowly with stirring to the hot ethanolic zinc solution, 10 g of clay material was added, and the mixture was left under stirring for 90 min at 50 °C. The resulting gel was placed in an oven at 80 °C for 24 h.

The sample was calcined at 500 °C for 3 h. The ZnO-modified clay powder was light gray in color.

2.2.3.2. Clay/TiO_2 Material

For the preparation of hybrid clay/TiO_2 powder, the same protocol of preparation of a pure TiO_2 sample was used. When the mixture “TTIP + IsoP” was obtained, it was added to acidified water under controlled stirring, and the liquid was left under stirring for 4 h at 80 °C. To the obtained sol, clear blue in color, 10 g of clayey material was added and left under stirring for 2 h. The soil was dried for 24 h under an ambient air flow. The powders were dried at 100 °C for 1 h, and hybrid clay/TiO_2 powders were obtained.

2.2.4. Characterization of samples

The actual composition of the raw and modified clays was determined by inductively coupled plasma–atomic emission spectroscopy (ICP–AES), equipped with an ICAP 6500 THERMO Scientific device (Waltham, MA, USA). The mineralization is fully described in [31]. The samples undergo an alkaline fusion, for which the following steps are made: 0.2 g of Na-KCO_3, 2 g of Na_2O_2, and 0.2 g of the sample are mixed in a zirconium crucible, and the mixture is

heated to its melting point; after cooling and solidification of the mixture, the crucible is placed in a 500 mL flask with deionized water. After the reaction, the crucible is removed from the flask, and 6 mL of HNO_3 is added. The mixture is heated to its boiling point and boiled for 5 min; the solution is transferred to a volumetric flask, which, after cooling, is filled to the calibration mark with deionized water. The solution is then analyzed using the ICP-AES device; however, we used HF instead of HNO_3 before the mixture was heated.

The crystallographic properties were observed through the X-ray diffraction (XRD) patterns recorded with a Bruker D8 Twin-Twin powder diffractometer (Bruker, Billerica, MA, USA) using Cu-K_α radiation, under 40 kV and 30 mA operating conditions, to identify the mineralogical phases of the bulk clayey samples. The XRD patterns on the < 63 μm fraction were recorded between 2° and 70° using a step scan of 0.02° and a step time of 3 s. Additional XRD measurements were made on oriented aggregates, and the data were recorded between 2° and 30° (2θ) using a step scan of 0.02° and a step time of 0.6 s. These oriented aggregates were subjected to three successive treatments: air drying, glycolation, and heating to 500 °C for 4 h, to confirm the type of clay mineral phases. The Greene-Kelley test, modified from Jackson *et al.* [32], was used to distinguish between octahedral and tetrahedral negative layer-charge deficiencies in the smectites. The test consists of saturating the < 2 μm clay fractions with a 2 M LiCl solution overnight. The Li-exchanged fractions were then rinsed with demineralized water, and oriented aggregates were prepared on glass slides. The XRD analyses on oriented clay fractions were conducted in sequence on the air-dried slide, heated at 300 °C, and finally, overnight glycerol solvated. A *d* spacing (001) reflection at 9.6 to 10 Å is indicative of montmorillonite (octahedral negative layer charge), while a spacing at 16.7 to 17.7 Å indicates beidellite (tetrahedral negative layer charge).

The specific surface area of samples was determined by nitrogen adsorption-desorption isotherms in an ASAP 2420 multi-sampler volumetric device from Micromeritics (Norcross, GA, USA) at – 196 °C. Sample Preparation consists first of all by degassing: To eliminate any pre-adsorbed moisture or impurities from the sample surface. it is heated under vacuum in a different preparation station before analysis. This guarantees that the nitrogen will adsorb onto an uncontaminated surface.

Sample Analysis: The prepared sample is moved to an analysis port and cooled to a precise, stable cryogenic temperature.

Gas Dosing and Adsorption: Using a precisely defined manifold volume, a known volume of nitrogen gas (adsorptive) is gradually dosed into the sample cell.

Equilibration and Pressure Measurement: The gas is allowed to reach equilibrium with the sample surface at each dose step. The instrument precisely monitors the pressure and temperature within the sample cell. The amount of gas adsorbed by the sample is calculated from the difference between the amount of gas dosed and the amount of gas remaining in the "free space" at equilibrium, using the ideal gas law with corrections for non-ideal behavior.

SEM micrographs were obtained using a Jeol-JSM-6360LV microscope (Tokyo, Japan) under high vacuum at an acceleration voltage of 20 kV. The images were obtained while operating in a secondary electron detector at a voltage of 10 kV. In order to maintain their natural structure and prevent charging under the electron beam, clay samples meant for scanning electron microscopy (SEM) must be carefully prepared. To eliminate free water without changing the mineral layers, especially in smectitic clays, the clay is first air-dried or oven-dried at 40–50°C. Agglomerates are separated by ultrasonating a small amount (≈0.1 g) of the dried material in ethanol for 30 s to 1 min. After that, a drop of this suspension is placed onto an aluminum SEM stub that has been wrapped with conductive carbon tape. It is then left to dry fully at ambient temperature, creating a thin, homogeneous coating that is appropriate for imaging. Metallization is a crucial stage because clay particles are electrically insulating. To prevent surface charge and enhance image clarity and contrast, a thin conductive coating (5–15 nm) of gold (Au), platinum (Pt), palladium (Pd), or carbon (C) is deposited using a sputter coater [33]. Stable imaging and high-resolution detail are ensured by this conductive coating, which permits the electron beam to disperse appropriately across the material. Lastly, the coated sample is examined under the SEM at an accelerating voltage of 5–20 kV using backscattered electrons (BSE) for compositional contrast and secondary electrons (SE) to reveal surface morphology.

TEM was performed on the LEO 922 OMEGA Energy Filter TEM (Zeiss, Oberkochen, Germany) operating at 120 kV. Sample preparation consisted of dispersing a few milligrams of each sample in water using sonication. Then, a few drops of the supernatant were placed on a holed carbon film deposited on a copper grid (CF-1.2/1.3-2 Cu-50, C-flat™, Protochips, Morrisville, NC, USA).

2.2.5. Adsorption Experiments

Concerning the adsorption experiments, only the Raw clay and clay/Cu^{2+} samples were assessed. The adsorption of two types of model pollutants, fluorescein (FL) and *p*-nitrophenol (PNP), was tested. For an adsorption experiment, six vials were prepared, each containing 5, 10, 15, 20, 25, and 30 mg of powdered clay and 20 mL of pollutant solution in water. The initial concentration of FL was 6 *10^{-5} M and 10^{-4} M for PNP. The samples were under continuous

stirring. The remaining concentration in solution was evaluated every hour for 6 h with a Genesys 10S UV-Vis spectrophotometer (Thermo Scientific) after filtration with a syringe filter. The main absorption peaks were located at 317 and 485 nm for PNP and FL, respectively, as shown in Figures 2.6 and 2.7, UV/visible spectra of the model pollutants.

2.2.6. Photocatalytic Experiments

The degradation of PNP was studied under UVA light (λ = 365 nm) to determine the photocatalytic activity of the synthesized materials. The lamp was an Osram Sylvania, Blacklight-Bleu Lamp, F 18W/BLB-T8, considered monochromatic at 365 nm. Each sample was placed in a Petri dish with 20 mL of 10^{-4} M of PNP solution in water.

The degradation of PNP was evaluated from absorbance measurements with a Genesys 10S UV-Vis spectrophotometer (Thermo Scientific) at 317 nm. Previously, adsorption tests were performed in the dark (dark tests) to show whether PNP was adsorbed on the surface of the samples. A blank test, consisting of irradiating the pollutant solution for 24 h in a Petri dish without any catalyst, showed that PNP concentration under UVA illumination remained constant. The Petri dishes with catalysts and pollutants were stirred on orbital shakers and illuminated for 8 h. Aliquots of PNP were sampled at 0, 4, and 8 h. The photocatalytic degradation was equal to the total degradation of PNP, taking the catalyst adsorption (dark test) into account. Each photocatalytic measurement was triplicated to assess the reproducibility of the data. In each box, the catalyst concentration was equal to 1 g/L.

2.3. Results and Discussion

2.3.1. Composition

Macroscopically, the raw clays, the Cu^{2+}-modified clays, and the TiO_2-modified clays are pale yellow. The ZnO-modified clays are slightly gray. The main compositions of the six different clay samples, determined by ICP-AES, are presented in Table 2.1.

Table 2.1. Sample compositions by ICP-AES.

	Al	**Si**	**Fe**	**Cu**	**TiO_2**	**ZnO**
	wt%	**wt%**	**wt%**	**wt%**	**wt%**	**wt%**
Raw clay	10.1	20.9	3.7	<0.1	<0.1	<0.1
clay/ Cu^{2+}	11.5	21.2	4.2	0.8	<0.1	<0.1
clay / ZnO	5.2	9.2	1.6	<0.1	<0.1	28.1
clay/Cu^{2+}/ZnO/	6.4	11.6	1.8	0.4	<0.1	30.3
clay/ TiO_2	5.7	10.2	1.6	<0.01	28.8	<0.1
clay/Cu^{2+}/TiO_2	5.9	11.6	1.2	0.3	27.6	<0.1

The clays contain 9–21% of Si, 5–11% of Al, and 1–4% of Fe with an atomic Si/Al ratio equal to 2, consistent with a smectic composition [25]. The amount of copper increases up to 0.8% in the Cu^{2+}-modified samples. The percentage of ZnO reaches 28.1% and 30.3% in the clay/ZnO and clay/ZnO/Cu^{2+} samples, respectively. The percentage of TiO_2 is 28.8% and 27.6% in the clay/TiO_2 and clay/TiO_2/Cu^{2+} samples, respectively. The XRD patterns of the eight samples (Figure 2.1) allow us to estimate the crystallinity of the samples.

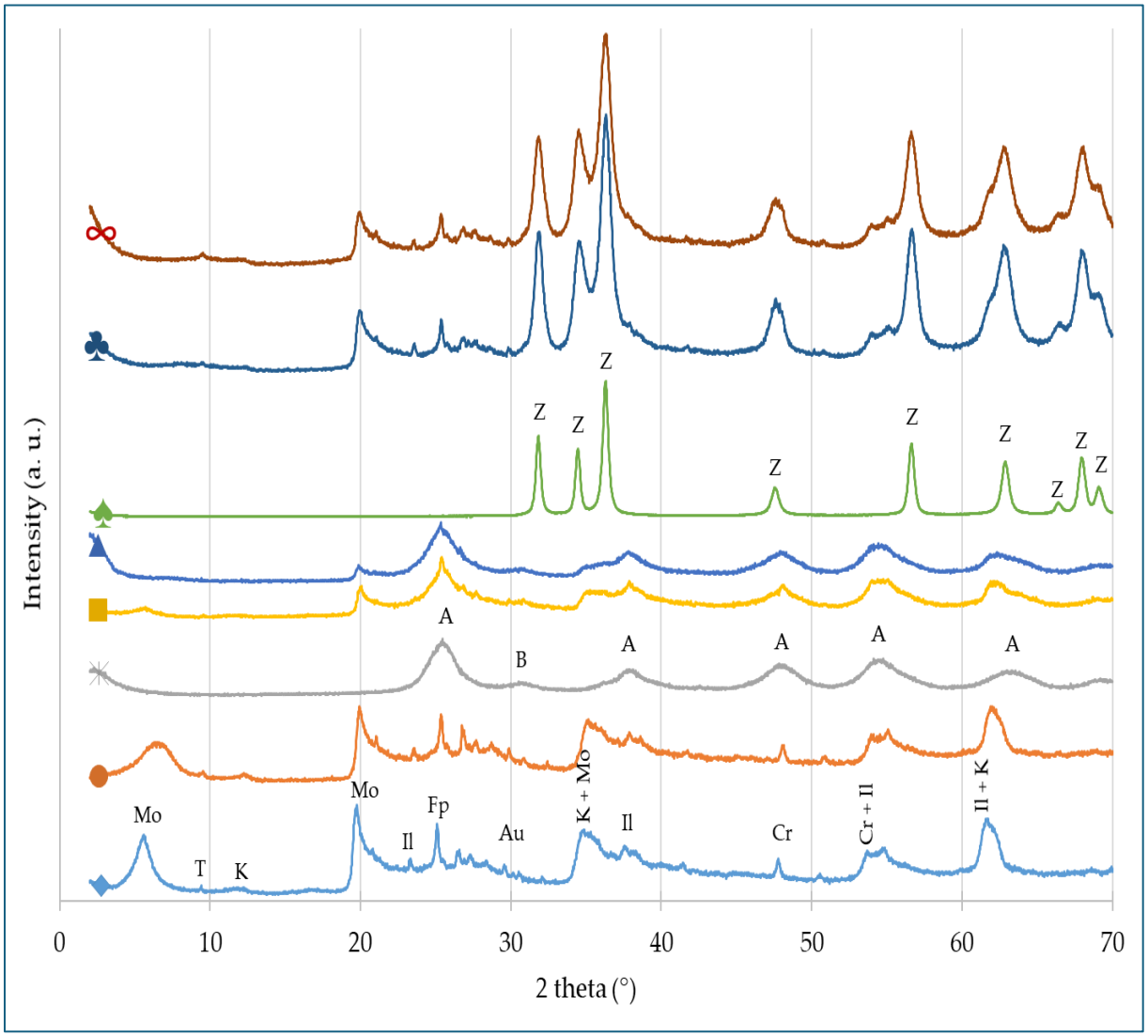

Figure 2.1. XRD patterns of samples: (♦) Raw clay, (●) clay/Cu^{2+}, (*) pure TiO_2, (■) clay/TiO_2, (▲) clay/Cu^{2+}/TiO_2, (♠) Pure ZnO, (♣) clay/ZnO, (∞) clay/Cu^{2+}/ZnO. The positions of the reference peaks are indicated on the three pure materials (raw clay, TiO_2 and ZnO) by the following letters: (A) Anatase, (B) Brookite, (Z) Wurzite, (Mo) Montmorillonite, (T) Talc, (K) Kaolinite, (Il) Illite, (Fp) Feldspar, (Au) Augite and (Cr) Cristobalite. The positions are not indicated on the composite materials to avoid overloading the figure.

The bare clay (♦) is mainly composed of smectite (all the following phases are observed: Augite, Cristobalite, Montmorillonite, Illite, Kaolinite, Feldspar, and Talc).

When Cu^{2+} ions are introduced to the network (clay/Cu^{2+} sample, in orange (●) in Figure 2.6), a similar XRD pattern was recorded; however, the peak around 5–6 degrees was spread due to the Cu^{2+} insertion.

The pure TiO_2 sample (Figure 2.3, pattern in gray (*)) is composed of anatase with a small amount of brookite (denoted A and B in Figure 2.6). These mixed phases were previously

observed in aqueous sol-gel synthesis [41]. The pure ZnO sample (Figure 2.1, pattern in green (♠)) is made of the wurtzite phase, as expected with this synthesis method [29].

The XRD results (Figure 2.1) confirm the successful production of hybrid clay–photocatalytic materials. Indeed, when the clay is modified with TiO_2, the corresponding XRD patterns (patterns in yellow (■) and mid blue (▲) in Figure 2.1) present the characteristic TiO_2 and clay peaks for both clay/TiO_2 and clay/Cu^{2+}/TiO_2 samples if the peak positions are compared to the bare samples. The XRD patterns of the ZnO-modified clays (patterns in red (∞) and dark blue (♣) in Figure 2.1) likely present characteristic peaks of both wurtzite and clays.

2.3.2. Texture and Morphology

Table 2.2 presents the specific surface area (S_{BET}) values for the different samples, ranging from 30 to 325 m^2/g. The raw clay sample has a relatively low specific surface area (45 m^2/g), which increases slightly when Cu^{2+} ions are intercalated (55 m^2/g). This increase results from the insertion of cations into the smectite network [40]; indeed, this insertion is evident in the XRD patterns (Figure 2.1), as indicated by the broadening of the peak at approximately 5°. The pure TiO_2 sample exhibits an S_{BET} value of 180 m^2/g, in agreement with the literature data [41]. When the clay is modified with TiO_2, S_{BET} values increase to 325 and 240 m^2/g for clay/TiO_2 and clay/Cu^{2+}/TiO_2 samples, respectively. This is logical, as these composite materials are produced with nanospheres (around 8 nm) of TiO_2, which present a high specific surface area. They can also enter into the clay network to expand the material and thus increase its specific surface area. The pure ZnO sample presents a low S_{BET} value (30 m^2/g). When clay is modified with ZnO, the specific surface area increases for the clay/ZnO sample (125 m^2/g), but it stays relatively low for clay/Cu^{2+}/ ZnO (50 m^2/g). The increased surface area of the clay/ZnO sample could come from the insertion of some ZnO particles inside the clay network.

Table 2.2. Specific surface area of samples.

Sample	Specific surface area (m^2/g) ± 5
Raw clay	45
clay/Cu^{2+}	55
Pure TiO_2	180
clay/TiO_2	325
clay/Cu^{2+}/TiO_2	240
Pure ZnO	30
clay/ZnO	125
clay/Cu^{2+}/ZnO	50

Concerning the nitrogen adsorption-desorption isotherms, two different types are observed between all samples: (i) type I isotherm with a sharp increase at low pressure followed by a plateau corresponding to a microporous solid; (ii) type IV isotherm characterized by a broad hysteresis at high pressure (mesoporous solid). Samples containing TiO_2 have type I isotherms with a small hysteresis between p/p_0 = 0.4 and p/p_0 = 0.6; the other samples have type IV isotherms. As an example, the isotherms of raw clay and clay/TiO_2 samples are plotted in Figure 2.2. The other isotherms are represented in Annex II.

SEM pictures of several samples are presented in Figure 2.3 for raw clay, clay/TiO_2, and clay/ZnO samples at two different magnifications. Raw clay and clay/ZnO samples have a similar aspect (Figures 2.3a and 2.3c) with large granular powder, while clay/TiO_2 powder is finely dispersed (Figure 2.3b). These observations are in agreement with the higher specific surface area of clay/TiO_2 and clay/Cu^{2+}/TiO_2 samples, characteristic of smaller hybrid particles, and so smaller voids between particles. This finely dispersed aspect comes from the TiO_2 nanoparticles, which are very small (5-10 nm) as observed with TEM pictures on pure TiO_2 samples (Figure 2.4a). Contrarily, the pure ZnO sample has larger particles (Figure 2.4b), explaining that the composite material with clay is more like the bare clay. The samples with Cu^{2+} ions (Clay/Cu^{2+}, Clay/Cu^{2+}/TiO_2, and Clay/Cu^{2+}/ZnO samples) keep a similar aspect and are represented in Annex II.

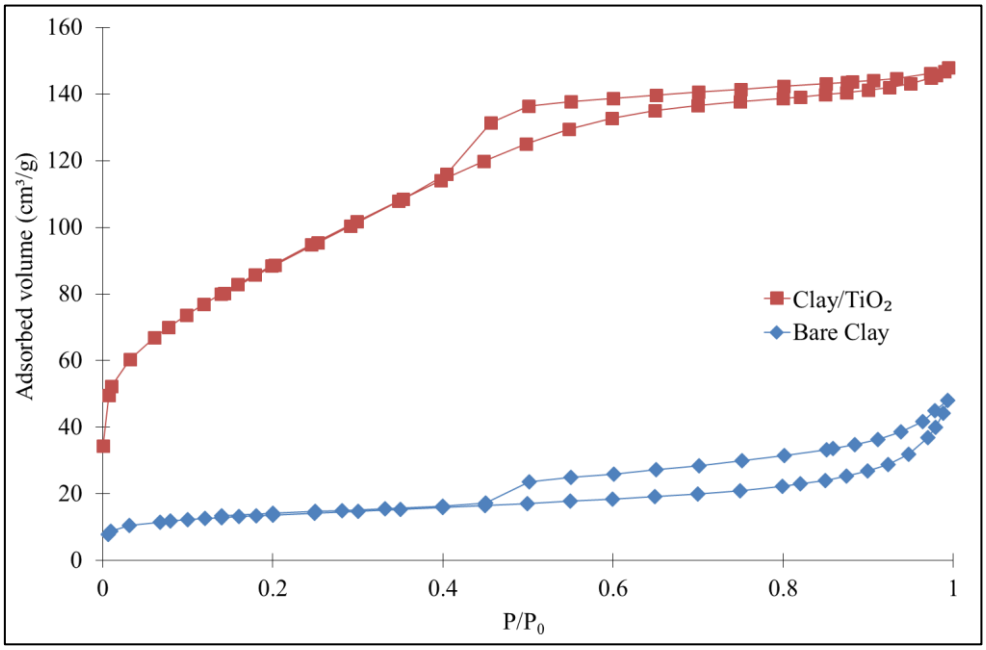

Figure 2.2. Nitrogen adsorption-desorption isotherms for (♦) Raw clay and (■) Clay/TiO_2 samples.

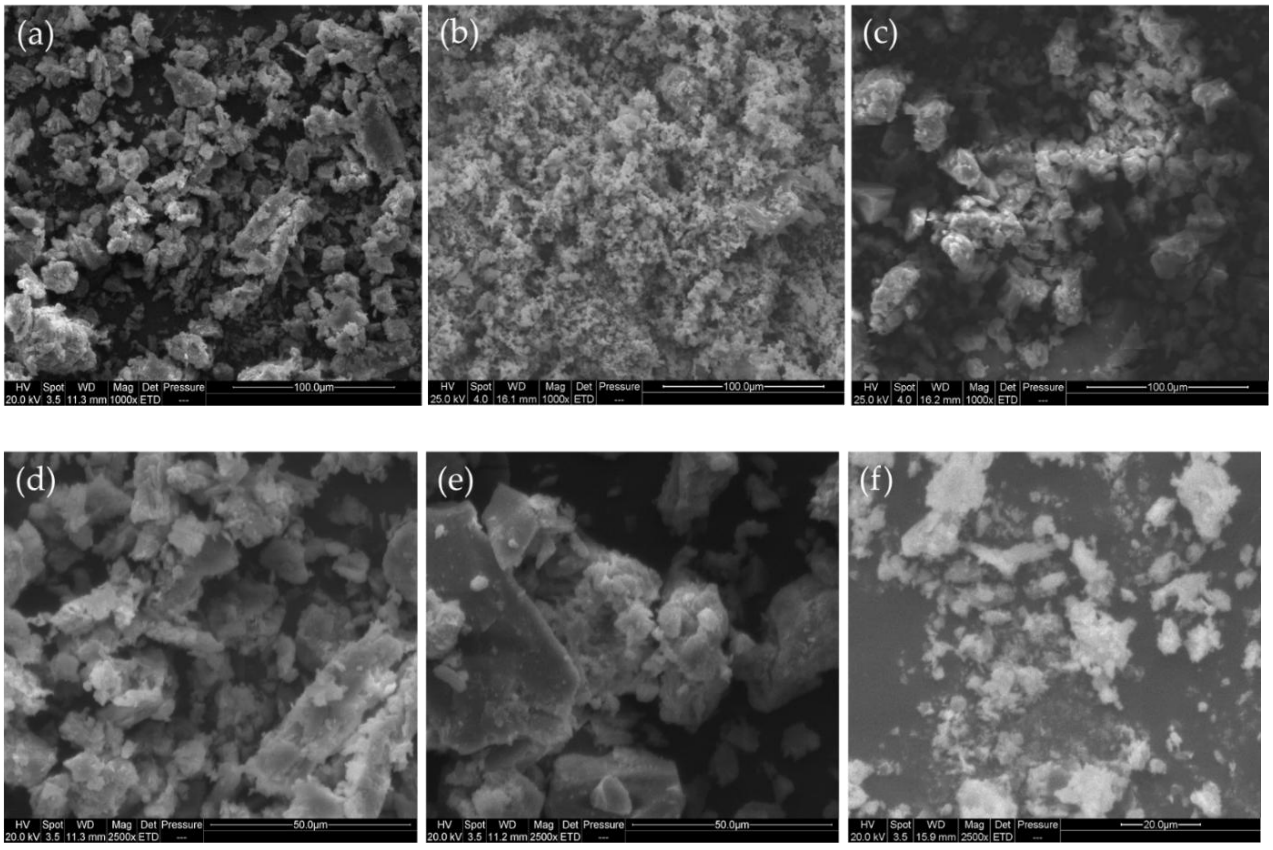

Figure 2.3. SEM pictures of (a) Raw clay, (b) clay/TiO_2, and (c) clay/ZnO samples at a 1000x magnification and of the same samples ((d) Raw clay, (e) clay/TiO_2, and (f) clay/ZnO) at 2500x magnification.

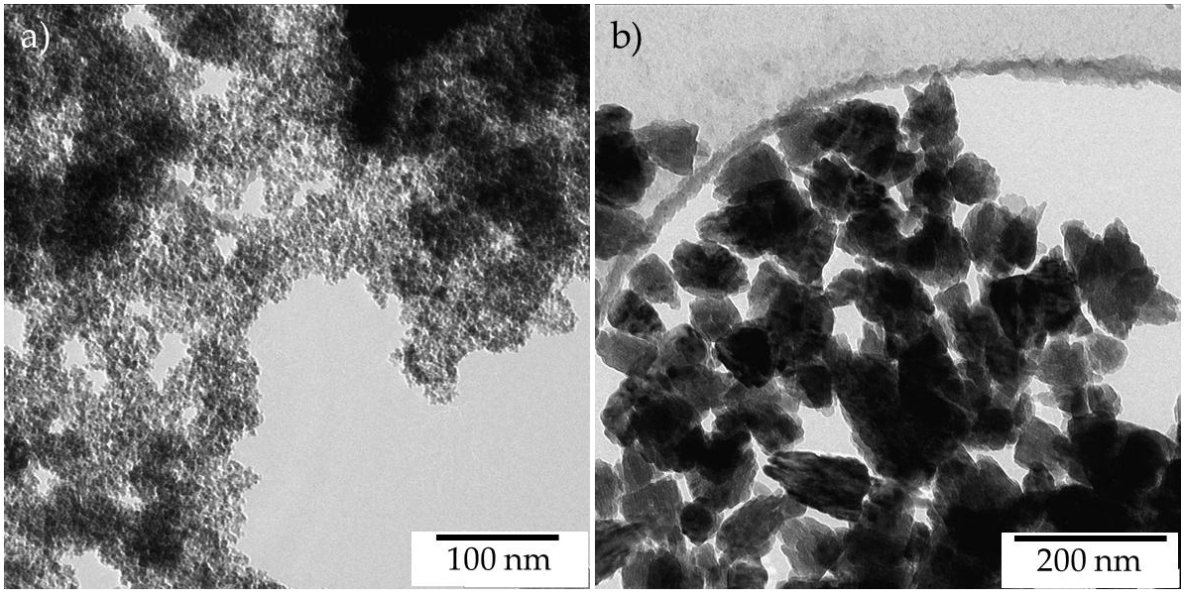

Figure 2.4. TEM pictures of (a) pure TiO_2 and (b) pure ZnO samples.

2.3.3. Adsorption study

The experimental results of fluorescein (FL) adsorption are transformed with the following equation (Equation 2.1) to determine the amount of FL adsorbed by g of clay (q_e):

$$q_e = \frac{(C_0 - C_e) * V}{W} \quad (2.1)$$

where C_0 and C_e are the initial and equilibrium liquid-phase concentrations of FL ($mg_{FL}\ L^{-1}$), respectively, V is the volume of the FL solution (L), and W is the mass of clay used (g_{clay}). The amount of adsorbed FL molecules at the equilibrium, q_e, as a function of C_e is represented in Figure 2.5a after 6 h of adsorption for raw clay and clay/Cu^{2+} samples. Similar curves are obtained for both samples; indeed, they present similar specific surface area values (Table 2.2).

In Figure 2.5b, the evolution of the FL concentration (C/C_0) ratio with time is represented for raw clay and clay/Cu^{2+} samples with a concentration of 30 mg of powder sample. After 0.5 h of experiment, more than 75 % of FL are adsorbed for both samples, and the concentration does not decrease much after 6 h; the equilibrium is reached.

The PNP adsorption study shows that PNP is not adsorbed on the clay. Indeed, the concentration in solution remains constant with time. The removal of this kind of pollutant requires a photocatalytic property.

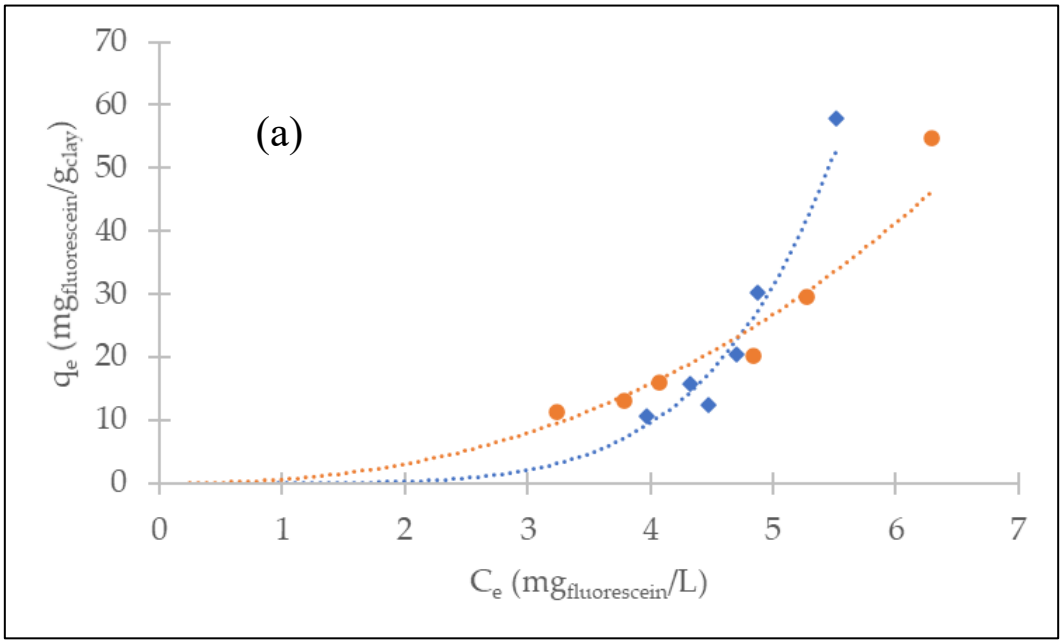

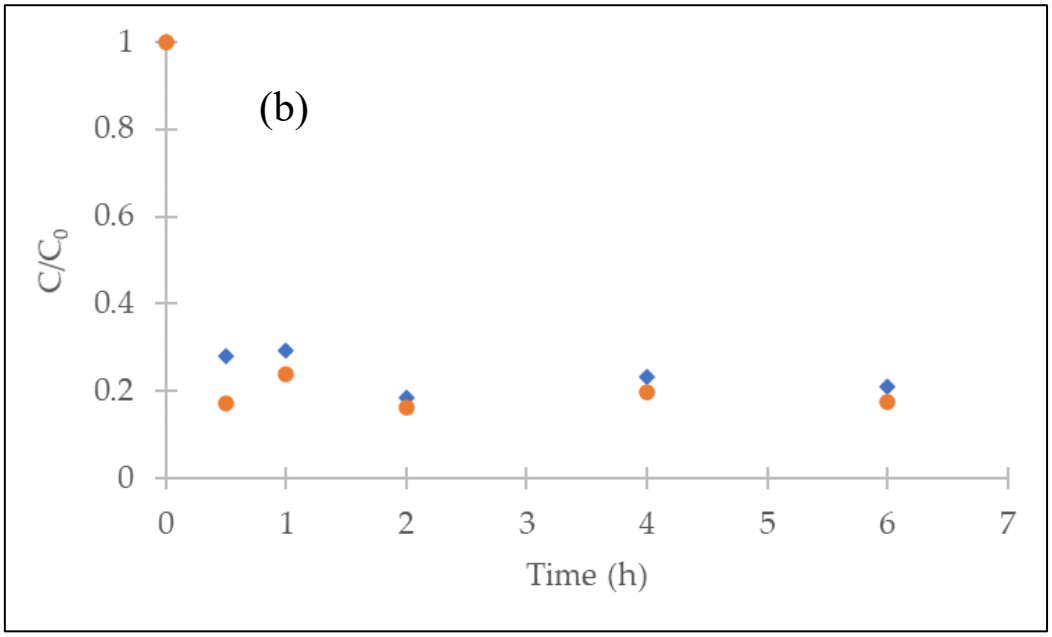

Figure 2.5. (a) Experimental FL adsorption experiment representing the amount of FL adsorbed by g of clay in function of the equilibrium liquid-phase concentrations of FL after 6 h of adsorption test for the 6 different concentrations of powder sample for (♦) raw clay and (●) clay/Cu^{2+} samples and (b) C/C_0 evolution with time for a concentration of powder sample of 30 mg for (♦) raw clay and (●) clay/Cu^{2+} samples.

Figure 2.6 represents the FL UV/visible spectrum recorded for the initial FL solution (6 x 10-5 M). After adsorption for 6 h with the bare Clay sample, the spectrum intensity decreases, as shown in Figure 2.6. The maximum peak is at 485 nm [34].

Figure 2.7 represents the PNP UV/visible spectrum recorded for the initial PNP solution (10-4 M) and the spectrum after 8 h in the photocatalytic experiment with the clay/TiO_2 sample. The

decrease in the maximum peak is well observed after photocatalysis. The maximum peak is located at 317 nm [35,36].

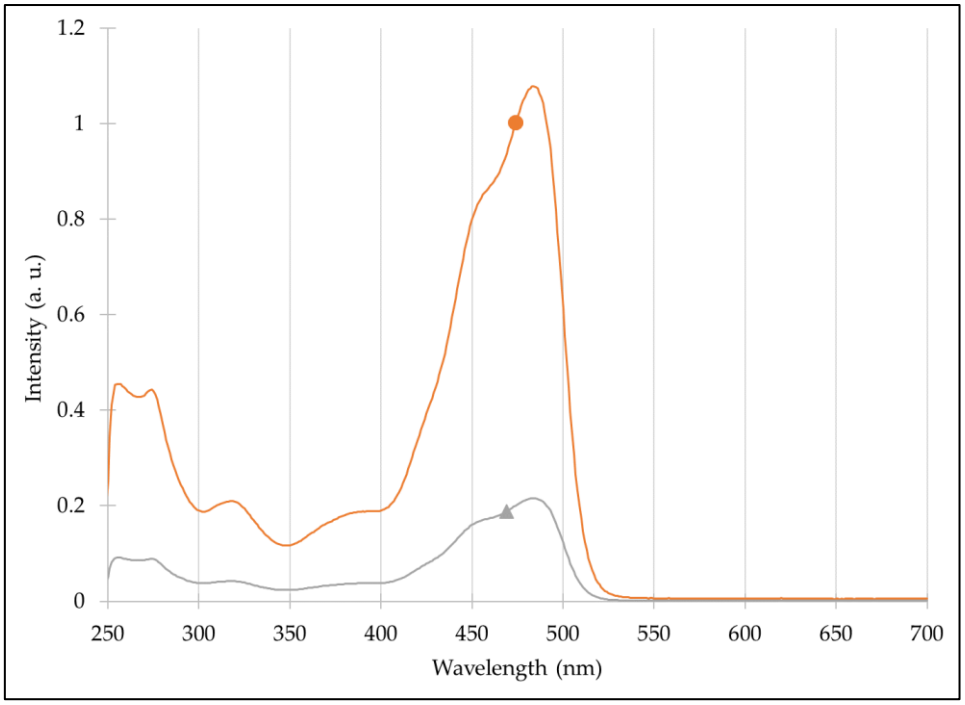

Figure 2.6. FL UV/visible spectrum for (●) initial FL solution and (▲) after 6 h in the adsorption experiment with the raw sample.

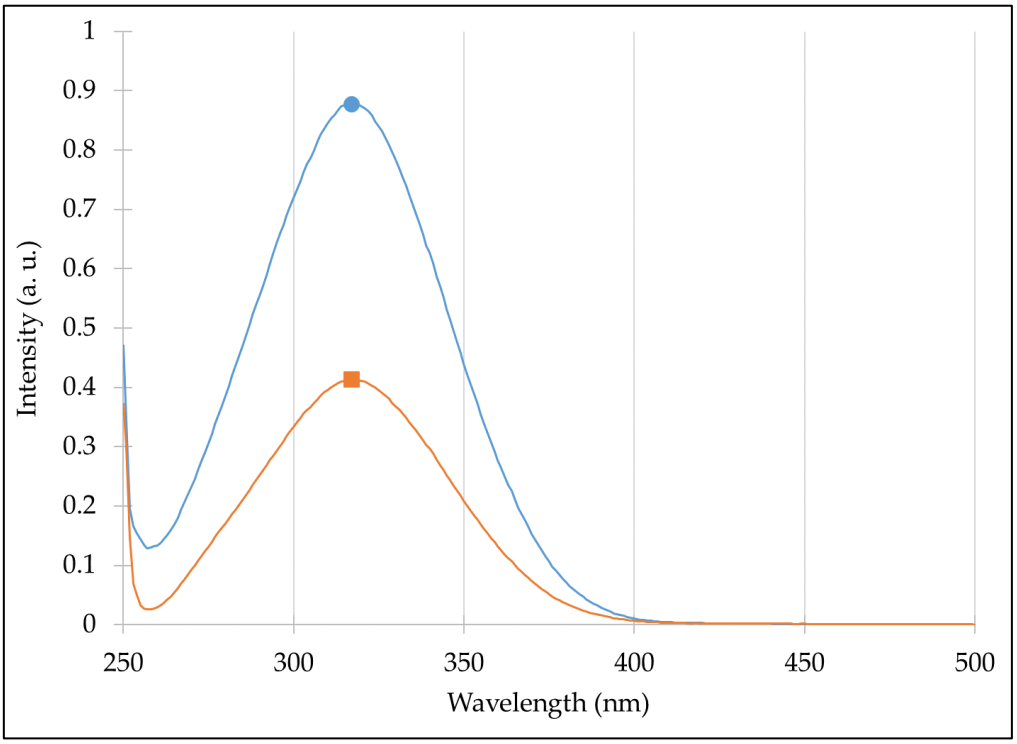

Figure 2.7. PNP UV/visible spectrum for (●) initial PNP solution and (■) after 8 h in photocatalytic experiment with clay/TiO_2 sample.

2.3.4. Photocatalytic activity

As observed in the previous section, the clay can adsorb some pollutants like dye, but is not efficient in adsorbing, for instance, PNP. Therefore, the clay was doped with photocatalysts to degrade molecules that cannot be efficiently adsorbed. Adsorption experiments in the dark (to avoid an interaction with room light, which can activate the photocatalytic materials) were also performed on all 8 samples in contact with PNP for 8 h. No change in the PNP concentration was observed, showing that none of the 8 samples adsorbs the PNP molecules. The photocatalytic property is evaluated on the PNP degradation under UVA illumination after 8 h of exposure (Figure 2.8.a). The raw clay and clay/Cu^{2+} samples present no photocatalytic properties. However, such a property is reached after doping with either TiO_2 or ZnO. PNP is degraded from 45 to 92% according to the samples. Among them, Clay/Cu^{2+}/ZnO is the most efficient material with a percentage of PNP degradation of 92%. The pure TiO_2 and ZnO materials, also tested, reach 100% of PNP degradation as observed in previous studies [18,19].

For the same amount of semiconductor material (TiO_2 or ZnO), the ZnO-modified clay is more efficient than the TiO_2-modified one. As previously observed [18,42], ZnO material has better activity than TiO_2, due to less recombination of photogenerated species. The addition of Cu^{2+} ions increases the photoactivity due to an additional photo-Fenton effect that improves the PNP degradation [43].

Indeed, Cu^{2+} ions can react with water when exposed to UV radiation to produce additional $^{\bullet}OH$ radicals [43]. These radicals can degrade the organic molecules and so enhance the photoactivity [43]. The equation of Cu^{2+} photo-Fenton effects is the following:

$$Cu^{2+} + H_2O + h\nu \rightarrow Cu^{+} + {}^{\bullet}OH + H^{+} \quad (2.2)$$

where h is the Planck constant (6,63 * 10^{-34} J.s), and ν is the light frequency (Hz).

For the two best composite materials (Clay/Cu^{2+}/TiO_2 and Clay/Cu^{2+}/ZnO samples), the evolution of the PNP degradation over time is presented in Figure 2.8b. The evolution of the degradation is linear, and it is assumed that the degradation is then first order.

It has been reported that if the degradation of PNP is not complete, specific peaks of the intermediate molecules appear in the range 200-500 nm of the UV/Visible spectrum [44,45].

Due to the absence of these peaks during the measurements, a complete mineralization can be considered here. Moreover, total mineralization of PNP during homologous photocatalytic tests using a similar installation has been shown in a previous work [45], where the photocatalytic activity of the different films has been evaluated by monitoring the photocatalytic degradation of *p*-nitrophenol under UV light and UV–Visible light. By adjusting a first-order model taking

into account the variation of the volume inside the photoreactor due to sampling on the experimental data, the value of the reaction rate coefficient has been estimated for each catalyst.

The results highlight that the organic additive induces an alteration of the surface roughness and hence, a modification of the active surface of the films.

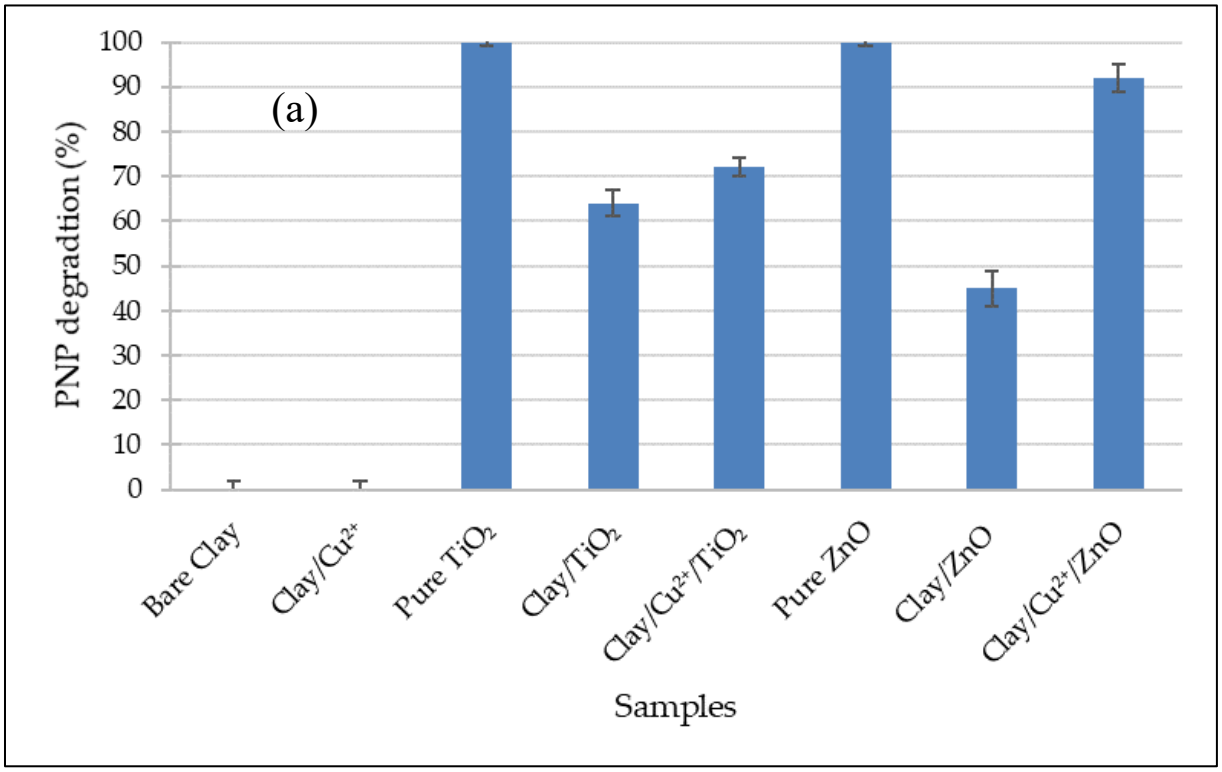

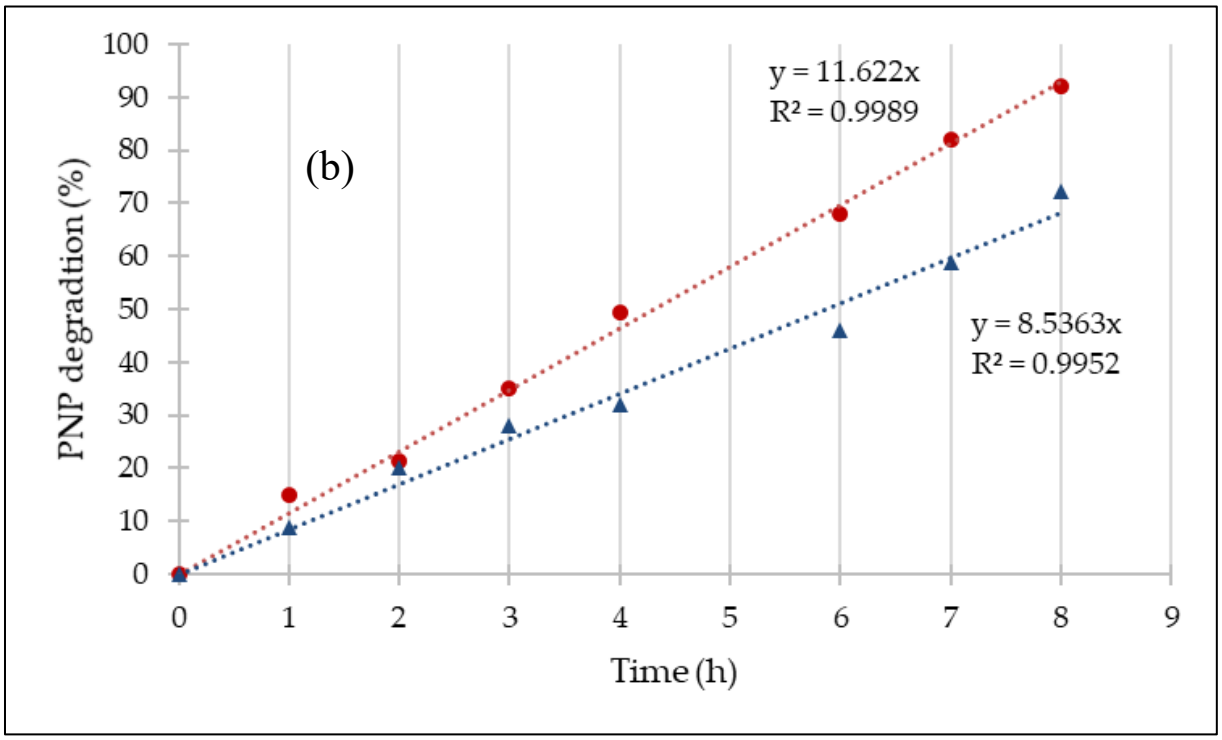

Figure 2.8. (a) PNP degradation (%) under UVA illumination for 8 h with all samples and (b) PNP degradation evolution over 8 h for the two best composite samples (▲) Clay/Cu^{2+}/TiO_2 and (●) Clay/Cu^{2+}/ZnO samples.

The results show that Cu^{2+}-doped clay-photocatalyst composites are much more effective at breaking down PNP when exposed to UVA light. A key component is the cooperation between the semiconductor photocatalyst and the clay support: TiO_2 or ZnO guarantees quick photogeneration of electron–hole pairs, while the clay matrix concentrates PNP at the catalyst surface through adsorption. By inhibiting charge recombination and encouraging the production of extremely reactive •OH and O_2•$^-$ radicals, Cu^{2+} doping further enhances performance. Thus, in comparison to undoped materials, the Clay/Cu^{2+}/TiO_2 and Clay/Cu^{2+}/ZnO systems produce larger mineralization yields and faster degradation kinetics. These results validate the promise of inexpensive clay-based photocatalytic composites as sustainable and effective materials for the elimination of persistent micropollutants from wastewater, especially in areas with plentiful clay resources and high solar irradiation.

2.4. Conclusions

In this chapter, natural clays were used to remove pollutants from water by adsorption and photocatalysis processes. The approach was applied to smectite-rich Cameroon clays. The main clay mineral is montmorillonite (≥ 70 %) associated to kaolinite and mica. Accessory minerals such as anatase, feldspars and quartz are also present. The clays were preliminarily treated with Cu^{2+} ions and then with semiconductors TiO_2 and ZnO to produce hybrid clays. The aim was to increase the depollution efficiency of these modified clayey materials by their photocatalytic properties. The protocol was controlled by XRD and ICP-AES measurements. The modified clays displayed an increase of specific surface area in comparison with natural clay. XRD measurements confirmed the presence of crystalline TiO_2 and ZnO.

The adsorption experiments confirmed that the bare clays can adsorb fluorescein, but they were not efficient for *p*-nitrophenol. In this case, the doping of clays with photocatalysts like TiO_2 or ZnO is important to create new properties for these clays.

Photocatalytic experiments on PNP realized with UVA light gave degradation levels of 45% to 90% after 8 h of exposition with the TiO_2- and ZnO-modified clays, respectively. This study emphasizes the importance of composite clays to remove pollutants via combined processes like adsorption and photocatalysis. Such approaches offer an opportunity, especially in developing countries, to use natural clay materials with slight modifications for water purification.

References

[1] Kemgang Lekomo, Y.; Mwebi Ekengoue, C.; Douola, A.; Fotie Lele, R.; Christian Suh, G.; Obiri, S.; Kagou Dongmo, A. Assessing Impacts of Sand Mining on Water Quality in Toutsang Locality and Design of Waste Water Purification System. Cleaner Engineering and Technology 2021, 2, doi:10.1016/j.clet.2021.100045.

[2] Auriol, M.; Filali-Meknassi, Y.; Dayal Tyagi, R. Présence et Devenir Des Hormones Stéroïdiennes Dans Les Stations de Traitement Des Eaux Usées. Occurrence and Fate of Steroid Hormones in Wastewater Treatment Plants. Revue des Sciences de l'Eau 2007, 20, 89–108.

[3] Ekengoue, C.M.; Lele, R.F.; Dongmo, A.K. Influence De L'exploitation Artisanale Du Sable Sur La Santé Et La Sécurité Des Artisans Et L'environnement: Cas De La Carrière De Nkol'Ossananga, Région Du Centre Cameroun. European Scientific Journal, ESJ 2018, 14, 246, doi:10.19044/esj.2018.v14n15p246.

[4] Https://Minepded.Gov.Cm/Fr/Novembre2019

[5] Nkoumbou, C.; Njopwouo, D.; Villiéras, F.; Njoya, A.; Yonta Ngouné, C.; Ngo Ndjock, L.; Tchoua, F.M.; Yvon, J. Talc Indices from Boumnyebel (Central Cameroon), Physico-Chemical Characteristics and Geochemistry. Journal of African Earth Sciences 2006, 45, 61–73, doi:10.1016/j.jafrearsci.2006.01.007.

[6] Filice, S.; Bongiorno, C.; Libertino, S.; Compagnini, G.; Gradon, L.; Iannazzo, D.; la Magna, A.; Scalese, S. Structural Characterization and Adsorption Properties of Dunino Raw Halloysite Mineral for Dye Removal from Water. Materials 2021, 14, doi:10.3390/ma14133676.

[7] Mache JR, Signing P., Mbey JA, Razafitianamaharavo A, Njopwouo D, Fagel N. Mineralogical and physico-chemical characteristics of Cameroonian smectitic clays after treatment with weakly sulfuric acid. Clay Minerals. 2015 ;50(5) :649-661. Doi : 10.1180/claymin.. 2015.050.5.08

[8] Djoufac Woumfo, E.; Elimbi, A.; Panczer, G.; Nyada Nyada, R.; Njopwouo, D. Physico-Chemical and Mineralogical Characterization of Garoua Vertisols (North Cameroon). Annales de chimie (Paris. 1914) 2006, 31, 75–90.

[9] Léonard, G.L.-M.; Malengreaux, C.M.; Mélotte, Q.; Lambert, S.D.; Bruneel, E.; van Driessche, I.; Heinrichs, B. Doped Sol–Gel Films vs. Powders TiO2: On the Positive Effect Induced by the Presence of a Substrate. Journal of Environmental Chemical Engineering 2016, 4, 449–459, doi:10.1016/j.jece.2015.11.040.

[10] Parsons, S. Advanced Oxidation Processes for Water and Wastewater Treatment; IWA publishing, 2004; ISBN 1843390175.

[11] Bhowmick, M.; Semmens, M.J. Ultraviolet Photooxidation for the Destruction f VOCs in Air. Wat. Res 1994, 28, 2407–2415.

[12] Ikehata, K.; El-Din, M.G. Aqueous Pesticide Degradation by Hydrogen Peroxide/Ultraviolet Irradiation and Fenton-Type Advanced Oxidation Processes: A Review. Journal of Environmental Engineering and Science 2006, 5, 81–135, doi:10.1139/s05-046.

[13] Filice, S.; Fiorenza, R.; Reitano, R.; Scalese, S.; Sciré, S.; Fisicaro, G.; Deretzis, I.; la Magna, A.; Bongiorno, C.; Compagnini, G. TiO_2 Colloids Laser-Treated in Ethanol for Photocatalytic H_2 Production. ACS Applied Nano Materials 2020, 3, 9127–9140, doi:10.1021/acsanm.0c01783.

[14] Goncharuk, V. v; Potapchenko, N.G.; Savluk, O.S.; Kosinova, V.N.; Sova, A.N. Study of Various Conditions for O_3/UV Disinfection of Water. Khimiya i Tecknologiya Vody 2003, 25, 487–496.

[15] Drogui, P.; Blais, J.-F.; Mercier, G. Review of Electrochemical Technologies for Environmental Applications. Recent Patents on Engineering 2007, 1, 257–272.

[16] Douven, S.; Mahy, J.G.; Wolfs, C.; Reyserhove, C.; Poelman, D.; Devred, F.; Gaigneaux, E.M.; Lambert, S.D. Efficient N, Fe Co-Doped TiO_2 Active under Cost-Effective Visible LED Light: From Powders to Films. Catalysts 2020, 10, 547, doi:10.3390/catal10050547.

[17] Mahy, J.G.; Wolfs, C.; Vreuls, C.; Drot, S.; Dircks, S.; Boergers, A.; Tuerk, J.; Hermans, S.; Lambert, S.D. Advanced Oxidation Processes for Waste Water Treatment: From Lab-Scale Model Water to on-Site Real Waste Water. Environmental Technology (United Kingdom) 2021, 42, 3974–3986, doi:10.1080/09593330.2020.1797894.

[18] Mahy, J.G.; Lejeune, L.; Haynes, T.; Body, N.; de Kreijger, S.; Elias, B.; Marcilli, R.H.M.; Fustin, C.A.; Hermans, S. Crystalline ZnO Photocatalysts Prepared at Ambient Temperature: Influence of Morphology on p-Nitrophenol Degradation in Water. Catalysts 2021, 11, doi:10.3390/catal11101182.

[19] Bodson, C.J.; Heinrichs, B.; Tasseroul, L.; Bied, C.; Mahy, J.G.; Wong Chi Man, M.; Lambert, S.D. Efficient P- and Ag-Doped Titania for the Photocatalytic Degradation of Waste Water Organic Pollutants. Journal of Alloys and Compounds 2016, 682, 144–153, doi:10.1016/j.jallcom.2016.04.295.

[20] Cheng, T.; Gao, H.; Liu, G.; Pu, Z.; Wang, S.; Yi, Z.; Wu, X.; Yang, H. Preparation of Core-Shell Heterojunction Photocatalysts by Coating CdS Nanoparticles onto $Bi_4Ti_3O_{12}$ Hierarchical Microspheres and Their Photocatalytic Removal of Organic Pollutants and Cr(VI) Ions. Colloids and Surfaces A: Physicochemical and Engineering Aspects 2022, 633, doi:10.1016/j.colsurfa.2021.127918.

[21] Xiong, S.; Yin, Z.; Zhou, Y.; Peng, X.; Yan, W.; Liu, Z.; Zhang, X. The Dual-Frequency (20/40 KHz) Ultrasound Assisted Photocatalysis with the Active Carbon Fiber-Loaded Fe3+-TiO_2 as Photocatalyst for Degradation of Organic Dye. Bulletin of the Korean Chemical Society 2013, 34, 3039–3045, doi:10.5012/bkcs.2013.34.10.3039.

[22] Li, Y.; Li, M.; Xu, P.; Tang, S.; Liu, C. Efficient Photocatalytic Degradation of Acid Orange 7 over N-Doped Ordered Mesoporous Titania on Carbon Fibers under Visible-Light Irradiation Based on Three Synergistic Effects. Applied Catalysis A: General 2016, 524, 163–172, doi:10.1016/j.apcata.2015.01.050.

[23] Tang, N.; Li, Y.; Chen, F.; Han, Z. In Situ Fabrication of a Direct Z -Scheme Photocatalyst by Immobilizing CdS Quantum Dots in the Channels of Graphene-Hybridized and Supported Mesoporous Titanium Nanocrystals for High Photocatalytic Performance under Visible Light. RSC Advances 2018, 8, 42233–42245.

[24] Lin, X.; Li, M.; Li, Y.; Chen, W. Enhancement of the Catalytic Activity of Ordered Mesoporous TiO_2 by Using Carbon Fiber Support and Appropriate Evaluation of Synergy between Surface Adsorption and Photocatalysis by Langmuir-Hinshelwood (L-H) Integration Equation. RSC Advances 2015, 5, 105227–105238, doi:10.1039/c5ra21083f.

[25] Ndé, H.S.; Tamfuh, P.A.; Clet, G.; Vieillard, J.; Mbognou, M.T.; Woumfo, E.D. Comparison of HCl and H_2SO_4 for the Acid Activation of a Cameroonian Smectite Soil Clay: Palm Oil Discolouration and Landfill Leachate Treatment. Heliyon 2019, 5, doi:10.1016/j.heliyon.2019.e02926.

[26] Olad, A. 7 Polymer/Clay Nanocomposites. In Advances in Diverse Industrial Applications of Nanocomposites; Reddy, B., Ed.; InTechOpen, 2011.

[27] Yeop Lee, S.; Jin Kim, S. Expansion of smectite by hexadecyltrimethylammonium. Clays and Clay Minerals 2002, 50, 435–445.

[28] J.D. Lee. Explains solubility of barium salts and the chemistry behind sulfate precipitation, Concise Inorganic Chemistry, 5th Edition, Wiley India, 2008.

[29] Mahy, J.G.; Léonard, G.L.-M.; Pirard, S.; Wicky, D.; Daniel, A.; Archambeau, C.; Liquet, D.; Heinrichs, B. Aqueous Sol-Gel Synthesis and Film Deposition Methods for the Large-Scale Manufacture of Coated Steel with Self-Cleaning Properties. Journal of Sol-Gel Science and Technology 2017, 81, 27–35, doi:10.1007/s10971-016-4020-5.

[30] Benhebal, H.; Chaib, M.; Leonard, A.; Lambert, S.D.; Crine, M. Photodegradation of Phenol and Benzoic Acid by Sol-Gel-Synthesized Alkali Metal-Doped ZnO. Materials Science in Semiconductor Processing 2012, 15, 264–269, doi:10.1016/j.mssp.2011.12.001.

[31] Léonard, G.L.-M.; Pàez, C.A.; Ramírez, A.E.; Mahy, J.G.; Heinrichs, B. Interactions between Zn^{2+} or ZnO with TiO_2 to Produce an Efficient Photocatalytic, Superhydrophilic and Aesthetic Glass. Journal of Photochemistry and Photobiology A: Chemistry 2018, 350, doi:10.1016/j.jphotochem.2017.09.036.

[32] Jackson, M.L., Lim, C.H. and Zelazny, L.W. (1986) Oxides, Hydroxides and Aluminosilicates. In: Klute, A., Ed., Methods of Soil Analysis, Part 1, Physical and Mineralogical Methods, 2nd Edition, Agronomy Monogram 9, ASA and SSSA, Madison, 101-150.

[33] J. I. Goldstein J. I. Goldstein Dale E. Newbury Joseph Richard Michael David C. Joy. Scanning Electron Microscopy and X-Ray Microanalysis, January 2018 doi: 10.1007/978-1-4939-6676-9

[34] Paola, A. di; Augugliaro, V.; Palmisano, L.; Pantaleo, G.; Savinov, E. Heterogeneous Photocatalytic Degradation of Nitrophenols. 2003, 155, 207–214.

[35] Augugliaro, V.; Palmisano*, L.; Schiavello, M.; Sclafani, A.; Marchese, L.; Martra, G.; Miano, F. Photocatalytic Degradation of Nitrophenols in Aqueous Titanium Dioxide Dispersion. Applied Catalysis 1991, 69, 323–340, doi:http://dx.doi.org/10.1016/S0166-9834(00)83310-2.

[36] Xia, H.; Zhang, W.; Yang, Z.; Dai, Z.; Yang, Y. Spectrophotometric Determination of p -Nitrophenol under ENP Interference. Journal of Analytical Methods in Chemistry 2021, 2021, doi:10.1155/2021/6682722.

[37] Paola, A. di; Augugliaro, V.; Palmisano, L.; Pantaleo, G.; Savinov, E. Heterogeneous Photocatalytic Degradation of Nitrophenols. 2003, 155, 207–214.

[38] Augugliaro, V.; Palmisano*, L.; Schiavello, M.; Sclafani, A.; Marchese, L.; Martra, G.; Miano, F. Photocatalytic Degradation of Nitrophenols in Aqueous Titanium Dioxide

Dispersion. Applied Catalysis 1991, 69, 323–340, doi:http://dx.doi.org/10.1016/S0166-9834(00)83310-2

[39] Malengreaux, C.M.; Léonard, G.M.-L.; Pirard, S.L.; Cimieri, I.; Lambert, S.D.; Bartlett, J.R.; Heinrichs, B. How to Modify the Photocatalytic Activity of TiO2 Thin Films through Their Roughness by Using Additives. A Relation between Kinetics, Morphology and Synthesis. Chemical Engineering Journal 2014, 243, 537–548, doi:10.1016/j.cej.2013.11.031.

[40] Theo Kloprogge, J.; Komarnenl, S.; Amonetie, J.E. Synthesis Of Smectite Clay Minerals: A Critical Review. Clays and Clay Minerals 1999, 47, 529–554.

[41] K.G. Geology, Petrology and Geochemistry of the Tertiary Bana Volcano-Plutonic Complex, West Cameroon, Central Africa, 2004.

[42] Bi Tra, T. Etude Pédologique et Cartographique à l'échelle 1/50000 d'un Secteur de l'Ouest-Cameroun (Région de Bafang); ORSTOM.; 1980;

[43] Benhebal, H.; Chaib, M.; Crine, M.; Leonard, A.; Lambert, S.D. Photocatalytic Decolorization of Gentian Violet with Na-Doped (SnO2 and ZnO). Chiang Mai Journal of Science 2016, 43, 584–589.

[44] Mahy, J.G.; Lambert, S.D.; Léonard, G.L.M.; Zubiaur, A.; Olu, P.Y.; Mahmoud, A.; Boschini, F.; Heinrichs, B. Towards a Large Scale Aqueous Sol-Gel Synthesis of Doped TiO2: Study of Various Metallic Dopings for the Photocatalytic Degradation of p-Nitrophenol. Journal of Photochemistry and Photobiology A: Chemistry 2016, 329, 189–202, doi:10.1016/j.jphotochem.2016.06.029.

[45] Charline M. Malengreaux, Géraldine M.-L. Léonard, Sophie L. Pirard, Iolanda Cimieri, Stéphanie D. Lambert, John R. Bartlett, Benoît Heinrichs. How to modify the photocatalytic activity of TiO2 thin films through their roughness by using additives. A relation between kinetics, morphology and synthesis. Chemical Engineering Journal, 243 (2014) 537–548, http://dx.doi.org/10.1016/j.cej.2013.11.031 .

CHAPITRE III: Hybrid clay-based materials for organic dyes and pesticides elimination in water

In this chapter, a natural clay extracted from Cameroon was modified by ion exchange to produce 4 different clays. These latter were modified with a photocatalytic semiconductor (ZnO) to produce efficient hybrid materials for pollutant removal in water.

The main questions answered in this chapter are: (i) to which smectite family do the clays belong, and what are their different crystalline phases? (ii) What is obtained when the hybrid materials are produced? (iii) What is the efficiency of hybrid clay materials on different model pollutants removal in water with the use of inexpensive natural clay modified with a low amount of photocatalytic material (ZnO around 30 wt%)?

To answer all these questions, the ICP-AES analysis was obtained for the 4 hybrid materials (30 wt% of ZnO and 70 wt% of clay). The SEM observation of the samples has been evaluated. Later on, the pollutant removal property of the samples was evaluated on three different model pollutants: *p*-nitrophenol (PNP), Malachite green (MG), and Brilliant violet diamond (DBV). This study showed the possibility of obtaining a very efficient hybrid.

This chapter is published through the following reference: Hybrid clay-based materials for organic dyes and pesticides elimination in water: Marlène Huguette Tsaffo Mbognou, Stéphanie D. Lambert, Joachim Caucheteux, Antoine Farcy, Christelle Alié, Nathalie Fagel, Emmanuel Djoufac Woumfo, Julien G. Mahy: Journal of Sol-Gel Science and Technology 14 (2024) 100183; https://doi.org/10.1007/s10971-022-06005-6.

3.1. Introduction

As a raw material, clay is a mixture of clay minerals and crystalline impurities in the form of rock debris of infinitely diverse composition. The interest given in recent years to the study of clays by many laboratories around the world [1] is justified by their abundance in nature, the importance of the specific surfaces they develop [2], the presence of surface charges, and especially the exchangeability of the interfoliar cations. The latter, also called mobile or compensating cations, are the main elements responsible for hydration, swelling, and plasticity, and they give these clays hydrophilic properties.

Nevertheless, faced with the emergence of numerous refractory micropollutants in wastewater, conventional techniques, such as adsorption on clays, coagulation/flocculation, and biological treatment, are increasingly ineffective in the face of the complexity of effluents [3]. Moreover, these techniques require an additional investment for the treatment of the liquid/solid concentrate formed.

To overcome these problems, efficient and ecological treatment strategies have been developed. Among these is the application of advanced oxidation processes (AOPs), which are based on the production of hydroxyl radicals, very reactive and strongly oxidizing species. These processes include heterogeneous photocatalysis under UV and/or visible light [4–7], homogeneous phase chemical oxidation processes: H_2O_2/Fe^{2+} (Fenton's reagent) [8], O_3/OH^- (ozonation) [9]; photochemical processes: UV only, H_2O_2/UV, O_3/UV, H_2O_2/Fe^{3+}/UV (photo-Fenton) [8,10]; electrochemical processes [11,12] (anodic oxidation, electro-Fenton), sonication, as explained in Chapter 1. However, although effective for the mineralization of most organic pollutants, these processes require an external energy input (electric or magnetic) and consequently a relatively high cost for a strong mineralization of the pollutant. In this way, the combination of different processes like adsorption and photocatalytic oxidation seems a great alternative to treat this pollution [13–15].

In this chapter, the main goal is to produce hybrid materials made of good adsorbent materials (clay) and efficient photocatalyst (ZnO) at a low price. Indeed, the goal is to develop a hybrid material that can depollute water either with adsorption or photocatalytic processes. To reach this goal, natural clay extract from Cameroon will be used and also modified by an ion exchange process to increase its adsorption properties. The ZnO, introduced in clay, is synthesized by a green sol-gel process, and the amount added in the hybrid material is limited to 30 wt% to conserve low prices for these materials. The hybrid materials and the corresponding pure clay and ZnO samples are characterized to determine their composition and morphology. Then, the

pollutant removal property of these samples is evaluated on model water polluted with three different molecules: the *p*-nitrophenol (PNP), the malachite green (MG), and the Brilliant violet diamond (DBV). PNP and MG are commonly found in pesticides [16, 17], and MG and DBV are used as organic dyes [17, 18].

3.2. Materials and Methods

3.2.1. Natural Clays

Natural Clays were extracted from Bana in Cameroon as explained in Chapter 2, section 2.2.1.1. After extraction, the clays were dried to a constant weight. Then, some parts were modified to insert Cu^{2+}, $Na^{+,}$ or Zn^{2+} ions.

Copper ion insertion

The protocol is the same as explained in Chapter 2, section 2.2.1.2.

Sodium ion insertion

Sodium homo-ionization allows the replacement of all exchangeable cations of various natures by only sodium cations. 100 g of clay material (with particle sizes > 160 µm) is treated with magnetic stirring for 72 h in a solution of NaCl 1M. The material is dried at 100 °C for 24 h.

To ensure that the cation exchange reaction was effective, the dispersion of clay in the electrolyte solution was maintained under stirring for 4 h. After settling, the supernatant was removed, and the recovered solid was re-dispersed in the renewed salt solution. This operation has been repeated 4 times to achieve a complete cation exchange with Na^+ ions. The excess of Na^+ and Cl^- ions was washed with distilled water until the silver nitrate test (precipitation test) became negative. Indeed, when a solution containing Cl^- ions is in contact with $AgNO_3$, a white precipitate appears. If the test is negative, it proves that all Cl^- have been removed from the sample thanks to the washing step.

Zinc ions insertion

To produce a homogeneous cation exchange, 50 g of clay (with particle sizes > 160 µm) was mixed under stirring in 0.1 M $ZnCl_2$ solution for 4 h. After 2 h at rest, the supernatant was poured, and the agitation was repeated with a new solution of 0.1 M $ZnCl_2$. This operation was repeated twice, and excess Zn^{2+} and Cl^- ions were washed with distilled water until the silver nitrate test (precipitation test) became negative. The homoionic Zn^{2+} clay material was then oven-dried at 100 °C overnight.

3.2.2. ZnO synthesis

The synthesis of the pure photocatalytic ZnO sample is described in Chapter 2, Section 2.2.3.1.

3.2.3. Hybrid Clay-ZnO materials synthesis

For the preparation of hybrid clays with ZnO, the procedure was similar to that for pure ZnO material described in Chapter 2, Section 2.2.3.1.

However, when the oxalic acid solution was added slowly with stirring to the hot ethanolic zinc solution, 10 g of doped clay materials was added, and the mixture was left under stirring for 90 min at 50 °C. The resulting gel was placed in an oven at 80 °C for 24 h. The product was calcined at 500 °C for 3 h. The ZnO-modified clay powders were light gray in color.

3.2.4. Characterizations

Samples were measured by nitrogen adsorption and desorption isotherms in an ASAP multisampler device from Micromeritics.

The actual composition of the natural and hybrid clays was determined by inductively coupled plasma–atomic emission spectroscopy (ICP–AES), equipped with an ICAP 6500 THERMO Scientific device. The mineralization is fully described in Chapter 2, Section 2.2.5.

X-ray diffraction patterns were recorded The XRD analysis was done on a Bruker AXS model D8 Advance diffractometer, with Cu-Kα radiation, under 40 kV and 30 mA operating conditions, to identify the mineralogical phases of the bulk clayey samples. The XRD patterns on the < 63 μm fraction were recorded between 2° and 70° using a step scan 0.02° and a step time of 3 seconds. Additional XRD measurements were made on oriented aggregates (Moore and Reynolds, 1989) and the data were recorded between 2° and 30° (2θ) using a step scan 0.02° and a step time of 0.6 s. These oriented aggregates were subjected to three successive treatments: air drying, glycolation and heating to 500°C for 4 hours, in order to confirm the type of clay mineral phases. The Greene-Kelley test modified from Lim and Jackson (1986) was used to distinguish between octahedral and tetrahedral negative layer-charge deficiencies in the smectites. The test consists of saturating the < 2μm clay fractions with 2 M LiCl solution overnight. The Li-exchanged fractions were then rinsed with demineralized water, and oriented aggregates have been prepared on glass slides. The XRD analyses on oriented clay fractions were conducted in sequence on the air-dried slide (N), heated at 300°C (H300, 2H), and finally overnight glycerol solvated (Gl). A d spacing (001) reflection at 9.6 to 10 Å, is indicative of montmorillonite (octahedral negative layer charge), while a spacing at 16.7 to 17.7Å indicates beidellite (tetrahedral negative layer charge).

Scanning electron microscopy pictures were obtained on a TESCAN CLARA microscope operating at 15 kV. The samples are prepared as described in Chapter 2, section 2.2.5.

3.2.5. Photocatalytic experiments

The degradations of PNP, MG, and DBV were studied under UVA light (λ = 365 nm) to determine the photocatalytic activity of the synthesized material. The lamp was an Osram Sylvania, Blacklight-Bleu Lamp, F 18W/BLB-T8, with its maximum peak at 365 nm and an intensity of 1.2 mW/cm^2.

Each sample was placed in a Petri dish with 20 mL of the pollutant solution in water (14 mg/L for PNP, 4 mg/L for MG or DBV). The degradation of the pollutant was evaluated from absorbance measurements with a Genesys 10S UV-Vis spectrophotometer (Thermo Scientific). Previously, adsorption tests were performed in the dark (dark tests) to show whether the pollutant was adsorbed on the surface of the samples. A blank test, consisting of irradiating the pollutant solution for 24 h in a Petri dish without any catalyst, is made to assess the photolysis of the three pollutants under this illumination. The Petri dishes with catalysts and pollutants were stirred on orbital shakers (90 rpm) and illuminated for 24 h. Aliquots of the pollutant were sampled at 0, 2, 6, and 24 h. The photocatalytic degradation can be evaluated by taking the catalyst adsorption (dark test) into account. Each photocatalytic measurement was triplicated to assess the reproducibility of the data. In each box, the sample concentration was 1 g/L. Another experiment was also done with a catalyst concentration of 0.3 g/L only for the pure ZnO sample, to have the same amount of photocatalyst as the hybrid materials, which contain 30 wt% of ZnO.

The same experiments without light were performed to assess the adsorption properties of the samples on the three different model pollutants.

3.3. Results and Discussion

3.3.1. Composition and morphologies of the clay-based materials

Table 3.1 gives the composition of the different samples. The cation-modified clays have respectively higher amounts of the cation that was added during the modification process, as expected.

For the ZnO/Clay hybrid materials, the Si/Al ratio stays equal around 2, and the proportion of ZnO is around 30 wt% for each of the 4 hybrid materials, as expected.

Table 3.1. Sample composition given by ICP-AES.

Samples	Al (wt%)	Si (wt%)	Na (wt%)	Cu (wt%)	Zn (wt%) [and ZnO (wt%)]
Raw clay	10.1	20.9	<0.1	<0.1	<0.1
clay/Na^+	10.2	20.9	0.2	<0.1	<0.1
clay/Cu^{2+}	11.5	21.2	<0.1	0.8	<0.1
clay/Zn^{2+}	10.5	21.4	<0.1	<0.1	2.1
Pure ZnO	-	-	-	-	>99
clay/ZnO	5.2	9.2	<0.1	<0.1	18.9 [28.1]
clay/Na^+/ZnO	5.8	10.3	0.1	<0.1	23.0 [29.0]
clay/Cu^{2+}/ZnO	6.4	11.6	<0.1	0.4	23.3 [30.3]
clay/Zn^{2+}/ZnO	6.0	11.7	<0.1	<0.1	26.0 [31.2]

XRD patterns allow the estimation of the crystalline phase presented in the samples; the patterns are represented in Figure 3.1 for all samples.

For the 4 clays (raw clay, clay/Cu^{2+}, clay/Na^+, and clay/Zn^{2+} samples), similar patterns are observed with several crystalline phases that are pointed out in the bare Clay pattern. These patterns correspond to the smectite family, which encompasses the different phases observed, i.e., augite, cristobalite, montmorillonite, illite, kaolinite, feldspar, and talc. The pure ZnO sample (in green) is composed of the wurtzite phase (peaks denoted as Z) as expected.

When hybrid materials are formed (clay/ZnO, clay/Cu^{2+}/ZnO, clay/Na^+/ZnO, and clay/Zn^{2+}/ZnO samples), the patterns correspond to a mix of the initial Clay pattern with the wurtzite peaks, showing that the hybrid materials are successfully obtained.

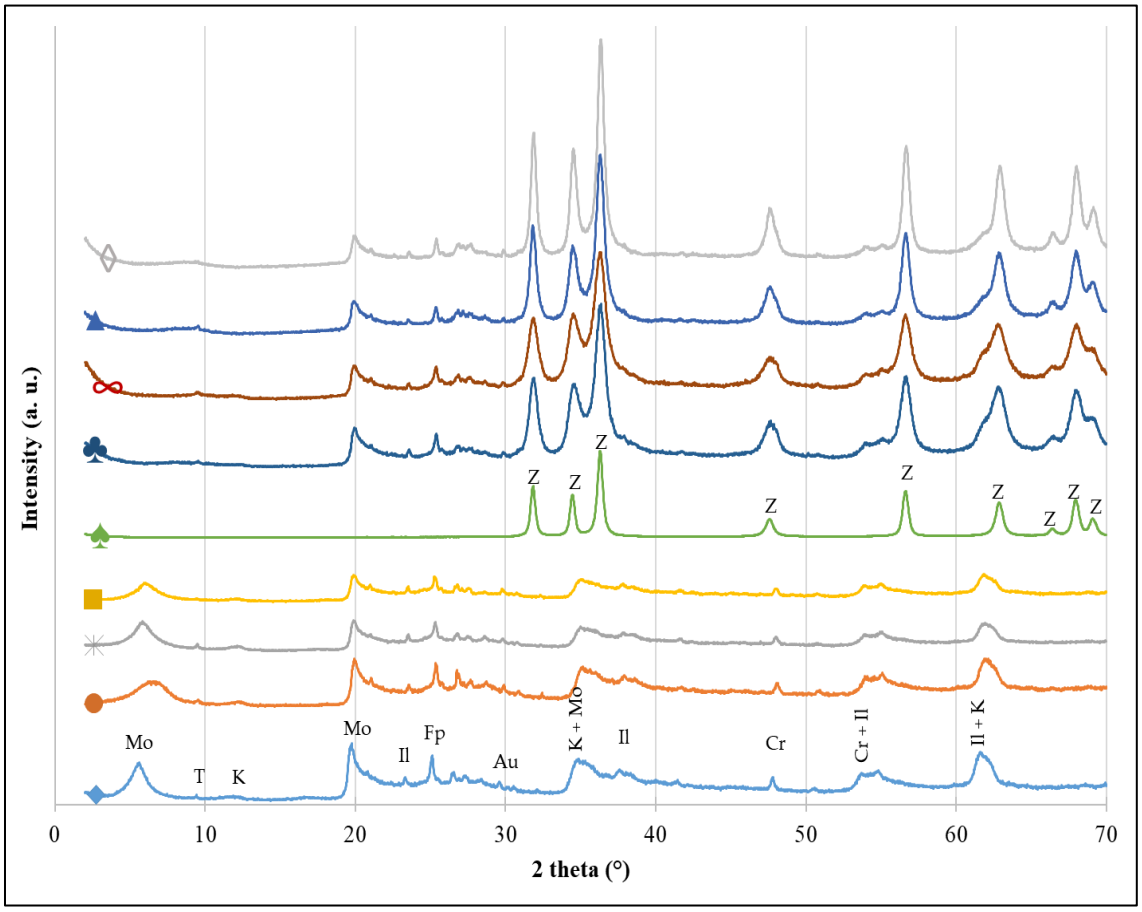

Figure 3.1. XRD patterns of samples: (♦) raw clay, (●) Clay/Cu^{2+}, (*) Clay/Na^{+}, (■) Clay/Zn^{2+}, (♠) Pure ZnO, (♣) Clay/ZnO, (∞) Clay/Cu^{2+}/ZnO, (▲) Clay/Na^{+}/ZnO, and (◊) Clay/Zn^{2+}/ZnO. The positions of the reference peaks are indicated on the two pure materials (bare Clay and ZnO) by the following letters: (A) Anatase, (B) Brookite, (Z) Wurzite, (Mo) Montmorillonite, (K) Kaolinite, (Fp) Feldspar, (Au) Augite, and (Cr) Cristobalite. The positions are not indicated on the composite materials to not overloading the figure.

Table 3.2 presents the specific surface area and the porous volume (V_p) for the different samples. The specific surface values are slightly increased from 45 to 55 m^2/g when cations are inserted into the clay network. Concerning the pure ZnO sample, a specific surface area value of 30 m^2/g is obtained. When the clay is modified with ZnO, a slight increase is also observed for the bare clay. Nevertheless, the specific surface area of the samples already modified with the cations Na^{+}, $Cu^{2+,}$ and Zn^{2+} is not modified when these clays are doped with ZnO. Moreover, a high increase in porous volume is also observed for all samples when ZnO is incorporated in the samples. Indeed, the grafting of the ZnO particles at the surface of the sheets of clay (explained in the next paragraph and observed on the SEM images in Figure 3.3) produces a rougher surface with more pore volume. Figure 3.2 gives an example of the isotherms that are obtained for clay/Zn^{2+} and clay/Zn^{2+}/ZnO samples, and that are very similar for all the samples. These

isotherms correspond mainly to the type IV isotherm characterized by a hysteresis at high pressure (mesoporous solid).

Table 3.2. Specific surface area and porous volume of samples.

Samples	**Specific surface area (m^2/g) ± 5**	**V_p (cm^3/g) ± 0.01**
Raw clay	45	0.07
clay/Na^+	50	0.08
clay/Cu^{2+}	55	0.09
clay/Zn^{2+}	50	0.09
Pure ZnO	30	0.14
clay/ZnO	60	0.44
clay/Na^+/ZnO	55	0.25
clay/Cu^{2+}/ZnO	50	0.21
clay/Zn^{2+}/ZnO	50	0.18

Figure 3.3 gives an overview of the 9 samples observed by SEM. For the 4 clays ((a) raw clay, (b) clay/Cu^{2+}, (c) clay/Na^+, and (d) clay/Zn^{2+} samples), sheet-like materials are observed as expected for clay materials [23, 24], with a smooth surface. No difference between the samples is noted.

When a hybrid material is formed (Figures 3.3f to 3.3i), the sheet-like structure is still observed, but rough surfaces are observed with the presence of spherical materials covering the surface.

These spheres correspond to the ZnO material as it is observed on the pure ZnO sample in Figure 3.3e. So, the hybrid material is composed of the clay as a bone structure covered by ZnO particles. It is important to obtain photocatalytic properties so that the ZnO materials are present at the surface to be in contact with the light.

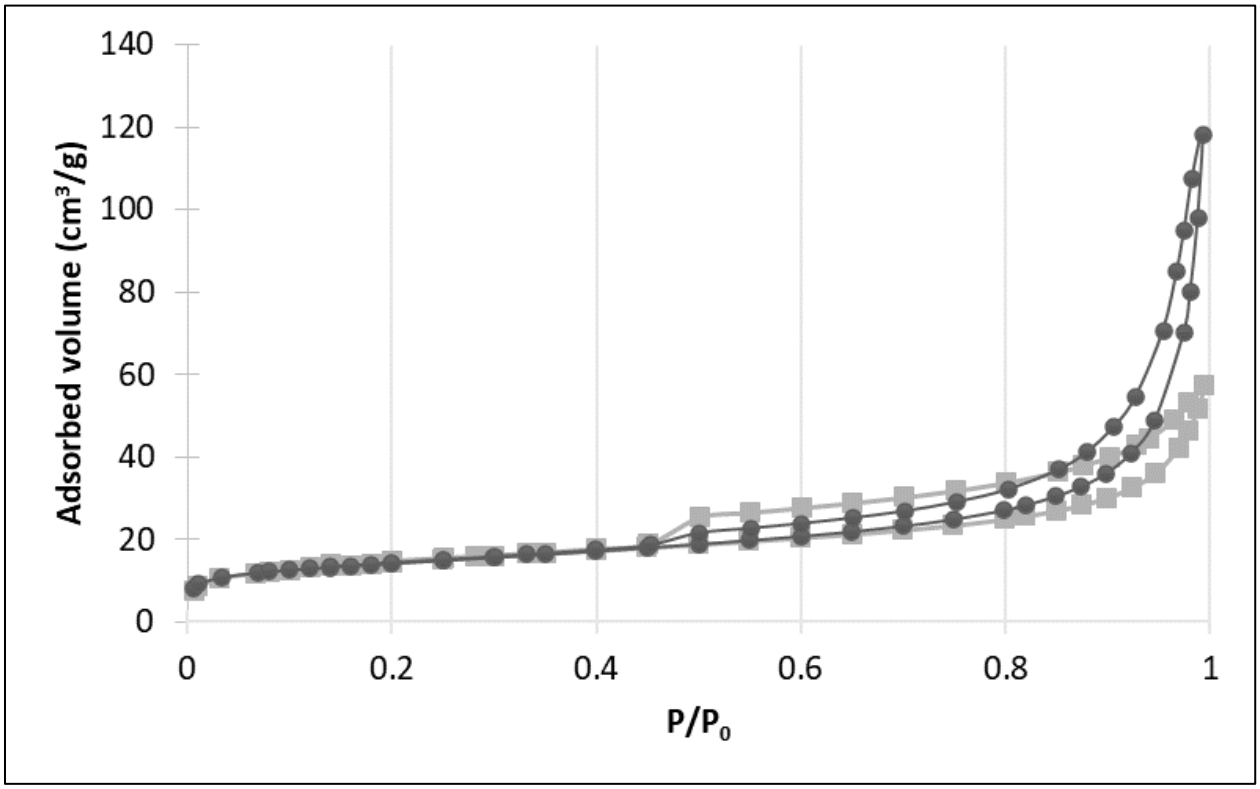

Figure 3.2. Nitrogen adsorption–desorption isotherms for (■) clay/Zn^{2+} and (●) clay/Zn^{2+}/ZnO samples.

Hybrid materials are successfully obtained, composed of 30 wt% of ZnO and 70 wt% of clay, with the ZnO present at the surface.

3.3.2. Adsorption capacity and photocatalytic activity of samples

The materials are evaluated for pollutant removal via the photocatalytic degradation. Their efficiencies are estimated on three different pollutants (PNP, MG, and DBV) to show versatility. Firstly, the blank test showed that the 3 pollutant concentrations under UVA illumination remained constant and that no photolysis occurred.

The first pollutant to eliminate is the PNP commonly found in pesticides. The results are presented in Figure 3.4. First, during the experiments of adsorption made in the dark, no adsorption on any of the 9 samples was observed, so the adsorption results are not represented in Figure 3.4.

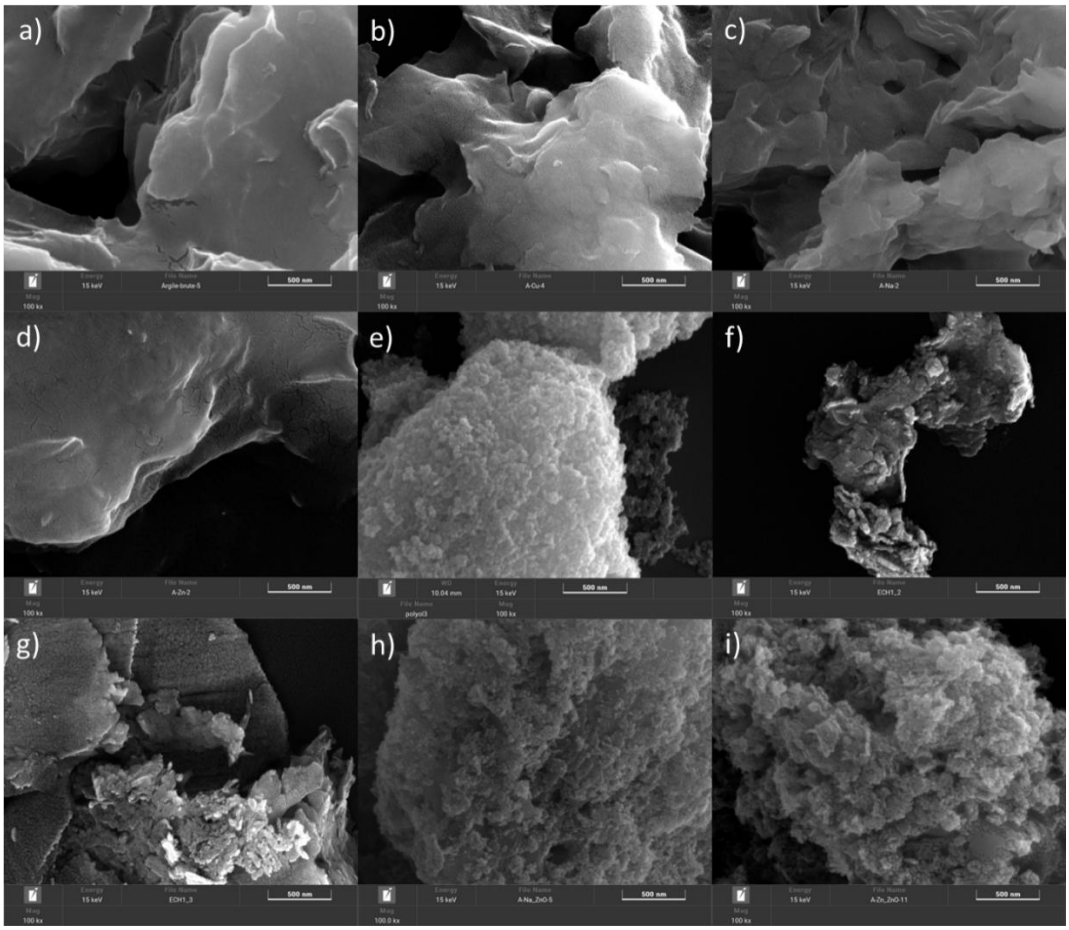

Figure 3.3. SEM pictures of (a) Raw clay, (b) clay/Cu^{2+}, (c) clay/Na^{+}, (d) clay/Zn^{2+}, (e) Pure ZnO, (f) clay/ZnO, (g) clay/Cu^{2+}/ZnO, (h) clay/Na^{+}/ZnO, and (i) clay/Zn^{2+}/ZnO samples.

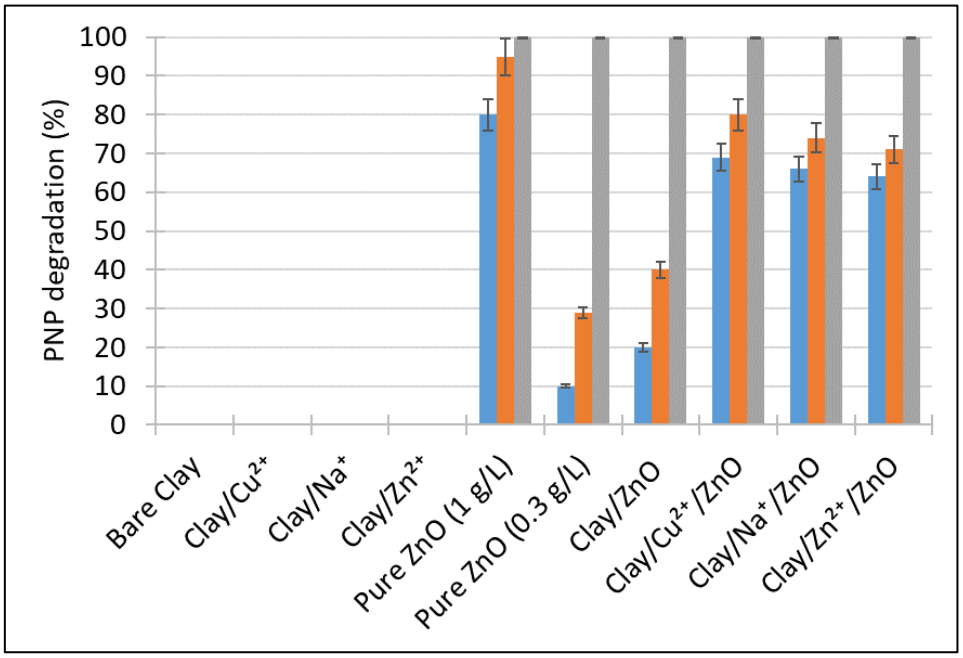

Figure 3.4. PNP degradation (%) under UV-A illumination for 2, 6, and 24 h with all samples. (blue) = after 2 h, (orange) = after 6 h, and (grey) = after 24 h.

Also in Figure 3.4, the photocatalytic degradation of the PNP is presented after 2, 6, and 24 h of elimination for the 9 synthesized samples. Concerning the pure ZnO sample, it is tested with two concentrations: 1 g/L and 0.3 g/L. Indeed, the concentration at 1 g/L is to have the same mass as the other samples, and the concentration of 0.3 g/L is to have the same amount of ZnO as in the hybrid samples, which are made of 30 wt% of ZnO and of 70 wt% of clay. For the 4 clays (raw clay, clay/Cu^{2+}, clay/Na^{+}, and clay/Zn^{2+} samples), no degradation is observed because clay alone is not a photocatalytic material. As previously reported [19, 20, 25], pure ZnO (at 1 g/L) degrades PNP with 95% after 6 h, as ZnO is a photocatalytic material active under UV-A illumination. When the concentration of ZnO is decreased to 0.3 g/L, the degradation rate also decreases, reaching only 30% after 6 h. When hybrid materials are formed (clay/ZnO, clay/Cu^{2+}/ZnO, clay/Na^{+}/ZnO, and clay/Zn^{2+}/ZnO samples), photocatalytic degradation of PNP is still observed for each hybrid material. Among the 4 hybrid materials, the three modified with cations present higher degradation than the clay/ZnO sample. Indeed, the presence of these ions can increase the photocatalytic activity via photo-Fenton reaction for Cu^{2+} and Zn^{2+} ions [21, 26, 27]. For Na^{+} ions, it was reported that if Na^{+} ions were doped the ZnO, it could increase its photocatalytic properties. By adding oxygen vacancies and defect sites to the ZnO lattice, Na^{+} ions reduce electron–hole recombination and improve charge separation by acting as charge carrier traps. Furthermore, band-gap narrowing or the creation of intermediate energy levels can be brought about by Na^{+} doping, which increases ZnO's photocatalytic reaction by allowing it to absorb more visible light. Additionally, these structural and electrical changes improve ZnO's surface reactivity. These results have been supported by a number of studies: Na-doped ZnO showed practically total degradation of organic pollutants under direct sunlight [23] and increased methylene blue degradation efficiency under visible light [24]. As a result, Na^{+} doping successfully enhances ZnO's surface activity, charge separation, and light absorption, resulting in better photocatalytic performance [28].

Finally, the degradation of PNP for all hybrid materials is higher than that of ZnO at a concentration of 0.3 g/L. This can be explained by the specific morphology observed with SEM (Figure 3.3), showing that the ZnO particles are distributed at the surface of the clay sheet, allowing a very good contact between the pollutant and the photocatalytic material.

In Figures 3.5 and 3.6, the adsorption and photocatalytic activity of the samples are represented for MG and DBV removal. Similar tendencies are obtained for both pollutants and are described in the same paragraph. MG is a compound mainly used as a dye or pesticide [21], and DBV is a molecule used as a textile dye [22].

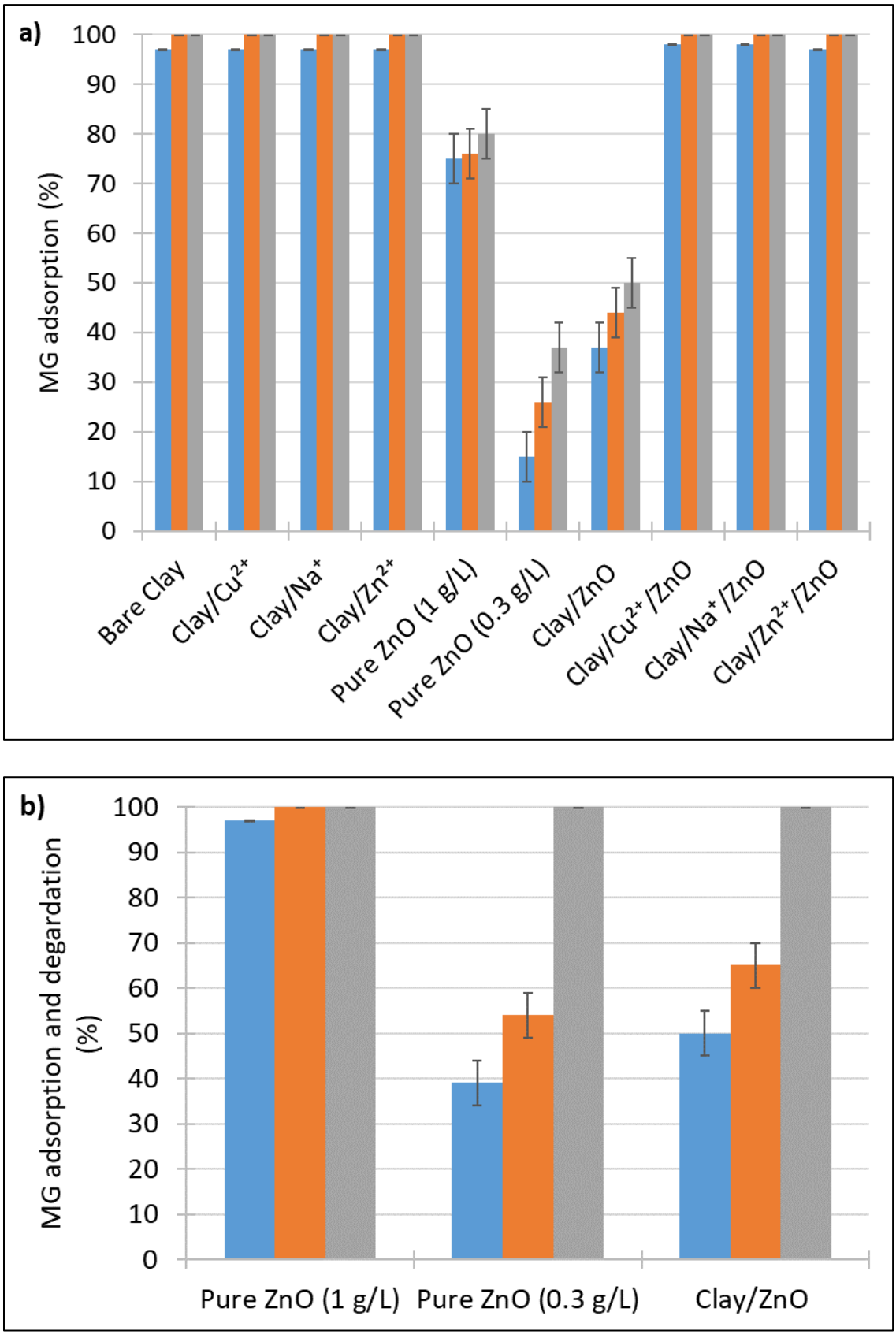

Figure 3.5. (a) MG adsorption (%) and (b) degradation under UVA illumination (%) for 2, 6, and 24 h with all samples. (blue) = after 2 h, (orange) = after 6 h, and (grey) = after 24 h.

From Figures 3.5a and 3.6a, a high adsorption capacity of the clays and hybrid materials is noticed. Indeed, after 2 h of adsorption, more than 95% of both molecules are adsorbed, showing that clay has a high affinity for both dyes. Only the pure ZnO (at both concentrations) and clay/ZnO samples do not totally adsorb the two pollutants after 24 h of experiments. Indeed, 80, 37, and 50% of MG are adsorbed on pure ZnO (1 g/L), pure ZnO (0.3 g/L), and clay/ZnO, respectively, after 24 h. For DBV, 73, 25, and 42% are adsorbed, respectively.

So for the three samples, pure ZnO (1 g/L), pure ZnO (0.3 g/L), and clay/ZnO, the photocatalytic degradation is necessary to eliminate 100% of the molecules from the water. It is represented in Figures 3.5b and 3.6b; in this case, the elimination is due to adsorption and degradation simultaneously. After 24 h of illumination, MG and DBV are eliminated in these three samples. It illustrated the advantage of having a hybrid material that can combine multiple properties to degrade various molecules depending on their resistance to one process over another. As for the PNP degradation, the degradation for the hybrid materials (Figures 3.5b and 3.6b) is higher than the ZnO at the concentration of 0.3 g/L, it can be explained by the specific morphology observed with SEM (Figure 3.3) showing that the ZnO particles are distributed at the surface of clay sheet allowing a very good contact between the pollutant and the photocatalytic material.

Thanks to these pollutant removal experiments, the hybrid materials showed their versatile properties for the elimination of different kinds of molecules throughout the adsorption and/or the photocatalytic degradation of these molecules.

If the affinity between the pollutant and the solid is high, the adsorption capacity is very high, and the pollutant is quickly removed from the water to be fixed on the solid. When the affinity between the pollutant and the solid is low, the photocatalytic property is needed to degrade the pollutant and treat the water. In this study, MG and DBV have a high affinity for the hybrid materials and are mainly removed by adsorption, while PNP has no affinity for the hybrid materials and is totally degraded thanks to the photocatalytic property brought by the ZnO. These different adsorption behaviors are due to the 3 molecules, which have different surface groups that can interact differently with the material surface at the working pH = 7.

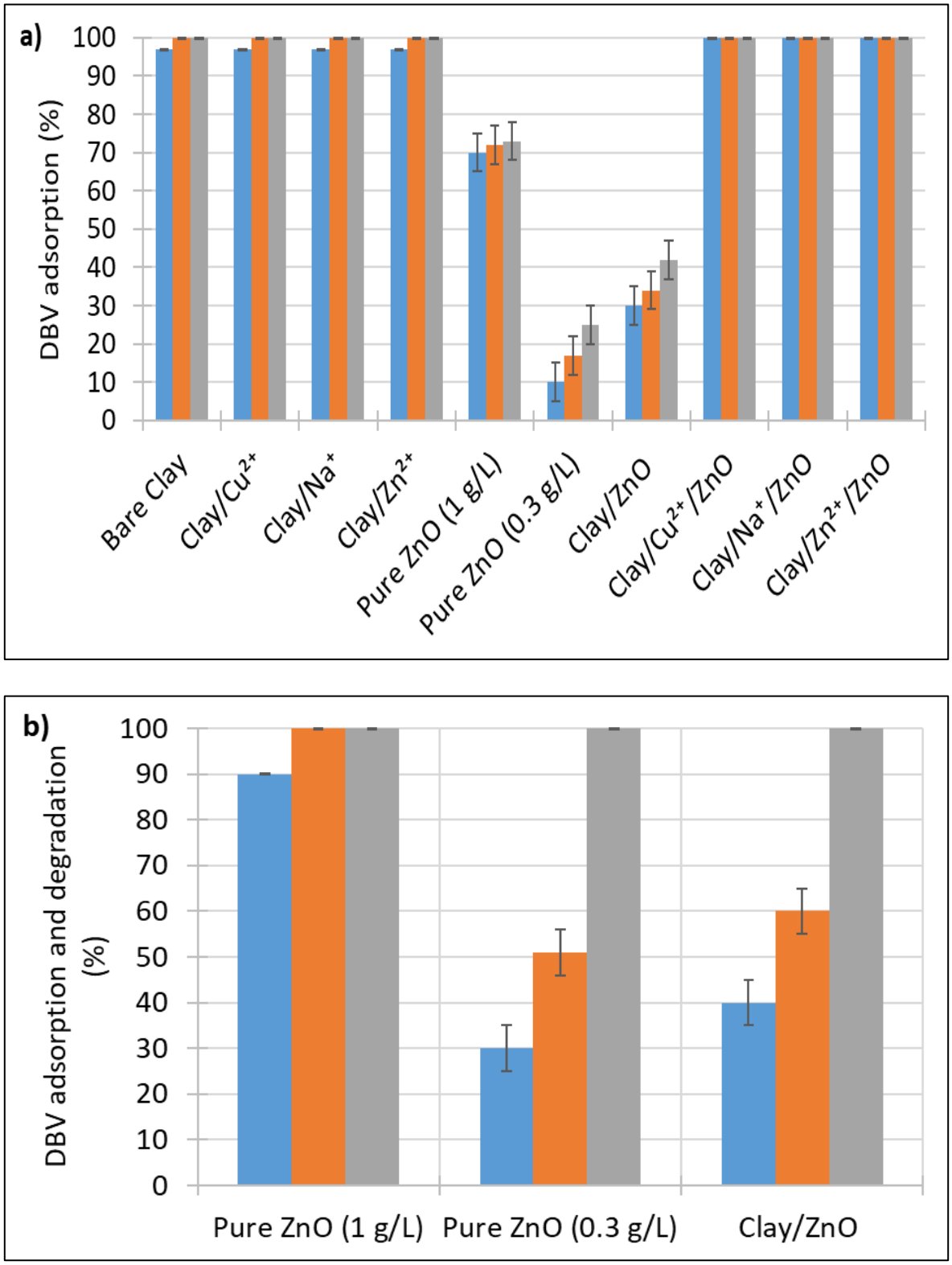

Figure 3.6. (a) DBV adsorption (%) and (b) degradation under UVA illumination (%) for 2, 6, and 24 h with all samples. (blue) = after 2 h, (orange) = after 6 h, and (grey) = after 24 h.

3.4. Conclusions

In this chapter, natural clay extracted from Cameroon was modified with different cations by the exchange process. These latter were also altered with the photocatalytic semiconductor ZnO. The goal was to produce efficient hybrid materials for pollutant removal in water thanks to adsorption and/or photocatalytic mechanisms. The pure ZnO sample and hybrid Clay/ZnO materials were synthesized in soft conditions, either at low temperature and low pressure.

The XRD results showed that the clay belonged to the smectite family and was composed of different crystalline phases, such as augite, cristobalite, montmorillonite, illite, kaolinite, feldspar, and talc. The pure ZnO was made of the wurtzite phase. When the hybrid materials were produced, mixed crystalline patterns were obtained with both smectite and wurtzite phases. The ICP-AES analysis showed that a similar ratio between ZnO and clay was obtained for the 4 hybrid materials (30 wt% of ZnO and 70 wt% of clay). Specific surface areas were obtained for all samples in the range of 30-60 m^2/g. Nevertheless, the porous volume values of the 4 hybrid materials increased when ZnO was incorporated inside the clays (from 0.09 cm^3/g for the bare clay until 0.44 cm^3/g for the Clay/ZnO sample).

The SEM observation of the samples had shown that the hybrid materials presented the clay structure as a skeletal structure (sheet-like structure) with the ZnO spherical materials grafted at the surface, giving a good exposure to light to maintain the photocatalytic property.

Then, the pollutant removal property of the samples was evaluated on three different model pollutants: PNP, MG, and DBV. On PNP, no adsorption was observed, and a photocatalytic property is necessary to eliminate this molecule. With the best hybrid material (clay/Cu^{2+}/ZnO sample), 80% of PNP degradation is observed after 6 h of illumination. On MG and DBV, similar behavior was observed. Indeed, the clays and three out of four hybrid materials adsorbed both pollutants completely after 2 h of contact. Only pure ZnO and clay/ZnO needed illumination to completely remove both molecules from water. A synergistic effect is observed when the clay is modified with ZnO concerning the photocatalytic degradation activity.

This work showed the possibility of obtaining very efficient hybrid materials for pollutant removal in water with the use of inexpensive natural clay modified with a low amount of catalytic material (ZnO around 30 wt%). It opens an innovative way for the development of polluted water treatment processes in developing countries at a lower cost.

References

[1] Srivastava R, Fujita S, Arai M (2009) Synthesis and adsorption properties of smectite-like materials prepared using ionic liquids. Appl Clay Sci 43:1–8. https://doi.org/10.1016/j.clay.2008.06.015

[2] Akçay G, Kilinç E, Akçay M (2009) The equilibrium and kinetics studies of flurbiprofen adsorption onto tetrabutylammonium montmorillonite (TBAM). Colloids Surf A Physicochem Eng Asp 335:189–193. https://doi.org/10.1016/j.colsurfa.2008.11.009

[3] Mahy JG, Wolfs C, Mertes A, et al (2019). Advanced photocatalytic oxidation processes for micropollutant elimination from municipal and industrial water. J Environ Manage 250:. https://doi.org/10.1016/j.jenvman.2019.109561

[4] Mahy JG, Lejeune L, Haynes T, et al (2021) Crystalline ZnO photocatalysts prepared at ambient temperature: Influence of morphology on p-nitrophenol degradation in water. Catalysts 11:. https://doi.org/10.3390/catal11101182

[5] Mahy JG, Tilkin RG, Douven S, Lambert SD (2019) TiO_2 nanocrystallites photocatalysts modified with metallic species: Comparison between Cu and Pt doping. Surfaces and Interfaces 17:. https://doi.org/10.1016/j.surfin.2019.100366

[6] Douven S, Mahy JG, Wolfs C, et al (2020) Efficient N, Fe Co-doped TiO_2 active under cost-effective visible LED light: From powders to films. Catalysts 10:. https://doi.org/10.3390/catal10050547

[7] Bodson CJ, Heinrichs B, Tasseroul L, et al (2016) Efficient P- and Ag-doped titania for the photocatalytic degradation of waste water organic pollutants. J Alloys Compd 682:144–153. https://doi.org/10.1016/j.jallcom.2016.04.295

[8] Pignatello JJ, Oliveros E, MacKay A (2006) Advanced oxidation processes for organic contaminant destruction based on the fenton reaction and related chemistry. Crit Rev Environ Sci Technol 36:1–84. https://doi.org/10.1080/10643380500326564

[9] Issaka E, AMU-Darko JNO, Yakubu S, et al (2022) Advanced catalytic ozonation for degradation of pharmaceutical pollutants—A review. Chemosphere 289:. https://doi.org/10.1016/j.chemosphere.2021.133208

[10] Mahy JG, Tasseroul L, Zubiaur A, et al (2014) Highly dispersed iron xerogel catalysts for p-nitrophenol degradation by photo-Fenton effects. Microporous and Mesoporous Materials 197:164–173. https://doi.org/10.1016/j.micromeso.2014.06.009

[11] Hu Z, Cai J, Song G, et al (2021) Anodic oxidation of organic pollutants: Anode fabrication, process hybrid and environmental applications. Curr Opin Electrochem 26:. https://doi.org/10.1016/j.coelec.2020.100659

[12] Drogui P, Blais J-F, Mercier G (2007) Review of Electrochemical Technologies for Environmental Applications. Recent Patents on Engineering 1:257–272

[13] Cheng T, Gao H, Liu G, et al (2022) Preparation of core-shell heterojunction photocatalysts by coating CdS nanoparticles onto $Bi_4Ti_3O_{12}$ hierarchical microspheres and their photocatalytic removal of organic pollutants and Cr(VI) ions. Colloids Surf A Physicochem Eng Asp 633:. https://doi.org/10.1016/j.colsurfa.2021.127918

[14] Xiong S, Yin Z, Zhou Y, et al (2013) The dual-frequency (20/40 kHz) ultrasound assisted photocatalysis with the active carbon fiber-loaded Fe^{3+}-TiO_2 as photocatalyst for degradation of organic dye. Bull Korean Chem Soc 34:3039–3045. https://doi.org/10.5012/bkcs.2013.34.10.3039

[15] Tang N, Li Y, Chen F, Han Z (2018) In situ fabrication of a direct Z -scheme photocatalyst by immobilizing CdS quantum dots in the channels of graphene-hybridized and supported mesoporous titanium nanocrystals for high photocatalytic performance under visible light. RSC Adv 8:42233–42245

[16] Mahy JG, Lambert SD, Tilkin RG, et al (2019) Ambient temperature ZrO_2-doped TiO_2 crystalline photocatalysts: Highly efficient powders and films for water depollution. Mater Today Energy 13:. https://doi.org/10.1016/j.mtener.2019.06.010

[17] Alderman DJ (1985) Malachite green: a review. J Fish Dis 8:289–298

[18] Lalonger L (1994) La transition des colorants naturels aux colorants synthétiques et ses répercussions. Material Culture Review 40:

[19] Mahy JG, Mbognou MHT, Léonard C, et al (2022) Natural Clay Modified with ZnO/TiO_2 to Enhance Pollutant Removal from Water. Catalysts 12 :https://doi.org/10.3390/catal12020148

[20] Benhebal H, Chaib M, Crine M, et al (2016) Photocatalytic decolorization of gentian violet with Na-doped (SnO_2 and ZnO). Chiang Mai Journal of Science 43:584–589

[21] Benhebal H, Chaib M, Leonard A, et al (2012) Photodegradation of phenol and benzoic acid by sol-gel-synthesized alkali metal-doped ZnO. Mater Sci Semicond Process 15:264–269. https://doi.org/10.1016/j.mssp.2011.12.001

[22] Mahy JG, Lambert SD, Léonard GLM, et al (2016) Towards a large scale aqueous sol-gel synthesis of doped TiO_2: Study of various metallic dopings for the photocatalytic degradation of p-nitrophenol. J Photochem Photobiol A Chem 329:189–202. https://doi.org/10.1016/j.jphotochem.2016.06.029

[23] M. H. Elsayed, T. M. Elmorsi, A. M. Abuelela, A. E. Hassan, A. Z. Alhakemy, M. F. Bakr, H.-H. Chou J. Direct sunlight-active Na-doped ZnO photocatalyst for the mineralization of organic pollutants at different pH mediums. Taiwan Inst. Chem. Eng., 115 (2020), pp. 187-197 https://doi.org/10.1016/j.jtice.2020.10.018

[24] Kim, HM., Park, JH. & Lee, SK. Fiber optic sensor based on ZnO nanowires decorated by Au nanoparticles for improved plasmonic biosensor. Sci Rep 9, 15605 (2019). https://doi.org/10.1038/s41598-019-52056-1

[25] Seo YJ, Seol J, Yeon SH, et al (2009). Structural, mineralogical, and rheological properties of methane hydrates in smectite clays. J Chem Eng Data 54:1284–1291. https://doi.org/10.1021/je800833y

[26] Pirhashemi M, Habibi-Yangjeh A, Rahim Pouran S (2018) Review on the criteria anticipated for the fabrication of highly efficient ZnO-based visible-light-driven photocatalysts. Journal of Industrial and Engineering Chemistry 62:1–25. https://doi.org/10.1016/j.jiec.2018.01.012

[27] Rauf MA, Meetani MA, Hisaindee S (2011) An overview on the photocatalytic degradation of azo dyes in the presence of TiO2 doped with selective transition metals. Desalination 276:13–27. https://doi.org/10.1016/j.desal.2011.03.071

[28] Romero V, Acevedo S, Marco P, et al (2016) Enhancement of Fenton and photo-Fenton processes at initial circumneutral pH for the degradation of the β-blocker Metoprolol. Water Res 88:449–457. https://doi.org/http://dx.doi.org/10.1016/j.watres.2015.10.035

[29] Lin SS, Lu JG, Ye ZZ, et al (2008) p-type behavior in Na-doped ZnO films and ZnO homojunction light-emitting diodes. Solid State Commun 148:25–28. https://doi.org/10.1016/j.ssc.2008.07.028

CHAPITRE IV: Silane-modified clay for enhanced dye pollution adsorption in water

In this chapter, a natural clay from Bakotcha (Cameroon) used in previous chapters was modified with two silanes: tetramethoxysilane (TMOS) and [3-(2-aminoethyl)aminopropyl] trimethoxysilane (EDAS), to increase its adsorption properties.

The main questions explored in this chapter are: (i) What is the structure of montmorillonite when it's diluted with silanes? (ii) What morphology is obtained with TMOS, highly porous materials, with the formation of silica particles at the surface of the clay? (iii) With EDAS, what morphology is obtained? (iv) With both morphologies, which adsorption behaviors are observed on the 3 model pollutants FL, MG et DBV?

To answer these questions, all samples have been characterized and tested by adsorption. The tuning of raw clay with silane opens the way for developing highly efficient adsorbents for pollutants in water from natural and inexpensive materials.

This chapter is published through the following reference: Silane-modified clay for enhanced dye pollution adsorption in water. Marlène Huguette Tsaffo Mbognou, Stéphanie D. Lambert, Ernestine Mimba Mumbfu, Joachim Caucheteux, Antoine Farcy, Nathalie Fagel, Emmanuel Djoufac Woumfo, Julien G. Mahy; Results in Surfaces and Interfaces 14 (2024) 100183; https://doi.org/10.1016/j.rsurfi.2024.100183.

4.1. Introduction

Silicates belonging to the clay mineral family are increasingly studied as an important class of solids that can yield nanostructured materials with interesting properties [1][2]. Important studies have focused on the functionalization of clay materials to obtain hybrid compounds where inorganic and organic components are linked by covalent and ionic-covalent bonds. This research has focused on achieving a high percentage of clay sheet exfoliation in polymer matrices by improving the interactions between clay surfaces and polymer chains through various surface modification approaches [3].

There exist many attractive characteristics on clay surfaces, such as hydroxyl groups on the edges, silanol groups of crystal defects, etc, providing many surface modification and functionalization strategies. Increasingly, the method used to modify the surface of clays is the cation exchange reaction with alkylammonium. This increases the interlayer space and creates a favorable organophilic environment.

A novel modification approach involving a direct grafting reaction to form covalent bonds on clay surfaces has attracted much attention [4] [5]. The organosilanes were covalently bound to the clay surfaces via a condensation reaction with the surface silanol groups (Si-OH), resulting in closer interactions between the organic components and the clay than ionic interaction and physical adsorption [6]. Indeed, for a few years, silicon alkoxides have been used either to modify the textural properties of inorganic materials used as catalysts in the gaseous phase [7][8][9], or to play the role of a link between organic molecules and inorganic photocatalytic materials [10][11].

Functionalizing swelling aluminosilicate clays of the smectite type, such as montmorillonite, would generally result in limited amounts of -OH groups [12] [13]. For grafting organic ligands onto the interlamellar surface of such clays, the literature is sparse, and the resulting materials may suffer from impeded access to binding sites, as shown by less than complete adsorption of heavy metal species relative to the total number of ligands [14].

To overcome the limitation of the surface grafting modification method, the sol-gel route is used to synthesize organoclay using silicon alkoxides as the primary source of silica. Carrado *et al.* [15] provided an approach that allows a large amount of silanes to covalently attach to the clay surface due to the *in-situ* process and more silanol moieties. Nevertheless, the high degree of organosilane incorporation is often accompanied by distortions and structural defects [16].

These modifications allow the formation of hybrid materials with increased adsorption properties for pollutant removal. Indeed, with the expansion of industries during the past two centuries, pollution has increased greatly all around the world, and the development of depollution techniques using inexpensive materials became essential [17][18][19]. Natural clay represents an inexpensive material, available in a lot of developing countries, that can be a good candidate for organic pollutant adsorption from water [20] [21] [22] [23].

The objectives of this chapter are to explore the possibilities of using natural Cameroonian as raw material for the preparation of organic-inorganic hybrid compounds by grafting with silanol groups, either tetramethoxysilane (TMOS) or [3-(2-aminoethylamino)propyl] trimethoxysilane (EDAS), using a well-controlled and facile sol-gel procedure. Then the resulting nanocomposite materials are evaluated as adsorbents for dyes such as fluorescein, malachite green, and brilliant purple diamond present in water polluted by textile industries. The experiments are performed with raw clays from the locality of Bakotcha (West Cameroon). Several physicochemical techniques are used to evaluate the efficiency of the functionalization process.

4.2. Materials and Methods

4.2.1. Clay material and chemical reagents

A smectite-type clay material from the locality of Bakotcha (West Cameroon) was used in this work. It's a Montmorillonite clay with little cristobalite and feldspar as shown by the X-ray diffractogram in Chapter 2, section 2.3.1. The silica precursors and the solvent were tetramethoxysilane (TMOS, 98%) from Alfa Aesar, [3-(2-aminoethyl)aminopropyl] trimethoxysilane (EDAS, 80%) from Sigma Aldrich, and Ethanol absolute (ACS grade) from Merck. Hydrochloric acid (HCl 36-38%, Merck) was used to adjust the pH of the solution. All solutions were prepared with deionized water.

4.2.2. Sol-gel method to modify clay with alkoxides

Clays doped with organosilanes were prepared by the sol-gel process to saturate the material with silica. The synthesis method is the following :

- **TMOS Hydrolysis :**

$$Si(OCH_3)_4 + 4\,H_2O \rightarrow Si(OH)_4 + 4\,CH_3OH \qquad (4.1)$$

- **TMOS Condensation :**

$$2\,Si(OH)_4 \rightarrow (OH)_3 - Si - O - Si - (OH)_3 + H_2O \quad (4.2)$$

$$Si(OH)_4 + Si(OCH_3)_4 \rightarrow (OH)_3 - Si - O - Si - (OCH_3)_3 + CH_3OH \quad (4.3)$$

- **Grafting onto Montmorillonite :**

$$Mont - OH + Si(OH)_4 \rightarrow Mont - O - Si(OH)_3 + H_2O \quad (4.4)$$

TMOS forms the **inorganic silica network** that reacts to the clay surface [24].

- **EDAS Hydrolysis :**

$$NH_2 - (CH_2)_2 - NH - (CH_2)_3 - Si - (OCH_3)_3 + 3\,H_2O \rightarrow NH_2 - (CH_2)_2 - NH - (CH_2)_3 - Si(OH)_3 + 3\,CH_3OH \quad (4.5)$$

- **EDAS Condensation :**

$$2\,NH_2 - (CH_2)_2 - NH - (CH_2)_3 - Si(OH)_3 \rightarrow NH_2 - (CH_2)_2 - NH - (CH_2)_3 - Si(OH)_2 - O - Si(OH)_2 - (CH_2)_3 - NH - (CH_2)_2 - NH_2 + H_2O \quad (4.6)$$

$$NH_2 - (CH_2)_2 - NH - (CH_2)_3 - Si(OH)_3 + NH_2 - (CH_2)_2 - NH - (CH_2)_3 - Si - (OCH_3)_3 \rightarrow NH_2 - (CH_2)_2 - NH - (CH_2)_3 - Si(OH)_2 - O - Si(OCH_3)_2 - (CH_2)_3 - NH - (CH_2)_2 + CH_3OH \quad (4.7)$$

- **Grafting onto Montmorillonite:**

$$Mont - OH + NH_2 - (CH_2)_2 - NH - (CH_2)_3 - Si(OH)_3 \rightarrow Mont - O - Si(OH)_2 - (CH_2)_3 - NH - (CH_2)_2 + H_2O \quad (4.8)$$

EDAS introduces **amine functionality** and forms covalent bonds with the clay surface [25,26].

Different alkoxide/clay mass ratios were taken to evaluate the reagent composition. Table 4.1 represents the different ratios.

Table 4.1. clay/TMOS and clay/EDAS mass ratios.

Ratio clay/TMOS (w/w)	Ratio clay/EDAS (w/w)
3/3	3/3
10/3	10/3
3/10	not gelation

50 mL of deionized water was acidified with hydrochloric acid (36-38%, Merck) to pH 1.5. The mixture was put under magnetic stirring at room temperature. Then, 3.10 g of montmorillonite

clay were added to the initial mixture, still under continuous stirring. A specific amount of TMOS or EDAS, depending on the aimed ratio (Table 4.1), was taken and introduced into 10 mL of absolute ethanol. The previous mixture was added to the initial solution, stirred at 25 °C, until a light brown sol was formed. The gel is aged in an oven for 24 h at 25 °C to allow for condensation, and then dried at 60 °C for 48 h. The procedure used is called the acid-catalyzed procedure because the acid catalyzes the sol-gel process [27]. The syntheses of samples with EDAS were similar to the ones with TMOS, except that the gel was aged for 3 days in an oven at 80 °C for condensation and finally dried at 150 °C for 24 h. Only two ratios were synthesized. Indeed, the clay/EDAS ratio 3/10 was so viscous that it was impossible to dry and work with it.

4.2.3. Material characterization methods

Nitrogen adsorption-desorption isotherms of all samples were determined in an ASAP multisampler device from Micromeritics at -196 °C.

X-ray diffraction patterns were recorded on a Bruker D8 Twin-Twin powder diffractometer (Bruker, Billerica, MA, USA) using Cu-Kα radiation.

Scanning electron microscopy pictures were obtained on a TESCAN CLARA microscope operating at 15 kV. The samples were prepared as described in Chapter 2, Section 2.2.5.

The actual composition of the clay materials was determined by inductively coupled plasma–atomic emission spectroscopy (ICP–AES), equipped with an ICAP 6500 THERMO Scientific device. The mineralization is described in Chapter 2, Section 2.2.5.

4.2.4. Adsorption experiments

The adsorption tests were evaluated on the raw clay material and on the TMOS and EDAS functionalized clay samples with the different mass ratios (6 samples in total). Three model pollutants and dyes used in the pesticide and textile industries were tested as in Chapter 3: malachite green (MG), fluorescein (FL), and diamond bright violet (DBV). Six vials containing sample powders of 5, 10, 15, 20, 25, and 30 mg with 20 mL of pollutant solution in water were prepared for the adsorption experiment. Initial solution concentrations of pollutants were 20 mg/L for FL and 4 mg/L for MG and DBV. The different samples were shaken continuously in the dark. Aliquots of pollutants were taken every 10, 20, 60 min up to 2 h. Residual concentrations of pollutants were assessed with a Genesis 150S UV-Vis spectrophotometer (Thermo Scientific) without filtration. Previously, calibration curves were made for each pollutant. The main adsorption peaks were located at 485 nm for FL, 550 nm for DBV, and 660 nm for MG.

4.3. Results and discussion

4.3.1. Composition of modified clays

Silica-clay nanocomposites were prepared at different ratios as described in the experimental section (section 4.2.2). Variable amounts of silicon alkoxysilanes (TMOS and EDAS) mixed with ethanol were slowly added to dispersions of clays acidified with hydrochloric acid. Each mixture was homogenized under continuous stirring at room temperature. HCl was added to allow TMOS or EDAS to be covalently bound to the surface of the clays so that it could react with other hydrolyzed molecules of the same type. Depending on the amount of TMOS added, gelation of the system occurred after 30 min for the sample clay/TMOS 3/10, and after 2 h for the sample clay/TMOS 10/3. When EDAS is used, there is no gelation of the samples. The clay/EDAS 3/10 sample did not yield any powder product after drying; the gel remained soft. The different capacities of silanes to insert themselves into the clay sheets could explain these observations. Diffusion is facilitated by the lower steric hindrance presented by TMOS (small molecular size) compared to EDAS. The condensation step is slower when the number of silanol groups on the alkoxysilane is smaller [4]. The surfaces of the clays were fixed by silane arrays or silica nanoparticles, depending on the clay/TMOS or clay/EDAS ratio [16].

The Al and Si composition measured by ICP is given in Table 4.2. As expected, the addition of silane increases the amount of silicon in the sample, and the ratio Si/Al increases. Clay/TMOS samples contain more silicon than clay/EDAS samples.

Table 4.2. Al and Si compositions of all samples measured by ICP

Sample	Al (wt%)	Si (wt%)	Si/Al
Raw clay	11.40	20.7	1.82
clay/TMOS 3/10	9.74	21	2.16
clay/TMOS 3/3	7.24	23.4	3.23
clay/TMOS 10/3	10.20	22.7	2.23
clay/EDAS 3/3	7.82	19.9	2.54
clay/EDAS 10/3	10.50	22	2.10

4.3.2. Crystallinity of samples

Figure 4.1 shows the XRD patterns of the different samples, which allowed us to estimate the crystalline structure of the samples. The raw Clay is characterized by the following minerals: Montmorillonite, Talc, Kaolinite, Illite, Feldspar, Augite, and Cristobalite.

In the case of the clay/TMOS sample series (Figure 4.1), the intensity of the clay diffraction peaks decreases when the clay is modified with TMOS. It becomes practically nonexistent when the clay/TMOS ratio is equal to 3/10. This result suggests that the clay platelets were delaminated during the synthesis reaction [16] and that a large amount of amorphous silica is introduced into the sample.

In the clay/EDAS samples (3/3) and (10/3) (Figure 4.1), the peaks of the different minerals present in the raw material are still visible after the EDAS modification, with similar intensities. This would mean that with the low proportion of EDAS used during the syntheses, its incorporation in the clay did not change the initial structure of the material.

4.3.3. Texture and morphology of samples

The textural properties of the samples were confirmed by nitrogen adsorption-desorption measurements. Table 4.3 shows the specific surface area (S_{BET}), the microporous volume (V_{micro}), and the porous volume (V_P) values of the different samples. The Raw clay sample has a relatively low specific surface area (45 m^2/g), which increases highly when TMOS is used (between 135 and 660 m^2/g). This increase is due to the intercalations of the silica groups into the smectite lattice [16]. Indeed, this insertion is observed in the XRD diagrams (Figure 4.1) with the peak spreading around 5°: the montmorillonite peak disappears with the increase of the TMOS amount used during the syntheses. When EDAS is grafted, only a slight specific surface area increase is observed (around 55 m^2/g) and a reduction of the porous volume (Table 4.3).

The isotherms corresponding to the clay/TMOS and clay/EDAS series are represented in Figures 4.2 and 4.3, respectively. For the clay/TMOS series, the isotherms evolve from a type IV isotherm (mesoporous solid for the raw clay) to a type I (microporous solid for the clay/TMOS 3/10) when the amount of TMOS increases compared to the clay. In all samples, a hysteresis is noticed due to the presence of mesopores. For the clay/EDAS series, the shape of the isotherm stays the same, only the volume at saturation decreases due to fewer mesopores probably filled with EDAS molecules.

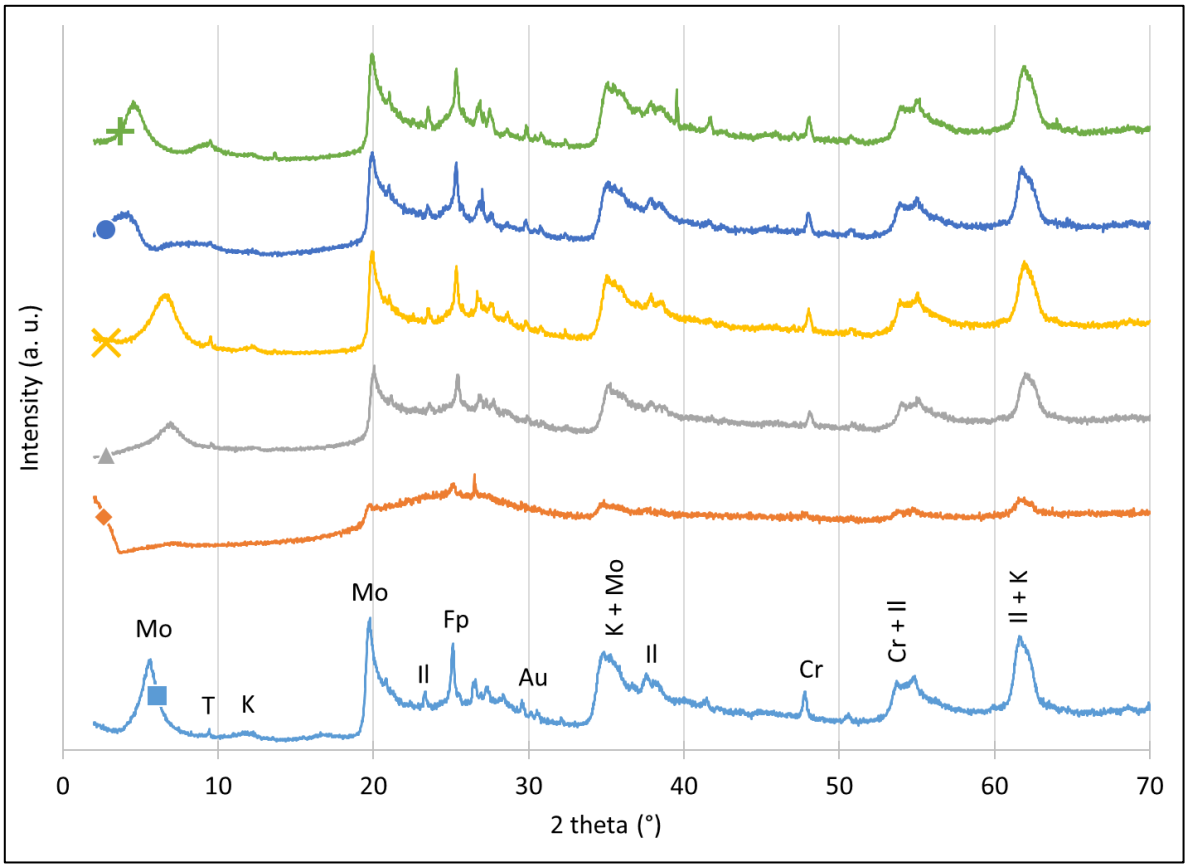

Figure 4.1. XRD patterns of samples: (■) Raw Clay, (♦) clay/TMOS 3/10, (▲) clay/TMOS 3/3, (x) clay/TMOS 10/3, (●) clay/EDAS 3/3, and (+) clay/EDAS 10/3. The positions of the reference peaks are indicated on the Raw Clay by the following letters: (Mo) montmorillonite, (T) talc, (K) kaolinite, (Il) illite, (Fp) feldspar, (Au) augite, and (Cr) cristobalite. The positions are not indicated on the composite materials to avoid overloading the figure.

Table 4.3. Texture of samples.

Sample	**S_{BET} (m^2/g) ± 5**	**V_{micro} (cm^3/g) ± 0.01**	**V_P (cm^3/g) ± 0.01**
Raw clay	45	0.03	0.07
clay/TMOS 3/10	660	0.30	0.39
clay/TMOS 3/3	285	0.14	0.20
clay/TMOS 10/3	135	0.07	0.12
clay/EDAS 3/3	55	0.02	0.03
clay/EDAS 10/3	55	0.02	0.04

S_{BET}: specific surface area obtained by the BET method; V_{micro}: microporous volume ; V_p: specific liquid volume adsorbed at saturation pressure of nitrogen.

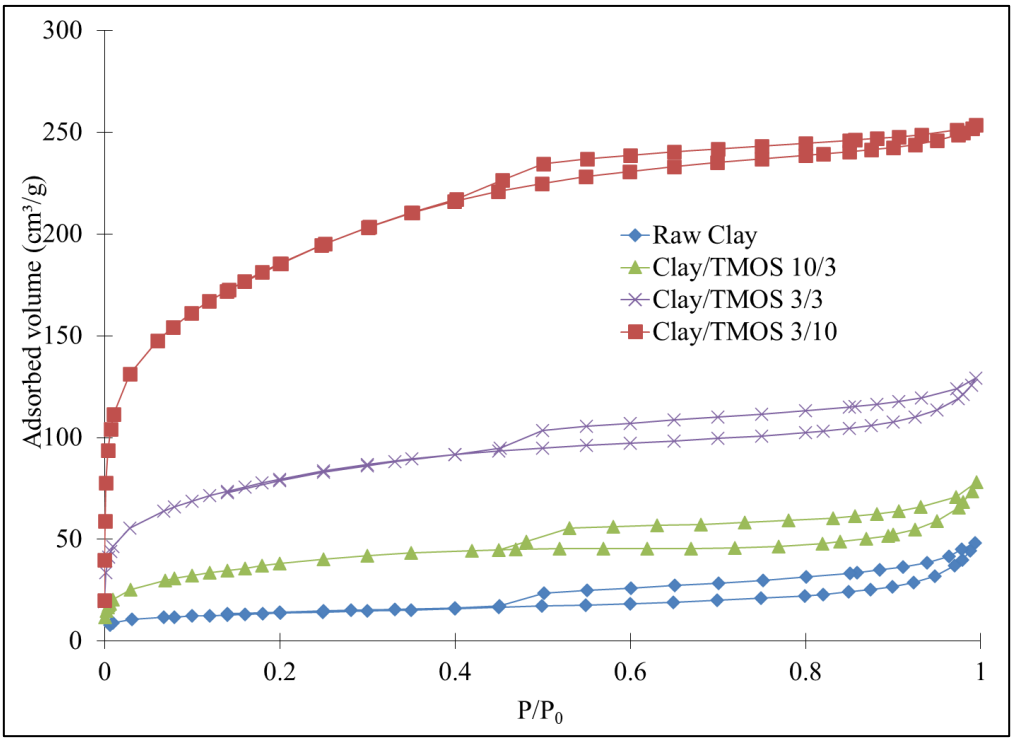

Figure 4.2. Nitrogen adsorption–desorption isotherms for (♦) Raw Clay, (▲) clay/TMOS 10/3, (x) clay/TMOS 3/3, and (■) clay/TMOS 3/10 samples.

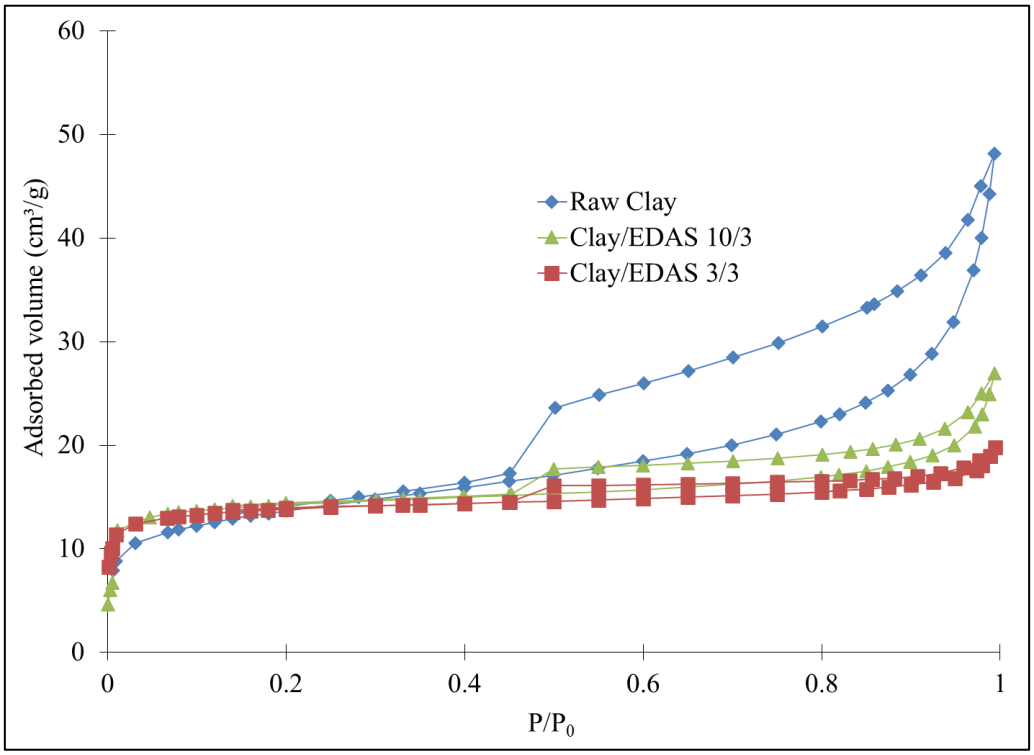

Figure 4.3. Nitrogen adsorption–desorption isotherms for (♦) Raw clay, (▲) clay/EDAS 10/3, and (■) clay/EDAS 3/3 samples.

A more detailed study of the morphology was carried out by SEM (Figure 4.4). It is observed that the surface of the silica-pillared clays by the sol-gel process is considerably affected in some samples, as shown in the images in Figure 4.4. On the raw material, the montmorillonite-type clay sheets are present (Figure 4.4a); however, on the clay/TMOS series, the surfaces of the samples are covered with large continuous silica networks, giving a rougher aspect of the surface (Figures 4.4b-d). These results are in agreement with the high specific surface areas found for the clay/TMOS series. Contrarily, the clay/EDAS series (Figures 4.4e-f) does not show big differences with the raw clay sample.

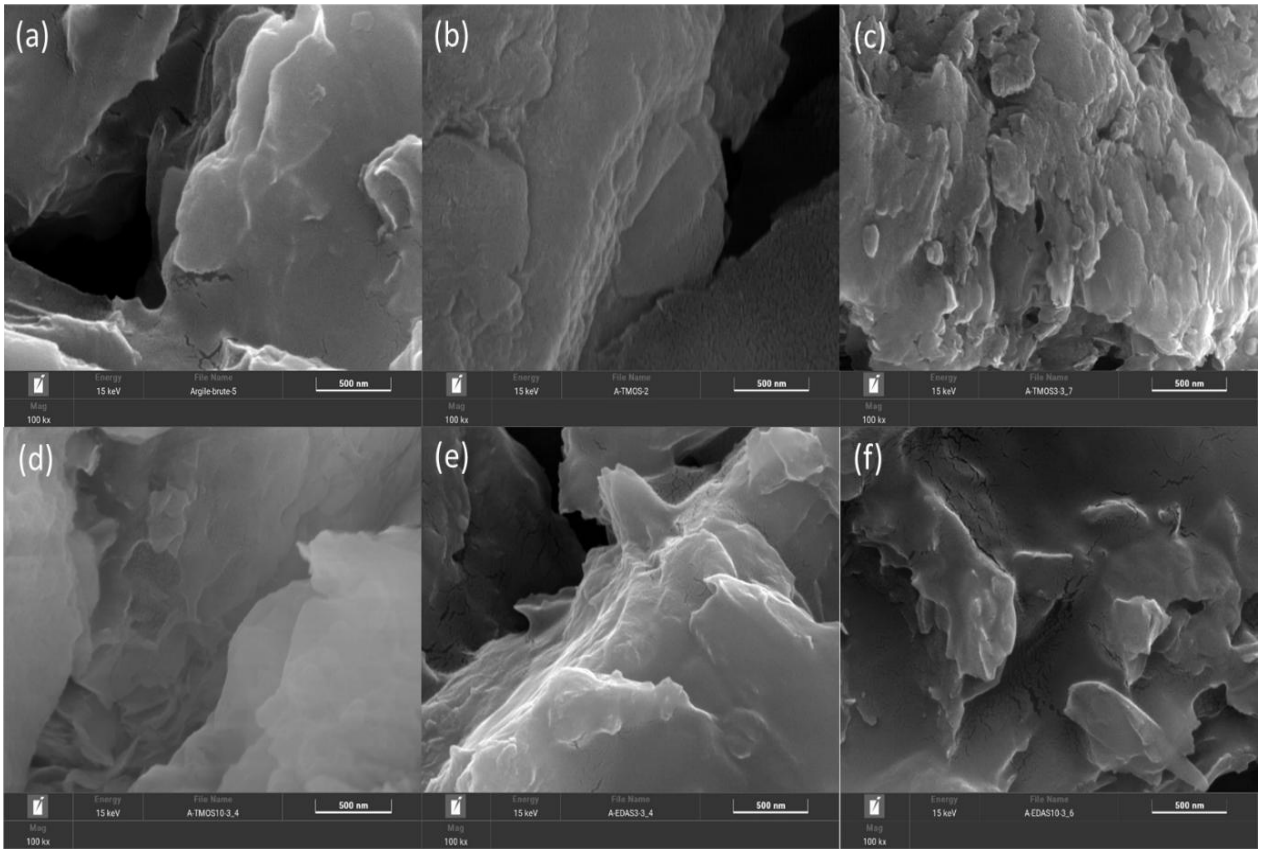

Figure 4.4. SEM pictures of (a) Raw Clay, (b) clay/TMOS 3/10, (c) clay/TMOS 3/3, (d) clay/TMOS 10/3, (e) clay/EDAS 3/3, and (f) clay/EDAS 10/3 samples.

The differences observed in the SEM images, XRD patterns and nitrogen adsorption-desorption isotherms in the TMOS and EDAS series can be explain by two different mechanisms in the two series: (i) in the clay/TMOS series, the addition of TMOS produces amorphous silica network mixed with the clay (Figure 4.1) leading to a porous hybrid material (Table 4.3) where porous silica particles cover the surface of the clay sheets (Figures 4.4b, 4.4c and 4.4d); (ii) in the clay/EDAS series, the EDAS molecules are probably grafted to the surface of the clay

producing a continuous dense coating at the surface with similar aspect to the raw clay (Figure 4.4e and 4.4f) reducing the porous volume of the raw clay (Table 4.3) and keeping the same crystallinity of the raw clay (Figure 4.1).

The formation of both different structures leads to two series of hybrid materials with new surface properties, one with a high surface area containing a lot of silica surface groups, and one with silane grafted at the surface containing amine groups. These materials can have interesting adsorption properties due to high porosity or specific amine groups at the surface; their adsorption capacities are explored in the next section.

4.3.4. Adsorption properties of hybrid samples

The adsorption efficiency of functionalized clays was tested on the removal of 3 model pollutants: FL, MG, and DBV, which are represented in Figure 4.5. These pollutants are listed among those generally used in the pesticide and textile industry [28] [29] [30]. For each pollutant, the evolution of the pollutant concentration over time is estimated with different concentrations of adsorbent materials between 5 and 30 mg of sample for 20 mL of pollutant solution. The initial pH for the three pollutant solutions is 4.8, 5.1, and 5.7 for FL, MG, and BVD, respectively.

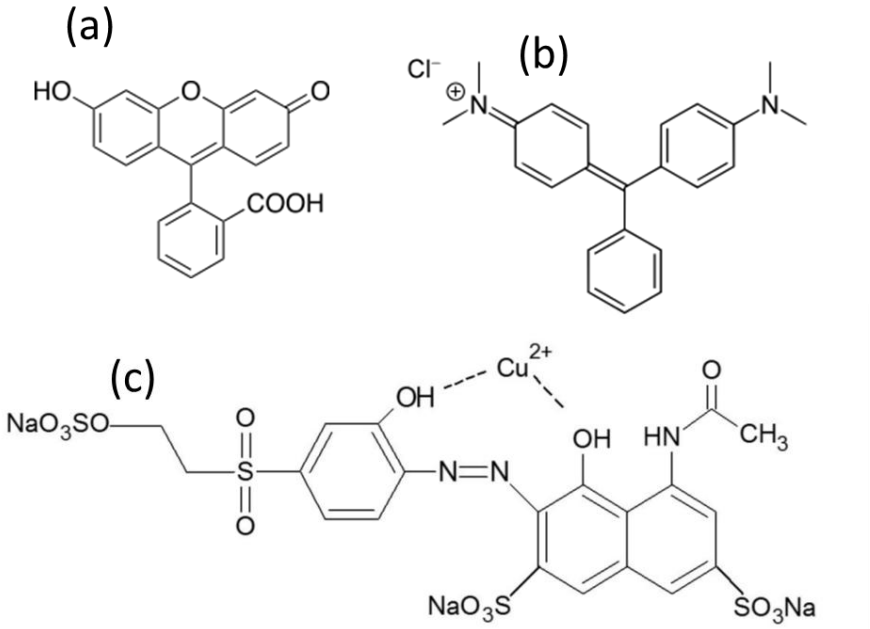

Figure 4.5: Molecular structure of (a) fluorescein, (b) malachite green, and (c) diamond bright violet.

For FL, Figure 4.6 represents the evolution of the concentration (C/C_0) during 1 h for the 6 samples. With the raw clay, around 80% of FL is adsorbed during the experiment (Figure 4.6a).

The modifications with TMOS (Figures 4.6b to 4.6d) allow for an increase in the adsorption capacity of the sample, leading to a total FL adsorption during the experiments.

Indeed, it is shown that this modification greatly increases the specific surface area (Table 4.3) [31]. Nevertheless, the specific surface area is not the only parameter involved in the adsorption process; the nature of the surface groups of the adsorbent also plays a role. In fact, for the samples modified with EDAS (Figure 4.6e), even if the specific surface area is a little bit increased (Table 4.3), no adsorption occurs during the experiments. The insertion of the ethylenediamine groups of the EDAS has no affinity with FL.

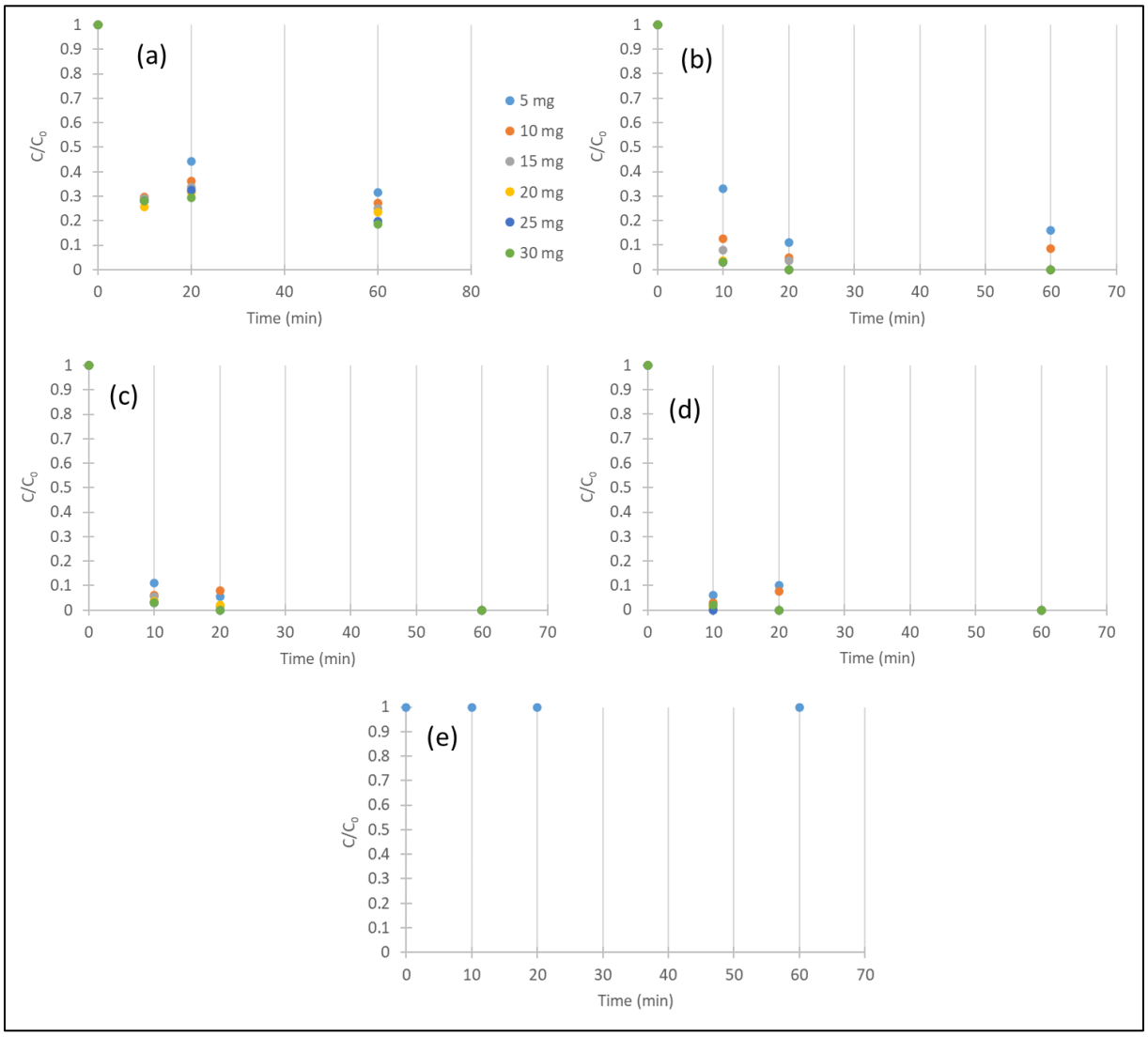

Figure 4.6. C/C_0 fluorescein evolution with time for 5-30 mg concentration range for (a) Raw clay, (b) clay/TMOS 10/3, (c) clay/TMOS 3/3, (d) clay/TMOS 3/10, and (e) clay/EDAS 3/3 samples. Both samples modified with EDAS (clay/EDAS 3/3 and clay/EDAS 10/3) do not adsorb fluorescein, regardless of the adsorbent concentration. It is why only one set of points is represented on Figure 4.6e.

For MG, Figure 4.7 represents the evolution of the concentration (C/C_0) during 1 h for the 6 samples. The raw clay and the samples modified with TMOS adsorb MG totally after 10 min, while the samples modified with EDAS take 2 h to adsorb it totally. The presence of the ethylenediamine groups slows the MG adsorption.

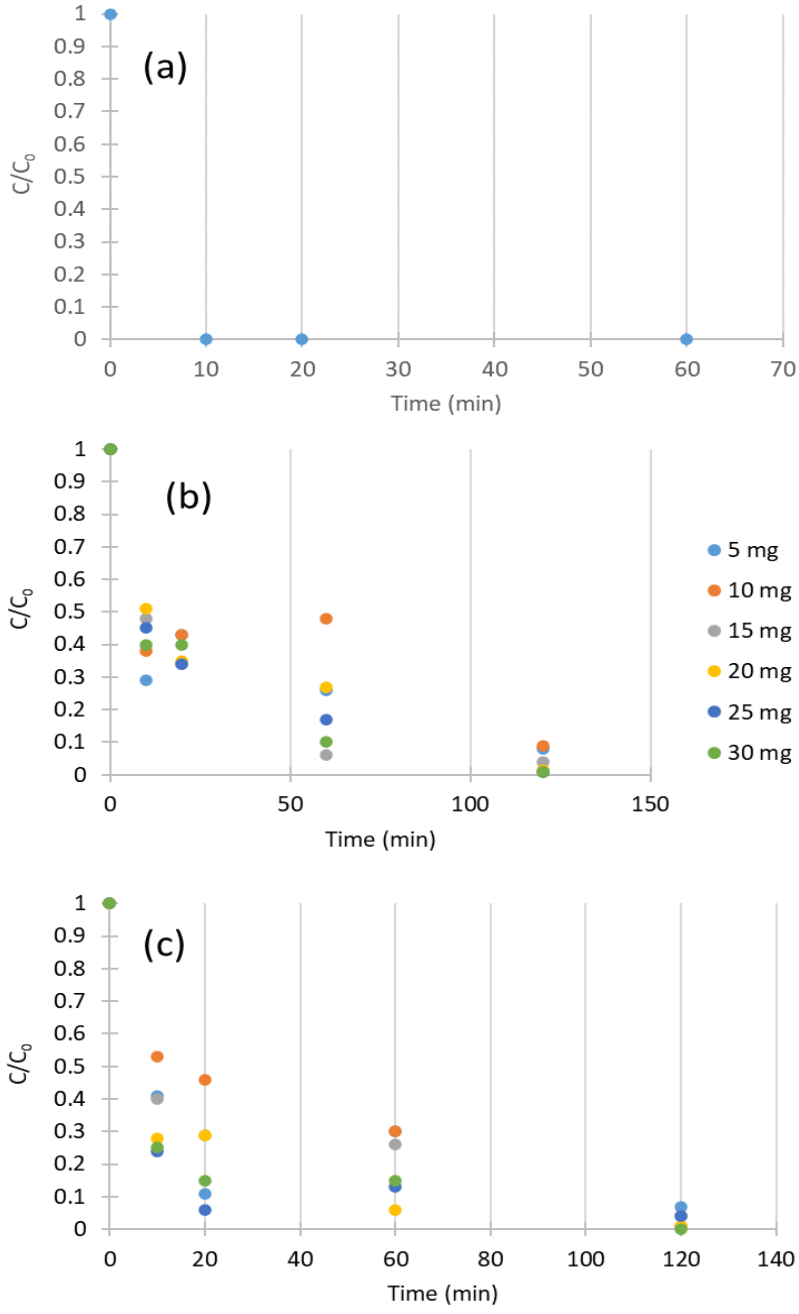

Figure 4.7. C/C_0 malachite green evolution with time for 5-30 mg concentration range for (a) raw clay, (b) clay/EDAS 10/3, and (c) clay/EDAS 3/3. Raw clay, and the 3 samples modified with TMOS have the same behavior as represented in Figure 4.7a with a complete adsorption

of MG after 10 min, whatever the adsorbent concentration. It is why only one set of points is represented in Figure 4.7a.

For DBV, the same adsorption behavior is noticed for all samples (Figure 4.8), with a quick adsorption of this pollutant in 10 min. For this pollutant, the modification of the clay is not necessary.

Throughout the adsorption of the 3 model pollutants, it is noticed that the morphology obtained with samples doped with TMOS brings the most promising adsorbent materials. Indeed, these materials present the highest specific surface area. Depending on the type of pollutant and the surface groups of the adsorbent, very different behaviors can be obtained.

When clay and modified clays are added, the pH of the solution is modified following these tendencies: when raw clay or clay/TMOS is added, the pH becomes more acidic, while with clay/EDAS, the pH becomes more basic. So, the addition of raw clay and clay/TMOS samples will result in a pollutant with more charges that will have more affinity to adsorb on the solid [32]. Contrarily, the clay/EDAS samples will induce pollutants with fewer surface charges and lower adsorption affinity.

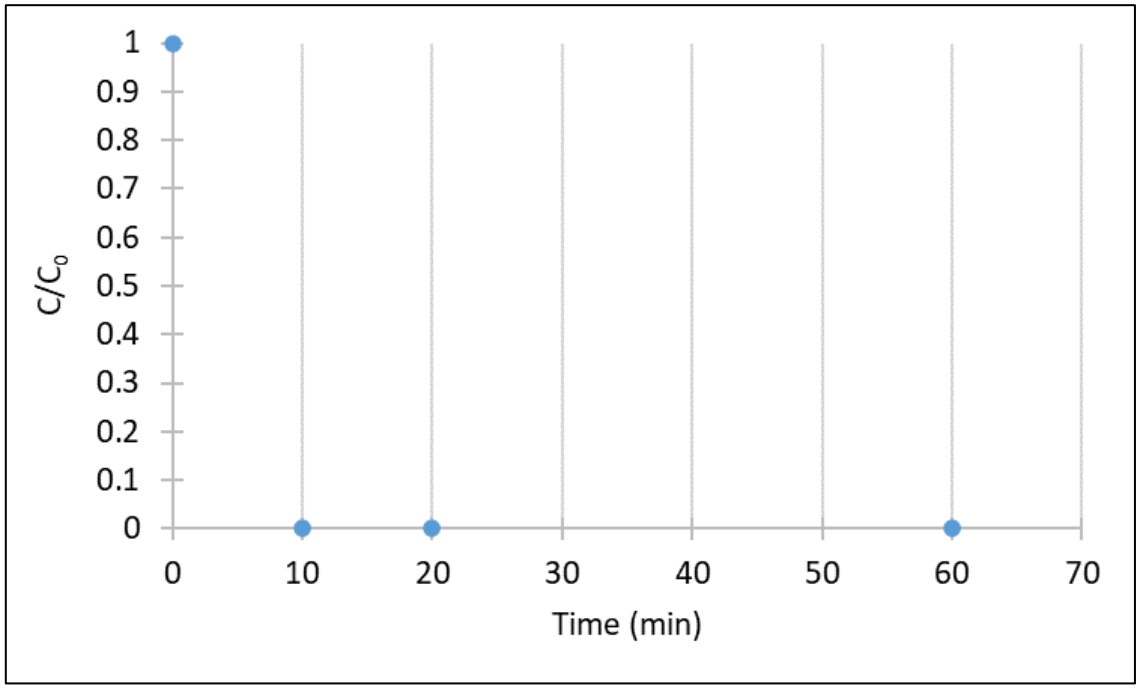

Figure 4.8. C/C_0 brilliant violet diamond evolution with time for 5 mg concentration for raw clay. All other samples in any concentration have the same behavior as represented with a complete adsorption of BVD after 10 min, regardless of the adsorbent concentration, which is why only one set of points is represented in Figure 4.8.

4.4. Conclusions

In this chapter, smectite clay from Cameroon is modified with two silicon alkoxide molecules, tetramethoxysilane (TMOS) and [3-(2-aminoethylamino)propyl]trimethoxysilane (EDAS), in different proportions. The goals of these modifications are to produce hybrid materials with modified morphology, higher specific surface area, and different surface groups (hydroxyl or ethylenediamine groups) to increase their adsorption capacity. Indeed, these materials are used as organic pollutant adsorbents for water depollution, and three model pollutants in water are explored.

The XRD patterns show a dilution of the raw clay when it is modified with TMOS, while the modification with EDAS keeps its original crystalline structure. The SEM and BET measurements confirm that two types of materials are produced depending on the silane used: (i) with TMOS, highly porous materials are produced with the formation of silica particles at the surface of the clay with the porosity increasing with the amount of TMOS; (ii) with EDAS, a similar morphology as raw clay is obtained with only a small increase in porosity. In this case, EDAS molecules are grafted at the surface of the clay, producing a layer at the surface with new surface ethylenediamine groups.

Both morphologies give two different adsorption behaviors on the 3 model pollutants. For the raw clay and the TMOS-modified clays, similar adsorption properties are obtained with better adsorption when the specific surface increases (when the TMOS content increases). In all these samples, similar surface groups are present: the surface groups of the clay and the surface groups of the produced silica (mainly OH groups). When clay is modified with EDAS, the adsorption properties change as the surface groups are different due to the grafting of EDAS and a large presence of ethylenediamine groups. These EDAS-modified samples have less affinity with fluorescein and malachite green, reducing the adsorption capacity for this kind of pollutant.

The tuning of the raw clay with silane opens the way for the development of a highly efficient adsorbent for pollutants in water from natural and inexpensive materials.

References

[1] J. Dong et J. Zhang, « Biomimetic Super Anti-Wetting Coatings from Natural Materials: Superamphiphobic Coatings Based on Nanoclays », *Sci Rep*, vol. 8, nº 1, p. 12062, août 2018, doi: 10.1038/s41598-018-30586-4.

[2] C. H. Zhou, L. Z. Zhao, A. Q. Wang, T. H. Chen, et H. P. He, « Current fundamental and applied research into clay minerals in China », *Applied Clay Science*, vol. 119, p. 3-7, janv. 2016, doi: 10.1016/j.clay.2015.07.043.

[3] P. Viville, R. Lazzaroni, E. Pollet, M. Alexandre, et P. Dubois, « Controlled Polymer Grafting on Single Clay Nanoplatelets », *J. Am. Chem. Soc.*, vol. 126, nº 29, p. 9007-9012, juill. 2004, doi: 10.1021/ja048657y.

[4] H. He, J. Duchet, J. Galy, et J.-F. Gerard, « Grafting of swelling clay materials with 3-aminopropyltriethoxysilane », *Journal of Colloid and Interface Science*, vol. 288, nº 1, p. 171-176, août 2005, doi: 10.1016/j.jcis.2005.02.092.

[5] P. A. Wheeler, J. Wang, J. Baker, et L. J. Mathias, « Synthesis and Characterization of Covalently Functionalized Laponite Clay », *Chem. Mater.*, vol. 17, nº 11, p. 3012-3018, mai 2005, doi: 10.1021/cm050306a.

[6] I. K. Tonle, E. Ngameni, D. Njopwouo, C. Carteret, et A. Walcarius, « Functionalization of natural smectite-type clays by grafting with organosilanes: physico-chemical characterization and application to mercury(ii) uptake », *Phys. Chem. Chem. Phys.*, vol. 5, nº 21, p. 4951, 2003, doi: 10.1039/b308787e.

[7] V. Claude, J. G. Mahy, J. Geens, C. Courson, et S. D. Lambert, « Synthesis of Ni/γ-Al2O3SiO2 catalysts with different silicon precursors for the steam toluene reforming », *Microporous and Mesoporous Materials*, vol. 284, p. 304-315, août 2019, doi: 10.1016/j.micromeso.2019.04.027.

[8] S. Lambert *et al.*, « Tailor-made morphologies for Pd/SiO2 catalysts through sol–gel process with various silylated ligands », *Microporous and Mesoporous Materials*, vol. 115, nº 3, p. 609-617, nov. 2008, doi: 10.1016/j.micromeso.2008.03.003.

[9] J. G. Mahy, V. Claude, L. Sacco, et S. D. Lambert, « Ethylene polymerization and hydrodechlorination of 1,2-dichloroethane mediated by nickel(II) covalently anchored to silica xerogels », *J Sol-Gel Sci Technol*, vol. 81, nº 1, p. 59-68, janv. 2017, doi: 10.1007/s10971-016-4272-0.

[10] J. G. Mahy, C. Carcel, et M. W. Chi Man, « Evonik P25 photoactivation in the visible range by surface grafting of modified porphyrins for p-nitrophenol elimination in water », *AIMSMATES*, vol. 10, nº 3, p. 437-452, 2023, doi: 10.3934/matersci.2023024.

[11] J. G. Mahy *et al.*, « Porphyrin-based hybrid silica-titania as a visible-light photocatalyst », *Journal of Photochemistry and Photobiology A: Chemistry*, vol. 373, p. 66-76, mars 2019, doi: 10.1016/j.jphotochem.2019.01.001.

[12] R. Celis, M. C. HermosÍn, et J. Cornejo, « Heavy Metal Adsorption by Functionalized Clays », *Environ. Sci. Technol.*, vol. 34, nº 21, p. 4593-4599, nov. 2000, doi: 10.1021/es000013c.

[13] K. Song et G. Sandí, « Characterization of Montmorillonite Surfaces After Modification by Organosilane », *Clays and clay miner.*, vol. 49, nº 2, p. 119-125, avr. 2001, doi: 10.1346/CCMN.2001.0490202.

[14] L. Mercier et T. J. Pinnavaia, « Heavy Metal Ion Adsorbents Formed by the Grafting of a Thiol Functionality to Mesoporous Silica Molecular Sieves: Factors Affecting Hg(II) Uptake », *Environ. Sci. Technol.*, vol. 32, nº 18, p. 2749-2754, sept. 1998, doi: 10.1021/es970622t.

[15] K. A. Carrado, « Synthetic organo- and polymer–clays: preparation, characterization, and materials applications », *Applied Clay Science*, vol. 17, nº 1-2, p. 1-23, juill. 2000, doi: 10.1016/S0169-1317(00)00005-3.

[16] Z. Qian, G. Hu, S. Zhang, et M. Yang, « Preparation and characterization of montmorillonite–silica nanocomposites: A sol–gel approach to modifying clay surfaces », *Physica B: Condensed Matter*, vol. 403, nº 18, p. 3231-3238, sept. 2008, doi: 10.1016/j.physb.2008.04.008.

[17] Y. Kemgang Lekomo *et al.*, « Assessing impacts of sand mining on water quality in Toutsang locality and design of waste water purification system », *Cleaner Engineering and Technology*, vol. 2, p. 100045, juin 2021, doi: 10.1016/j.clet.2021.100045.

[18] L. C. Paredes-Quevedo, N. J. Castellanos, et J. G. Carriazo, « Influence of Porosity and Surface Area of a Modified Kaolinite on the Adsorption of Basic Red 46 (BR-46) », *Water Air Soil Pollut*, vol. 232, nº 12, p. 509, déc. 2021, doi: 10.1007/s11270-021-05450-3.

[19] H. Shayesteh, A. Rahbar-Kelishami, et R. Norouzbeigi, « Adsorption of malachite green and crystal violet cationic dyes from aqueous solution using pumice stone as a low-cost

adsorbent: kinetic, equilibrium, and thermodynamic studies », *Desalination and Water Treatment*, vol. 57, nº 27, p. 12822-12831, juin 2016, doi: 10.1080/19443994.2015.1054315.

[20] G. Akçay, E. Kılınç, et M. Akçay, « The equilibrium and kinetics studies of flurbiprofen adsorption onto tetrabutylammonium montmorillonite (TBAM) », *Colloids and Surfaces A: Physicochemical and Engineering Aspects*, vol. 335, nº 1-3, p. 189-193, mars 2009, doi: 10.1016/j.colsurfa.2008.11.009.

[21] R. Nodehi, H. Shayesteh, et A. R. Kelishami, « Enhanced adsorption of congo red using cationic surfactant functionalized zeolite particles », *Microchemical Journal*, vol. 153, p. 104281, mars 2020, doi: 10.1016/j.microc.2019.104281.

[22] R. Srivastava, S. Fujita, et M. Arai, « Synthesis and adsorption properties of smectite-like materials prepared using ionic liquids », *Applied Clay Science*, vol. 43, nº 1, p. 1-8, janv. 2009, doi: 10.1016/j.clay.2008.06.015.

[23] G. Tchanang, C. N. Djangang, C. F. Abi, D. L. M. Moukouri, et P. Blanchart, « Synthesis of reactive silica from kaolinitic clay: Effect of process parameters », *Applied Clay Science*, vol. 207, p. 106087, juin 2021, doi: 10.1016/j.clay.2021.106087.

[24] Sanchez, C., et al. (2005). “Applications of hybrid organic–inorganic nanocomposites.” Journal of Materials Chemistry, 15, 3559–3592.

[25] Zhao, D., et al. (1997). “Surface modification of montmorillonite by organosilanes.” Journal of Materials Chemistry, 7, 1877–1882.

[26] Yuan, P., et al. (2008). “Surface modification of montmorillonite by APTES for adsorption applications.” Journal of Colloid and Interface Science, 318, 392–399.

[27] J. G. Mahy, M. H. Tsaffo Mbognou, C. Léonard, N. Fagel, E. D. Woumfo, et S. D. Lambert, « Natural Clay Modified with ZnO/TiO_2 to Enhance Pollutant Removal from Water », *Catalysts*, vol. 12, nº 2, p. 148, janv. 2022, doi: 10.3390/catal12020148.

[28] S. S. Prakash, C. J. Brinker, et A. J. Hurd, « Silica aerogel films at ambient pressure », *Journal of Non-Crystalline Solids*, vol. 190, nº 3, p. 264-275, oct. 1995, doi: 10.1016/0022-3093(95)00024-0.

[29] J. G. Mahy *et al.*, « Towards a large scale aqueous sol-gel synthesis of doped TiO2: Study of various metallic dopings for the photocatalytic degradation of p-nitrophenol », *Journal of Photochemistry and Photobiology A: Chemistry*, vol. 329, p. 189-202, oct. 2016, doi: 10.1016/j.jphotochem.2016.06.029.

[30] D. J. Alderman, « Malachite green: a review », *Journal of Fish Diseases*, vol. 8, nº 3, p. 289-298, mai 1985, doi: 10.1111/j.1365-2761.1985.tb00945.x.

[31] L. Lalonger, « La transition des colorants naturels aux colorants synthétiques et ses répercussions ».

[32] J. G. Mahy *et al.*, « Ambient temperature ZrO_2-doped TiO_2 crystalline photocatalysts: Highly efficient powders and films for water depollution », *Materials Today Energy*, vol. 13, p. 312-322, sept. 2019, doi: 10.1016/j.mtener.2019.06.010.

CHAPITRE V: Dual-function Cameroonian clay-supported ZnO and TiO_2 photocatalysts for ibuprofen mineralization and bacterial inactivation under UV light

In this chapter, photocatalytic materials, synthesized previously in Chapters II and III by doping natural Cameroonian clay with ZnO and TiO_2, are used for efficient degradation of ibuprofen and bacterial inhibition under UV light.

The primary queries addressed in this chapter are: (i) How was the successful dispersion of semiconductors on the clay matrix confirmed? (ii) What did the composites achieve in degradation efficiencies under UV light? (iii) What dual functionality was demonstrated by materials regarding pharmaceutical and microbial removal from wastewater?

To answer these questions, all the samples were characterized to confirm the semiconductors' successful dispersion on the clay matrix. Under UV irradiation, the composites achieved significant degradation efficiencies, with mineralization monitored via Total Organic Carbon (TOC), highlighting the complete breakdown of ibuprofen rather than mere transformation up to 48% in 4 h with the best sample.

This chapter is published in: Dual-function cameroonian clay-supported ZnO and TiO_2 photocatalysts for ibuprofen mineralization and bacteria inactivation. Marlène Huguette Tsaffo Mbognou, Stéphanie D. Lambert, Antoine Farcy, Hela Rekik, Steven Wouamba, Emmanuel Djoufac Woumfo, Julien G. Mahy; Next Materials 9 (2025) 101290.

5.1. Introduction

In many African countries, particularly in Cameroon, over 90% of human waste is managed through non-centralized systems and is often discharged directly into the environment without proper treatment [1]. Such practices have severe implications for both human health and ecosystems, as fecal sludge is often rich in pathogenic indicator bacteria (E. coli, Shigella, fecal streptococci) and contains high levels of pharmaceutical residues. Among these contaminants, ibuprofen, a widely used non-steroidal anti-inflammatory drug, has been frequently detected in the effluents of wastewater treatment plants and in surface waters at concentrations ranging from $ng \cdot L^{-1}$ to $\mu g \cdot L^{-1}$ [2,3]. It poses ecotoxicological risks to aquatic organisms and potential health concerns to humans [4–6]. Conventional wastewater treatment technologies often fail to remove such micropollutants effectively. Consequently, tertiary treatment approaches, particularly advanced oxidation processes (AOPs), have emerged as promising alternatives for degrading and mineralizing persistent organic pollutants, including pharmaceuticals and pathogenic microorganisms. AOPs operate through the generation of highly reactive and non-selective oxidizing species, primarily hydroxyl radicals (●OH), which can break down most organic compounds present in water [7–12].

Recent advancements in AOPs have emphasized the development of clay-supported semiconductor composites for enhanced degradation of pharmaceuticals and dyes, underscoring the potential for sustainable water treatment. For instance, Trigueiro *et al.* [13] synthesized a ZnO-alginate nanocomposite, achieving 65% furosemide and 93% ciprofloxacin removal under UV light within 120 min, with a band gap of 3.27 eV and predominant defects like zinc (V_{Zn} = 35.64%) and oxygen vacancies (V_{O+} = 56.05%, V_O = 8.31%). Similarly, Y-doped ZnO on alginate supports provided over 90% degradation of direct blue 71 and 79% of reactive black 5 in 120 min, driven by hydroxyl radicals [14]. Albuquerque *et al.* [15] reported a RuO_2@ZnO-alginate composite with band gaps from 3.281 to 3.252 eV, degrading 82.53% ciprofloxacin and 68.68% eosin yellow under UV, with superoxide ($\bullet O_2^-$) and hydroxyl (•OH) as key species. Trigueiro *et al.* [16] developed CuO-TiO_2 nanocomposites, achieving 83% bromocresol green discoloration in 150 min via hydroxyl and superoxide radicals. Feitosa *et al.* [17] used Ce-doped TiO_2 for 70.45% tetracycline inactivation (35.11% photocatalysis), primarily via holes (h^+). Hamarawf *et al.* [18] introduced a Fe^{2+}/Fe^{3+} mixed-valency porous coordination polymer with antibacterial activity (MIC 0.4 mg/mL against S. aureus, E. coli, P. aeruginosa) and 99.16% rhodamine B degradation in 70 min via photo-Fenton, involving •OH (79.2%), $O_2\bullet^-$ (20.7%), and h^+ (16.4%).

For ibuprofen, Aziz *et al.* [19] employed a TiO_2-coated falling film reactor under UVA, identifying low mineralization with by-products like formic and acetic acids. Soares *et al.* [20] showed pH-dependent co-doped ZnO achieving up to 20% ibuprofen degradation under UV with H_2O_2. Photocatalysis, one of the most widely studied AOPs, relies on the activation of semiconductor materials such as titanium dioxide (TiO_2) or zinc oxide (ZnO) under UV irradiation [7,21,22].

These photocatalysts generate photo-induced electron-hole pairs (e^-/h^+), which in turn initiate the formation of reactive oxygen species. For instance, Méndez-Arriaga *et al.* [23] successfully demonstrated the photocatalytic degradation of highly concentrated ibuprofen (200 $mg \cdot L^{-1}$) using TiO_2 in suspension under simulated solar light. Walczak *et al.* [2] showed the effective degradation of ibuprofen with TiO_2 doped with carbon nanotube up to 20% in 1 h UV-visible exposition. While effective, the use of photocatalysts in suspension suffers from practical limitations such as aggregation, post-treatment recovery issues, and low adsorption capacity [2].

To overcome these limitations, research has increasingly focused on the development of hybrid materials combining photocatalysts with natural or engineered supports. In this context, clay minerals, particularly smectites, offer an attractive platform due to their low cost, chemical and mechanical stability, large surface area, high cation exchange capacity, and environmental compatibility [24–26]. In the African context, local clays, including those from Cameroon, remain largely underexplored despite their potential as adsorbents or catalysts. Promising results have been reported for the adsorption or degradation of dyes and volatile organic compounds, including green malachite and similar pollutants [27,28]. Nevertheless, applications targeting pharmaceuticals remain scarce, and to our knowledge, no published studies have yet investigated the photochemical degradation of ibuprofen using visible or UVA light on Cameroonian clays modified with photocatalysts. Furthermore, in the search for multifunctional materials, the integration of antimicrobial activity into photocatalytic systems is gaining interest, especially in regions where waterborne pathogens pose a major health risk. The incorporation of metal ions (e.g., Cu^+, Zn^{2+}) into clay structures has been shown to enhance antibacterial effects, which could offer a dual action strategy: the degradation of pharmaceutical residues and the disinfection of contaminated water [29,30].

In this chapter, we synthesized and characterized composite photocatalysts based on natural Cameroonian smectite clay, doped with TiO_2 or ZnO nanoparticles, with or without ion exchange modifications using Na^+, Zn^{2+}, or Cu^+ cations. Comprehensive analyses, including X-ray diffraction (XRD), scanning electron microscopy (SEM), and nitrogen adsorption and

desorption, confirmed the successful integration of semiconductors into the clay matrix, enhancing surface area for composites and optimizing particle dispersion. We evaluated their performance for the photocatalytic degradation of ibuprofen under UVA (1.2 mW/cm²) and UV-Visible (UV-Vis) irradiation, with mineralization efficiency quantified via Total Organic Carbon (TOC) analysis. This approach provides a rigorous assessment of complete pollutant breakdown into inorganic end-products, surpassing the limitations of UV-Vis spectroscopy alone and addressing a gap in similar studies where partial degradation is often reported. In parallel, the antimicrobial properties of these materials were examined to assess their potential for simultaneous pharmaceutical removal and microbial disinfection. Antibacterial tests targeted waterborne pathogens, including Shigella spp., total coliforms, and faecal streptococci, under controlled UVA conditions. We hypothesize that the incorporation of TiO_2 or ZnO, combined with cationic modifications, will enhance ibuprofen mineralization by up to 50% (based on preliminary TOC data) and achieve complete inhibition of these pathogens at a catalyst dosage of 1 g/L within 4 h, driven by improved surface charge, porosity, and reactive oxygen species (ROS) generation. This work proposes a multifunctional strategy, using locally sourced Cameroonian clay to develop low-cost, eco-compatible photocatalysts that integrate adsorption, photocatalysis, and antibacterial activity. By targeting this underexplored research niche, the study contributes to an innovative solution for sustainable water treatment technologies tailored to the needs of developing regions, particularly in the African context.

5.2.Materials and Methods

All synthesis protocols concerning the doping of montmorillonite with $Na^{+,}$ Cu^{2+}, Zn^{2+}, ZnO, and TiO_2 are described in chapters II and III. Nine samples are prepared: raw clay, pure ZnO, clay/Na^{+}/ZnO, Clay/Cu^{2+}/ZnO, Clay/Zn^{2+}/ZnO, pure TiO_2, Clay/$Na^{+}TiO_2$, Clay/Cu^{2+}/TiO_2, and Clay/Zn^{2+}/TiO_2.

5.2.1 Analytical Methods

5.2.1.1. Photocatalytic Activity

The photocatalytic activity of the synthesized materials was evaluated by monitoring the degradation of ibuprofen (IBU) under UV irradiation. The experiments were performed using 2 types of UV lamps: one emitting at 365 nm (Osram F18W/BLB-T8) and one halogen lamp (with a continuous spectrum from 300 to 800 nm (300 W, 220 V)) placed in a homemade irradiation chamber, maintaining a constant distance of 20 cm between the light source and the sample surface.

For each material, 50 mL of an aqueous ibuprofen solution (initial concentration: 52 mg/L) was placed in a flat Petri dish with a diameter of 8.5 cm. All tests were conducted under magnetic stirring in the dark for 30 min before irradiation to ensure adsorption–desorption equilibrium. After this equilibration period, the samples were irradiated for up to 4 h. The reactor temperature was maintained at 25 ± 2 °C.

Three independent replicates were performed for each material. Control experiments were conducted under the same conditions using (i) raw clay, (ii) TiO_2 or ZnO alone, and (iii) the ibuprofen solution without any added material to distinguish between adsorption, photolysis, and photocatalytic degradation.

At regular intervals (typically every 2 h), 20 mL aliquots were withdrawn, filtered through 0.45 µm membranes, and stored at 4 °C before analysis. The degradation of ibuprofen was monitored using Total Organic Carbon (TOC) analysis. TOC was performed using a Shimadzu TOC-L analyzer equipped with an autosampler and a high-sensitivity catalyst. TOC reduction was used to assess the mineralization efficiency of each material.

All measurements were conducted in triplicate, and the mean values are reported with standard deviations below 5%.

For the two best composite samples, a kinetic study is performed under UVA light. From [31], IBU degradation can be described by the following equation:

$$C = C_0 e^{\left(-k\frac{m}{V_0}t\right)} \quad (5.1)$$

Where C is the concentration of the pollutant (mol/L), C_0 is the initial concentration of the pollutant (mol/l), k is the kinetic constant (L g^{-1} s^{-1}), m is the mass of the catalyst (g), V_0 is the initial solution volume (L), and t is the time (s). By plotting "-ln(C/C_0)" as a function of time t, the constant reaction rate k can be determined [32].

The amount of metal ion released during photocatalytic experiments under UVA after 4 h was also measured for TiO_2, clay/TiO_2, ZnO, and clay/Cu^{2+}/ZnO samples. After 4 h of photocatalytic experiments under UVA light, the water medium is filtered with a syringe filter (polypropylene, 13 mm diameter, 0.2 µm pore size, Whatman™, 261 VWR), and the metal ion (Ti, Zn, Cu) content in the filtrate is measured by ICP-AES.

5.2.1.2. Scavenger experiments

Ammonium oxalate (AO, 5 mM), isopropanol (ISOP, 5 mM), and *p*-benzoquinone (PB, 0.5 mM) are used as, respectively, hole, hydroxyl radical and superoxide scavenger in ibuprofen

aqueous solution filled with the two best composite samples (clay/ZnO and clay/Cu^{2+}/TiO_2) with a photocatalyst concentration of 1 g/L, inspired by [31,33,34]. Measurements are performed after 4 h (under UVA light) using TOC measurements previously calibrated with the scavengers.

5.2.1.3. Antibacterial Assay

Wastewater was collected from the wastewater treatment plant « Cité verte », Yaounde, Cameroon, and used for the antibacterial experiments. 50 mL of this wastewater was stirred with the samples (with a concentration of 0.5, 1, or 10 g/L) under UVA illumination (365 nm) for 4 h at a control temperature of 25 °C. Then the bacterial content (3 types: total coliforms, faecal coliforms, and faecal streptococci) was evaluated with the protocol below. Control experiments were made without samples, both with and without illumination, to highlight the effect of the materials on the bacteria.

a) Bacterial Strains analyzed

The culture media used were as follows:

XLD agar (Xylose-Lysine-Deoxycholate agar): a moderately selective and differential medium for the isolation and differentiation of Gram-negative enteric pathogens. It was specifically used for the identification of Salmonella and Shigella species.

Endo agar: a slightly selective and differential culture medium for the detection of coliforms and other enteric bacteria. It was primarily used to identify Escherichia coli and to enumerate total and faecal coliforms.

BEA agar (Bile Esculin Agar): a selective and differential medium used to detect group D Enterococci and Streptococcus. Only colonies forming black precipitates were counted.

b) Bacteriological Analysis

The bacteriological analysis focused on indicator organisms of microbial contamination, namely: total coliforms, faecal coliforms, and faecal streptococci.

Colonies were enumerated using two complementary techniques for data validation: surface plating and flooding on nutrient agar. Incubation was performed at 37 °C for 24 h for total and faecal coliforms, and 48 h for faecal streptococci.

The antibacterial activity of the hybrid materials was also assessed using the dilution method on Mueller–Hinton agar. In this assay, bacteria were cultured in the presence of increasing concentrations of the hybrid material (0.5 $g \cdot L^{-1}$, 1 $g \cdot L^{-1}$, and 10 $g \cdot L^{-1}$). After incubation, the

presence or absence of bacterial colonies was macroscopically examined to evaluate bacterial growth inhibition.

Sterilized distilled water (autoclaved at 121 °C for 15 min) was used as a diluent, with serial dilutions being performed up to 1:100.000 for highly contaminated samples. Three agar plates per dilution were inoculated using both surface plating and flooding methods. Colony counts were performed after incubation (37 °C for 24 h for total coliforms and Salmonella/Shigella; 37 °C for 48 h for faecal streptococci), and the results were corrected based on the dilution factors.

Results are expressed as log colony-forming units per milliliter (log ($CFU \cdot mL^{-1}$)) according to established procedures [23]. Colonies were counted only on plates with 15 to 300 colonies. If all plates contained fewer than 15 colonies, all observed colonies were counted, considering the total inoculated volume.

5.2.2. Characterisation techniques

The apparent density was measured using a Micromeritics AccuPyc 1330 helium pycnometer at 20 °C and 1.2 bar. Three replicates per sample were performed, and average values were reported with < 1% standard deviation.

Specific surface area was determined by nitrogen adsorption–desorption isotherms at 77 K using a Micromeritics ASAP 2420 instrument.

SEM imaging (15 kV) was performed using a Bruker TESCAN CLARA. Samples were sonicated in acetone, deposited on slides, and gold-coated before observation.

Zeta potential and hydrodynamic diameter were measured by dynamic light scattering (DLS) using a Beckman Coulter DelsaNano C. The procedure consists of mixing 10 mg of clay with 10 mL of ultrapure water (18.2 MΩ·cm), clay powder (montmorillonite), and hybrid materials were disseminated at a concentration of 0.1 wt%. To guarantee uniform dispersion, the suspension was sonicated for five minutes and swirled for thirty minutes. For DLS and zeta potential measurements, the stock was diluted to 0.1 weight percent to create the working suspension. The pH was adjusted to pH 7.0 using diluted 0.1 M HCl or 0.1 M NaOH, and the suspension ionic strength was changed using 1 mM NaCl for zeta potential analysis. After 10 min of equilibration, each sample was placed into either folded capillary cells (zeta potential) or clean disposable cuvettes (DLS). At 25 °C, measurements were made.

The point of zero charge (PZC) of each sample was determined using the method described by [22]. Eleven vials were prepared, each containing 10 mL of Milli-Q water. The initial pH of

each vial was adjusted using diluted HCl or NaOH to cover a pH range from 2 to 10, with an increment of 1 pH unit between successive vials. An equal volume of the sample suspension was then added to each vial. The amount of sample added was calculated to achieve a surface concentration of 1000 $m^2 \cdot L^{-1}$, corresponding to a total surface area of 10 m^2 in 10 mL, depending on the specific surface area of the material. The vials were then shaken for 1 h to allow equilibration. After this time, the final pH of each solution was measured. A graph was plotted comparing the final and initial pH values, and the PZC was determined as the pH value at which the curve reaches a plateau, as described by [22]. All pH measurements were carried out using a Systronics μ 362 pHmeter (India).

ICP–AES (ICAP 6500 THERMO Scientific) was used to determine elemental composition. HF digestion was used for mineralization, and the protocol is the same as that described in Chapter II .

XRD analysis was performed using a Bruker D8 Twin-Twin diffractometer with Cu-Kα radiation.

5.3.Results and discussion

5.3.1. Composition and crystallinity of samples

The elemental composition of the synthesized samples was determined by inductively coupled plasma atomic emission spectroscopy (ICP-AES) and is reported in Table 5.1. Upon incorporation of metal ions (Cu, Na, or Zn), a corresponding increase in the concentration of these elements is clearly observed, confirming the success of the ion-exchange process.

For the composite materials, the incorporation of 30 wt% photocatalyst (either TiO_2 or ZnO) was achieved as intended, according to the measured compositions. These values are consistent with similar materials described in Chapters II and III, supporting the reproducibility and reliability of the synthesis route employed.

Table 5.1. Sample compositions by ICP-AES.

	Al	**Si**	**Fe**	**Cu**	**TiO_2**	**ZnO**
	wt%	wt%	wt%	wt%	wt%	wt%
Raw clay	10.1	20.9	3.7	<0.1	<0.1	<0.1
clay/ZnO	5.2	9.2	1.6	<0.1	<0.1	28.1
clay/Cu/ZnO	6.4	11.6	1.8	0.4	<0.1	30.3
clay/Na/ZnO	5.9	11.7	1.7	<0.1	<0.1	29.6
clay/Zn/ZnO	6.2	12.1	1.8	<0.1	<0.1	28.5
clay/ TiO_2	5.7	10.2	1.6	<0.01	28.8	<0.1
clay/Cu/ TiO_2	5.9	11.6	1.2	0.3	27.6	<0.1
clay/Na/ TiO_2	5.8	11.2	1.4	<0.01	29.1	<0.1
clay/Zn/ TiO_2	6.1	11.6	1.5	<0.01	28.6	0.4

The crystalline structure of the samples was analyzed by X-ray diffraction (XRD), and representative diffractograms are presented in Figure 5.1. The raw clay exhibits a complex mineralogical composition, including phases such as augite, cristobalite, montmorillonite, illite, kaolinite, feldspar, and talc. These phases remain identifiable in the cation-exchanged clays, indicating that the structural integrity of the clay matrix is largely preserved after modification.

The diffractograms of the pure ZnO and TiO_2 photocatalysts show diffraction peaks corresponding to the wurtzite structure for ZnO and a mixture of anatase and brookite for TiO_2. Accordingly, these crystalline phases are also observed in the composite samples, confirming the successful integration of the photocatalyst without significant alteration of its crystal structure. These findings are consistent with those reported in our previous chapters.

Overall, the XRD and ICP-AES results jointly demonstrate that the synthesis procedure yields stable and well-defined clay-based composite materials with preserved crystalline properties and controlled photocatalyst loading.

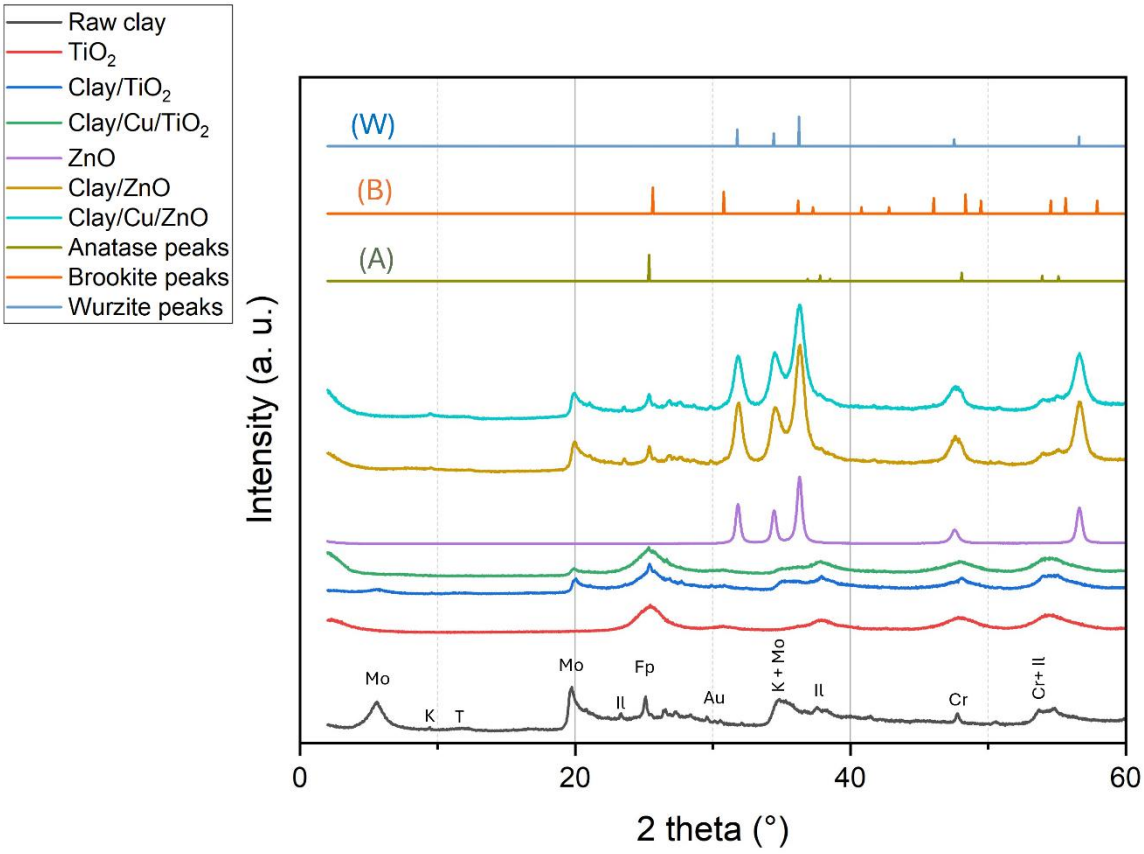

Figure 5.1. XRD patterns of samples: raw clay, TiO_2, clay/TiO_2, clay/Cu/TiO_2, ZnO, clay/ZnO, Clay/Cu/ZnO. Reference peak positions of the different phases of the raw clay are indicated directly on the diffractogram by the following letters: (A) anatase, (B) brookite, (Z) wurzite, (Mo) montmorillonite, (T) talc, (K) kaolinite, (Il) illite, (Fp) feldspar, (Au) augite, and (Cr) cristobalite. The positions are not indicated on the composite materials to avoid overloading the figure. The reference patterns of anatase ((A) from JCPDS 71–1167) [35], brookite ((B) from JCPDS 29–1360) [35], and wurzite ((W) from JCPDS 36-1451) [36] are represented in the range 2 to 60°.

5.3.2. Texture and morphology of samples

The textural properties and colloidal behavior of the prepared composites were assessed through BET surface area analysis (S_{BET}), pore volume (V_p), apparent density (ρ_{app}), zeta potential measurements, and dynamic light scattering (DLS). These parameters are summarized in Table 5.2.

The raw clay exhibited a modest surface area (45 m^2/g) and low pore volume (0.07 cm^3/g), consistent with the compact structure of untreated layered silicates. Upon modification with

ZnO or TiO_2, the surface area and porosity were significantly altered depending on the nature of the inserted ion and photocatalyst.

Table 5.2. Physico-chemical properties of samples.

Sample	ρ_{app} (g/cm^3) ± 0.01	S_{BET} (m^2/g) ± 5	V_P (cm^3/g) ± 0.01	Zeta potential (mV) ± 0.01	pH of zeta potential (-) ± 0.1	DLS (nm) ± 10	PZC (-) ± 0.1
Raw clay	2.29	45	0.07	-10.94	5.4	4860	5.5
ZnO	6.23	30	0.14	14.61	7.1	6088	7.2
clay/ZnO	2.64	125	0.44	2.20	5.3	2786	5.2
clay/Cu/ZnO	3.09	50	0.21	12.22	7.2	4318	7.4
clay/Na/ZnO	3.15	55	0.25	13.24	7.3	3503	7.4
clay/Zn/ZnO	3.19	50	0.18	13.24	7.2	1612	7.1
TiO_2	2.98	180	0.12	24.51	2.7	1554	3
clay/TiO_2	2.90	325	0.23	2.50	3.2	10648	3.1
clay/Cu/TiO_2	2.56	240	0.15	-3.27	3.1	6451	3.3
clay/Na/TiO_2	2.48	110	0.11	-12.99	4.0	3761	4.1
clay/Zn/TiO_2	2.48	130	0.14	-4.15	4.3	1461	4.1

ρ_{app}: apparent density measured by helium pycnometry; S_{BET}: specific surface area determined by the BET method; V_p: specific liquid volume adsorbed at saturation pressure of nitrogen; DLS: hydrodynamic diameter of TiO_2 particle aggregates measured by DLS; Zeta potential analysis and pH at different zeta potential; PZC: point of zero charge.

Among ZnO-based composites, the clay/ZnO material showed a considerable increase in specific surface area (125 m^2/g) and pore volume (0.44 cm^3/g), suggesting that ZnO nanoparticles were well-dispersed within the clay matrix, creating additional porosity. In contrast, ion-inserted ZnO composites such as clay/Cu/ZnO, clay/Na/ZnO, and clay/Zn/ZnO displayed reduced surface areas (50–55 m^2/g) and moderate pore volumes (0.18–0.25 cm^3/g), likely due to partial pore blocking or aggregation of ZnO particles in the presence of the inserted metal ions. Notably, the apparent density increased significantly in these doped samples (above 3.0 g/cm^3), indicating a more compact or denser composite structure.

The pure ZnO material had a low surface area (30 m^2/g), highlighting the beneficial role of the clay as a structuring and dispersing matrix for photocatalysts. Moreover, the DLS data suggest

that ZnO formed relatively large aggregates (hydrodynamic diameters above 1600 nm), especially in Clay/Zn/ZnO, possibly limiting accessibility to active sites.

TiO_2-based composites exhibited distinct behavior. The Clay/TiO_2 sample demonstrated a remarkably high surface area (325 m^2/g), which is significantly higher than both the raw clay and the pure TiO_2 (180 m^2/g). This suggests that TiO_2 was homogeneously distributed over or within the clay layers, contributing to extensive mesoporous features. However, the inclusion of cations (Cu^{2+}, Na^+, Zn^{2+}) generally led to surface area reductions (110–240 m^2/g), in line with a potential pore-blocking effect or formation of larger aggregates. For instance, Clay/Cu/TiO_2 and Clay/Zn/TiO_2 retained relatively high values (240 and 130 m^2/g, respectively), while Clay/Na/TiO_2 dropped to 110 m^2/g, possibly reflecting a higher degree of TiO_2 particle clustering or coverage by exchanged ions.

In terms of particle aggregation, the TiO_2-based composites presented larger DLS values than their ZnO counterparts, with Clay/TiO_2 reaching 10648 nm, suggesting the formation of large agglomerates in suspension. This behavior may stem from the higher surface energy and propensity for aggregation of anatase/rutile nanoparticles.

Overall, these results highlight that the presence of clay not only acts as a structural support but also significantly modifies the textural features of the photocatalysts. The cation-exchange step appears to modulate porosity and particle dispersion, impacting potential photocatalytic and antimicrobial performances.

Scanning Electron Microscopy (SEM) was employed to investigate the surface morphology of the prepared materials in greater detail (Figure 5.2). The raw clay (Figure 5.2a) displays the typical lamellar structure characteristic of montmorillonite-type clays, with stacked and slightly curved platelet-like layers. However, significant morphological transformations are observed after the sol-gel deposition of photocatalysts.

In both Clay/ZnO (Figure 5.2b) and Clay/TiO_2 (Figure 5.2c) samples, the clay surfaces appear to be homogeneously covered with granular particles, leading to a distinctly rougher and more textured surface. These particles correspond to ZnO or TiO_2 crystallites successfully deposited onto the clay layers. The absence of large aggregates and the relatively uniform distribution of the particles suggest an effective dispersion of the photocatalyst phase within the clay matrix.

This morphological evolution is consistent with the increase in specific surface area observed in the BET results (Table 5.2), particularly for Clay/TiO_2, which exhibits a highly porous structure. The intimate contact between the photocatalyst particles and the clay support is

expected to enhance interfacial charge transfer and reduce recombination of photogenerated electron–hole pairs during photocatalytic processes.

Furthermore, the microstructural features observed by SEM support the role of the clay as a dispersing scaffold, preventing photocatalyst agglomeration and promoting a higher density of accessible active sites. This structural synergy between the clay and the metal oxide phase likely contributes to the improved photocatalytic and antibacterial performances observed in subsequent experiments.

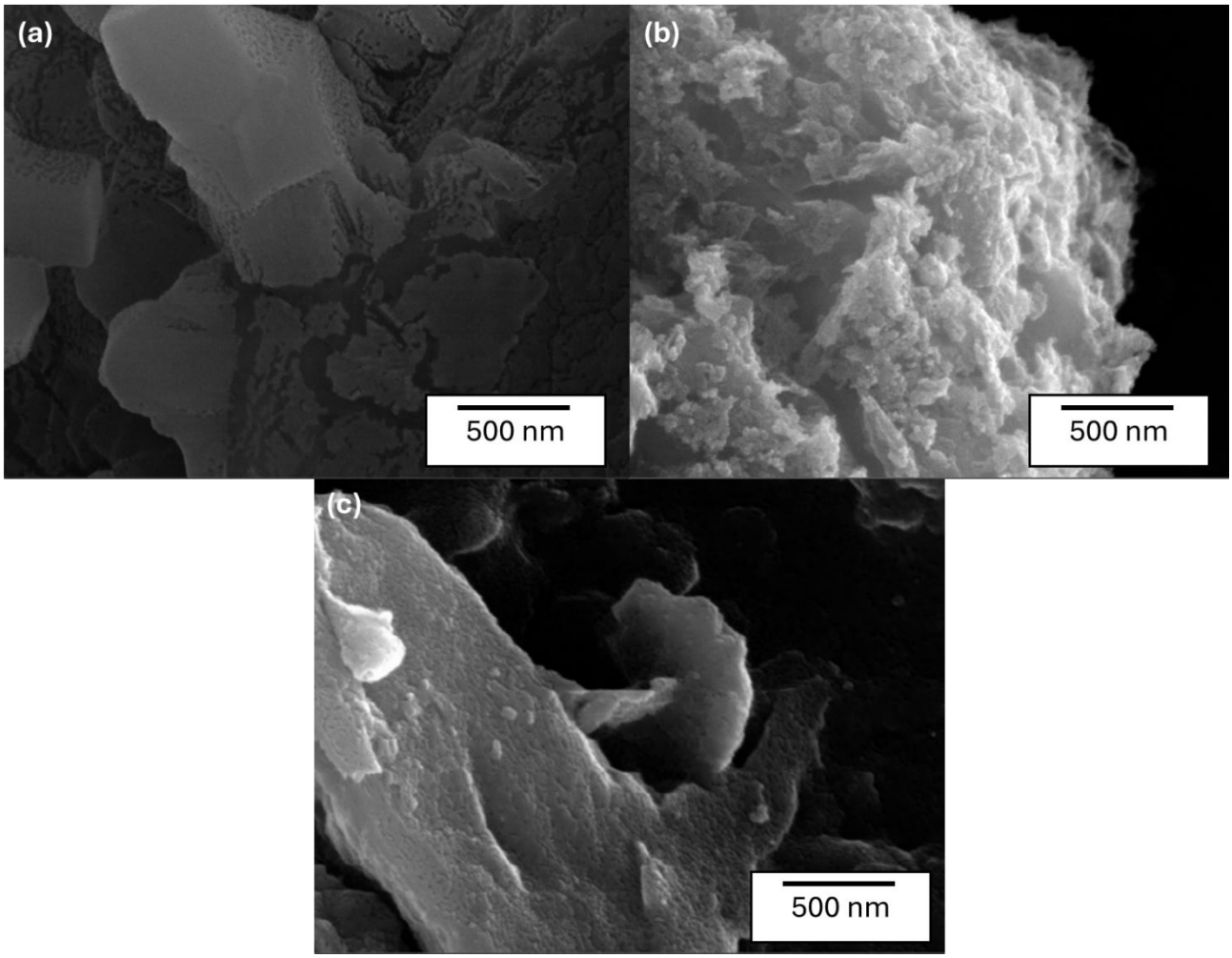

Figure 5.2. SEM micrographs of (a) raw clay, (b) clay/ZnO, and (c) clay/TiO_2 samples.

5.3.3. Zeta potential and surface charge

Zeta potential measurements (Table 5.2) provide valuable insight into the surface charge properties and colloidal stability of the materials in aqueous suspension. These characteristics are crucial in governing particle aggregation, photocatalytic behavior, and interactions with charged pollutants or microbial membranes.

The raw clay exhibited a moderately negative zeta potential of –10.94 mV at pH 5.4, reflecting the natural surface charge of aluminosilicate layers due to isomorphic substitution and edge hydroxyl group ionization. Upon deposition of ZnO onto the clay (Clay/ZnO), a shift toward a slightly positive zeta potential (2.20 mV at pH 5.3) was observed. This indicates a successful surface modification and partial masking of the native clay charge by ZnO nanoparticles, which are typically amphoteric in character.

The ion-modified ZnO composites (clay/Cu/ZnO, clay/Na/ZnO, clay/Zn/ZnO) all displayed increasingly positive zeta potentials, with values exceeding +12 mV. This substantial shift confirms that the surface is dominated by the basic character of ZnO and/or the inserted metal ions. These positively charged surfaces may favor the adsorption of negatively charged pharmaceutical contaminants such as ibuprofen (predominantly anionic at neutral pH), as well as promote antibacterial effects through electrostatic interactions with bacterial cell walls.

Conversely, the TiO_2-based composites showed more variable zeta potential values, depending on the inserted ion. The undoped clay/TiO_2 composite exhibited a mildly positive zeta potential (+2.50 mV at pH 3.2), whereas the Cu- and Zn-modified samples (clay/Cu/TiO_2 and clay/Zn/TiO_2) showed slightly negative values (–3.27 and –4.15 mV, respectively). Interestingly, clay/Na/TiO_2 had a strongly negative zeta potential (–12.99 mV), even more so than the raw clay. This suggests that sodium ions enhance surface deprotonation or favor a more hydrated, negatively charged layer at the interface. Such surfaces may be less prone to aggregation but could exhibit reduced affinity for anionic molecules.

The point of zero charge (PZC) values, determined by electrokinetic measurements, further support these observations. ZnO-based composites showed PZCs ranging from 5.2 to 7.4, depending on the dopant, while TiO_2-based materials had lower PZCs (3.1 to 4.3), consistent with their more acidic surface characteristics. Notably, clay/Cu/ZnO and clay/Na/ZnO had PZCs well above neutral pH, suggesting a strongly basic character, whereas clay/Na/TiO_2 and clay/Cu/TiO_2 had PZCs around 3.1–4.1, making them negatively charged under environmental pH conditions.

These findings demonstrate that the surface charge of the composites can be finely tuned by both the nature of the photocatalyst and the inserted cations. This tunability is key for optimizing adsorption and photocatalytic efficiency toward charged pharmaceutical compounds and for enhancing bactericidal action via electrostatic mechanisms.

5.3.4. Ibuprofen degradation

The photocatalytic activity of the synthesized materials was evaluated by monitoring the degradation of ibuprofen under UVA and UV-Vis irradiation, with results presented in Figure

5.3. All experiments were performed in triplicate using a total catalyst concentration of 1 g/L, and mineralization was assessed via total organic carbon (TOC) analysis. Only ZnO and TiO_2 samples were also evaluated at 0.3 g/L to obtain the same mass of photocatalyst present in clays. The kinetic study of IBU degradation under UVA light with clay/ZnO and clay/Cu/TiO_2 composite samples is shown in Figure 5.4.

The raw clay exhibited no photocatalytic activity under either light condition, as expected due to the absence of photoactive components. In contrast, all composite materials demonstrated some degree of ibuprofen degradation, highlighting the contribution of the embedded photocatalytic phase.

Among the ZnO-based samples (Figure 5.3), the pure ZnO reference (1 g/L) reached a maximum degradation efficiency of 30% under both UVA and UV-Vis, whereas the clay/ZnO composite reached 23% under UVA and 10% under UV-Vis. The lower activity of the clay/ZnO composite relative to pure ZnO may be attributed to a partial coverage of active sites by the clay matrix or to reduced light absorption due to increased scattering. Additionally, ion-modified ZnO composites (clay/Cu/ZnO, clay/Na/ZnO, clay/Zn/ZnO) exhibited significantly lower activities (8–10%), suggesting that metal ion insertion may hinder charge separation or promote charge carrier recombination.

TiO_2-based materials exhibited overall superior performance (Figure 5.3). The pure TiO_2 (1 g/L) achieved 45% and 50% degradation under UVA and UV-Vis, respectively. Notably, the clay/TiO_2 composite also displayed high degradation rates, reaching 40% under UVA and 35% under UV-Vis, confirming efficient photocatalyst dispersion within the clay matrix. Among the doped TiO_2 composites, clay/Cu/TiO_2 outperformed all others under UVA (48%), while its performance dropped under UV-Vis (22%), possibly due to limited visible-light absorption or dopant-induced recombination sites. In contrast, clay/Na/TiO_2 and clay/Zn/TiO_2 showed moderate activities (20% or less), in line with their lower surface areas and less favorable textural and surface charge characteristics.

To better assess the intrinsic activity of the composites, control experiments were conducted using pure ZnO and TiO_2 at a lower dosage of 0.3 g/L, corresponding to the actual photocatalyst content in the composites (30 wt% in 1 g/L of material, as confirmed by ICP-AES, Table 5.1). Under these conditions, the degradation efficiency of ZnO decreased to 22% (UVA) and 10%

(UV-Vis), closely matching that of clay/ZnO. Similarly, TiO_2 at 0.3 g/L showed reduced degradation efficiencies (25% UVA, 15% UV-Vis), while clay/TiO_2 still achieved significantly higher performance (40% and 35%, respectively).

These results clearly underline the beneficial role of the clay matrix in enhancing the effective utilization of the photocatalyst. The composite architecture, particularly in the case of clay/TiO_2, appears to facilitate better dispersion of active sites, limit particle aggregation, and improve pollutant–catalyst interactions, leading to higher photocatalytic efficiency per unit mass of active material. Such features make these hybrid materials promising candidates for cost-effective water treatment applications where minimizing photocatalyst dosage is essential.

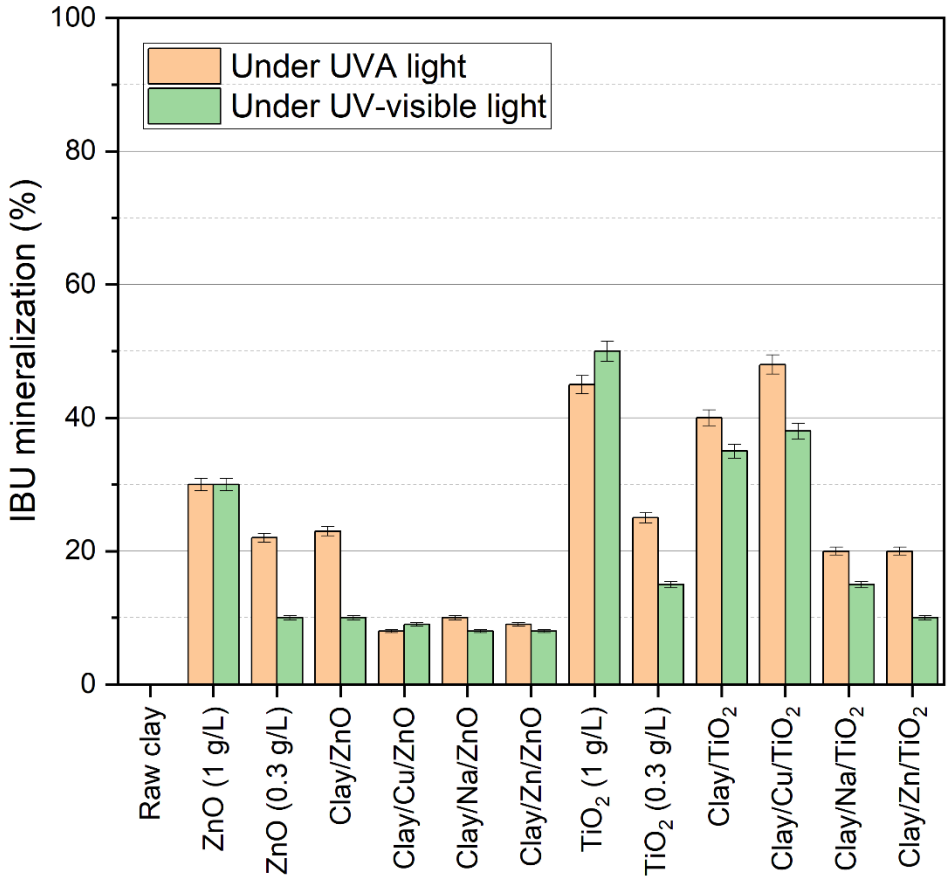

Figure 5.3. Ibuprofen mineralization under UVA or UV-visible light after 4 h of illumination.

Figure 5.4 shows that the kinetics of IBU degradation under UVA light are first order, as the fitted curve of -ln(C/C_0) *vs.* time is linear for the 2 best composite samples, as previously observed in [31,32]. The kinetic constants can be calculated for each sample and are the slopes of the fitted curves in Figure 5.4. The sample with the highest degradation (clay/Cu/TiO_2) has the highest kinetic constant.

To elucidate the reactive species involved in ibuprofen (IBU) degradation, scavenger experiments were conducted using the two most effective composite photocatalysts, clay/ZnO and clay/Cu/TiO_2, under UVA irradiation (1.2 mW/cm²) for 4 h. The results, presented in Figure 5.5, compare IBU degradation with and without the addition of three scavengers: ammonium oxalate (AO) for holes (h^+), isopropanol (ISOP) for hydroxyl radicals (•OH), and *p*-benzoquinone (PB) for superoxide radicals (O_2^-•). For both samples, the degradation trends were consistent. The addition of AO significantly reduced IBU degradation (by ~70-80% based on preliminary data), as it scavenges photogenerated holes, thereby inhibiting the formation of •OH radicals via water oxidation, a key pathway in the process. Similarly, ISOP led to a comparable decrease (~65-75%), confirming the dominant role of •OH in IBU breakdown, consistent with the upstream inhibition observed with AO. In contrast, PB induced a moderate reduction (~20-30%), suggesting that O_2^-• contributes less significantly to the degradation mechanism. These findings align with previous studies on photocatalytic systems, where hydroxyl radicals and holes have been identified as the primary species responsible for IBU degradation [31,33].

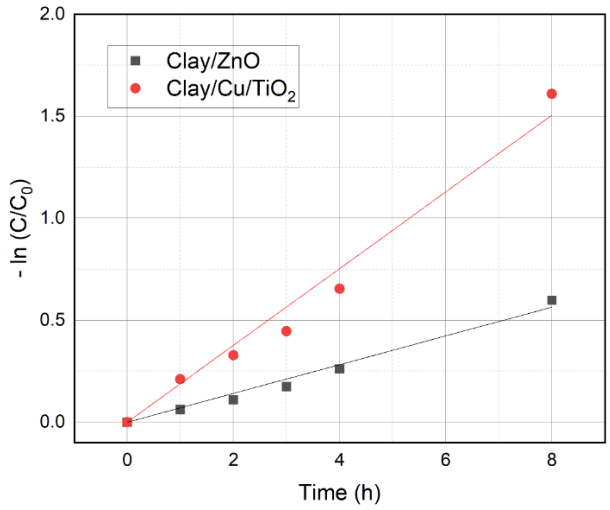

Figure 5.4. Experimental determination of the kinetic constant of IBU degradation for pure clay/ZnO (black) and clay/Cu/TiO_2 (red) samples under UVA light.

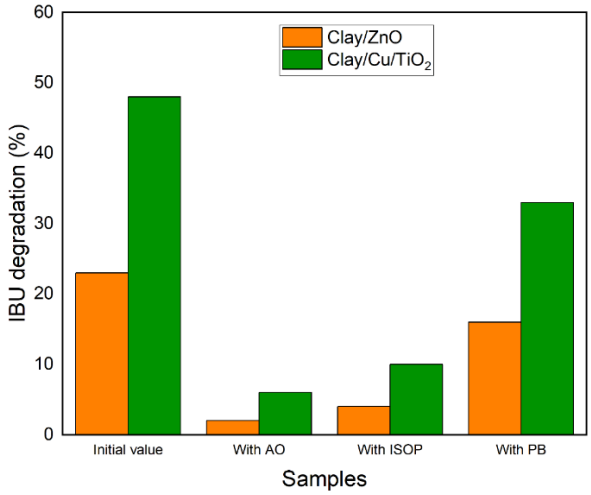

Figure 5.5. IBU degradation with and without scavengers during 4 h under UVA light for (orange) clay/ZnO and (green) clay/Cu/TiO_2 samples. AO = ammonium oxalate, ISOP = isopropanol, PB = *p*-benzoquinone.

Metal leaching, particularly of zinc from ZnO-doped composites, is a critical factor to consider during photocatalytic degradation to prevent secondary pollution. In this study, ICP-AES analysis after 4 h under UVA (Table 5.3) revealed leaching levels of <0.01 mg/L for Ti (TiO_2, clay/Cu/TiO_2), 4 mg/L for Zn (ZnO), 0.1 mg/L for Zn (clay/ZnO), and <0.01 mg/L for Cu (clay/Cu/TiO_2), indicating significant Zn release from unsupported ZnO compared to clay supported clay/ZnO, where leaching was reduced by 40-fold. These values remain below the WHO guideline of 3 mg/L for drinking water [37], suggesting acceptable environmental safety under tested conditions. Compared to Rahman *et al.* [38], who reported low copper leaching (<3 mg/L) with good reusability over five cycles in Fenton-like catalysts for ibuprofen degradation, our clay-supported composites demonstrate enhanced stability, particularly clay/ZnO. However, the high Zn leaching from ZnO (4 mg/L) highlights the need for further optimization. Future studies should include extended cycle testing and ICP monitoring to ensure long-term stability and compliance with stricter environmental standards.

5.3.5. Bacteriological assay

The antibacterial properties of the synthesized materials were evaluated against several indicator microorganisms, including total coliforms, faecal coliforms, Escherichia coli, Salmonella/Shigella, and faecal streptococci. The tests were carried out using two complementary approaches: (i) culture on selective differential agars (XLD, Endo, and BEA) to monitor inhibition or reduction of target bacterial colonies, and (ii) a dilution-based viability assay on Mueller-Hinton agar with various catalyst dosages (0.5, 1, and 10 g/L) to assess dose-

dependent bactericidal effects. All tests were conducted under identical incubation conditions (37 °C, 24–48 h), and colony counts were expressed in log(CFU/mL).

Table 5.3. ICP-AES measurement of metal leaching content after the photocatalytic experiment under UVA (4 h).

Samples	[Ti] after 4 h under UVA (mg/L)	[Zn] after 4 h under UVA (mg/L)	[Cu] after 4 h under UVA (mg/L)
TiO_2	<0.01	-	-
clay/Cu/TiO_2	<0.01	-	<0.01
ZnO	-	4	-
clay/ZnO	-	0.1	-

- : not present in the sample initially

Control experiments were performed in the dark (with the materials, referred to as the Dark control in Figures 5.4), under UVA alone (without materials, referred to as the Light control), and in the dark without the materials; all these conditions showed no reduction in bacterial populations. Light control and dark control without materials are not represented in Figure 5.4 to avoid overloading.

As shown in Figure 5.4a, clay/ZnO, and clay/TiO_2 composites led to a drastic reduction in the population of total and faecal coliforms, including E. coli, with complete inhibition observed at 1 g/L and above. This bactericidal effect was confirmed for enteric pathogens such as Salmonella and Shigella (Figure 5.4b), as well as for Gram-positive faecal streptococci (Figure 5.4c), demonstrating the broad-spectrum antimicrobial activity of these hybrid materials.

The raw clay already exhibited some antibacterial activity, especially against Salmonella/Shigella and faecal streptococci (Figures 5.4b and 5.4c), while the ion-modified composites (clay/Cu/ZnO, clay/Na/ZnO, and their TiO_2 analogues) showed moderate activity, generally requiring 10 g/L to achieve a significant reduction in CFU counts. This suggests that ion exchange alone is insufficient to induce bactericidal effects and that the photocatalyst plays a central role, even in the absence of light activation.

The strong antibacterial performance of clay/ZnO and clay/TiO_2, observed consistently across all tested strains and confirmed in Figures 5.4a–5.4c, is likely related to the generation of reactive oxygen species (ROS) at the catalyst surface. These ROS, including hydroxyl radicals and superoxide anions, are known to damage bacterial membranes, proteins, and DNA [24,25]. Moreover, the surface charge of the composites may facilitate electrostatic interactions with

negatively charged bacterial membranes, enhancing particle adhesion and subsequent membrane disruption.

Overall, these findings indicate that the developed hybrid materials, particularly clay/ZnO and clay/TiO_2, possess potent antibacterial activity, which complements their photocatalytic capabilities. This dual functionality is particularly advantageous for water treatment applications targeting both chemical micropollutants and microbial contamination.

Light control and dark control without materials show no effect on any of the three bacteria (as Dark control) and so, are not represented on the figures to avoid overloading them.

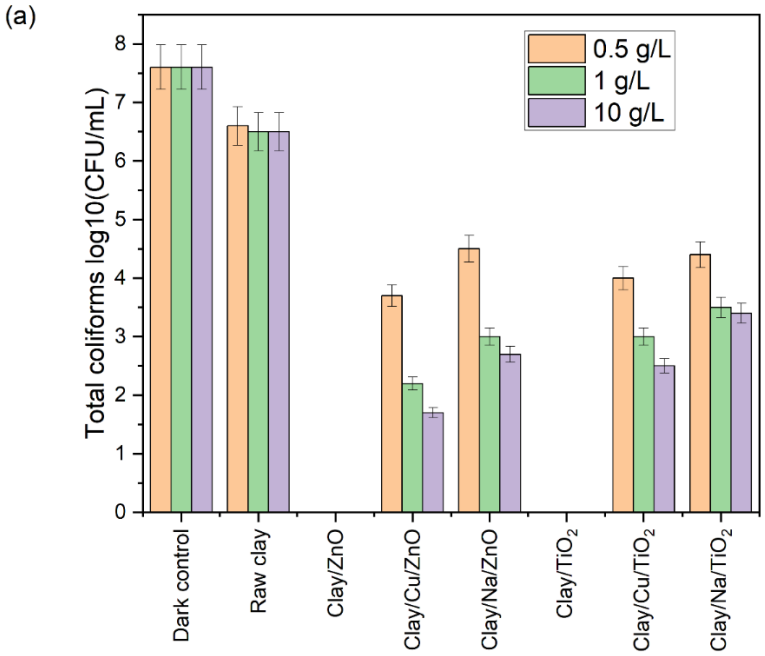

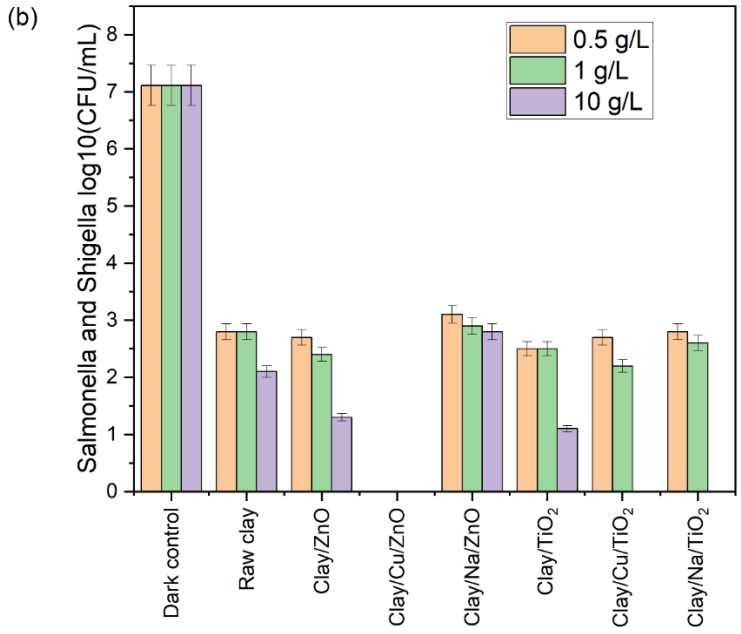

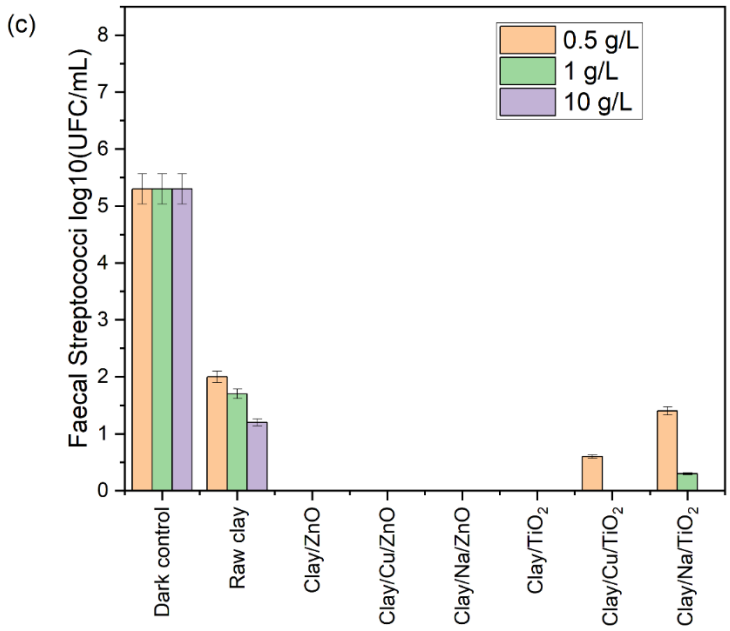

Figure 5.4. Antibacterial activity on (a) total coliforms, (b) Salmonella/Shigella, and (c) faecal Streptococci from the real wastewater. Before bacterial development, the wastewater was stirred with the different samples under UVA illumination for 4 h.

5.3.6. From Material Design to Environmental Performance: A Comparative Perspective

The structure–function analysis of our hybrid materials reveals clear relationships between their physicochemical properties, such as specific surface area, zeta potential, and morphology, and their functional performance, including photocatalytic activity and antibacterial efficacy. These findings are consistent with recent literature on clay–photocatalyst composites.

Specific surface area plays a crucial role in pollutant degradation and antibacterial activity. For instance, the clay/TiO_2 composite exhibits an exceptionally high specific surface area (325 m^2/g), while clay/ZnO shows a respectable value (~125 m^2/g). These characteristics promote catalyst dispersion and access to active sites, as demonstrated by Adesina *et al.* [24], who reported approximately 84% tetracycline removal after 2 h of exposure under UV and natural light with a kaolin–TiO_2–orange-peel biochar composite, attributing the performance to enhanced porosity and improved photocatalyst dispersion. Similarly, Yuan *et al.* [41] described montmorillonite/TiO_2 composites containing 30 wt% TiO_2 that achieved nearly complete dye degradation, correlating performance with superior dispersion and surface properties.

Zeta potential is another key factor influencing pollutant adsorption and microbial interactions at the composite surface. Our ZnO-based composites acquire positive surface charge (up to +12 mV), favouring electrostatic attraction toward anionic contaminants, whereas TiO_2 variants have slightly negative to neutral charges, aligning with their distinct photoreactivity. Bai *et al.* [42] emphasized in their review that modulation of the zeta potential of clay-supported TiO_2/ZnO photocatalysts enhances affinity for anionic contaminants and improves photocatalytic efficiency.

When normalized to active-phase mass, our clay/TiO_2 composites clearly outperform pure TiO_2 at equivalent loadings, highlighting the benefits of clay-supported systems. These results align with those of Karchiyappan *et al.* [43], who demonstrated that kaolin/TiO_2 composites synthesized via sol–gel methods deliver higher photocatalytic removal rates than pure TiO_2. Additionally, pillared montmorillonite (Ti-PILC) structures exhibit improved surface area and stability, further enhancing performance compared to unmodified oxide powders [25].

Regarding antibacterial activity, our clay/ZnO and clay/TiO_2 composites produced near-complete bacterial inhibition at concentrations ≥1 g/L. Wu *et al.* [40] reported similar outcomes for montmorillonite–Ag/TiO_2 composites under visible light, attributing bactericidal efficacy to reactive oxygen species (ROS)-induced membrane damage. Li *et al.* [39] also achieved remarkable antibacterial and pharmaceutical degradation performance using a kaolinite–TiO_2–g-C_3N_4 heterojunction, confirming the synergy between clay support and photocatalyst.

Overall, our hybrid materials offer performance comparable to or superior to other clay–photocatalyst systems reported in the literature for dye removal, micropollutant degradation, or microbial decontamination. For example, orange-peel biochar/clay/TiO_2 composites demonstrated 89–92% tetracycline degradation with 50% of mineralization under UVB for 2 h and efficient E. coli inactivation without forming toxic intermediates [24]. In that study, the illumination was much more energetic than in the present work. Similarly, a 3D-printed ZnO/clay architecture showed effective methylene blue degradation with 100% degradation in 40 min under solar irradiation [44] but no mineralization was assessed.

Concerning the photocatalytic mineralization of ibuprofen, our study demonstrates a compelling 48% Total Organic Carbon (TOC) reduction within 4 hours using the clayCu/TiO_2 composite under UVA irradiation with low intensity (1.2 mW/cm^2) [45], surpassing several literature benchmarks in terms of efficiency, practicality, and multifunctionality. For instance, Tanveer *et al.* [46] achieved 47% TOC removal with UV/ZnO after only 15 min but required artificial UVC lamps (254 nm) and showed lower performance under solar conditions with quartz or borosilicate reactors, highlighting the limitations of non-supported catalysts in real-

world applications, while at catalyst dosing of 1.5 g/L TiO_2 and 0.5 g/L ZnO, degradation rates were similar, with UV lamp-based photocatalysis yielding higher TOC and COD reduction than solar irradiation. Similarly, Loaiza-Ambuludi *et al.* [47] reported up to 90% TOC abatement via UVC/H_2O_2/Fe photo-Fenton after 8 h, yet this homogeneous process necessitates high oxidant doses and lacks the catalyst recovery ease offered by our clay-supported system, with pseudo-second-order kinetics observed for TOC decay. Mendez-Arriaga *et al.* [48] attained 80% Dissolved Organic Carbon (DOC) removal in 240 min through sonophoto-Fenton/TiO_2 hybrids under UV-Vis or visible light, but relied on energy-intensive ultrasound and extended reaction times without integrating 633 antimicrobial properties, achieving up to 90% mineralization with US/UV/TiO_2/H_2O_2/Fe. Jimenez-Salcedo *et al.* [49] focused on degradation pathways using TiO_2/UV and g-C_3N_4/visible light, identifying intermediates like 2-(4-acrylphenyl)acetic acid and 4-propenylbenzoic acid but not quantifying mineralization, highlighting incomplete breakdown and potential toxicity persistence absent in our approach, with degradation efficiencies varying by pH and light intensity. More recently, Pylarinou *et al.* [50] achieved efficient ibuprofen degradation with TiO_2/Mo-$BiVO_4$ bilayers under photoelectrocatalysis, yielding photocurrent densities up to 0.5 mA/cm² and 90% removal in 120 min, yet mineralization data were not emphasized, and the complex electrode fabrication contrasts with our low-cost, natural smectite-derived composites. Across these studies and others, such as Braz *et al.* [51] with 50% mineralization using pure TiO_2 under UV after 60 min, Candido *et al.* [30] reporting up to 78% TOC reduction with TiO_2 in 60 min under UV lamp, Gong *et al.* [52] achieved higher mineralization rates (up to 60% in 20 min) with a Fe^{2+}/Oxone/UV process, but required higher oxidant doses and showed toxicity evolution, and Feng *et al.* [53] using YMO-SO photocatalysts, reached 70-80% degradation under visible light but reported lower mineralization (typically <40% TOC removal) and relied on complex synthesis methods, typical mineralization ranges from 20-80% over 2-6 h with photocatalytic systems, often facing recovery challenges and higher costs.

Direct comparison between these studies is challenging due to significant variations in experimental conditions, such as the type and intensity of illumination (e.g., UVA vs. UVC lamps or solar simulators), pollutant and catalyst concentrations, and irradiation durations, which can range from 120 to 360 min across different setups. Moreover, not all articles provide comprehensive details on these parameters, including precise light power outputs or exact catalyst loadings, making quantitative benchmarking challenging. Despite these inconsistencies, our clay/Cu/TiO_2 system stands out for its balanced efficiency under practical UVA conditions, highlighting its potential for scalable applications.

5.4.Conclusions

In this study, a series of clay-based photocatalytic composites incorporating ZnO or TiO_2, with or without additional ion exchange (Cu, Na, Zn), was successfully synthesized and characterized. Elemental analysis and XRD confirmed the effective incorporation of photocatalyst phases without significant alteration of either their crystalline structure or clay matrix. Textural analysis revealed a substantial influence of both the photocatalyst type and the exchanged cations on surface area, porosity, and particle dispersion. TiO_2-based materials generally exhibited higher surface areas and more favorable morphologies than their ZnO-based counterparts, especially in undoped configurations.

Zeta potential and point of zero charge analyses showed that the surface charge of the composites could be finely tuned via cationic modification, influencing their colloidal stability and potential interaction with charged pollutants or microbial membranes. SEM imaging further confirmed the homogeneous dispersion of photocatalyst particles on the clay surface, contributing to the accessible active surface.

Photocatalytic degradation tests using ibuprofen as a model contaminant demonstrated that all composites exhibited measurable activity under UVA and UV-Vis irradiation, with TiO_2-based composites showing superior performance overall. Among these, the Cu-doped TiO_2 sample (Clay/Cu/TiO_2) achieved the highest degradation under UVA, suggesting a synergistic effect between copper doping and the clay support. However, performance under visible light was generally lower, indicating room for improvement in enhancing visible-light responsiveness.

Overall, the results highlight the potential of these hybrid materials as efficient and tunable photocatalytic platforms for water treatment applications. The structural, textural, and surface properties can be adjusted by choice of photocatalyst and exchanged ions, enabling the rational design of multifunctional materials for both pollutant degradation and antimicrobial applications. Future work will focus on optimizing the photocatalyst loading, improving visible-light activity, and assessing long-term stability and regeneration potential in real water matrices.

References

[1] G.R.K. Kenmogne, F. Rosillon, H.G. Mpakam, A. Nono, Enjeux sanitaires, socio-économiques et environnementaux liés à la réutilisation des eaux usées dans le maraîchage urbain: cas du bassin versant de l'Abiergué (Yaoundé-Cameroun), VertigO La Revue Électronique En Sciences de l'environnement (2010).

[2] N. Walczak, A. Krzyszczak-Turczyn, B. Czech, Unveiling the effect of SWCNT as the dopants of TiO2 in pharmaceutical mixture photocatalytic removal from water and wastewater, J Photochem Photobiol A Chem 467 (2025). https:// doi.org/10.1016 /j.jphotochem.2025 .116437.

[3] N. Dammak, N. Fakhfakh, S. Fourmentin, M. Benzina, Natural clay as raw and modified material for efficient o-xylene abatement, J Environ Chem Eng 1 (2013) 667– 675. https://doi.org/10.1016/j.jece.2013.07.001.

[4] M.R. Eskandarian, H. Choi, M. Fazli, M.H. Rasoulifard, Effect of UV-LED wavelengths on direct photolytic and TiO2 photocatalytic degradation of emerging contaminants in water, Chemical Engineering Journal 300 (2016) 414–422. https://doi.org/10.1016/j.cej.2016.05.049.

[5] D.S. Villarreal-Lucio, V.S. Galván-Romero, C. López-Saldaña, B.V. Loera-García, K.X. Vargas-Berrones, R. Ocampo-Pérez, J.C. Serna-Carrizalez, R. Flores-Ramírez, Molecularly imprinted polymer with photocatalytic activity for ibuprofen adsorption, degradation, and detection in real water samples, J Contam Hydrol 273 (2025). https://doi.org/10.1016/j. jconhyd.2025.104600.

[6] M. Gros, M. Petrović, A. Ginebreda, D. Barceló, Removal of pharmaceuticals during wastewater treatment and environmental risk assessment using hazard indexes, Environ Int 36 (2010) 15–26. https://doi.org/10.1016/j.envint.2009.09.002.

[7] N. Bashir, T. Sawaira, A. Jamil, M. Awais, A. Habib, A. Afzal, Challenges and prospects of main-group metal-doped TiO_2 photocatalysts for sustainable water remediation, Materials Today Sustainability 27 (2024). https://doi.org/10.1016/j.mtsust.2024.100869.

[8] M.I. Din, R. Khalid, Photocatalysis of pharmaceuticals and organic dyes in the presence of silver-doped TiO2 photocatalyst–A critical review, Int J Environ Anal Chem 105(2025) 276–300. https://doi.org/10.1080/03067319.2023.2258795.

[9] S. Douven, J.G. Mahy, C. Wolfs, C. Reyserhove, D. Poelman, F. Devred, E.M. Gaigneaux, S.D. Lambert, Efficient N, Fe Co-Doped TiO2 Active under Cost-Effective Visible LED Light: From Powders to Films, Catalysts 10 (2020) 547. https://doi.org/10.3390/catal10050547.

[10] J.G. Mahy, M.H.T. Mbognou, C. Léonard, N. Fagel, E.D. Woumfo, S.D. Lambert, Natural Clay Modified with ZnO/TiO2 to Enhance Pollutant Removal from Water, Catalysts 12 (2022). https://doi.org/10.3390/catal12020148.

[11] J.G. Mahy, C. Wolfs, C. Vreuls, S. Drot, S. Dircks, A. Boergers, J. Tuerk, S. Hermans, S.D. Lambert, Advanced oxidation processes for waste water treatment: From lab-scale model water to on-site real waste water, Environmental Technology (United Kingdom) 42 (2021) 3974–3986. https://doi.org/10.1080/09593330.2020.1797894.

[12] H. Benhebal, C. Wolfs, S. Kadi, R.G. Tilkin, B. Allouche, D. Lambert, J.G. Mahy, Visible Light Sensitive SnO2/ZnCo2O4 Material for the Photocatalytic Removal of Organic Pollutants in Water, Inorganics (Basel) 7 (2019) 77.

[13] P. Trigueiro, A.G. Jerônimo, W.A. Albuquerque, W.L. da Silva, J.A. Osajima, M. Jaber, R.R. Peña-Garcia, Shaping a ZnO-alginate-hectorite nanocomposite for improved photocatalytic drug removal, Appl Mater Today 44 (2025). https://doi.org/10.1016/j.apmt.2025.102680.

[14] P. Trigueiro, W.A. Albuquerque, A.G. Jerônimo, R. Barbosa, M. Jaber, R.R. Peña- Garcia, Tailoring Y-doped ZnO loaded onto eco-friendly support alginate-hectorite for azo dye removal, Appl Surf Sci 704 (2025). https://doi.org/10.1016/j.apsusc.2025.163461.

[15] W. Albuquerque, P. Trigueiro, B. V. Silva, L. Neves, L.C. Almeida, R.R. Peña-Garcia, A novel RuO_2@ZnO-Alginate-Halloysite composite for the effective degradation of Eosin Yellow dye and Ciprofloxacin drug, Mater Res Bull 182 (2025). https://doi.org/10.1016/j.materresbull.2024.113178.

[16] P. Trigueiro, W.A. Albuquerque, A.G. Jerônimo, M.S. Rodrigues, E.L.T. França, R.R. Peña-Garcia, CuO-TiO2–Saponite Ternary Nanocomposite for Efficient Removal of Bromocresol Green Dye, Minerals 14 (2024). https://doi.org/10.3390/min14121268.

[17] R.P. Feitosa, I.S. de Lima, Y. Guerra, E.C. da Silva-Filho, M.B. Furtini, L. Almeida, R.R. Peña-Garcia, I.B. Martín, J.A. Cecília, J.A. Osajima, Cerium-Doped TiO2 and Sepiolite Nanocomposites for Tetracycline Inactivation in Water Treatment, ACS Appl Nano Mater 8 (2025) 4324–4338. https://doi.org/10.1021/acsanm.4c01068.

[18] R.F. Hamarawf, D.I. Tofiq, K.H.H. Aziz, H.Q. Hassan, K.A. Abdalkarim, S.J. Mohammed, Antibacterial activity and photo-Fenton catalytic degradation of a novel FeII/FeIII mixed-valency porous coordination polymer, J Environ Chem Eng 13 (2025). https://doi.org/10.1016/j.jece.2025.116765.

[19] K.H.H. Aziz, K.M. Omer, A. Mahyar, H. Miessner, S. Mueller, D. Moeller, Application of photocatalytic falling film reactor to elucidate the degradation pathways of pharmaceutical diclofenac and ibuprofen in aqueous solutions, Coatings 9 (2019). https://doi.org/10.3390/coatings9080465.

[20] A.S. Soares, F.P. Araujo, R. França, J.A. Osajima, Y. Guerra, S. Castro-Lopes, E.C. Silva-Filho, F.E. Santos, L.C. Almeida, B.C. Viana, R.R. Peña-Garcia, Effect of pH of the growth

and ibuprofen photocatalytic response of Zn1 − xCoxO compound synthesized by the co-precipitation method, J Mater Res 38 (2023) 2439–2452. https://doi.org/10.1557/s43578-023-00980-4.

[21] J.G. Mahy, L. Lejeune, T. Haynes, N. Body, S. De Kreijger, B. Elias, R.H.M. Marcilli, C.A. Fustin, S. Hermans, Crystalline ZnO photocatalysts prepared at ambient temperature: Influence of morphology on p-nitrophenol degradation in water, Catalysts 11 (2021). https://doi.org/10.3390/catal11101182.

[22] J.G. Mahy, C.A. Paez, J. Hollevoet, L. Courard, E. Boonen, S.D. Lambert, Durable photocatalytic thin coatings for road applications, Constr Build Mater 215 (2019) 422– 434. https://doi.org/10.1016/j.conbuildmat.2019.04.222.

[23] F. Méndez-Arriaga, S. Esplugas, J. Giménez, Photocatalytic degradation of non-steroidal anti-inflammatory drugs with TiO2 and simulated solar irradiation, Water Res 42 (2008) 585–594. https://doi.org/10.1016/j.watres.2007.08.002.

[24] M.O. Adesina, M.O. Alfred, H. Seitz, K. Brennenstuhl, H.M. Rawel, P. Wessig, J. Kim,A. Wedel, W. Koopman, C. Günter, E.I. Unuabonah, A. Taubert, Orange peel biochar/clay/titania composites: low cost, high performance, and easy-to-reuse photocatalysts for the degradation of tetracycline in water, Environ Sci (Camb) 10 (2024) 1432–1450. https://doi.org/10.1039/d4ew00037d.

[25] M. Chauhan, V.K. Saini, S. Suthar, Ti-pillared montmorillonite clay for adsorptive removal of amoxicillin, imipramine, diclofenac-sodium, and paracetamol from water, J Hazard Mater 399 (2020). https://doi.org/10.1016/j.jhazmat.2020.122832.

[26] E.G. Garrido-Ramírez, B.K.G. Theng, M.L. Mora, Clays and oxide minerals as catalysts and nanocatalysts in Fenton-like reactions - A review, Appl Clay Sci 47 (2010) 182–192. https://doi.org/10.1016/j.clay.2009.11.044.

[27] H. Bel Hadjltaief, P. Da Costa, M.E. Galvez, M. Ben Zina, Influence of operational parameters in the heterogeneous photo-fenton discoloration of wastewaters in the presence of an iron-pillared clay, Ind Eng Chem Res 52 (2013) 16656–16665. https://doi.org/10.1021/ie4018258.

[28] M.H.T. Mbognou, S.D. Lambert, J. Caucheteux, A. Farcy, C. Alié, N. Fagel, E.D. Woumfo, J.G. Mahy, Hybrid clay-based materials for organic dyes and pesticides elimination in water, J Solgel Sci Technol 105 (2023) 461–470. https://doi.org/10.1007/s10971-022-06005-6.

[29] K.H. Hama Aziz, H. Miessner, S. Mueller, D. Kalass, D. Moeller, I. Khorshid, M.A.M. Rashid, Degradation of pharmaceutical diclofenac and ibuprofen in aqueous solution, a direct

comparison of ozonation, photocatalysis, and non-thermal plasma, Chemical Engineering Journal 313 (2017) 1033–1041. https://doi.org/10.1016/j.cej.2016.10.137.
[30] J.P. Candido, S.J. Andrade, A.L. Fonseca, F.S. Silva, M.R.A. Silva, M.M. Kondo, Ibuprofen removal by heterogeneous photocatalysis and ecotoxicological evaluation of the treated solutions, Environmental Science and Pollution Research 23 (2016) 19911– 19920. https://doi.org/10.1007/s11356-016-6947-z.
[31] A.S. Sá, R.P. Feitosa, L. Honório, R. Peña-Garcia, L.C. Almeida, J.S. Dias, L.P. Brazuna, T.G. Tabuti, E.R. Triboni, J.A. Osajima, E.C. da Silva-Filho, A brief photocatalytic study of zno containing cerium towards ibuprofen degradation, Materials 14 (2021). https://doi.org/10.3390/ma14195891.
[32] N. Shafeei, G. Asadollahfardi, G. Moussavi, M.M. Akbar Boojar, Degradation of ibuprofen in the photocatalytic process with doped TiO_2 as catalyst and UVA-LED as existing source, Desalination Water Treat 142 (2019) 341–352. https://doi.org/10.5004/dwt.2019.23214.
[33] C.B. Anucha, I. Altin, E. Bacaksiz, I. Degirmencioglu, T. Kucukomeroglu, S. Yılmaz, V.N. Stathopoulos, Immobilized TiO_2/zno sensitized copper (Ii) phthalocyanine heterostructure for the degradation of ibuprofen under uv irradiation, Separations 8 (2021) 1–21. https://doi.org/10.3390/separations8030024.
[34] A. Farcy, M. Mathy, L. Lejeune, P. Eloy, S. Hermans, P. Drogui, J.G. Mahy, Ce2O3 and TiO2 p-n heterojunction for enhanced degradation of p-nitrophenol under visible light, J Photochem Photobiol A Chem 463 (2025). https://doi.org/10.1016/j.jphotochem.2025.116284.
[35] G. Zerjav, K. Zizek, J. Zavasnik, A. Pintar, Brookite vs. rutile vs. anatase: What's behind their various photocatalytic activities?, J Environ Chem Eng 10 (2022). https://doi.org/10.1016/j.jece.2022.107722.
[36] W.A. Freitas, B.E.C.F. Soares, M.S. Rodrigues, P. Trigueiro, L.M.C. Honorio, R. Peña-Garcia, A.C.S. Alcântara, E.C. Silva-Filho, M.G. Fonseca, M.B. Furtini, J.A. Osajima, Facile synthesis of ZnO-clay minerals composites using an ultrasonic approach for photocatalytic performance, J Photochem Photobiol A Chem 429 (2022). https://doi.org/10.1016/j.jphotochem.2022.113934.
[37] World Health Organization (WHO), Guidelines for Drinking-water Quality FOURTH EDITION INCORPORATING THE FIRST ADDENDUM, Geneva, 2017.
[38] K.O. Rahman, K.H.H. Aziz, Utilizing scrap printed circuit boards to fabricate efficient Fenton-like catalysts for the removal of pharmaceutical diclofenac and ibuprofen from water, J Environ Chem Eng 10 (2022). https://doi.org/10.1016/j.jece.2022.109015.
[39] C. Li, Z. Sun, W. Zhang, C. Yu, S. Zheng, Highly efficient g-C3N4/TiO2/kaolinite

composite with novel three-dimensional structure and enhanced visible light responding ability towards ciprofloxacin and S. aureus, Appl Catal B 220 (2018) 272–282. https://doi.org/10.1016/j.apcatb.2017.08.044.
[40] T.S. Wu, K.X. Wang, G.D. Li, S.Y. Sun, J. Sun, J.S. Chen, Montmorillonite-Supported Ag/TiO2 nanoparticles: An efficient visible-Light bacteria photodegradation material, ACS Appl Mater Interfaces 2 (2010) 544–550. https://doi.org/10.1021/am900743d.
[41] L. Yuan, D. Huang, W. Guo, Q. Yang, J. Yu, TiO2/ montmorillonite nanocomposite for removal of organic pollutant, Appl Clay Sci 53 (2011) 272–278. https://doi.org/10.1016/j.clay.2011.03.013.
[42] N. Bai, X. Liu, Z. Li, X. Ke, K. Zhang, Q. Wu, High-efficiency TiO2/ZnO nanocomposites photocatalysts by sol–gel and hydrothermal methods, J Solgel Sci Technol 99 (2021) 92–100. https://doi.org/10.1007/s10971-021-05552-8.
[43] T. Karchiyappan, R. Rao, K. Mohammad, H. Dehghani, Water Science and Technology Library Industrial Wastewater Treatment Emerging Technologies for Sustainability, Springer, 2022. https://www.springer.com/gp/.
[44] S. Ali, M.T. Aljarrah, A. Al-Otoom, N. Abdelaziz, Development and Testing of Robust 3D Printed ZnO/Clay Photocatalysts for Sustainable Wastewater Treatment, ACS Omega (2025). https://doi.org/10.1021/acsomega.4c09879.
[45] K.M. Reza, A. Kurny, F. Gulshan, Parameters affecting the photocatalytic degradation of dyes using TiO2: a review, Appl Water Sci 7 (2017) 1569–1578. https://doi.org/10.1007/s13201-015-0367-y.
[46] M. Tanveer, G.T. Guyer, G. Abbas, Photocatalytic degradation of ibuprofen in water using TiO2 and ZnO under artificial UV and solar irradiation, Water Environment Research 91 (2019) 822–829. https://doi.org/10.1002/wer.1104.
[47] S. Loaiza-Ambuludi, M. Panizza, N. Oturan, M.A. Oturan, Removal of the antiinflammatory drug ibuprofen from water using homogeneous photocatalysis, Catal Today 224 (2014) 29–33. https://doi.org/10.1016/j.cattod.2013.12.018.
[48] F. Méndez-Arriaga, R.A. Torres-Palma, C. Pétrier, S. Esplugas, J. Gimenez, C. Pulgarin, Mineralization enhancement of a recalcitrant pharmaceutical pollutant in water by advanced oxidation hybrid processes, Water Res 43 (2009) 3984–3991. https://doi.org/10.1016/j.watres.2009.06.059.
[49] M. Jiménez-Salcedo, M. Monge, M.T. Tena, Photocatalytic degradation of ibuprofen in water using TiO2/UV and g-C3N4/visible light: Study of intermediate degradation products by liquid chromatography coupled to high-resolution mass spectrometry, Chemosphere 215 (2019) 605–618. https://doi.org/10.1016/j.chemosphere.2018.10.053.

[50] M. Pylarinou, E. Sakellis, S. Gardelis, V. Psycharis, M.G. Kostakis, N.S. Thomaidis, V. Likodimos, Bilayer TiO2/Mo-BiVO4 Photoelectrocatalysts for Ibuprofen Degradation, Materials 18 (2025). https://doi.org/10.3390/ma18020344.

[51] F.S. Braz, M.R.A. Silva, F.S. Silva, S.J. Andrade, A.L. Fonseca, M.M. Kondo, Photocatalytic Degradation of Ibuprofen Using TiO₂ and Ecotoxicological Assessment of Degradation Intermediates against <i>Daphnia similis</i>, J Environ Prot (Irvine, Calif) 05 (2014) 620–626. https://doi.org/10.4236/jep.2014.57063.

[52] H. Gong, W. Chu, S.H. Lam, A.Y.C. Lin, Ibuprofen degradation and toxicity evolution during Fe2+/Oxone/UV process, Chemosphere 167 (2017) 415–421. https://doi.org/10.1016/j.chemosphere.2016.10.027.

[53] Z. Feng, Synthesis and full-spectrum-responsive photocatalytic activity from UV/Vis to near-infrared region of S-O decorated YMnO3 nanoparticles for photocatalytic degradation of ibuprofen, Front Chem 12 (2024). https://doi.org/10.3389/fchem.2024.1424548.

General conclusions and perspectives

The overall objective of this thesis was to contribute to the project of valorizing clay materials in Cameroon and remedying the pollution of micropollutants present in water, specifically in wastewater from treatment plants. To achieve this, an advanced oxidation process such as photocatalysis was used. The approach taken consisted of developing, characterizing, and optimizing suitable materials. The work was divided into five chapters.

The main wastewater problems in Cameroon and the demand for effective, reasonably priced treatment options were discussed in Chapter I. The useful qualities of clay materials, which are widely accessible in the area, for the adsorption of pollutants have been demonstrated. In addition, the photocatalytic process, as a viable solar-powered method , presented the capacity to break down persistent pollutants. In this way, , combining the photocatalytic process with the adsorption ability of clay materials seems to be an economical and sustainable way to enhance wastewater treatments in Cameroon.

Chapter II focused on synthesizing raw clays extracted from Bana, in Western Cameroon. In a first time, Cu^{2+} ions were added to the clay by ion exchange to increase the specific surface area. In a second time, the samples were modified with photocatalytic semiconductors (TiO_2 and ZnO). The presence of TiO_2 and ZnO was confirmed by the detection of anatase and wurtzite, respectively, using X-ray diffraction. These crystallographic phases of anatase for TiO_2 and wurtzite for ZnO present photocatalytic properties with a bang gap equal to 3.2 eV. Furthermore, when TiO_2 or ZnO modifies the clay, the specific surface area of these new photocatalyst/clay composites is largely increased (from 45 m^2/g to 325 m^2/g for TiO^2-doped clays and from 45 m^2/g to 125 m^2/g for ZnO-doped clays). The adsorption property of the raw clay and new photocatalyst/clay composites was evaluated on two pollutants, namely fluorescein (FL) and *p*-nitrophenol (PNP). The experiments showed that the samples adsorb FL but not PNP. It is why the new composites were illuminated with UV-A light for 8 h. It is observed that for sample Clay/Cu^{2+}/ZnO, 90% of PNP is degraded after 8 h. So the new photocatalytic/clay composites combine adsorption and photocatalytic properties to remove pollutants present in waste waters.

In the third part of this work, the clay material extracted from Cameroon was doped with Cu^{2+}, Na^+, Zn^{2+} ions and with photocatalytic ZnO semiconductor . From X-Ray measurements, mixed crystalline patterns were obtained with both smectite (raw clay) and wurtzite ZnO phases. SEM observations of the samples showed that the hybrid materials present a clay structure as a skeletal structure (sheet structure) with spherical ZnO particles grafted onto the surface,

providing good light exposure to maintain the photocatalytic properties . Next, the adsorption efficiency of the samples was evaluated on three different model pollutants: *p*-nitrophenol (PNP), Malachite Green (MG), and Diamond Bright Violet (DBV). All the samples adsorbed 100% of MG and DBV after 24 h, but no adsorption was observed on PNP. As in Chapter II, the samples doped with ZnO were again illuminated under UV-A for 2 h, 6 h and 24 h to measure their degradation ability of pollutants. It was observed that the 3 pollutants are totally degraded under UV-A after 24 h for all the samples.

Tetramethoxysilane (TMOS) and [3-(2-aminoethyl)aminopropyl]trimethoxysilane (EDAS) were used in Chapter IV to chemically functionalize the clay material and improve its adsorption ability. The goal of this functionalization was to create effective clay-based adsorbents for the elimination of organic contaminants from aquatic settings. Three clay/TMOS samples and two clay/EDAS samples with different silane-to-clay ratios were synthesized and characterized by nitrogen adsorption-desorption measurements, ICP, XRD, and SEM. It was observed a strong dependence on the type of silane was observed: EDAS-modified samples maintained a layered morphology nearly identical to the raw clay structure, with EDAS molecules grafted onto the surface, whereas TMOS-modified samples are highly porous and present aggregates of amorphous silica nanoparticles on the clay surface. Using FL, MG, and DBV as representative organic contaminants, the adsorption capabilities of these new silane/clay composites were examined. It was also observed different adsorption behaviors as a function of TMOS-doping or EDAS-doping : (i) all TMOS/clay composites adsorbed 100% of the three organic pollutants after 10 min. Indeed, the samples present the highest specific surface area (up to 660 m^2/g compared to 55 m^2/g for EDAS/clay composites) ; (ii) for EDAS/clay composites, the adsorption rate of organic pollutants was very slow because a high amount of ethylenediamine groups of EDAS are present at the surface of the samples. In this case, this high steric hindrance limited the interactions between organic pollutants and the surface of clays.

The increasing presence of pharmaceuticals in wastewater, such as ibuprofen, which raises serious environmental and public health concerns, particularly in developing regions, was demonstrated in Chapter V. Furthermore, in this study, photocatalytic materials were used to analyse their disinfection properties in the presence of different bacteria (total coliforms, Salmonella/Shigella, and faecal Streptococci). Under UV-A irradiation, the photocatalyst/clay composites achieved significant degradation efficiencies, highlighting the complete degradation of ibuprofen into CO_2 and H_2O in 4 h with the best sample. In parallel, antibacterial tests revealed notable inhibition against the different bacteria. Indeed, the clay/ZnO and

clay/TiO_2 composites produced near-complete bacterial inhibition at concentrations ≥1 g/L after 4 h under illumination at 365 nm. Under illumination, these hybrid composites produced a high amount of reactive oxygen species (ROS), resulting in the destruction of bacterial cell membranes.

At the end of this study, a few areas that warrant further investigation have emerged. For example.

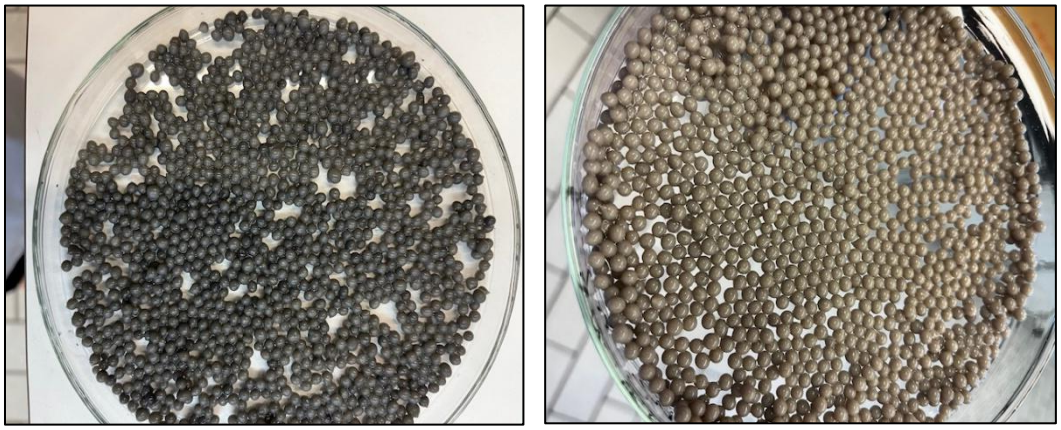

Figure 6.1: Alginate beads developed with clay-based photocatalyst TiO_2 and ZnO.

In this way, a first cost estimation is realized for a cylindrical column with a diameter of cm and a height of 1 m that is filled with photocatalyst/clay beads. Assuming a bulk density of beads around 0.8 $g \cdot cm^{-3}$, such a column has an interior volume equal to 7.85 L, which translates to a composite mass of about 6–6.5 kg. Under continuous flow circumstances, this column can treat about 4.5–5.0 m^3 of wastewater per day at a conservative hydraulic loading rate.

The column could remove around 60–65 g of organic micropollutants before reaching saturation or needing regeneration, based on an efficient combined adsorption–photocatalytic capacity of about 10 mg of pollutant per gram of composite. This translates to a total treated water volume of roughly 600–650 m^3 at each operational cycle for a representative influent concentration of 100 $\mu g \cdot L^{-1}$, which is typical of pharmaceutical residues like ibuprofen in treated municipal effluents.

Therefore, depending on the applied flow rate and pollutant load, the column's anticipated service life before regeneration would be between four and six months. Either in situ photocatalytic oxidation under UV or solar irradiation or straightforward washing followed by mild thermal treatment can accomplish regeneration, allowing for numerous reuse cycles (5–10 cycles).

Because of its low energy consumption, a 10 cm diameter column continues to have low operating costs from an economic standpoint. The annual running cost per column is anticipated to be between 128 € and 215 € when pumping, and UV-A irradiation is taken into account, and the treated water volume reaches about 1,600 to 1,800 m³. This leads to a particular treatment cost of about 0,09–0,14 €/m³, which is far less than the majority of traditional tertiary treatment technologies, such as ozonation (0.52 €/m³) or activated carbon adsorption followed by pyrolysis of these carbons (from 0.23 €/m³ up to 1.36 €/m³ as a function of the type and the concentration of micropollutant) .

ANNEXES

Annex I: Description of the wastewater treatment process of the Camp of the "Cité-Verte"

The WWTP of the camp of the "Cité-Verte" is a station that treats wastewater, including a hybrid system, filters, and plants. The four steps of the treatment are as follows: (i) the network for collecting wastewater; (ii) pre- and primary treatment; (iii) secondary (biological) treatment; and (iv) release into the environment. The network used to collect wastewater is unique. Hence, it is made up of: (i) a collection of primary sewer/manhole shapes that enable wastewater to be collected from homes and dumped into a public sewer, and (ii) a set of collectors/intermediate manholes that accept wastewater that also comes from private collectors [56]. Preparing wastewater for further treatment is the goal of pretreatment or primary treatment. This is done to get rid of substances that can obstruct further purification in the rest of the WWTP. It consists of two parts: (i) a screen to catch coarse materials that are likely to wind up in the wastewater, and (ii) a desander to get rid of suspended solids. (iii) a degreaser/oil remover to remove fats and oils through the flotation process. These particles can harm or clog pipes. Skimming the surface removes these fats and oils, which can then be used, for instance, to make biogas; (iv) settling tanks are used to collect the streams of sludge produced by the degreaser/oil remover (caused by the outlet water). This prevents the biological basin from becoming overloaded with sludge, which would increase the water's turbidity, and (v) a transition and appreciation tank to monitor the effectiveness of the pre-treatment. Whenever water from primary treatment is being analyzed, it also functions as a sampling location. A transition tank between primary and secondary (biological) treatment is also provided by it [57]. A hybrid system, filters, and plants are used for secondary treatment. The filter/plant basin, which consists of an artificial tank filled with water, substrate, and vascular plants, receives wastewater. The substrate is made up of stones, gravel, and sand (ballast). These materials' permeability will be used to keep the waste and sediment in the treated water in place. Pollutants like metals and nitrogen can be removed since the saturation of the substrate renders it anaerobic.

The effluent is evacuated and directed through PolyVinyl Chloride (PVC) pipes to the receiver after treatment. The Abiergue watercourse, a tributary of the Mfoundi River, serves as the receiving system. When more stringent regulations are in place, preventing eutrophication does not suffice. What techniques, then, can a WWTP use to further purify water?

Distillation could be considered, but that would be incredibly expensive, so this application is limited to the production of distilled water. Mechanical evaporators, which are cheaper to

operate, are an option when the water is highly polluted and the flow rates are low. Solvent extraction can be used to transfer toxic organic pollutants to a non-aqueous phase. Ion exchange is sometimes used to remove toxic ions in water by exchanging them 10with non-toxic ions present in a solid.

Microfiltration, ultrafiltration, and reverse osmosis are all membrane-based processes that can treat very small particles or even dissolved matter. This makes reverse osmosis a technique widely used for the production of potable water from saline water.

Annex II: Additional figures from Chapter 2

The adsorption-desorption isotherms are represented in Figure AII.1 for pure TiO_2 and pure ZnO samples and in Figure AII.2 for Clay/Cu^{2+}, Clay/TiO_2/Cu^{2+}, Clay/ZnO/Cu^{2+}, and Clay/ZnO samples. As explained in section 2.3.2, two types of isotherms are clearly observed: (i) type I isotherm (microporous solid) for pure TiO_2 and Clay/TiO_2/Cu^{2+} samples; and (ii) type IV isotherm (mesoporous sample) for pure ZnO, Clay/Cu^{2+}, Clay/ZnO/Cu^{2+}, and Clay/ZnO samples.

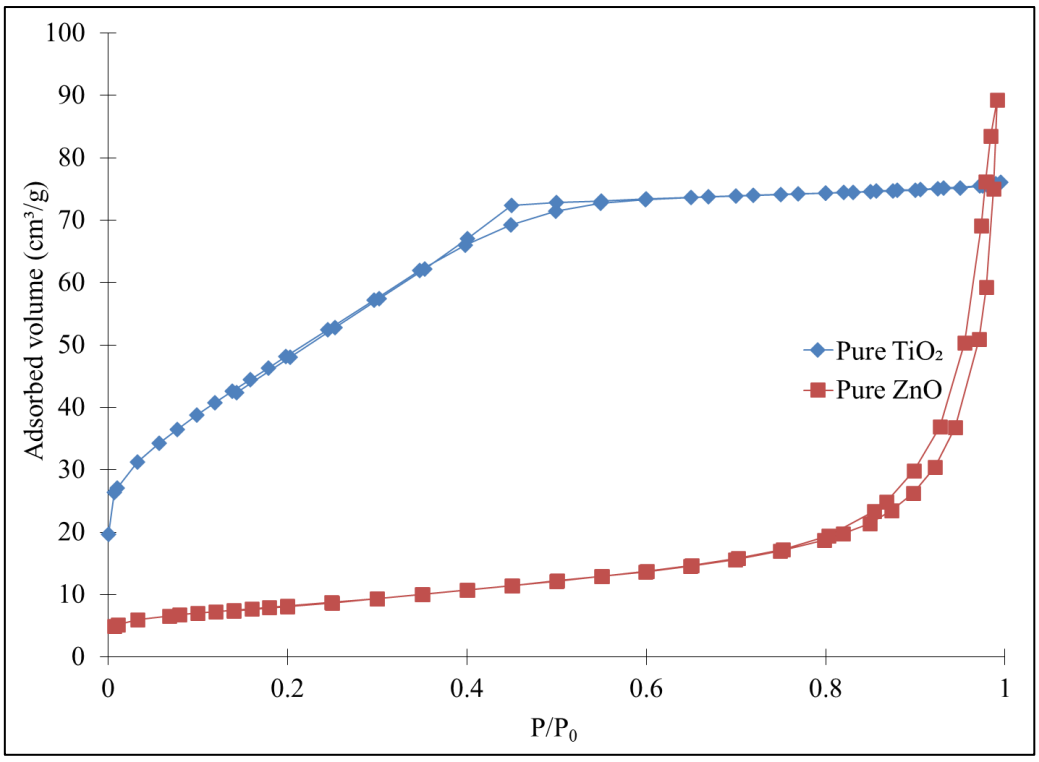

Figure AII.1: Nitrogen adsorption desorption isotherms for (♦) pure TiO_2 and (■) pure ZnO samples.

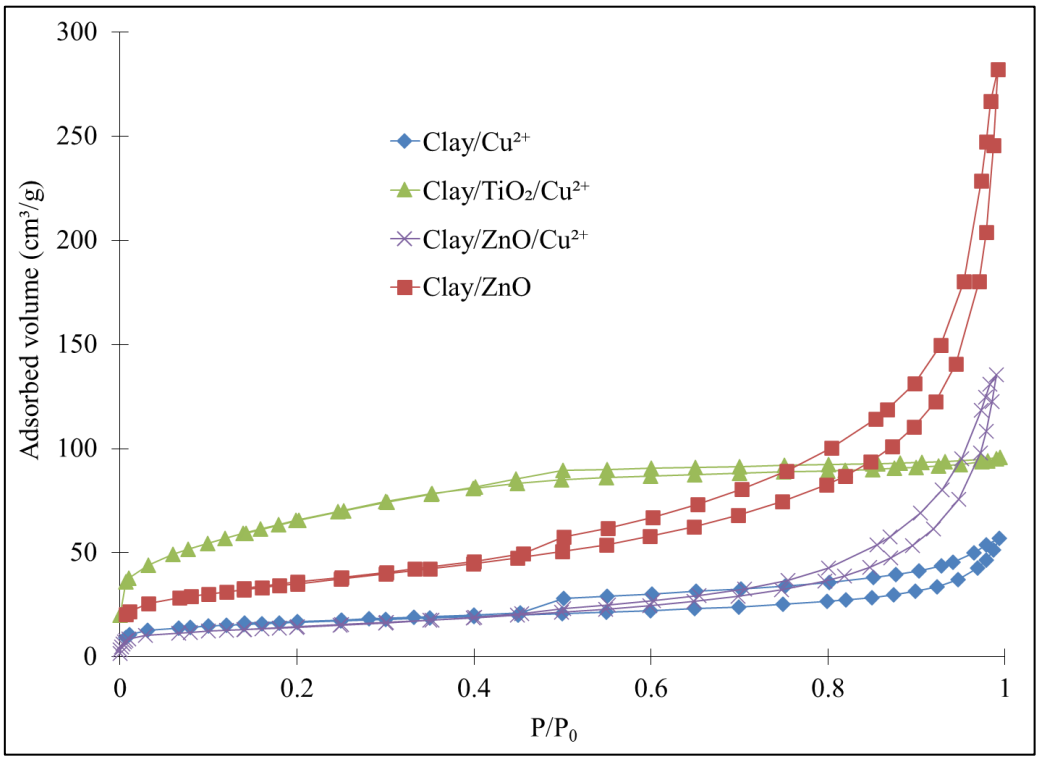

Figure AII.2: Nitrogen adsorption desorption isotherms for (♦) Clay/Cu^{2+}, (▲) Clay/TiO_2/Cu^{2+}, (×) Clay/ZnO/Cu^{2+} and (■) Clay/ZnO samples.

The samples with Cu^{2+} ions (Clay/Cu^{2+}, Clay/TiO_2/Cu^{2+}, and Clay/ZnO/Cu samples) keep are represented in Figure AII.3.

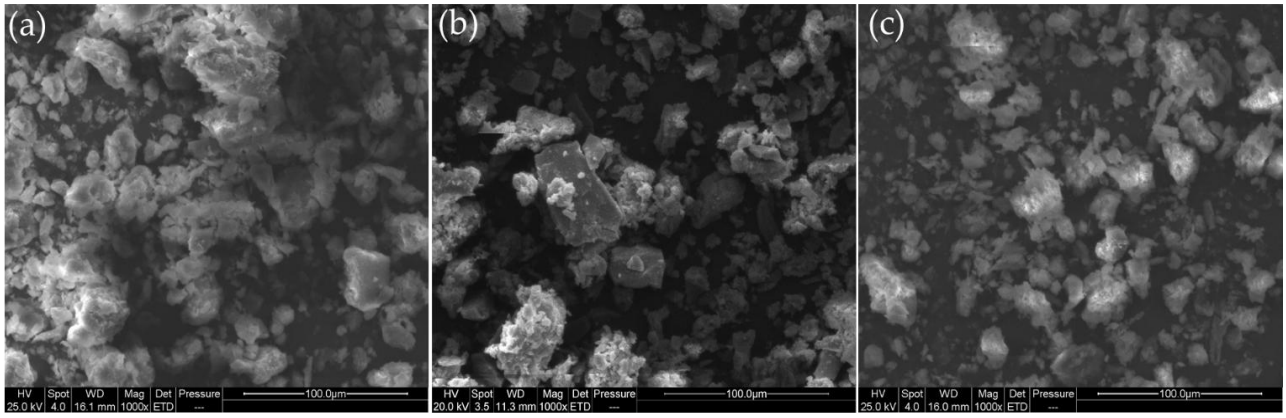

Figure AII.3: SEM pictures of (a) Clay/Cu^{2+}, (b) Clay/TiO_2/Cu^{2+}, and (c) Clay/ZnO/Cu^{2+} samples at a 1000x magnification.

Annex 4: Curriculum Vitae

Annex 5: List of publications

Marlène Tsaffo Mbognou, PhD

P.O BOX 4110 Yaounde - Cameroon, 00237 694 021 456

tsaffombognou@yahoo.fr / mhtmbognou@doct.uliege.be

PROFESSIONAL SUMMARY

I am a conscientious, highly motivated, ambitious, and trustworthy individual driven by results. My research is focused on applied chemistry, specifically in the synthesis of mineral materials through photocatalysis to create high-performance substances capable of degrading micro pollutants found in wastewater. Given their potential applications across various industries, nanomaterial's hold significant importance. Within applied chemistry, numerous experiments are conducted to evaluate new materials in laboratory settings, aiming to develop effective solutions for water depollution and environmental sanitation.

FIELD OF RESEARCH

Chemistry and Environmental Chemistry of Nanomaterials: Focus areas include photocatalysis, porous materials, degradation of micropollutants, and photocatalytic degradation.

EDUCATION

Liege University - Belgium and University of Yaoundé I
ULIEGE/PACODEL Doctorate Mobility Fund. Financing of a mobility grant within the framework of Research and Development Project (PRD)
Defense Thesis: Physico-Chemical and Mineralogical Characterisation of Clay Material from the Bakotcha Locality: Application to Wastewater Treatment.
Supervisor: Prof. Lambert Stéphanie and Prof. Djoufac Woumfo Emmanuel

- PhD in Applied Chemistry

University of Yaoundé I-Cameroon
Supervisor: Prof. Djoufac Woumfo Emmanuel

- M.Sc. Inorganic Chemistry (Honors)

University of Dschang-Cameroon
Supervisor: Prof. Nkouathio David

- M.Sc. Mining and Petroleum

University of Dschang-Cameroon

- B.Sc. Inorganic Chemistry

PROFESSIONAL EXPERIENCE

Ministry of Scientific Research and Innovation (MINRESI) **Yaounde- Cameroon**
Institute of mining and geological research (IRGM) 01/2006- Present

Researcher

Key Achievements:

March 2021: Geochemist Prospector in the Eseka-Cameroon

- Conducted evaluation of the mining potential through a comprehensive geological and geochemical mapping project on a national scale.
- Played a pivotal role in assessing geological and geochemical data to identify potential mineral resources.

Project Financed and supervised by the Institute of Mining and Geological Research (IRGM), Yaounde, Cameroon.

February 2020: Geochemist Prospector in the PRECASEM

- Contributed to a national geological and geochemical mapping project aimed at identifying mineral resources.
- Played a crucial role in data collection, analysis, and interpretation to support resource exploration efforts.

Project Financed by World Bank, under the supervision of BRGM, GTK, BEIG 3 and Institute of Mining and Geological Research (IRGM), Yaounde, Cameroon

2017 to 2018: Geochemist Prospector in the PRECASEM

- Participated in a national geological and geochemical mapping project supported by the World Bank.
- Contributed to the identification and assessment of mineral potential across different regions, laying the foundation for future resource development initiatives.

Project Financed by World Bank, under the supervision of BRGM, GTK, BEIG 3 and Institute of Mining and Geological Research (IRGM), Yaounde, Cameroon.

SYSTEMS EXPERIENCE

Operating Systems: Microsoft Office products: Excel, Word, Outlook, PowerPoint, MS-Project,
Reporting and Visualization: Dashboards, charts, and graphs
Software: ArcGis, Qgis, Surfer, Global Mapper
Skills: Geological and Mining Research, Data Collection and Analysis, Geological Mapping and Surveying, Research Methodologies, Laboratory Techniques

REFERENCES

- Prof. Lambert Stéphanie, Liege University, Begium: stephanie.lambert@uliege.be
- Prof. Djoufac Woumfo Emmanuel, University of Yaounde I, Cameroon: edjoufac2000@yahoo.fr
- Dr. Bassahak Jean, Institute of Mining and Geological Research (IRGM), Yaounde, Cameroon, jeanbassahak@yahoo.fr
- Dr. Mahy Julien, Liege University, Belgium: Julien.mahy@uliege.be

PUBLICATIONS

- P1. **Marlène Huguette Tsaffo Mbognou**, Stéphanie D. Lambert, Antoine Farcy, Hela Rekik, Steven Wouamba, Emmanuel Djoufac Woumfo, Julien G. Mahy « Dual-function cameroonian clay-supported ZnO and TiO2 photocatalysts for ibuprofen mineralization and bacteria inactivation », Next Materials 9 (2025) 101290, https://doi.org/10.1016/j.nxmate.2025.101290

- P2. **Marlène Huguette Tsaffo Mbognou**, Stéphanie D. Lambert , Ernestine Mimba Mumbfu , Joachim Caucheteux, Antoine Farcy , Nathalie Fagel , Emmanuel Djoufac Woumfo , Julien G. Mahy « Silane modified clay for enhanced dye pollution adsorption in water », Results in Surfaces and Interfaces 14 (2024) 100183, https://doi.org/10.1016/j.rsurfi.2024.100183

- P3. **Marlène Huguette Tsaffo Mbognou**, Stéphanie D. Lambert, Joachim Caucheteux, Antoine Farcy, Christelle Alié Nathalie Fagel, Emmanuel Djoufac Woumfo, Julien G. Mahy « Hybrid clay-based materials for organic dyes and pesticides elimination in water » Journal of Sol-Gel Science and Technology, https://doi.org/10.1007/s10971-022-06005-6

- P4. Julien G. Mahy, **Marlène Huguette Tsaffo Mbognou**, Clara Léonard, Nathalie Fagel, Emmanuel Djoufac Woumfo and Stéphanie D. Lambert, « Natural Clay Modified with ZnO/TiO2 to Enhance Pollutant Removal from Water», Catalysts 2022, 12, 148. https://doi.org/10.3390/catal12020148

- P5. **Tsaffo Mbognou Marlene Huguette**, Assomo Ngono Gaëlle Sandra and Fossi Donald Hermann, « GIS, Remote Sensing and Analytical Hierarchy Process-Based Identification ofGroundwater Potential Zones in Mokolo, Northern Cameroon», Int. J. of Multidisciplinary and Current research, Vol.9 (May/June 2021), https://doi.org/10.14741/ijmcr/v.9.3.5

- P6. H. Soh Nde, P. Azinwi Tamfuh, G. Clet, J. Vieillard, **Tsaffo Mbognou Marlene Huguette**, E. Djoufac Woumfo, « Comparison of HCl and H2SO4 for the acid activation of a cameroonian smectite soil clay: palm oil discolouration and landfill leachate treatment», Heliyon, https://doi.org/10.1016/j.heliyon.2019.e02926

catalysts

MDPI

Article

Natural Clay Modified with ZnO/TiO_2 to Enhance Pollutant Removal from Water

Julien G. Mahy [1,*], Marlène Huguette Tsaffo Mbognou [1,2,3], Clara Léonard [1], Nathalie Fagel [4], Emmanuel Djoufac Woumfo [2] and Stéphanie D. Lambert [1]

[1] Department of Chemical Engineering—Nanomaterials, Catalysis & Electrochemistry, University of Liège, B6a, Quartier Agora, Allée du Six Août 11, 4000 Liège, Belgium; tsaffombognou@yahoo.fr (M.H.T.M.); leonardclara1@gmail.com (C.L.); stephanie.lambert@uliege.be (S.D.L.)

[2] Laboratoire de Physico-Chimie des Matériaux Minéraux, University of Yaounde I, Yaounde 337, Cameroon; edjoufac2000@yahoo.fr

[3] Institute of Geological and Mining Research (IRGM), Ministère de la Recherche Scientifique et de L'innovation du Cameroun, Yaounde 4410, Cameroon

[4] Laboratoire Argiles, Géochimie et Environnements Sédimentaires (AGEs), Department of Geology, Faculty of Sciences, University of Liège, 4000 Liège, Belgium; nathalie.fagel@uliege.be

* Correspondence: julien.mahy@uliege.be; Tel.: +32-366-3563

Abstract: Raw clays, extracted from Bana, west Cameroon, were modified with semiconductors (TiO_2 and ZnO) in order to improve their depollution properties with the addition of photocatalytic properties. Cu^{2+} ions were also added to the clay by ionic exchange to increase the specific surface area. This insertion of Cu was confirmed by ICP-AES. The presence of TiO_2 and ZnO was confirmed by the detection of anatase and wurzite, respectively, using X-ray diffraction. The composite clays showed increased specific surface areas. The adsorption property of the raw clays was evaluated on two pollutants, i.e., fluorescein (FL) and p-nitrophenol (PNP). The experiments showed that the raw clays can adsorb FL but are not efficient for PNP. To demonstrate the photocatalytic property given by the added semiconductors, photocatalytic experiments were performed under UVA light on PNP. These experiments showed degradation up to 90% after 8 h of exposure with the best ZnO-modified clay. The proposed treatment of raw clays seems promising to treat pollutants, especially in developing countries.

Keywords: smectite; adsorption; photocatalysis; pollutant removal; environment remediation

Citation: Mahy, J.G.; Tsaffo Mbognou, M.H.; Léonard, C.; Fagel, N.; Woumfo, E.D.; Lambert, S.D. Natural Clay Modified with ZnO/TiO_2 to Enhance Pollutant Removal from Water. *Catalysts* **2022**, *12*, 148. https://doi.org/10.3390/catal12020148

Academic Editor: María Victoria López Ramón

Received: 13 December 2021
Accepted: 21 January 2022
Published: 25 January 2022

1. Introduction

The population growth, intensive industrialization, and agricultural practices that occurred in recent decades have led to an increase in environmental pollution, which is now considered a global crisis [1]. This scourge has its origins in the constant improvement in the standard of living and the strong demands of consumers. In Cameroon, for example, many cotton, pharmaceutical, fertilizer, tanning, and pesticide manufacturing industries release pollutants such as dyes, pesticides, or bacteria into the environment, leading to disturbances of aquatic fauna and constituting a risk for human health [2]. Faced with this alarming situation, the global demand for water, the most vital natural resource, is increasing [3] and at the same time, the quality of freshwater sources is declining due to the presence of emerging contaminants. Most of these contaminants escape conventional wastewater treatment offered by wastewater treatment plants. The presence of these emerging pollutants in the environment is a matter of concern for most environmental agencies in developing countries [4]. This water should be treated as part of the recycling of wastewater that can be used by low-income populations for watering vegetable crops and washing cars and clothes in order to allow these populations to have a profitable and healthy economic activity.

In order to limit the arrival of these various types of refractory contaminants into the environment, effective and ecological treatment strategies have been developed, such as the use of local clays widely available in Cameroon from kaolinites, andosols, illites, and smectites [5], and globally, the use of adsorption as an efficient process to remove pollutants [6]. Clays have been the subject of different characterizations and applications [7]. For nearly three decades, many research works have been carried out on clay materials from Cameroon and their applications [8]. The search for new deposits and the characterization and valuation of clay materials are still relevant today.

Advanced oxidation processes (AOPs) have been applied in several sectors for the treatment of surface and groundwater [9,10] and for the elimination of odors and volatile organic compounds [11], as well as for water discoloration, the degradation of phytosanitary and pharmaceutical products [12], the production of molecules such as H_2 [13], and water disinfection [14]. AOPs can be used either as an oxidative pretreatment leading to easily biodegradable compounds, or as a tertiary treatment method for the removal or complete mineralization of residual pollutants [15]. This process is based on the generation of radical species able to degrade organic pollutants thanks to the use of a photocatalyst material activated by UV radiation [16]. The most-used UV-sensitive photocatalysts are TiO_2 and ZnO [17–19]. Different composites of photocatalysts have already been developed for pollutant removal [20–24].

In this work, a combination of adsorption and photocatalysis through the synthesis of mixed materials based on smectite-TiO_2 or smectite-ZnO is presented. Two types of pollutants are explored, one dye and one pesticide-type pollutant: fluorescein (FL) and p-nitrophenol (PNP), respectively. The physico-chemical properties of the pure and mixed materials are determined as well as their adsorption and photocatalytic activities. The production of mixed materials allows the use of a material already present in Cameroon and the addition of small fraction (<30%) of photocatalysts to increase the pollutant removal efficiency of the clay. The efficiency of the process and the cost can be studied and compared to other known methods.

The advantages of using semiconductor-modified clay materials for pollutant removal in water in developing countries are numerous: (i) the materials are composed primarily of natural material (the clay) directly located in the country where the pollution will be treated; (ii) the semiconductor material loading stays low (<30 wt %), reducing the cost of production; (iii) ZnO and TiO_2 are the most common semiconductor materials and can be produced with green synthesis with low use of organic reagents; (iv) the composite material presents both high adsorption capacity and photocatalytic properties, increasing its depollution properties compared to bare materials; and (v) the process for the production of the composite materials is simple.

2. Results and Discussion

2.1. Composition

Macroscopically, the raw clays, the Cu^{2+}-modified clays, and the TiO_2-modified clays are pale yellow. The ZnO-modified clays are slightly gray. The main compositions of the six different clay samples, determined by ICP-AES, are presented in Table 1.

The clays contain 9–21% of Si, 5–11% of Al, and 1–4% of Fe with an atomic Si/Al ratio equal to 2, consistent with a smectic composition [25]. The amount of copper increases up to 0.8% in the Cu^{2+}-modified samples (Table 1). The percentage of ZnO reaches 28.1% and 30.3% in the Clay/ZnO and Clay/ZnO/Cu^{2+} samples, respectively. The percentage of TiO_2 is 28.8% and 27.6% in the Clay/TiO_2 and Clay/TiO_2/Cu^{2+} samples, respectively.

The XRD patterns of the eight samples (Figure 1) allow us to estimate the crystallinity of the samples.

Table 1. Sample compositions by ICP-AES.

	Al	Si	Fe	Cu	TiO_2	ZnO
	wt %	wt %	wt %	wt %	wt %	wt %
Bare Clay	10.1	20.9	3.7	<0.1	<0.1	<0.1
Clay/Cu^{2+}	11.5	21.2	4.2	0.8	<0.1	<0.1
Clay/ZnO	5.2	9.2	1.6	<0.1	<0.1	28.1
Clay/ZnO/Cu^{2+}	6.4	11.6	1.8	0.4	<0.1	30.3
Clay/TiO_2	5.7	10.2	1.6	<0.01	28.8	<0.1
Clay/TiO_2/Cu^{2+}	5.9	11.6	1.2	0.3	27.6	<0.1

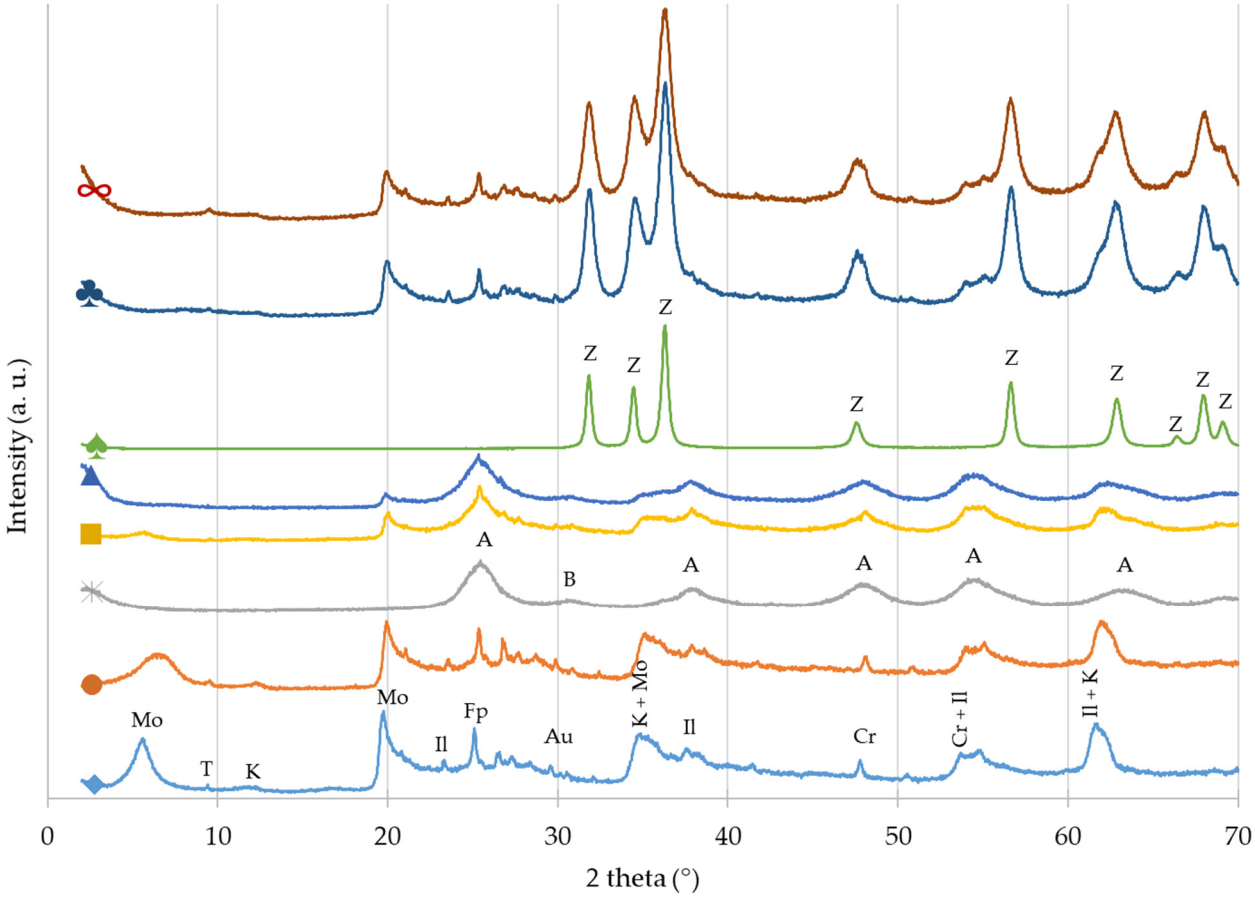

Figure 1. XRD patterns of samples: (♦) Bare Clay, (•) Clay/Cu^{2+}, (*) pure TiO_2, (■) Clay/TiO_2, (▲) Clay/TiO_2/Cu^{2+}, (♠) pure ZnO, (♣) Clay/ZnO, (∞) Clay/ZnO/Cu^{2+}. The positions of the reference peaks are indicated on the three pure materials (Bare Clay, TiO_2, and ZnO) by the following letters: (A) anatase, (B) brookite, (Z) wurzite, (Mo) montmorillonite, (T) talc, (K) kaolinite, (Il) illite, (Fp) feldspar, (Au) augite, and (Cr) cristobalite. The positions are not indicated on the composites materials to not overload the figure.

The Bare Clay (♦) is mainly composed of smectite, which is a family of different clay minerals observed in Figure 1 (all the following phases are observed: augite, cristobalite, montmorillonite, illite, kaolinite, feldspar, and talc). Smectite forms an important group of the phyllosilicate family of minerals, which are distinguished by layered structures composed of polymeric sheets of SiO_4 tetrahedra linked to sheets of (Al, Mg, Fe) $(O,OH)_6$ octahedra (Figure 2) [26–28].

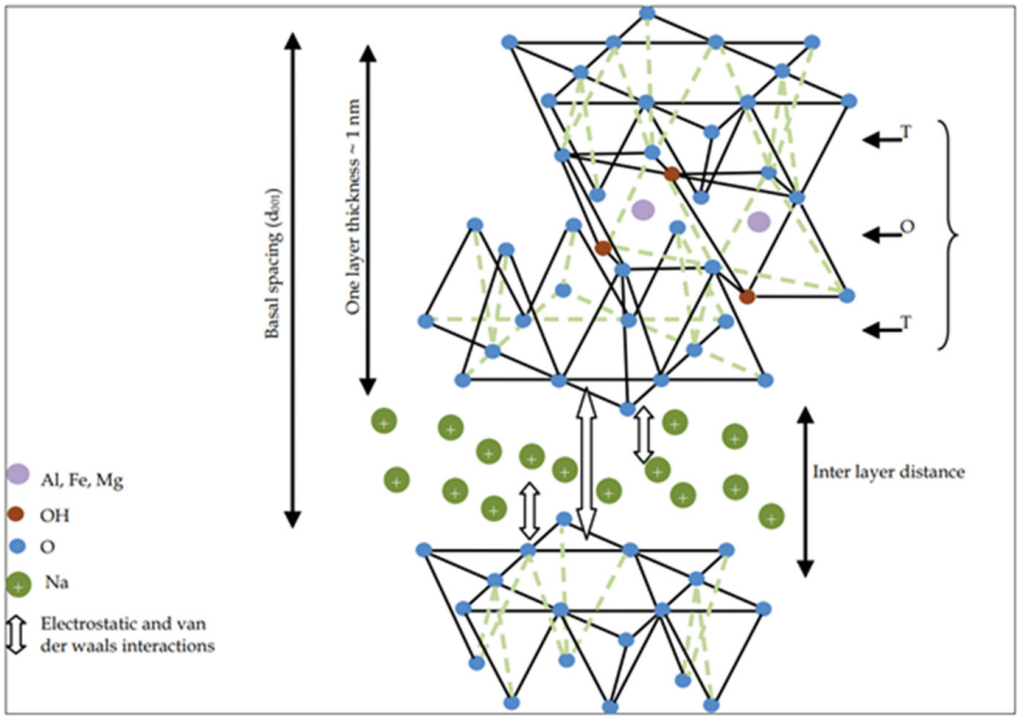

Figure 2. Smectite structure scheme from [26].

When Cu^{2+} ions are introduced to the network (Clay/Cu^{2+} sample, in orange (●) in Figure 1), a similar XRD pattern was recorded; however, the peak around 5–6° was spread due to the Cu^{2+} insertion.

The pure TiO_2 sample (Figure 1, pattern in gray (*)) is composed of anatase with a small amount of brookite (denoted A and B in Figure 1). These mixed phases were previously observed in aqueous sol-gel synthesis [29]. The pure ZnO sample (Figure 1, pattern in green (♠)) is made of wurtzite phase, as expected with this synthesis method [30].

The XRD results (Figure 1) confirm the successful production of hybrid clay–photocatalytic materials. Indeed, when the clay is modified with TiO_2, the corresponding XRD patterns (patterns in yellow (■) and mid blue (▲) in Figure 1) present the characteristic TiO_2 and clay peaks for both Clay/TiO_2 and Clay/TiO_2/Cu^{2+} samples if the peak positions are compared to the bare samples. The XRD patterns of the ZnO-modified clays (patterns in red (∞) and dark blue (♣) in Figure 1) likely present characteristic peaks of both wurtzite and clays.

2.2. Texture and Morphology

Table 2 presents the specific surface areas (S_{BET}) of the different samples, ranging from 30 to 325 m^2/g. The Bare Clay sample has a relatively low specific surface area (45 m^2/g), which increases slightly when Cu^{2+} ions are intercalated (55 m^2/g). This increase comes from the insertion of the cations in the smectite network [28]; indeed, this insertion is observed in the XRD patterns (Figure 1) with the spread of the peak around 5°. The pure TiO_2 sample presents an S_{BET} value equal to 180 m^2/g, in agreement with literature data [29]. When the clay is modified with TiO_2, S_{BET} increases to 325 and 240 m^2/g for Clay/TiO_2 and Clay/TiO_2/Cu^{2+} samples, respectively. This is logical, as these composite materials are produced with nanospheres of TiO_2, which have high specific surface area. They can also enter the clay network to expand the material and thus increase its specific surface area. The pure ZnO sample presents a low S_{BET} value (30 m^2/g). When clay is modified with ZnO, the specific surface area increases for Clay/ZnO sample (125 m^2/g), but it stays relatively low for Clay/ZnO/Cu^{2+} (50 m^2/g). The increased surface area of the Clay/ZnO sample could come from an insertion of some ZnO particles inside the clay network.

Table 2. Specific surface areas of samples.

Sample	Specific Surface Area (m^2/g) ± 5
Bare Clay	45
Clay/Cu^{2+}	55
Pure TiO_2	180
Clay/TiO_2	325
Clay/Cu^{2+}/TiO_2	240
Pure ZnO	30
Clay/ZnO calcine à 300 °C	125
Clay/Cu^{2+}/ZnO	50

Concerning the nitrogen adsorption–desorption isotherms, two different types are observed between all samples: (i) type I isotherm, with a sharp increase at low pressure followed by a plateau corresponding to microporous solid; and (ii) type IV isotherm, characterized by a broad hysteresis at high pressure (mesoporous solid). Samples containing TiO_2 have type I isotherms, and the other samples have type IV isotherms. As an example, the isotherms of Bare Clay and Clay/TiO_2 samples are plotted in Figure 3. The other isotherms are represented in Figures S1 and S2 in the Supplementary Materials.

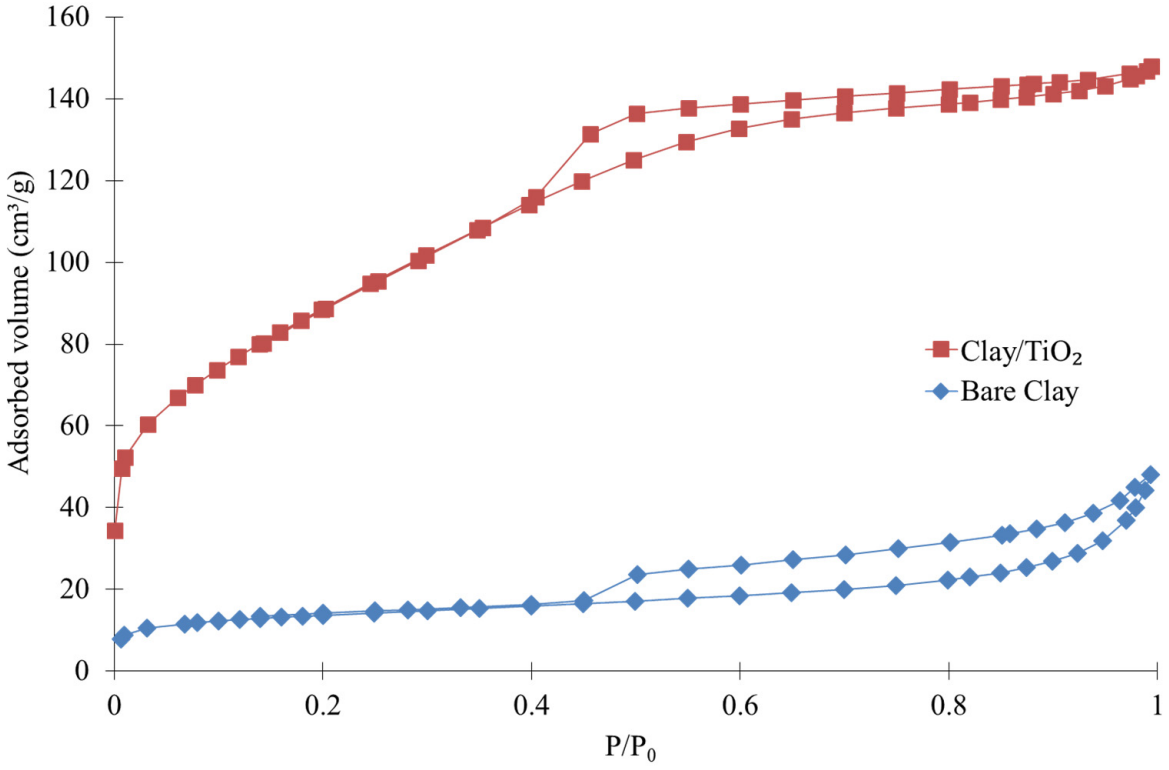

Figure 3. Nitrogen adsorption–desorption isotherms for (♦) Bare Clay and (■) Clay/TiO_2 samples.

SEM pictures of several samples are presented in Figure 4 for Bare Clay, Clay/TiO_2, and Clay/ZnO at two different magnifications. Bare Clay and Clay/ZnO samples have a similar aspect (Figure 4a,c), with large, granular powder, while the Clay/TiO_2 powder is finely dispersed (Figure 4b). These observations are in agreement with the higher specific surface area of Clay/TiO_2 and Clay/TiO_2/Cu^{2+} samples, characteristic of smaller hybrid particles and resulting in smaller voids between particles. This finely dispersed aspect comes from the TiO_2 nanoparticles, which are very small (5–10 nm), as observed in the TEM pictures of pure TiO_2 samples (Figure 5a). Contrarily, the pure ZnO sample has larger

particles (Figure 5b), indicating that the composite material with clay is more similar to the Bare Clay.

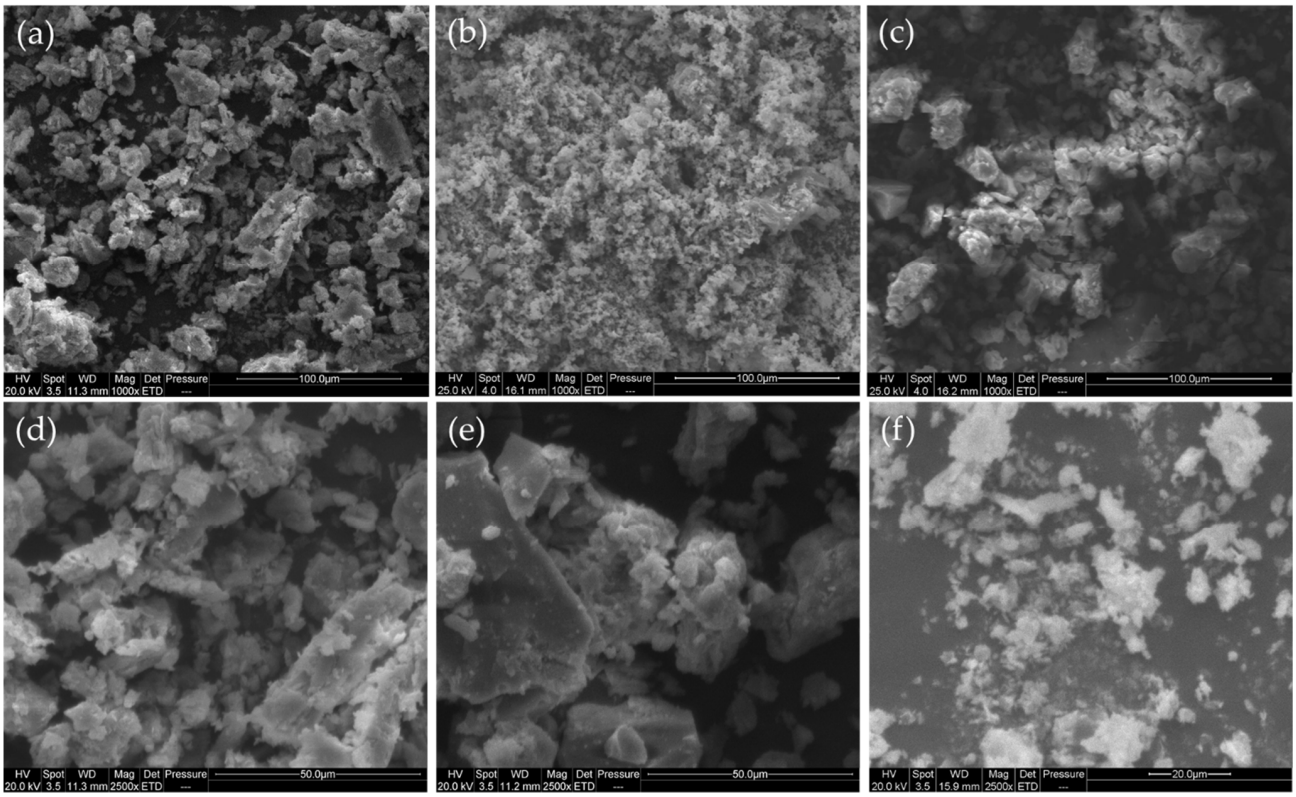

Figure 4. SEM pictures of (**a**) Bare Clay, (**b**) Clay/TiO_2, and (**c**) Clay/ZnO samples at 1000× magnification; (**d**) Bare Clay, (**e**) Clay/TiO_2, and (**f**) Clay/ZnO) at 2500× magnification.

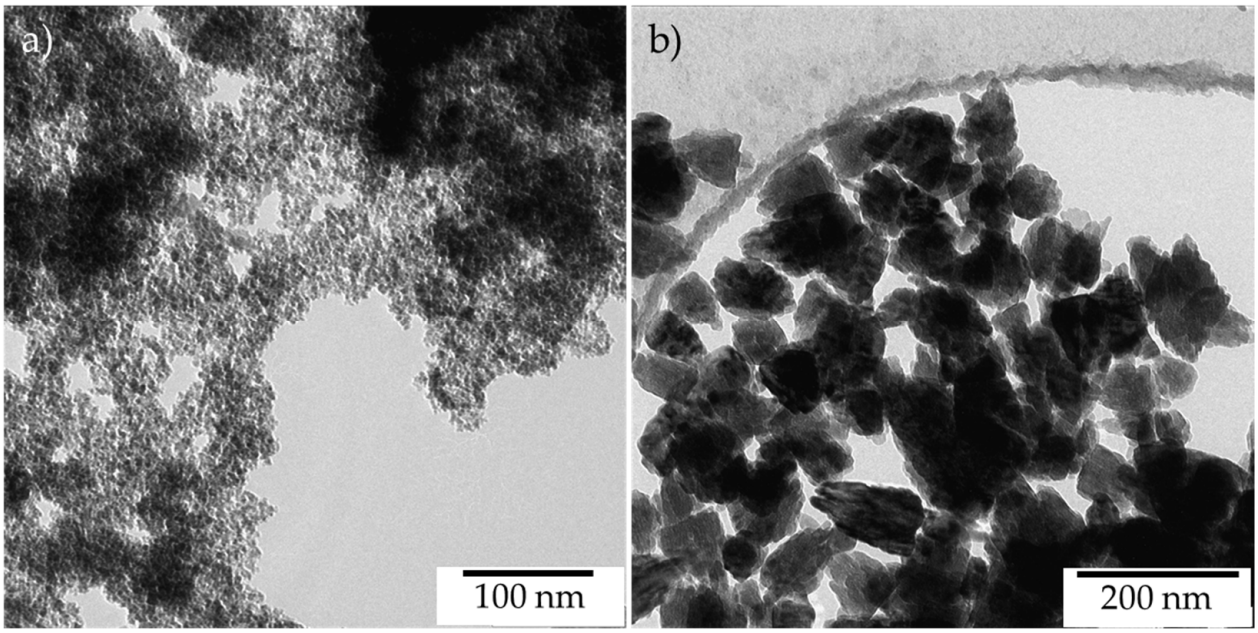

Figure 5. TEM pictures of (**a**) pure TiO_2 and (**b**) pure ZnO.

The samples with Cu^{2+} (Clay/Cu^{2+}, Clay/TiO_2/Cu^{2+} and Clay/ZnO/Cu^{2+}) have similar aspects and are represented in Supplementary Figure S3.

ICP results (Table 1) confirmed the presence of the semiconductor materials in the composite materials.

2.3. Adsorption Study

The experimental results of fluorescein adsorption are transformed with the following equation to determine the amount of FL adsorbed per g of clay (q_e):

$$q_e = \frac{(C_0 - C_e) * V}{W} \quad (1)$$

where C_0 and C_e are the initial and equilibrium liquid-phase concentrations of FL (mg_{FL} L^{-1}), respectively; V is the volume of the FL solution (L); and W is the mass of clay used (g_C).

q_e in function of C_e is represented in Figure 6a after 6 h of adsorption for Bare Clay and Clay/Cu^{2+} samples. Similar curves are obtained for both samples; indeed, they have similar specific surface areas (Table 2).

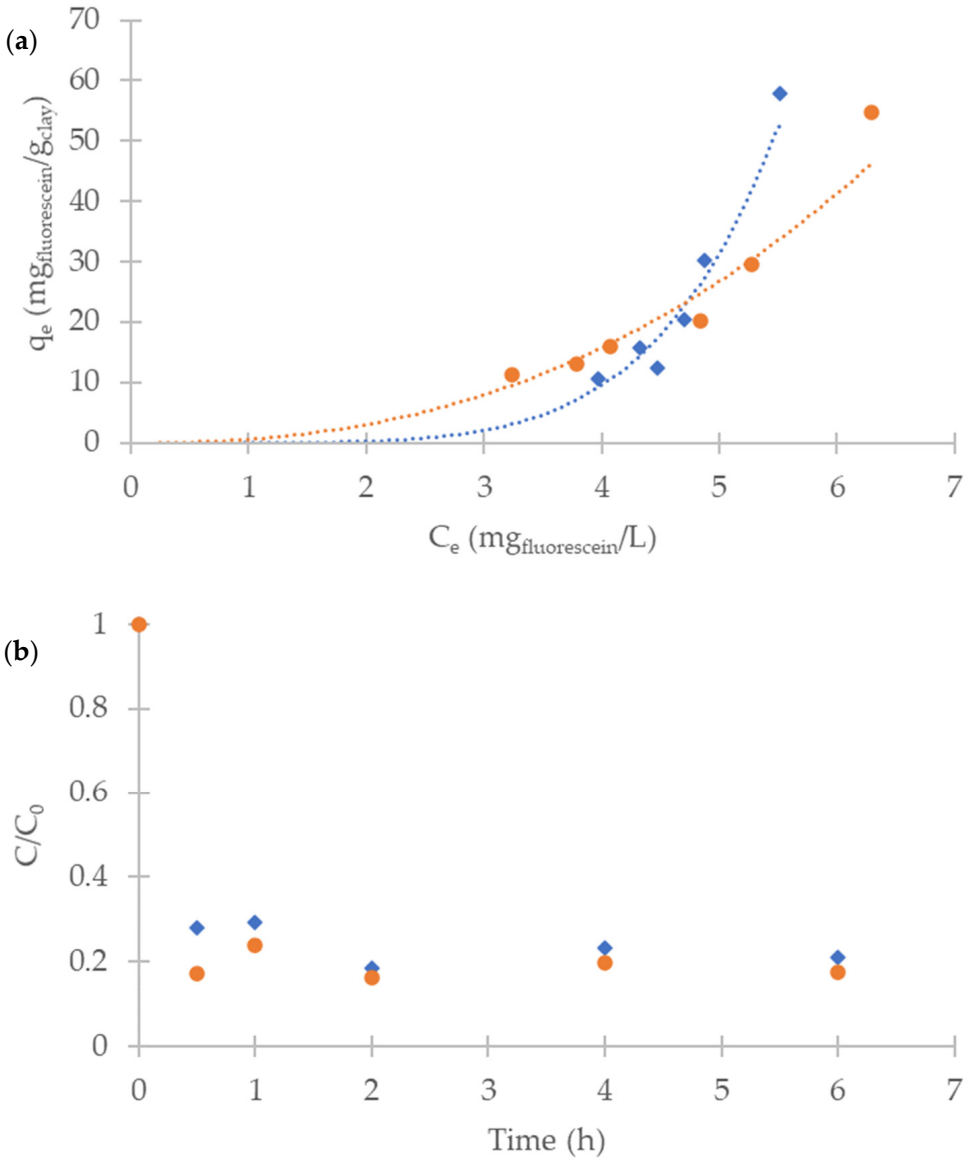

Figure 6. (**a**) Experimental fluorescein adsorption experiment representing the amount of FL adsorbed per g of clay in function of the equilibrium liquid-phase concentrations of FL after 6 h adsorption tests for the 6 different concentrations of powder samples for (♦) Bare Clay and (•) Clay/Cu^{2+} samples. (**b**) C/C_0 evolution with time for 30 mg concentrations of powder samples for (♦) Bare Clay and (•) Clay/Cu^{2+}.

In Figure 6b, the evolution of the FL concentration (C/C_0) with time is represented for Bare Clay and Clay/Cu^{2+} with 30 mg concentrations of powder samples. After 0.5 h of the experiment, more than 75% of FL were adsorbed for both samples (Figure 6b) and the concentration did not decrease much after 6 h; thus, the equilibrium was reached.

An example of the FL UV-visible spectrum is given in Figure S4 in the Supplementary Materials.

The PNP adsorption study shows that PNP is not adsorbed on the clay. Indeed, the concentration in solution remains constant with time. The removal of this kind of pollutant requires photocatalytic properties.

2.4. Photocatalytic Activity

As observed in the previous section, the clay can adsorb some pollutants such as dye, but it is not efficient to adsorb, for instance, PNP. Therefore, the clay was modified with photocatalysts to degrade molecules that cannot be efficiently adsorbed. Adsorption experiments in the dark (to avoid an interaction with room light which can activate the photocatalytic materials) were performed on all eight samples in contact with PNP for 8 h. No change in the PNP concentration was observed, showing that none of the samples adsorb the PNP molecule.

The photocatalytic property was evaluated on the PNP degradation under UVA illumination after 8 h of exposure (Figure 7a). An example of the PNP UV-visible spectrum is given in Figure S5 in the Supplementary Materials.

The Bare Clay and Clay/Cu^{2+} samples originally had no photocatalytic properties. However, such properties were attained after treatment with either TiO_2 or ZnO. PNP was degraded from 45% to 92% according to the samples. Clay/ZnO/Cu^{2+} is the most efficient material, with PNP degradation of 92%. The pure TiO_2 and ZnO materials reached 100% PNP degradation, as observed in previous studies [18,19].

For the same amount of semiconductor material (TiO_2 or ZnO), the ZnO-modified clay is more efficient than the TiO_2-modified one. As previously observed [18,31], ZnO materials have better activity than TiO_2, due to fewer recombinations of photogenerated species. The addition of Cu^{2+} ions increases the photoactivity due to an additional photo-Fenton effect that improves the PNP degradation [32]. Indeed, Cu^{2+} ions can react with water when exposed to UV radiation to produce additional $^{\bullet}OH$ radicals [32]. These radicals can degrade the organic molecules and thus enhance the photoactivity [32]. The equation of Cu^{2+} photo-Fenton effects is the following [32]:

$$Cu^{2+} + H_2O + h\nu \rightarrow Cu^{+} + {}^{\bullet}OH + H^{+}$$

where h is the Planck constant (6.63×10^{-34} J.s) and ν is the light frequency (Hz).

For the two best composite materials (Clay/TiO_2/Cu^{2+} and (•) Clay/ZnO/Cu^{2+}), the evolution of the PNP degradation over time is presented in Figure 7b. The evolution of the degradation is linear; then, the degradation is first order.

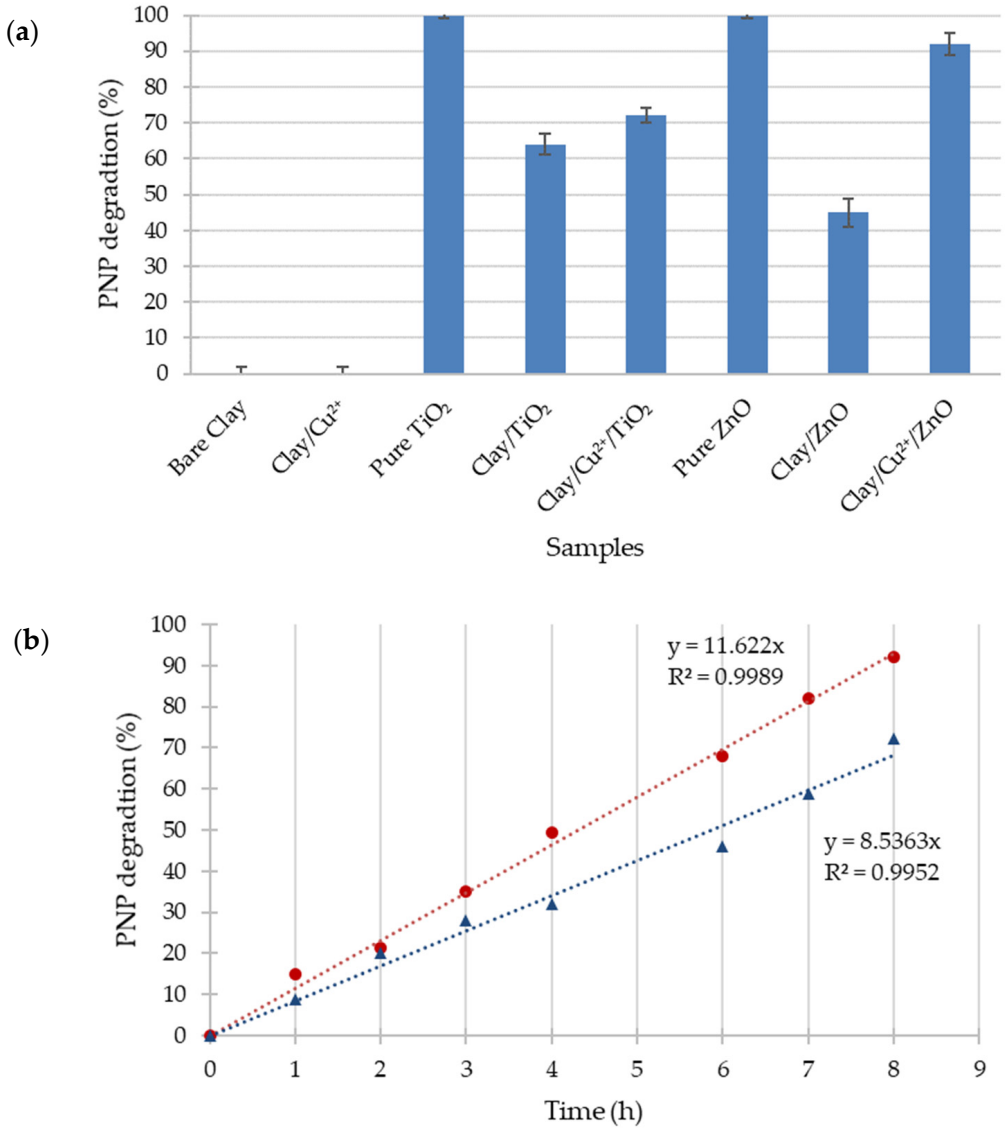

Figure 7. (**a**) PNP degradation (%) under UVA illumination for 8 h with all samples and (**b**) PNP degradation evolution over 8 h for the two best composite samples, (▲) Clay/TiO_2/Cu^{2+} and (●) Clay/ZnO/Cu^{2+}.

3. Materials and Methods

3.1. Description of the Clay and Modification with Cu^{2+} Ions

3.1.1. Presentation of the Clay

The clay material was whitish in color, sampled at 20 cm depth. The UTM coordinates of the sampling were north 5°06′08.3″ and east 10°17′28.0″, at an altitude of 1423 m. These coordinates corresponded to Mont Batcha, commonly called Bakotcha, in the district of Bana (West Cameroon). This region has an equatorial climate, characterized by average annual rainfall of 1300–2500 mm and a mean annual temperature of 21.23 °C [33]. The vegetation is highly anthropogenized post-forestry savannah with remains of a persisting semi-deciduous forest in areas of difficult accessibility [34]. The dominant soil types are red ferralitic soils, associated with brunified and hydromorphic soils [35]. The sampled clay was air-dried in the laboratory to a constant weight before grinding and sieving in a 160 µm diameter sieve.

3.1.2. Modification of Clay with Ions Cu^{2+} or Interfoliar Cation Exchange

This treatment does not destroy the structure of the clay material and it allows the insertion of ions (as shown in Figure 2). We used the following reagents: copper (II) sulfate pentahydrate (>98.0% from LabChem, Gauteng, South Africa), barium sulfate (99%, pure, from Laboratoriumdiscounter), clay powder (>160 µm), and distilled water.

In order to produce a homogeneous cation exchange, 50 g of clay was mixed under stirring in 0.1 M of $CuSO_4$ solution for 4 h. After 2 h rest, the supernatant was poured, and the agitation was repeated with a new solution of 0.1 M of $CuSO_4$. This operation was repeated twice, and excess Cu^{2+} and $SO_4{}^{2-}$ ions were washed with distilled water until the Baryum test (precipitation test) became negative. The homoionic Cu^{2+} clay material was then oven-dried at 110 °C overnight.

3.2. Synthesis of Pure TiO_2 and ZnO Photocatalysts

3.2.1. ZnO Sample

Pure zinc oxide powders were synthesized by the sol-gel method following Benhebal et al. [30,36]. The reagents were zinc acetate dihydrate (≥98%), oxalic acid dihydrate (≥99%), and absolute ethanol (ACS grade). They were obtained from BIOCHEM, Chemopharma (Cosne-Cours-sur-Loire, France), of analytical grade, and used directly as purchased.

Zinc acetate dihydrate (10.98 g) was treated with ethanol (300 mL) at 60 °C. The salt was completely dissolved in about 30 min. Oxalic acid dihydrate (12.6 g) was dissolved in ethanol (200 mL) at 60 °C for 30 min. The oxalic acid solution was added slowly, with stirring, to the hot ethanolic zinc solution, and the mixture was stirred for 90 min at 50 °C. The resulting gel was placed in an oven at 80 °C for 24 h. The product was calcined at 400 °C for 4 h. The color of the pure ZnO powder was white.

3.2.2. TiO_2 Sample

Pure titanium oxide powders were synthesized by the sol-gel method of Mahy et al. [32]. The reagents used were titanium (IV) tetraisopropoxide (TTIP > 97%, Sigma-Aldrich, St. Louis, MO, USA), nitric acid (HNO_3, 65%, Merck, Darmstadt, Germany), isopropanol (IsoP, 99.5%, Acros, Hull, Belgium), and distilled water.

Nitric acid HNO_3 (65%, Merck) was used to acidify 250 mL of distilled water to pH 1. Then, 15 mL of TTIP was added to 15 mL of isopropanol (IsoP), and the mixture was stirred for 30 min at room temperature. The resulting solution of TTIP + IsoP mixture was added to acidified water under controlled stirring. The liquid was left under stirring for 4 h at 80 °C. The obtained sol had a clear blue color. Then, the sol was dried for 10 h under an ambient air flow to obtain a xerogel. The powders were dried at 100 °C for 1 h and a pure TiO_2 powder of yellowish-white color was obtained [32].

3.3. Synthesis of Hybrid Clay/Photocatalyst Materials

3.3.1. Clay/ZnO Materials

For the preparation of modified clays with ZnO, the procedure was similar as for pure ZnO material. However, when the oxalic acid solution was added slowly with stirring to the hot ethanolic zinc solution, 10 g of clay materials was added, and the mixture was left under stirring for 90 min at 50 °C. The resulting gel was placed in an oven at 80 °C for 24 h. The product was calcined at 400 °C for 4 h. The ZnO-modified clay powders were light gray in color.

3.3.2. Clay/TiO_2 Materials

For the preparation of hybrid clay/TiO_2 powders, the same protocol of preparation of pure TiO_2 powder was used with the addition of 10 g of clay material. When the mixture TTIP + IsoP was obtained, it was added to acidified water under controlled stirring and the liquid was left under stirring for 4 h at 80 °C. To the obtained sol, clear blue in color, 10 g of clayey material was added and left under stirring for 2 h. The soil was dried for 24 h

under an ambient air flow. The powders were dried at 100 °C for 1 h and hybrid clay/TiO_2 powders were obtained.

3.4. Characterization of Samples

The actual composition of the bare and modified clays was determined by inductively coupled plasma–atomic emission spectroscopy (ICP–AES), equipped with an ICAP 6500 THERMO Scientific device (Waltham, MA, USA). The mineralization is fully described in [32]; however, we used HF instead of HNO_3.

The crystallographic properties were observed through the X-ray diffraction (XRD) patterns recorded with a Bruker D8 Twin-Twin powder diffractometer (Bruker, Billerica, MA, USA) using Cu-Kα radiation.

The specific surface area of samples was determined by nitrogen adsorption–desorption isotherms in an ASAP 2420 multi-sampler volumetric device from Micromeritics (Norcross, GA, USA) at 77 °K.

SEM micrographs were obtained using a Jeol-JSM-6360LV microscope (Tokyo, Japan) under high vacuum at an acceleration voltage of 20 kV.

Transmission electron microscopy was performed on the LEO 922 OMEGA Energy Filter Transmission Electron Microscope (Zeiss, Oberkochen, Germany) operating at 120 kV. Sample preparation consisted of dispersing a few milligrams of each sample in water, using sonication. Then, a few drops of the supernatant were placed on a holed carbon film deposited on a copper grid (CF-1.2/1.3-2 Cu-50, C-flat™, Protochips, Morrisville, NC, USA).

3.5. Adsorption Experiments

Concerning the adsorption experiments, only the Bare Clay and Clay/Cu^{2+} samples were assessed. The adsorption of two types of model pollutants, fluorescein (FL) and p-nitrophenol (PNP), was tested. For an adsorption experiment, 6 vials were prepared containing 5, 10, 15, 20, 25, and 30 mg of powder clay and 20 mL of pollutant solution in water. The samples were under continuous stirring. The remaining concentration in solution was evaluated every hour for 6 h with a Genesys 10S UV-Vis spectrophotometer (Thermo Scientific) after filtration with a syringe filter. The main absorption peaks were located at 317 and 485 nm for PNP and FL, respectively, as shown in Figures S4 and S5 in the Supplementary Materials. The initial concentration of FL was 6×10^{-5} M and 10^{-4} M for PNP.

3.6. Photocatalytic Experiments

The degradation of p-nitrophenol (PNP) was studied under UVA light (λ = 365 nm) to determine the photocatalytic activity of the synthesized material. The lamp was an Osram Sylvania, Blacklight-Bleu Lamp, F 18W/BLB-T8, considered as monochromatic at 365 nm.

Each sample was placed in a Petri dish with 20 mL of 10^{-4} M of PNP solution in water. The degradation of PNP was evaluated from absorbance measurements with a Genesys 10S UV-Vis spectrophotometer (Thermo Scientific) at λ = 317 nm. Previously, adsorption tests were performed in the dark (dark tests) to show whether PNP was adsorbed on the surface of samples. A blank test, consisting of irradiating the pollutant solution for 24 h in a Petri dish without any catalyst, showed that PNP concentration under UVA illumination remained constant. The Petri dishes with catalysts and pollutants were stirred on orbital shakers and illuminated for 8 h. Aliquots of PNP were sampled at 0, 4, and 8 h. The photocatalytic degradation was equal to the total degradation of PNP, taking the catalyst adsorption (dark test) into account. Each photocatalytic measurement was triplicated to assess the reproducibility of the data. In each box, the catalyst concentration was 1 g/L.

4. Conclusions

In this work, natural clays were used to remove pollutants from water by adsorption and photocatalysis processes. The approach was applied on smectite-rich Cameroon clays.

The clays were preliminarily treated with Cu^{2+} and then with semiconductors TiO_2 and ZnO to produce hybrid clays. The aim was to increase the depollution efficiency of these modified clayey materials by their photocatalytic properties. The protocol was controlled by XRD and ICP-AES measurements. The modified clays displayed an increase in their specific surface areas in comparison with natural clay properties. XRD confirmed the presence of crystalline TiO_2 and ZnO.

The adsorption experiments confirmed the bare clays can adsorb fluorescein, but they were not efficient on other pollutants, namely p-nitrophenol. The addition of semiconductor materials improved the degradation of the pollutants when exposed to UVA light. Photocatalytic experiments on PNP gave degradation levels of 70% to 90% after 8 h of exposition with the TiO_2- and ZnO-modified clays, respectively.

This study emphasizes the importance of composite clays to remove pollutants via adsorption and photocatalysis processes. Such approaches offer an opportunity, especially in developing countries, to use natural clay materials with slight modifications for water purification.

Supplementary Materials: The following are available online at https://www.mdpi.com/article/10.3390/catal12020148/s1, Figure S1: Nitrogen adsorption desorption isotherms for (♦) pure TiO_2 and (■) pure ZnO samples, Figure S2: Nitrogen adsorption desorption isotherms for (♦) Clay/Cu^{2+}, (▲) Clay/TiO_2/Cu^{2+}, (×) Clay/ZnO/Cu^{2+} and (■) Clay/ZnO samples, Figure S3: SEM pictures of (a) Clay/Cu^{2+}, (b) Clay/TiO_2/Cu^{2+} and (c) Clay/ZnO/Cu^{2+} samples at a 1000x magnification, Figure S4: FL UV/visible spectrum for (•) initial FL solution and (▲) after 6 h in adsorption experiment with bare Clay sample; Figure S5: PNP UV/visible spectrum for (•) initial PNP solution and (■) after 8 h in photocatalytic experiment with Clay/TiO_2 sample.

Author Contributions: Conceptualization, methodology, investigation, analysis, and writing, J.G.M., M.H.T.M. and S.D.L.; writing—original draft preparation, J.G.M., M.H.T.M. and S.D.L.; XRD characterizations analysis, M.H.T.M. and N.F.; adsorption experiments, J.G.M. and C.L.; supervision, funding acquisition, and project administration, E.D.W. and S.D.L. All the authors corrected the paper before submission and during the revision process. All authors have read and agreed to the published version of the manuscript.

Funding: This research was funded by PACODEL/University of Liège, bourse de mobilité doctorale.

Data Availability Statement: The raw/processed data required to reproduce these findings cannot be shared at this time as these data are part of an ongoing study.

Acknowledgments: J.G.M. and S.D.L. thank the Belgian National Funds for Scientific Research (F.R.S.-FNRS) for his postdoctoral fellowship and her senior associate researcher position, respectively. The authors thank the CARPOR platform of the University of Liège and its manager, Alexandre Léonard, for the nitrogen adsorption–desorption measurements.

Conflicts of Interest: The authors declare no conflict of interest.

References

1. Kemgang Lekomo, Y.; Mwebi Ekengoue, C.; Douola, A.; Fotie Lele, R.; Christian Suh, G.; Obiri, S.; Kagou Dongmo, A. Assessing Impacts of Sand Mining on Water Quality in Toutsang Locality and Design of Waste Water Purification System. *Clean. Eng. Technol.* **2021**, *2*, 100045. [CrossRef]
2. Auriol, M.; Filali-Meknassi, Y.; Dayal Tyagi, R. Présence et Devenir Des Hormones Stéroïdiennes Dans Les Stations de Traitement Des Eaux Usées. Occurrence and Fate of Steroid Hormones in Wastewater Treatment Plants. *Rev. Des Sci. L'eau* **2007**, *20*, 89–108.
3. Ekengoue, C.M.; Lele, R.F.; Dongmo, A.K. Influence De L'exploitation Artisanale Du Sable Sur La Santé Et La Sécurité Des Artisans Et L'environnement: Cas De La Carrière De Nkol'Ossananga, Région Du Centre Cameroun. *Eur. Sci. J. ESJ* **2018**, *14*, 246. [CrossRef]
4. Available online: Https://Minepded.Gov.Cm/Fr/ (accessed on 18 November 2021).
5. Nkoumbou, C.; Njopwouo, D.; Villiéras, F.; Njoya, A.; Yonta Ngouné, C.; Ngo Ndjock, L.; Tchoua, F.M.; Yvon, J. Talc Indices from Boumnyebel (Central Cameroon), Physico-Chemical Characteristics and Geochemistry. *J. Afr. Earth Sci.* **2006**, *45*, 61–73. [CrossRef]

6. Filice, S.; Bongiorno, C.; Libertino, S.; Compagnini, G.; Gradon, L.; Iannazzo, D.; la Magna, A.; Scalese, S. Structural Characterization and Adsorption Properties of Dunino Raw Halloysite Mineral for Dye Removal from Water. *Materials* **2021**, *14*, 3676. [CrossRef]
7. Jacques Richard, M. *Mineralogie et Proprietes Physico-Chimiques des Smectites de Bana et Sabga (Cameroun). Utilisation Dans La Décoloration d' Une Huile Végétale Alimentaire*; Université de Liège: Liège, Belgique, 2013.
8. Djoufac Woumfo, E.; Elimbi, A.; Panczer, G.; Nyada Nyada, R.; Njopwouo, D. Physico-Chemical and Mineralogical Characterization of Garoua Vertisols (North Cameroon). *Ann. Chim.* **2006**, *31*, 75–90.
9. Léonard, G.L.-M.; Malengreaux, C.M.; Mélotte, Q.; Lambert, S.D.; Bruneel, E.; van Driessche, I.; Heinrichs, B. Doped Sol–Gel Films vs. Powders TiO_2: On the Positive Effect Induced by the Presence of a Substrate. *J. Environ. Chem. Eng.* **2016**, *4*, 449–459. [CrossRef]
10. Parsons, S. *Advanced Oxidation Processes for Water and Wastewater Treatment*; IWA Publishing: London, UK, 2004; ISBN 1843390175.
11. Bhowmick, M.; Semmens, M.J. Ultraviolet Photooxidation for the Destruction f VOCs in Air. *Wat. Res.* **1994**, *28*, 2407–2415. [CrossRef]
12. Ikehata, K.; El-Din, M.G. Aqueous Pesticide Degradation by Hydrogen Peroxide/Ultraviolet Irradiation and Fenton-Type Advanced Oxidation Processes: A Review. *J. Environ. Eng. Sci.* **2006**, *5*, 81–135. [CrossRef]
13. Filice, S.; Fiorenza, R.; Reitano, R.; Scalese, S.; Sciré, S.; Fisicaro, G.; Deretzis, I.; la Magna, A.; Bongiorno, C.; Compagnini, G. TiO2 Colloids Laser-Treated in Ethanol for Photocatalytic H2 Production. *ACS Appl. Nano Mater.* **2020**, *3*, 9127–9140. [CrossRef]
14. Goncharuk, V.V.; Potapchenko, N.G.; Savluk, O.S.; Kosinova, V.N.; Sova, A.N. Study of Various Conditions for O3/UV Disinfection of Water. *Khimiya Tecknol. Vody* **2003**, *25*, 487–496.
15. Drogui, P.; Blais, J.-F.; Mercier, G. Review of Electrochemical Technologies for Environmental Applications. *Recent Pat. Eng.* **2007**, *1*, 257–272. [CrossRef]
16. Douven, S.; Mahy, J.G.; Wolfs, C.; Reyserhove, C.; Poelman, D.; Devred, F.; Gaigneaux, E.M.; Lambert, S.D. Efficient N, Fe Co-Doped TiO_2 Active under Cost-Effective Visible LED Light: From Powders to Films. *Catalysts* **2020**, *10*, 547. [CrossRef]
17. Mahy, J.G.; Wolfs, C.; Vreuls, C.; Drot, S.; Dircks, S.; Boergers, A.; Tuerk, J.; Hermans, S.; Lambert, S.D. Advanced Oxidation Processes for Waste Water Treatment: From Lab-Scale Model Water to on-Site Real Waste Water. *Environ. Technol.* **2021**, *42*, 3974–3986. [CrossRef] [PubMed]
18. Mahy, J.G.; Lejeune, L.; Haynes, T.; Body, N.; de Kreijger, S.; Elias, B.; Marcilli, R.H.M.; Fustin, C.A.; Hermans, S. Crystalline ZnO Photocatalysts Prepared at Ambient Temperature: Influence of Morphology on p-Nitrophenol Degradation in Water. *Catalysts* **2021**, *11*, 1182. [CrossRef]
19. Bodson, C.J.; Heinrichs, B.; Tasseroul, L.; Bied, C.; Mahy, J.G.; Man, M.W.C.; Lambert, S.D. Efficient P- and Ag-Doped Titania for the Photocatalytic Degradation of Waste Water Organic Pollutants. *J. Alloys Compd.* **2016**, *682*, 144–153. [CrossRef]
20. Cheng, T.; Gao, H.; Liu, G.; Pu, Z.; Wang, S.; Yi, Z.; Wu, X.; Yang, H. Preparation of Core-Shell Heterojunction Photocatalysts by Coating CdS Nanoparticles onto Bi4Ti3O12 Hierarchical Microspheres and Their Photocatalytic Removal of Organic Pollutants and Cr(VI) Ions. *Colloids Surf. A Physicochem. Eng. Asp.* **2022**, *633*, 127918. [CrossRef]
21. Xiong, S.; Yin, Z.; Zhou, Y.; Peng, X.; Yan, W.; Liu, Z.; Zhang, X. The Dual-Frequency (20/40 KHz) Ultrasound Assisted Photocatalysis with the Active Carbon Fiber-Loaded Fe3+-TiO2 as Photocatalyst for Degradation of Organic Dye. *Bull. Korean Chem. Soc.* **2013**, *34*, 3039–3045. [CrossRef]
22. Li, Y.; Li, M.; Xu, P.; Tang, S.; Liu, C. Efficient Photocatalytic Degradation of Acid Orange 7 over N-Doped Ordered Mesoporous Titania on Carbon Fibers under Visible-Light Irradiation Based on Three Synergistic Effects. *Appl. Catal. A Gen.* **2016**, *524*, 163–172. [CrossRef]
23. Tang, N.; Li, Y.; Chen, F.; Han, Z. In Situ Fabrication of a Direct Z-Scheme Photocatalyst by Immobilizing CdS Quantum Dots in the Channels of Graphene-Hybridized and Supported Mesoporous Titanium Nanocrystals for High Photocatalytic Performance under Visible Light. *RSC Adv.* **2018**, *8*, 42233–42245. [CrossRef]
24. Lin, X.; Li, M.; Li, Y.; Chen, W. Enhancement of the Catalytic Activity of Ordered Mesoporous TiO_2 by Using Carbon Fiber Support and Appropriate Evaluation of Synergy between Surface Adsorption and Photocatalysis by Langmuir-Hinshelwood (L-H) Integration Equation. *RSC Adv.* **2015**, *5*, 105227–105238. [CrossRef]
25. Ndé, H.S.; Tamfuh, P.A.; Clet, G.; Vieillard, J.; Mbognou, M.T.; Woumfo, E.D. Comparison of HCl and H_2SO_4 for the Acid Activation of a Cameroonian Smectite Soil Clay: Palm Oil Discolouration and Landfill Leachate Treatment. *Heliyon* **2019**, *5*, e02926. [CrossRef] [PubMed]
26. Olad, A. 7 Polymer/Clay Nanocomposites. In *Advances in Diverse Industrial Applications of Nanocomposites*; Reddy, B., Ed.; InTechOpen: London, UK, 2011.
27. Yeop Lee, S.; Jin Kim, S. Expansion of smectite by hexadecyltrimethylammonium. *Clays Clay Miner.* **2002**, *50*, 435–445.
28. Theo Kloprogge, J.; Komarnenl, S.; Amonetie, J.E. Synthesis of smectite clay minerals: A critical review. *Clays Clay Miner.* **1999**, *47*, 529–554. [CrossRef]
29. Mahy, J.G.; Léonard, G.L.-M.; Pirard, S.; Wicky, D.; Daniel, A.; Archambeau, C.; Liquet, D.; Heinrichs, B. Aqueous Sol-Gel Synthesis and Film Deposition Methods for the Large-Scale Manufacture of Coated Steel with Self-Cleaning Properties. *J. Sol-Gel Sci. Technol.* **2017**, *81*, 27–35. [CrossRef]
30. Benhebal, H.; Chaib, M.; Leonard, A.; Lambert, S.D.; Crine, M. Photodegradation of Phenol and Benzoic Acid by Sol-Gel-Synthesized Alkali Metal-Doped ZnO. *Mater. Sci. Semicond. Process.* **2012**, *15*, 264–269. [CrossRef]

31. Léonard, G.L.-M.; Pàez, C.A.; Ramírez, A.E.; Mahy, J.G.; Heinrichs, B. Interactions between Zn2+ or ZnO with TiO_2 to Produce an Efficient Photocatalytic, Superhydrophilic and Aesthetic Glass. *J. Photochem. Photobiol. A Chem.* **2018**, *350*, 32–43. [CrossRef]
32. Mahy, J.G.; Lambert, S.D.; Léonard, G.L.M.; Zubiaur, A.; Olu, P.Y.; Mahmoud, A.; Boschini, F.; Heinrichs, B. Towards a Large Scale Aqueous Sol-Gel Synthesis of Doped TiO_2: Study of Various Metallic Dopings for the Photocatalytic Degradation of p-Nitrophenol. *J. Photochem. Photobiol. A Chem.* **2016**, *329*, 189–202. [CrossRef]
33. Geology, K.G. Geology, Petrology and Geochemistry of the Tertiary Bana Volcano-Plutonic Complex, West Cameroon, Central Africa. Ph.D. Thesis, Kobe University, Kobe, Japan, 2004.
34. Aboubakar, Y. *Etude Pédologique Du Terroir de Bana*; ORSTOM: Yaounde, Cameroon, 1974.
35. Bi Tra, T. *Etude Pédologique et Cartographique à L'échelle 1/50000 d'un Secteur de L'ouest-Cameroun (Région de Bafang)*; ORSTOM: Yaounde, Cameroon, 1980.
36. Benhebal, H.; Chaib, M.; Crine, M.; Leonard, A.; Lambert, S.D. Photocatalytic Decolorization of Gentian Violet with Na-Doped (SnO_2 and ZnO). *Chiang Mai J. Sci.* **2016**, *43*, 584–589.

Journal of Sol-Gel Science and Technology
https://doi.org/10.1007/s10971-022-06005-6

ORIGINAL PAPER: SOL-GEL AND HYBRID MATERIALS FOR CATALYTIC, PHOTOELECTROCHEMICAL AND SENSOR APPLICATIONS

Hybrid clay-based materials for organic dyes and pesticides elimination in water

Marlène Huguette Tsaffo Mbognou[1,2,3] · Stéphanie D. Lambert[1] · Joachim Caucheteux[1] · Antoine Farcy[1] · Christelle Alié[1] · Nathalie Fagel[4] · Emmanuel Djoufac Woumfo[2] · Julien G. Mahy[1,5]

Received: 28 September 2022 / Accepted: 19 November 2022

Abstract

Natural clay, extracted from Cameroon, was modified by ion exchange to produce 4 different clays. These latter were modified with photocatalytic semiconductor like ZnO to produce efficient hybrid materials for pollutant removal in water. ZnO was synthesized by the soft sol–gel chemistry method. The results showed that the clay belonged to the smectite family and was composed of different crystalline phases. When the hybrid materials were produced, mix crystalline patterns were obtained with both smectite and ZnO wurtzite phases. The ICP-AES analysis showed that similar ratio between ZnO and clay were obtained for the 4 hybrid materials (30 wt% of ZnO and 70 wt% of clay). The SEM observation of the samples had shown that the hybrid materials had the clay structure as skeletal structure (sheet like structure) with the ZnO spherical materials grafted at the surface, giving a good exposure to light to maintain photocatalytic property. Then, the pollutant removal property of the samples was evaluated on three different model pollutants: p-nitrophenol (PNP), Malachite green (MG) and Diamant brilliant violet (DBV). On PNP, no adsorption was observed, and photocatalytic property was necessary to eliminate this molecule. With the best hybrid material (Clay/Cu^{2+}/ZnO), 80% of PNP degradation was observed after 6 h of illumination. On MG and DBV, similar behavior was observed. Indeed, the clays and three out of four hybrid materials adsorbed completely both pollutant after 2 h of contact. Only pure ZnO and Clay/ZnO needed illumination to degrade completely both molecules. This study showed the possibility to obtain very efficient hybrid materials for pollutant removal in water with the use of inexpensive natural clay modified with a low amount of photocatalytic material (ZnO around 30 wt.%).

✉ Julien G. Mahy
julien.mahy@uliege.be

[1] Department of Chemical Engineering – Nanomaterials, Catalysis & Electrochemistry, University of Liège, B6a, Quartier Agora, Allée du six Août 11, 4000 Liège, Belgium

[2] Laboratoire de Physico-chimie des matériaux minéraux, University of Yaounde I, 337 Yaounde, Cameroon

[3] Institute of Geological and Mining Research (IRGM), 4110 Yaounde, Cameroon

[4] Laboratoire Argiles, Géochimie et Environnements sédimentaires (AGEs), Department of Geology, Faculty of Sciences, University of Liège, B-4000 Liège, Belgium

[5] Institut National de la Recherche Scientifique (INRS), Centre-Eau Terre Environnement, Université du Québec, 490, Rue de la Couronne, Québec, QC G1K 9A9, Canada

Published online: 15 December 2022

Graphical abstract

In this work, hybrid clay-ZnO materials are synthesized and produce a specific morphology with a clay skeleton and the ZnO nanoparticles at the surface. These materials are very efficient for pollutant removal in water thanks to the combine processes of adsorption and photocatalysis.

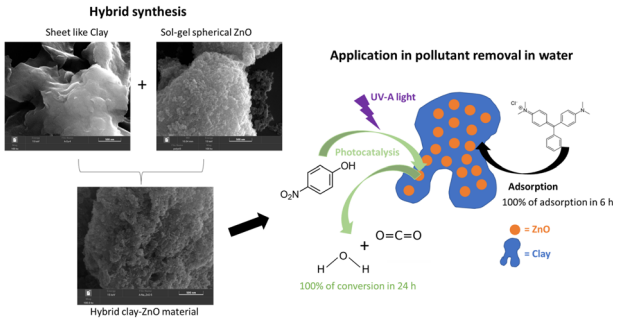

Keywords Adsorption · Photocatalysis · Smectite · ZnO · Green chemistry · Sol–gel

Highlight

- Natural clay was modified by ion exchange to produce 4 different clays.
- These clays were modified with ZnO to produce hybrid materials for pollutant removal in water.
- The hybrid materials had the clay structure with the ZnO spherical materials grafted at the surface.
- *p*-nitrophenol (PNP), Malachite green (MG) and Diamant brilliant violet (DBV) were used as model pollutants.
- All three molecules can be removed from the water either by adsorption and/or photocatalysis.

1 Introduction

In recent decades, environmental pollution by the excessive presence of bio-refractory organic pollutants in wastewater from domestic uses or industries is a serious environmental scourge [1]. Some of these compounds are recognized as capable of causing carcinogenic and mutagenic effects and interfering with the hormonal system of living beings. Among the pollutants commonly detected in industrial discharges are organic dyes, organochlorines, phenolic compounds, etc. [2]. These compounds are the cause of numerous disturbances of aquatic fauna and constitute a risk for human health [3]. Faced with this situation, several countries have been forced to set strict legislative and normative constraints towards manufacturers for the protection of the environment. Thus, the major challenge for industries is to find an effective and inexpensive technique to reduce the level of pollution to the threshold accepted by the legislation before any discharge into the environment. Attention was subsequently focused on the use of new adsorbents based on abundant natural materials. This is the case for clays [4]. As a raw material, clay is a mixture of clay minerals and crystalline impurities in the form of rock debris of infinitely diverse compositions. The interest given in recent years to the study of clays by many laboratories around the world [5] is justified by their abundance in nature, the importance of the specific surfaces they develop [6], the presence of surface charges and especially the exchangeability of the interfoliar cations. The latter, also called mobile or compensating cations, are the main elements responsible for hydration, swelling and plasticity, and they give these clays hydrophilic properties. Existing conventional techniques such as adsorption, coagulation/flocculation, and biological treatment are increasingly ineffective in the face of the complexity of effluents [7]. Moreover, these techniques require an additional investment, for the treatment of liquid/solid concentrate formed.

To overcome these problems, efficient and ecological treatment strategies have been developed. Among which is the application of advanced oxidation processes (AOPs), which are based on the production of hydroxyl radicals, very reactive and strongly oxidizing species. These processes include heterogeneous photocatalysis under UV and/or visible light [8–11], homogeneous phase chemical oxidation processes: H_2O_2/Fe^{2+} (Fenton's reagent) [12], O_3/OH^- (ozonation) [13]; photochemical processes: UV only, H_2O_2/UV, O_3/UV, H_2O_2/Fe^{3+}/UV (photo-Fenton) [12, 14]; electrochemical processes [15, 16] (anodic oxidation, electro-Fenton) etc… However, although effective for the mineralization of most organic pollutants, these processes require an external energy input (electric or magnetic) and consequently a relatively high cost for a strong mineralization of the pollutant. Hybrid materials having multiple pollutant removal properties can be of great interest to treat this pollution [17–19].

In this work, the main goal is to produce hybrid materials made of good adsorbent materials (clay) and efficient photocatalyst (ZnO) at low price. Indeed, the goal is to develop a hybrid material that can depollute water either with adsorption or photocatalytic processes. To reach this goal, natural clay extract from Cameroon will be used and also modified by ion exchange process to increase their adsorption properties. The ZnO, introduced in clay, is synthesized by a green sol–gel process and the amount added in the hybrid material is limited to 30 wt.% to conserve low prices for these materials. The hybrid materials and the corresponding pure clay and pure ZnO samples are characterized to determine their composition and morphology. Then, the pollutant removal property of these samples is evaluated on model water polluted with three different molecules: the *p*-nitrophenol (PNP), the malachite green (MG) and the Diamant brilliant violet (DBV). PNP and MG are commonly found in pesticide [20, 21] and MG and DBV are used as organic dye [21, 22].

2 Materials and methods

2.1 Natural clays

Natural clays were extracted from Bana in Cameroon, details were given in [23]. After extraction, the clays were dried to a constant weight. Then some part was modified to insert Cu^{2+}, Na^{+} or Zn^{2+} ions.

2.1.1 Copper ions insertion

The protocol is detail in [23] and summarized below.

The reagents used are the following: copper (II) sulfate pentahydrate (>98.0%, Sigma-Aldrich), barium sulfate (99%, Sigma-Aldrich), clay powder (>160 µm), distilled water [23].

In order to produce a homogeneous cation exchange, 50 g of clay was mixed under stirring in 0.1 M of $CuSO_4$ solution for 4 h. After 2 h at rest, the supernatant was poured, and the agitation was repeated with a new solution of 0.1 M of $CuSO_4$. This operation was repeated twice, and excess Cu^{2+} and SO_4^{2-} ions were washed with distilled water until the Baryum test (precipitation test) became negative. The homoionic Cu^{2+} clay material was then oven dried at 110 °C overnight [23].

2.1.2 Sodium ions insertion

The reagents used are the following: distilled water, sodium chloride (Dry Basis >99.5%, Fisher BioReagents), silver nitrate (99%, extra pure, Laboratorium discounter), clay powder (>160 µm).

Sodium homo-ionization allows to replace all exchangeable cations of various natures by only sodium cations. 100 g of clay material are treated with magnetic stirring for 72 h by a solution of NaCl 1 M. The material is dried at 100 °C for 24 h.

To ensure that the cation exchange reaction was effective, the dispersion of clay in the electrolyte solution was maintained under stirring for 4 h. After settling, the supernatant is removed, and the recovered solid is re-dispersed in the renewed salt solution. This operation has been repeated 4 times in order to achieve a complete cation exchange with Na^{+} ions. The excess of Na^{+} and Cl^{-} ions were washed with distilled water until the silver nitrate test (precipitation test) became negative. Indeed, when solution containing Cl^{-} ions is in contact with $AgNO_3$, a precipitate appears. If the test is negative, it proves that all Cl^{-} ions have been removed from the sample thanks to the washing step.

2.1.3 Zinc ions insertion

This treatment does not destroy the structure of the clay material and it allows the insertion of Zn ions. We used the following reagents: zinc (II) chloride (>97.0%, Laboratorium discounter), silver nitrate (99%, extra pure, Laboratorium discounter), clay powder (>160 µm), and distilled water. In order to produce a homogeneous cation exchange, 50 g of clay was mixed under stirring in 0.1 M of $ZnCl_2$ solution for 4 h. After 2 h at rest, the supernatant was poured, and the agitation was repeated with a new solution of 0.1 M of $ZnCl_2$. This operation was repeated twice, and excess Zn^{2+} and Cl^{-} ions were washed with distilled water until the silver nitrate test (precipitation test) became negative. Indeed, when solution containing Cl^{-} ions is in contact with $AgNO_3$, a precipitate appears. If the test is negative, it proves that all Cl^{-} ions have been removed from the sample thanks to the washing step. The homoionic Zn^{2+} clay material was then oven-dried at 100 °C overnight.

2.2 ZnO synthesis

Pure zinc oxide powders were synthesized by the sol–gel method following Benhebal et al. [24, 25]. The reagents were zinc acetate dihydrate (≥98%), oxalic acid dihydrate (≥99%), and absolute ethanol (ACS grade). They were obtained from BIOCHEM, Chemopharma (Cosne-Cours-sur-Loire, France), of analytical grade, and used directly as purchased.

Zinc acetate dihydrate (10.98 g) was treated with ethanol (300 mL) at 60 °C. The salt was completely dissolved in about 30 min. Oxalic acid dihydrate (12.6 g) was dissolved in ethanol (200 mL) at 60 °C for 30 min. The oxalic acid solution was added slowly, with stirring, to the hot ethanolic zinc solution, and the mixture was stirred for 90 min at 50 °C. The resulting gel was placed in an oven at 80 °C for 24 h. The product was calcined at 500 °C for 3 h.

Table 1 Sample composition given by ICP-AES

Samples	Al (wt.%)	Si (wt.%)	Na (wt.%)	Cu (wt.%)	Zn (wt.%) [and ZnO (wt.%)]
Bare Clay	10.1	20.9	<0.1	<0.1	<0.1
Clay/Na^+	10.2	20.9	0.2	<0.1	<0.1
Clay/Cu^{2+}	11.5	21.2	<0.1	0.8	<0.1
Clay/Zn^{2+}	10.5	21.4	<0.1	<0.1	2.1
Pure ZnO	–	–	–	–	>99
Clay/ZnO	5.2	9.2	<0.1	<0.1	18.9 [28.1]
Clay/Na^+/ZnO	5.8	10.3	0.1	<0.1	23.0 [29.0]
Clay/Cu^{2+}/ZnO	6.4	11.6	<0.1	0.4	23.3 [30.3]
Clay/Zn^{2+}/ZnO	6.0	11.7	<0.1	<0.1	26 [31.2]

2.3 Hybrid Clay-ZnO materials synthesis

For the preparation of hybrid clays with ZnO, the procedure was similar as for pure ZnO material.

However, when the oxalic acid solution was added slowly with stirring to the hot ethanolic zinc solution, 10 g of doped clay materials was added, and the mixture was left under stirring for 90 min at 50 °C. The resulting gel was placed in an oven at 80 °C for 24 h. The product was calcined at 500 °C for 3 h. The ZnO-modified clay powders were light gray in color.

2.4 Characterizations

Samples were measured by nitrogen adsorption–desorption isotherms in an ASAP multisampler device from Micromeritics.

The actual composition of the natural and hybrid clays was determined by inductively coupled plasma–atomic emission spectroscopy (ICP–AES), equipped with an ICAP 6500 THERMO Scientific device (Waltham, MA, USA). The mineralization is fully described in [26]; however, we used HF instead of HNO_3.

X-ray diffraction patterns were recorder on a Bruker D8 Twin-Twin powder diffractometer (Bruker, Billerica, MA, USA) using Cu-K_α radiation.

Scanning electron microscopy pictures were obtained on a TESCAN CLARA microscope operating at 15 keV.

2.5 Photocatalytic and adsorption experiments

The degradations of *p*-nitrophenol (PNP), Malachite Green (MG) and Diamant Brilliant Violet (DBV) were studied under UVA light ($\lambda = 365$ nm) to determine the photocatalytic activity of the synthesized material. The lamp was an Osram Sylvania, Blacklight-Bleu Lamp, F 18 W/BLB-T8, with its maximum peak at 365 nm and an intensity of 1.2 mW/cm^2.

Each sample was placed in a Petri dish with 20 mL of the pollutant solution in water (14 mg/L for PNP, 4 mg/L for MG or DBV). The degradation of the pollutant was evaluated from absorbance measurements with a Genesys 10S UV–Vis spectrophotometer (Thermo Scientific). Previously, adsorption tests were performed in the dark (dark tests) to show whether the pollutant was adsorbed on the surface of samples. A blank test, consisting of irradiating the pollutant solution for 24 h in a Petri dish without any catalyst, is made to assess the photolysis of the three pollutants under this illumination. The Petri dishes with catalysts and pollutants were stirred on orbital shakers (90 RPM) and illuminated for 24 h. Aliquots of pollutant were sampled at 0, 2, 6 and 24 h. The photocatalytic degradation can be evaluated by taking the catalyst adsorption (dark test) into account. Each photocatalytic measurement was triplicated to assess the reproducibility of the data. In each box, the catalyst concentration was equal to 1 g/L. Another experiment was also done with a catalyst concentration of 0.3 g/L only for the pure ZnO sample, in order to have the same amount of photocatalyst as the hybrid materials which contain 30 wt.% of ZnO.

The same experiments without light were performed to assess the adsorption properties of the samples on the three different model pollutants.

3 Results and discussion

3.1 Composition and morphologies of the clay-based materials

Table 1 gives the composition of the different samples. The bare Clay and the ion modified Clays have similar compositions with a Si/Al ratio around 2, characteristic ratio of smectite [27]. The ion modified clays have respectively higher amounts of the ion which was added during the modification process as expected.

For the ZnO/Clay hybrid materials, the Si/Al ratio stay equal around 2 and the proportion of ZnO is around 30 wt.% for each of the 4 hybrid materials as expected.

XRD patterns allow to estimate the crystalline phase presented in the samples, the patterns are represented in Fig. 1 for all samples.

For the 4 clays (bare Clay, Clay/Cu^{2+}, Clay/Na^+, and Clay/Zn^{2+} samples), similar patterns are observed with several crystalline phases that are pointed on bare Clay pattern. These patterns correspond to the smectite family

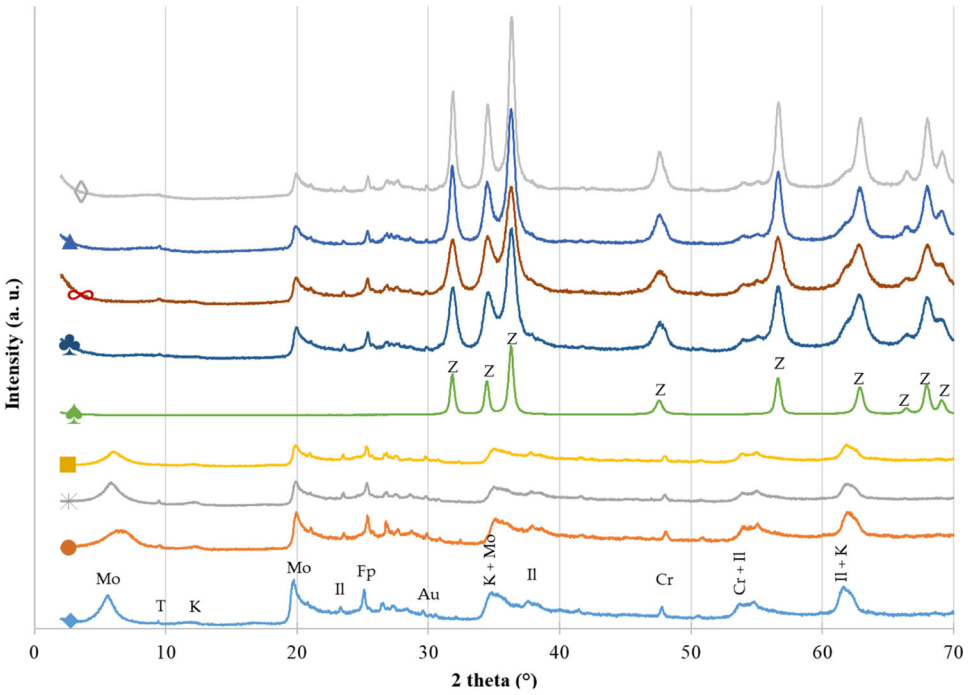

Fig. 1 XRD patterns of samples: (♦) bare Clay, (●) Clay/Cu^{2+}, (*) Clay/Na^{+}, (■) Clay/Zn^{2+}, (♠) Pure ZnO, (♣) Clay/ZnO, (∞) Clay/Cu^{2+}/ZnO, (▲) Clay/Na^{+}/ZnO, and (◊) Clay/Zn^{2+}/ZnO. The positions of the reference peaks are indicated on the two pure materials (bare Clay and ZnO) by the following letters: (Z) Wurzite, (Mo) Montmorillonite, (T) Talc, (K) Kaolinite, (Il) Illite, (Fp) Feldspath, (Au) Augite and (Cr) Cristobalite. The positions are not indicated on the composites materials to not overload the figure

Table 2 Specific surface area and porous volume

Samples	Specific surface area (m^2/g) ±5	V_p (cm^3/g) ±0.01
Bare Clay	45	0.07
Clay/Na^{+}	50	0.08
Clay/Cu^{2+}	55	0.09
Clay/Zn^{2+}	50	0.09
Pure ZnO	30	0.14
Clay/ZnO	60	0.44
Clay/Na^{+}/ZnO	55	0.25
Clay/Cu^{2+}/ZnO	50	0.21
Clay/Zn^{2+}/ZnO	50	0.18

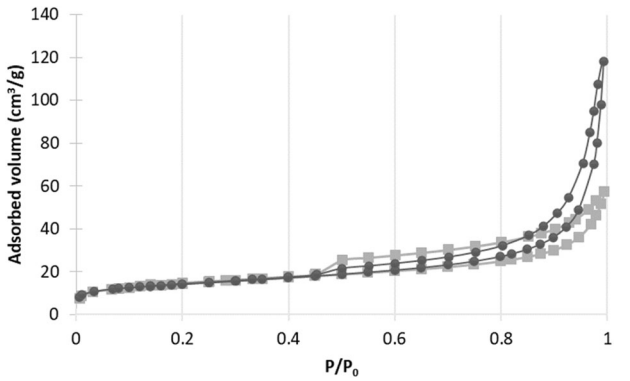

Fig. 2 Nitrogen adsorption–desorption isotherms for (■) Clay/Zn^{2+} and (●) Clay/Zn^{2+}/ZnO samples

which encompasses the different phases observed i.e., augite, cristobalite, montmorillonite, illite, kaolinite, feldspar, and talc. The pure ZnO sample (in green) is composed of wurtzite phase (peaks denoted as Z) as expected.

When hybrid materials are formed (Clay/ZnO, Clay/Cu^{2+}/ZnO, Clay/Na^{+}/ZnO, and Clay/Zn^{2+}/ZnO samples), the patterns correspond to a mix of the initial Clay pattern with the wurtzite peaks, showing that the hybrid materials are successfully obtained.

Table 2 presents the specific surface area and the porous volume (V_p) for the different samples. The specific surface values are slightly increased when ions are inserted in the clay network. Indeed, the specific surface area increases from 45 m^2/g to 50–55 m^2/g when cations are inserted (Table 2). An increase is also noted for the pore volume. Concerning the pure ZnO material, a specific surface value of 30 m^2/g is obtained. When the clay is modified with ZnO, a slight increase is observed for all the modified samples. Concerning the pore volume, an increase is also observed for all samples (Table 2). Indeed, the grafting of the ZnO particles at the surface of the sheets of clay (explained in the next paragraph and observed on the SEM images in Fig. 3) produces a rougher surface with more pore volume. Figure 2 gives an example of the isotherms that are obtained for Clay/Zn^{2+} and Clay/Zn^{2+}/ZnO samples and that are very similar for each sample. These isotherms correspond mainly to the type IV isotherm characterized by a broad hysteresis at high pressure (mesoporous solid).

Figure 3 gives an overview of the 9 samples observed by SEM. For the 4 clays ((a) bare Clay, (b) Clay/Cu^{2+}, (c) Clay/Na^{+}, and (d) Clay/Zn^{2+} samples), sheet like materials

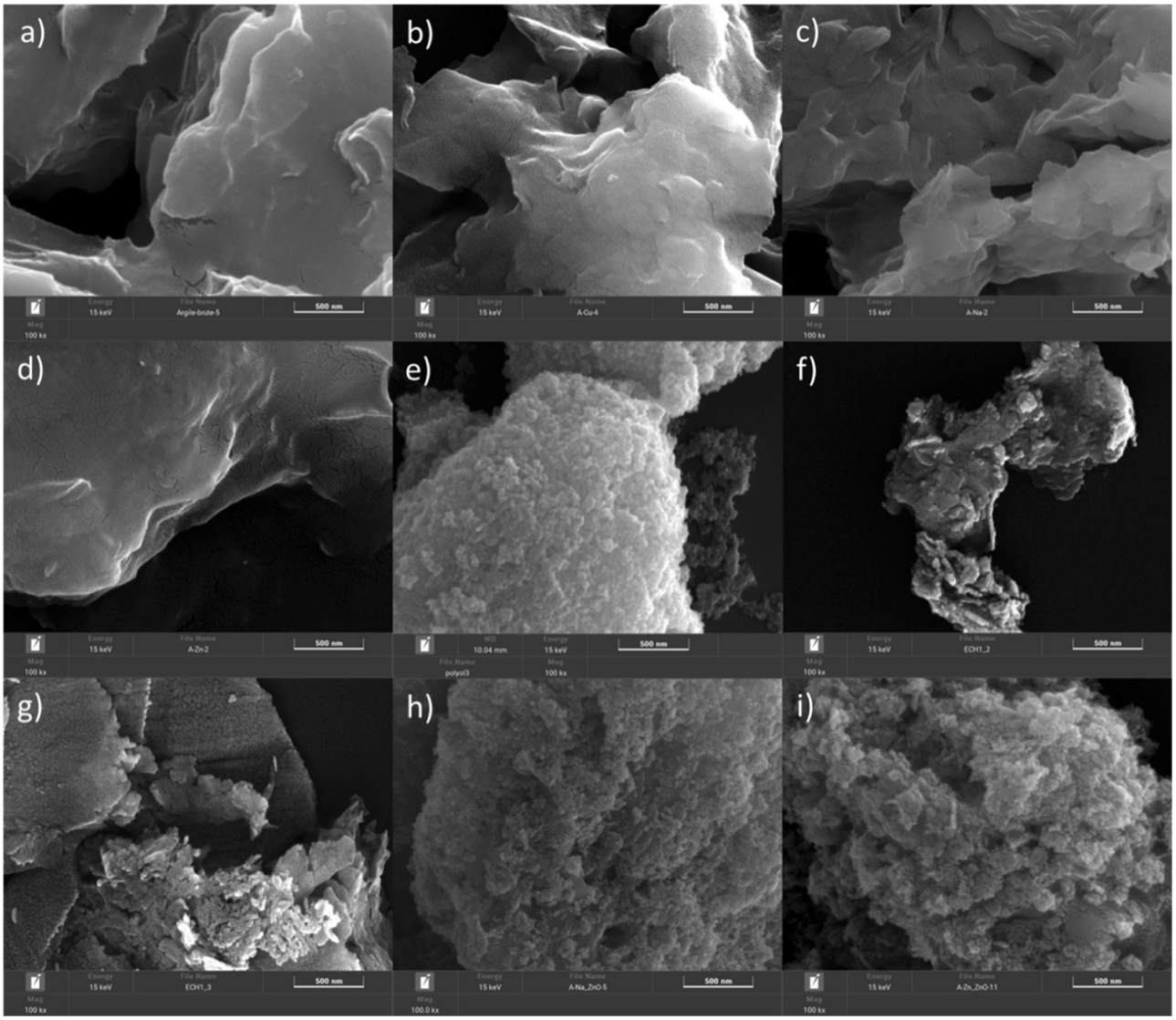

Fig. 3 SEM pictures of samples: (**a**) bare Clay, (**b**) Clay/Cu^{2+}, (**c**) Clay/Na^{+}, (**d**) Clay/Zn^{2+}, (**e**) Pure ZnO, (**f**) Clay/ZnO, (**g**) Clay/Cu^{2+}/ZnO, (**h**) Clay/Na^{+}/ZnO, and (**i**) Clay/Zn^{2+}/ZnO

are observed as expected for clay materials [28, 29], with smooth surface. No difference in the samples is noted.

When hybrid material is formed (Fig. 3f–i), the sheet like structure is still observed but rough surfaces are observed with the presence of sphere materials covering the surface. These spheres correspond to the ZnO material as it is observed on the pure ZnO sample in Fig. 3e. So the hybrid material is composed of the clay as bone structure covered by ZnO particles. It is important for the photocatalytic properties that the ZnO particles are present at the surface to be in contact with the light.

Hybrid materials are successfully obtained composed of 30 wt.% of ZnO and 70 wt.% of clay, with the ZnO particles present at the surface.

3.2 Photocatalytic activity and adsorption property on three different pollutants

The materials are evaluated for pollutant removal via two processes: the adsorption and the photocatalytic degradation. Their efficiencies are estimated on three different pollutants to show versatility. Firstly, the blank test showed that the 3 pollutant concentrations under UVA illumination remained constant and that no photolysis occurs.

The first pollutant to eliminate is the PNP, commonly found in pesticide. The results are presented on Fig. 4. First, during the experiments of adsorption made in the dark, no adsorption on any of the 9 samples was observed, so the adsorption results are not represented on Fig. 4.

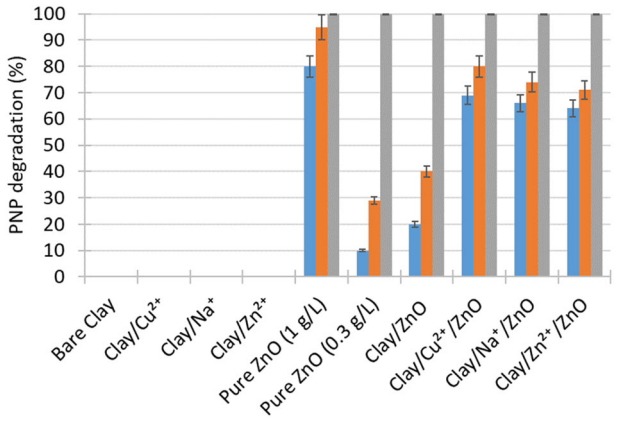

Fig. 4 PNP degradation (%) under UVA illumination for 2, 6, and 24 h with all samples. (**blue**) = after 2 h, (**orange**) = after 6 h, and (**grey**) = after 24 h

Also on Fig. 4, the photocatalytic degradation of the PNP is presented after 2, 6 and 24 h of illumination for the 9 samples, the pure ZnO sample is tested with two concentrations: 1 g/L and 0.3 g/L. Indeed, the concentration at 1 g/L is to have the same mass as the other samples and the concentration of 0.3 g/L is to have the same amount of photocatalyst as the hybrid samples, which are made of 30 wt.% of ZnO. For the 4 clays (bare Clay, Clay/Cu^{2+}, Clay/Na^{+}, and Clay/Zn^{2+} samples), no degradation is observed as clay alone is not a photocatalytic material. As previously reported [23, 24, 30], pure ZnO (at 1 g/L) degrades PNP with an efficiency equal to 95% after 6 h as ZnO is a photocatalytic material active under UV-A illumination. When the concentration of ZnO is decreased to 0.3 g/L, the degradation rate decreases also, reaching only 30% after 6 h. When hybrid materials are formed (Clay/ZnO, Clay/Cu^{2+}/ZnO, Clay/Na^{+}/ZnO, and Clay/Zn^{2+}/ZnO samples), photocatalytic degradation of PNP is still observed for each hybrid material. Between the 4 hybrid materials, the three one modified with ions present higher degradation that Clay/ZnO sample. Indeed, the presence of these ions can increase the photocatalytic activity via photo-Fenton reactions for Cu^{2+} and Zn^{2+} [26, 31, 32]. For Na^{+}, it was reported that if Na^{+} doped the ZnO, it can increase its photocatalytic properties [33]. The degradation of the hybrid materials is higher than the ZnO at the concentration of 0.3 g/L, it can be explained by the specific morphology observed with SEM (Fig. 3) showing that the ZnO particles are distributed at the surface of clay sheet allowing a very good contact between the pollutant and the photocatalytic material.

In Figs. 5 and 6, the adsorption and photocatalytic activity of the samples are represented for MG and DBV removal. Similar tendencies are obtained for both pollutants and so are described in the same paragraph. It is to remind that MG is a compound mainly used as dye or pesticide [21] and DBV is a molecule used as textile dye [22].

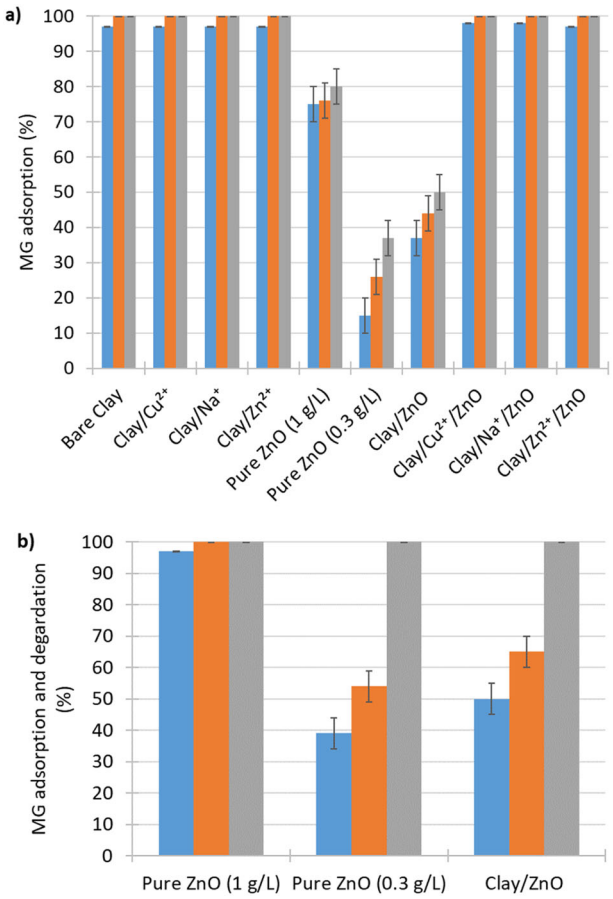

Fig. 5 (**a**) MG adsorption and (**b**) degradation (%) under UVA illumination for 2, 6, and 24 h with all samples. (**blue**) = after 2 h, (**orange**) = after 6 h, and (**grey**) = after 24 h

From Figs. 5a and 6a, a high adsorption capacity of the clays and hybrid materials are noticed. Indeed, after 2 h of adsorption, more than 95% of both molecules are adsorbed showing that clay has a high affinity for both dyes. Only the pure ZnO (at both concentrations) and Clay/ZnO samples do not totally adsorb the two pollutants after 24 h of experiments. Indeed, 80, 37 and 50% of MG are adsorbed on pure ZnO (1 g/L), pure ZnO (0.3 g/L) and Clay/ZnO respectively after 24 h. For DBV, 73, 25 and 42% are adsorbed respectively.

So for both materials, the photocatalytic degradation is necessary to eliminate 100% of the molecules from the water. It is represented on Figs. 5b and 6b, in this case the elimination is due to adsorption and degradation simultaneously. After 24 h of illumination, both molecules are eliminated on both materials. It illustrated the advantage to have a hybrid material that can combine multiple properties to degrade various molecules depending on their resistance to one process to another. As for the PNP degradation, the degradation of the hybrid materials (Figs. 5b and 6b) is higher than the ZnO at the concentration of 0.3 g/L, it can be explained by the specific morphology observed with

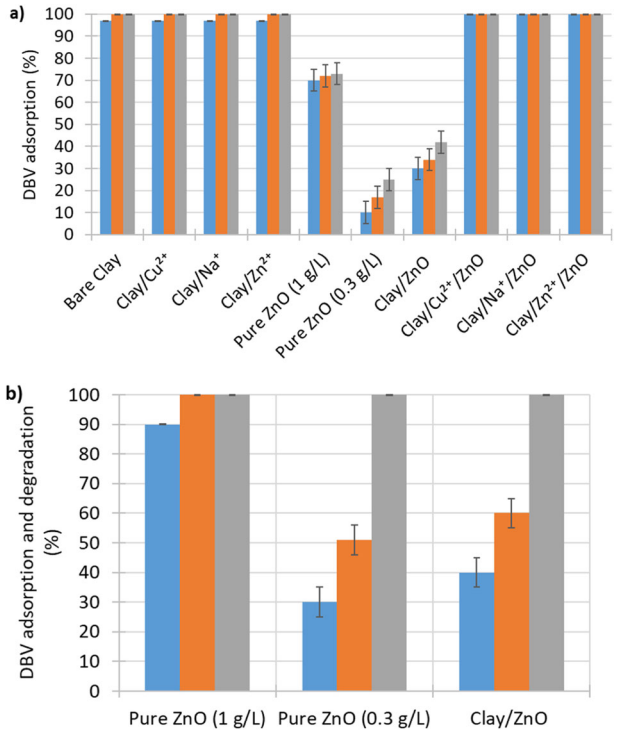

Fig. 6 (**a**) DBV adsorption and (**b**) degradation (%) under UVA illumination for 2, 6, and 24 h with all samples. (**blue**) = after 2 h, (**orange**) = after 6 h, and (**grey**) = after 24 h

SEM (Fig. 3) showing that the ZnO particles are distributed at the surface of clay sheet allowing a very good contact between the pollutant and the photocatalytic material.

Thanks to these pollutant removal experiments; the hybrid materials showed their versatile properties for the elimination of different kinds of molecule throughout the adsorption and/or the photocatalytic degradation of these molecules.

If the affinity between the pollutant and the solid is high, high adsorption occurs and the pollutant is removed from the water fixed on the solid. When the affinity is low, the photocatalytic property is needed to degrade the pollutant and treat the water. In this study, MG and DBV have a high affinity for the hybrid materials and are mainly removed by adsorption while PNP has no affinity for the hybrid materials and is totally degraded thanks to the photocatalytic property bring by the ZnO. These different adsorption behaviors are due to the 3 molecules which have different surface groups that can interact differently with the material surface.

4 Conclusions

In this work, natural clay extracted from Cameroon was modified with different ions by the exchange process. These latter were modified with a photocatalytic semiconductor, ZnO. The goal was to produce efficient hybrid materials for pollutant removal in water thanks to adsorption and/or photocatalytic processes. The ZnO that composed the hybrid material was produced by green sol–gel synthesis, a pure sample of ZnO was also produced for comparison purpose. The hybrid materials were synthesized in soft conditions of low temperature and low pressure.

The XRD results showed that the clay belonged to the smectite family and was composed of different crystalline phases as augite, cristobalite, montmorillonite, illite, kaolinite, feldspar, and talc. The pure ZnO was made of wurtzite phase. When the hybrid materials were produced, mix crystalline patterns were obtained with both smectite and wurtzite phases. The ICP-AES analysis showed that similar ratio between ZnO and clay were obtained for the 4 hybrid materials (30 wt.% of ZnO and 70 wt.% of clay). Specific surface areas were obtained for all samples in the range of 30–60 m^2/g with porous volumes evolving from 0.07 to 0.44 cm^3/g.

The SEM observation of the samples had shown that the hybrid materials had the clay structure as skeletal structure (sheet like structure) with the ZnO spherical particles grafted at the surface, giving a good exposure to light to maintain the photocatalytic property.

Then, the pollutant removal property of the samples was evaluated on three different model pollutants: PNP, MG and DBV. On PNP, no adsorption was observed, and photocatalytic property is necessary to eliminate this molecule. With the best hybrid material (Clay/Cu^{2+}/ZnO sample), 80% of PNP degradation is observed after 6 h of illumination. On MG and DBV, similar behavior was observed. Indeed, the clays and three out of four hybrid materials adsorbed completely both pollutant after 2 h of contact. Only pure ZnO and Clay/ZnO samples needed illumination to degrade completely both molecules. Synergistic effect is observed when the clay is modified by ZnO concerning the photocatalytic degradation activity.

This work showed the possibility to obtain very efficient hybrid materials for pollutant removal in waste waters with the use of inexpensive natural clay modified with a low amount of catalytic material (ZnO around 30 wt.%). It opens an innovative way for the development of polluted water treatment process in developing countries with lower cost.

Data availability

The raw/processed data required to reproduce these findings cannot be shared at this time as these data are part of an ongoing study

Acknowledgements JGM and SDL thank the F.R.S.-FNRS for their Postdoctoral Researcher position and Research Director position respectively. MHTM thanks the PACODEL for a doctoral grant. The

authors thank the CARPOR platform of the University of Liège and its manager, Dr. Alexandre Léonard, for the nitrogen adsorption–desorption measurements. JGM is grateful to the Rotary for a District 2160 grant, to the University of Liège and the FNRS for financial support for a post-doctoral stay in INRS Centre Eau, Terre, Environnement in Québec, Canada.

Author contributions MHTM: Conceptualization, Methodology, Writing – review & editing, Investigation, Formal analysis, Writing – original draft. SDL: Conceptualization, Methodology, Writing – original draft, Writing – review & editing, Funding acquisition, Project administration. JC: Investigation, Formal analysis. AF: Investigation, Formal analysis. CA: Investigation, Formal analysis. NF: Supervision, Funding acquisition, Project administration. EDW: Supervision, Funding acquisition, Project administration. JGM: Conceptualization, Methodology, Writing – original draft, Writing – review & editing, Investigation, Formal analysis, Supervision, Funding acquisition, Project administration.

Funding This research was funded by PACODEL/University of Liège, bourse de mobilité doctorale.

Compliance with ethical standards

Conflict of interest The authors declare no competing interests.

Consent to Participate All authors agreed to participate to this work.

Consent to Publish All authors agreed to this version for publication.

References

1. Kemgang Lekomo Y, Mwebi Ekengoue C, Douola A, et al. (2021) Assessing impacts of sand mining on water quality in Toutsang locality and design of waste water purification system. Clean Eng Technol 2, https://doi.org/10.1016/j.clet.2021.100045
2. Auriol M, Filali-Meknassi Y, Dayal Tyagi R (2007) Présence et devenir des hormones stéroïdiennes dans les stations de traitement des eaux usées. Occurrence and fate of steroid hormones in wastewater treatment plants. Rev des Sci de l'Eau 20:89–108
3. Zaviska F, Drogui P, Mercier G, Blais JF (2009) Advanced oxidation processes for waters and wastewaters treatment: Application to degradation of refractory pollutants. Rev des Sci de l'Eau 22:535–564. https://doi.org/10.7202/038330ar
4. Hocine O, Boufatit M, Khouider A (2004) Use of montmorillonite clays as adsorbents of hazardous polluants. Desalination 167:141–145. https://doi.org/10.1016/j.desal.2004.06.122
5. Srivastava R, Fujita S, Arai M (2009) Synthesis and adsorption properties of smectite-like materials prepared using ionic liquids. Appl Clay Sci 43:1–8. https://doi.org/10.1016/j.clay.2008.06.015
6. Akçay G, Kilinç E, Akçay M (2009) The equilibrium and kinetics studies of flurbiprofen adsorption onto tetrabutylammonium montmorillonite (TBAM). Colloids Surf A Physicochem Eng Asp 335:189–193. https://doi.org/10.1016/j.colsurfa.2008.11.009
7. Mahy JG, Wolfs C, Mertes A, et al. (2019) Advanced photocatalytic oxidation processes for micropollutant elimination from municipal and industrial water. J Environ Manage 250, https://doi.org/10.1016/j.jenvman.2019.109561
8. Mahy JG, Lejeune L, Haynes T, et al. (2021) Crystalline ZnO photocatalysts prepared at ambient temperature: influence of morphology on p-nitrophenol degradation in water. Catalysts 11, https://doi.org/10.3390/catal11101182
9. Mahy JG, Tilkin RG, Douven S, Lambert SD (2019) TiO_2 nanocrystallites photocatalysts modified with metallic species: comparison between Cu and Pt doping. Surfaces Interfaces 17, https://doi.org/10.1016/j.surfin.2019.100366
10. Douven S, Mahy JG, Wolfs C, et al. (2020) Efficient N, Fe Co-doped TiO2 active under cost-effective visible LED light: from powders to films. Catalysts 10, https://doi.org/10.3390/catal10050547
11. Bodson CJ, Heinrichs B, Tasseroul L et al. (2016) Efficient P- and Ag-doped titania for the photocatalytic degradation of waste water organic pollutants. J Alloy Compd 682:144–153. https://doi.org/10.1016/j.jallcom.2016.04.295
12. Pignatello JJ, Oliveros E, MacKay A (2006) Advanced oxidation processes for organic contaminant destruction based on the fenton reaction and related chemistry. Crit Rev Environ Sci Technol 36:1–84. https://doi.org/10.1080/10643380500326564
13. Issaka E, AMU-Darko JNO, Yakubu S, et al. (2022) Advanced catalytic ozonation for degradation of pharmaceutical pollutants——a review. Chemosphere 289, https://doi.org/10.1016/j.chemosphere.2021.133208
14. Mahy JG, Tasseroul L, Zubiaur A et al. (2014) Highly dispersed iron xerogel catalysts for p-nitrophenol degradation by photo-Fenton effects. Microporous Mesoporous Mater 197:164–173. https://doi.org/10.1016/j.micromeso.2014.06.009
15. Hu Z, Cai J, Song G, et al. (2021) Anodic oxidation of organic pollutants: anode fabrication, process hybrid and environmental applications. Curr Opin Electrochem 26, https://doi.org/10.1016/j.coelec.2020.100659
16. Drogui P, Blais J-F, Mercier G (2007) Review of electrochemical technologies for environmental applications. Recent Pat Eng 1:257–272
17. Cheng T, Gao H, Liu G, et al. (2022) Preparation of core-shell heterojunction photocatalysts by coating CdS nanoparticles onto Bi4Ti3O12 hierarchical microspheres and their photocatalytic removal of organic pollutants and Cr(VI) ions. Colloids Surf A Physicochem Eng Asp 633, https://doi.org/10.1016/j.colsurfa.2021.127918
18. Xiong S, Yin Z, Zhou Y et al. (2013) The dual-frequency (20/40 kHz) ultrasound assisted photocatalysis with the active carbon fiber-loaded Fe3+-TiO_2 as photocatalyst for degradation of organic dye. Bull Korean Chem Soc 34:3039–3045. https://doi.org/10.5012/bkcs.2013.34.10.3039
19. Tang N, Li Y, Chen F, Han Z (2018) In situ fabrication of a direct Z -scheme photocatalyst by immobilizing CdS quantum dots in the channels of graphene-hybridized and supported mesoporous titanium nanocrystals for high photocatalytic performance under visible light. RSC Adv 8:42233–42245
20. Mahy JG, Lambert SD, Tilkin RG, et al. (2019) Ambient temperature ZrO_2-doped TiO_2 crystalline photocatalysts: highly efficient powders and films for water depollution. Mater Today Energy 13, https://doi.org/10.1016/j.mtener.2019.06.010
21. Alderman DJ (1985) Malachite green: a review. J Fish Dis 8:289–298
22. Lalonger L (1994) La transition des colorants naturels aux colorants synthétiques et ses répercussions. Material Culture Review 40:19–28
23. Mahy JG, Mbognou MHT, Léonard C, et al. (2022) Natural Clay Modified with ZnO/TiO_2 to Enhance Pollutant Removal from Water. Catalysts 12, https://doi.org/10.3390/catal12020148
24. Benhebal H, Chaib M, Crine M et al. (2016) Photocatalytic decolorization of gentian violet with Na-doped (SnO_2 and ZnO). Chiang Mai J Sci 43:584–589
25. Benhebal H, Chaib M, Leonard A et al. (2012) Photodegradation of phenol and benzoic acid by sol-gel-synthesized alkali metal-doped ZnO. Mater Sci Semicond Process 15:264–269. https://doi.org/10.1016/j.mssp.2011.12.001
26. Mahy JG, Lambert SD, Léonard GLM et al. (2016) Towards a large scale aqueous sol-gel synthesis of doped TiO_2: Study of

various metallic dopings for the photocatalytic degradation of p-nitrophenol. J Photochem Photobio A Chem 329:189–202. https://doi.org/10.1016/j.jphotochem.2016.06.029
27. Ndé HS, Tamfuh PA, Clet G, et al. (2019) Comparison of HCl and H_2SO_4 for the acid activation of a cameroonian smectite soil clay: palm oil discolouration and landfill leachate treatment. Heliyon 5, https://doi.org/10.1016/j.heliyon.2019.e02926
28. Theo Kloprogge J, KOMARNENl S, Amonetie JE (1999) Synthesis of smectite clay minerals: a critical review. Clays Clay Min 47:529–554
29. Seo YJ, Seol J, Yeon SH et al. (2009) Structural, mineralogical, and rheological properties of methane hydrates in smectite clays. J Chem Eng Data 54:1284–1291. https://doi.org/10.1021/je800833y
30. Pirhashemi M, Habibi-Yangjeh A, Rahim Pouran S (2018) Review on the criteria anticipated for the fabrication of highly efficient ZnO-based visible-light-driven photocatalysts. J Ind Eng Chem 62:1–25. https://doi.org/10.1016/j.jiec.2018.01.012
31. Rauf MA, Meetani MA, Hisaindee S (2011) An overview on the photocatalytic degradation of azo dyes in the presence of TiO_2 doped with selective transition metals. Desalination 276:13–27. https://doi.org/10.1016/j.desal.2011.03.071
32. Romero V, Acevedo S, Marco P et al. (2016) Enhancement of Fenton and photo-Fenton processes at initial circumneutral pH for the degradation of the β-blocker Metoprolol. Water Res 88:449–457. https://doi.org/10.1016/j.watres.2015.10.035
33. Lin SS, Lu JG, Ye ZZ et al. (2008) p-type behavior in Na-doped ZnO films and ZnO homojunction light-emitting diodes. Solid State Commun 148:25–28. https://doi.org/10.1016/j.ssc.2008.07.028

Results in Surfaces and Interfaces 14 (2024) 100183

Contents lists available at ScienceDirect

Results in Surfaces and Interfaces

journal homepage: www.elsevier.com/locate/rsurfi

Silane modified clay for enhanced dye pollution adsorption in water

Marlène Huguette Tsaffo Mbognou [a,b,c], Stéphanie D. Lambert [a], Ernestine Mimba Mumbfu [c], Joachim Caucheteux [a], Antoine Farcy [a], Nathalie Fagel [d], Emmanuel Djoufac Woumfo [b], Julien G. Mahy [a,e,*]

[a] Department of Chemical Engineering – Nanomaterials, Catalysis & Electrochemistry, University of Liège, B6a, Quartier Agora, Allée du Six Août 11, 4000, Liège, Belgium
[b] Laboratoire de Physico-Chimie des Matériaux Minéraux, University of Yaounde I, 337, Yaounde, Cameroon
[c] Institute of Geological and Mining Research (IRGM), 4110, Yaounde, Cameroon
[d] Laboratoire Argiles, Géochimie et Environnements Sédimentaires (AGEs), Department of Geology, Faculty of Sciences, University of Liège, Liège, B-4000, Belgium
[e] Institut National de la Recherche Scientifique (INRS), Centre-Eau Terre Environnement, Université du Québec, 490, Rue de La Couronne, Québec (QC), G1K 9A9, Canada

ARTICLE INFO

Keywords:
Silicon alkoxides
Porous material
Water treatment
Pollution removal
Hybrid compounds

ABSTRACT

A natural clay from Bakotcha in Cameroon was modified with two silanes, tetramethoxysilane (TMOS) and [3-(2-aminoethyl)aminopropyl]trimethoxysilane (EDAS) to increase its adsorption properties. The modified clay is intended to be used as an efficient adsorbent for organic pollutant removal from water. Three Clay/TMOS and two Clay/EDAS samples with different [silane]/[clay] ratios were produced and characterized by X-ray diffraction, N_2 adsorption-desorption measurements, Inductively Coupled Plasma–Atomic Emission Spectroscopy and Scanning Electron Microscopy. Their adsorption properties were evaluated on three organic model pollutants (i.e. fluorescein, malachite green and brilliant violet diamond). A dilution of the montmorillonite structure of the raw clay is observed when it is modified with TMOS while its original crystalline structure is preserved with EDAS. The morphologies depended on the used silane: (i) with TMOS, highly porous materials with the formation of silica particles at the surface of the clay; (ii) with EDAS, a similar morphology as raw clay with EDAS grafted at the surface of the clay. Both morphologies give two different adsorption behaviors on the 3 pollutants. For the raw clay and the TMOS modified clays, similar adsorption properties are obtained with a better adsorption when the specific surface increases (when TMOS content increases). When clay is modified with EDAS, the adsorption properties change as the surface groups are different, these EDAS modified samples have less affinity with fluorescein and malachite green reducing the adsorption capacity for this kind of pollutants. The tuning of the raw clay with silane opens the way for the development of highly efficient adsorbent for pollutants in water from natural and inexpensive materials.

1. Introduction

Silicates belonging to the clay mineral family are increasingly studied as an important class of solids that can yield nanostructured materials with interesting properties as hydrophobicity, hydrophilicity, biocompatibility or as building block for more complex structures (Dong and Zhang, 2018; Zhou et al., 2016). Studies focused on the functionalization of clay materials to obtain hybrid compounds where inorganic and organic components are linked by covalent and ionic-covalent bonds. This research is focused on achieving a high percentage of clay sheet exfoliation in polymer matrices by improving the interactions between clay surfaces and polymer chains through various surface modification approaches (Viville et al., 2004).

There exist many attractive characteristics on clay surfaces, such as hydroxyl groups on the edges, silanol groups of crystal defects, providing surface modification and functionalization strategies. The common method used to modify the surface of clays is cation exchange reaction with alkylammonium (Viville et al., 2004; Park et al., 2005). This increases the interlayer space and creates a favorable organophilic environment (Viville et al., 2004; Park et al., 2005).

A novel modification approach involving a direct grafting reaction to form covalent bonds on clay surfaces has attracted much attention

* Corresponding author. Allée du Six Août 11, 4000 Liège, Belgium.
E-mail address: julien.mahy@uliege.be (J.G. Mahy).

https://doi.org/10.1016/j.rsurfi.2024.100183
Received 30 August 2023; Received in revised form 29 December 2023; Accepted 10 January 2024
Available online 12 January 2024

(Wheeler et al., 2005; He et al., 2005). The organosilanes were covalently bound to the clay surfaces via a condensation reaction with the surface silanol groups (Si–OH), resulting in closer interactions between the organic components and the clay than ionic interaction and physical adsorption (Tonle et al., 2003; He et al., 2013). Indeed, since a few years, silicon alkoxides are used either to modify the textural properties of inorganic materials used as catalysts in gaseous phase (Lambert et al., 2008; Claude et al., 2019; Mahy et al., 2017), or to play the role of link between organic molecules and inorganic photocatalytic materials (Mahy et al., 2019a, 2023).

Functionalizing swelling aluminosilicate clays of the smectite type, such as montmorillonite, would generally result in limited amounts of –OH groups (Celis et al., 2000; Song and Sandi, 2001). For grafting organic ligands onto the interlamellar surface of such clays, the literature is sparse, and the resulting materials may suffer from impeded access to binding sites, as shown by less than complete adsorption of heavy metal species relative to the total number of ligands (Mercier and Pinnavaia, 1998).

To overcome the limitation of the surface grafting modification method, the sol-gel route is used to synthesize organoclay using silicon alkoxides as the priority source of silica. Carrado et al. (Carrado, 2000) provided an approach that allows a large amount of silanes to covalently attach to the clay surface due to the *in-situ* process and more silanol moieties. Nevertheless, the high degree of organosilane incorporation is often accompanied by distortions and structural defects (Qian et al., 2008).

These modifications allow the formation of hybrid materials with increased adsorption properties for pollutant removal. Indeed, with the expansion of industries during the past two centuries, pollution has increased greatly all around the world and the development of depollution techniques using inexpensive materials became essential (Kemgang Lekomo et al., 2021; Shayesteh et al., 2015; Paredes-Quevedo et al., 2021). Natural clay represents an inexpensive material, available in a lot of developing countries, that can be a good candidate for organic pollutant adsorption from water (Srivastava et al., 2009; Akçay et al., 2009; Nodehi et al., 2020; Tchanang et al., 2021; Queiroga et al., 2019, 2021; De Queiroga et al., 2019).

The objectives of this work are to explore the possibilities of using natural Cameroonian clays as raw material for the preparation of organic-inorganic hybrid compounds by grafting with silanol groups, i.e. either tetramethoxysilane (TMOS) or [3-(2-aminoethylamino)propyl] trimethoxysilane (EDAS), using a well-controlled and easy sol-gel procedure. The resulting nanocomposite materials are evaluated as adsorbents for dyes such as fluorescein, malachite green and brilliant purple diamond present in water polluted by textile industries. The experiments are performed with raw clays from the locality of Bakotcha (West Cameroon). Several physico-chemical techniques were used to evaluate the efficiency of the functionalization process.

2. Material and methods

2.1. Clay material and chemical reagents

A smectite type clay material from the locality of Bakotcha, (West Cameroon) was used in this work. It corresponds to a montmorillonite clay with trace of cristobalite and feldspars as shown by the X-ray diffractogram in (Mahy et al., 2022). The sampled clay was air-dried in the laboratory to a constant weight before grinding and sieving in a 160 μm diameter sieve. The silica precursors and the solvent were tetramethoxysilane (TMOS, 98%, density = 1.032 g/mL) from Alfa Aesar, [3-(2-aminoethyl)aminopropyl]trimethoxysilane (EDAS, 80%, density = 1.028 g/mL) from Sigma Aldrich, Ethanol absolute (ACS grade) from Merck. Hydrochloric acid (HCl 36–38%, Merck) was used to adjust the pH of the solution. All solutions were prepared with deionized water.

2.2. Sol-gel method to modify clay with alkoxides

Clays modified with organosilanes were prepared by sol-gel process either to saturate the material with silica (TMOS) or graft amine groups (EDAS). The synthesis used was inspired from (Qian et al., 2008). Different alkoxide/clay mass ratios were taken in order to evaluate the influence of the reagent composition. Table 1 represents the different ratios.

2.2.1. TMOS modified clay samples

50 mL of deionized water was acidified with hydrochloric acid (36–38%, Merck) to pH 1.5 and put under magnetic stirring at room temperature. A weight of 3.10 g of montmorillonite clay was added to the initial solution under continuous stirring. Specific amount of TMOS, depending to the aimed ratio (Table 1), was taken and introduced into 10 mL of absolute ethanol. This second mixture was added to the initial solution under stirring at 25 °C until a light brown sol was formed. The gel is aged in an oven for condensation for 24 h at 25 °C and finally dried at 60 °C for 48 h. The procedure used is called acid-catalyzed procedure because the acid catalyzes the sol-gel process (Brinker and JeffreyScherer, 2013).

2.2.2. EDAS modified clay samples

The syntheses of samples with EDAS were similar to the ones with TMOS, except that the gel was aged for 3 days in an oven at 80 °C for condensation and finally dried at 150 °C for 24 h. Only two ratios were synthesized since the clay/EDAS ratio 3/10 was too viscous that it was impossible to dry and work with it.

2.3. Material characterization methods

Nitrogen adsorption-desorption isotherms of all samples were determined in an ASAP multisampler device from Micromeritics at −196 °C. The samples were degassed at 120 °C for 24 h before analysis.

X-ray diffraction (XRD) patterns were recorded on a Bruker D8 Twin-Twin powder diffractometer (Bruker, Billerica, MA, USA) using Cu-Kα radiation, with a step size of 0.002°, a scan speed of 2°/min, a 2 theta range of 2–70°, a current of 40 mA, and a voltage of 40 kV. Phase quantification was made with TOPAS software.

Fourier transform infrared (FTIR) spectra in the region of 400–4000 cm^{-1} are recorded at room temperature with a Thermo Nicolet Nexus FTIR spectrometer (Laboratoire de Minéralogie, ULiège). All catalyst powders are dispersed in KBr (1 wt % for all samples).

The zeta potential is measured on the different sample suspensions with a DelsaNano C device from Beckman Coulter.

The point of zero charge (PZC) is evaluated for each sample as follows (Schreier and Regalbuto, 2004): 11 vials are prepared with 10 mL of Milli-Q water. The pH of each of these vials is adjusted with diluted HCl and NaOH solutions to cover a pH range of 2–12 with a ΔpH of 1 between each vial. Then, an equal amount of sample is placed in each of the vials. The mass of sample to be added must be such that the surface concentration in a vial is 1000 $m^2\ L^{-1}$, i.e. a specific surface area of 10 m^2 in 10 mL. Once the sample is suspended in each vial, they are stirred for 1 h. After this time, the pH of each of the vials is measured again and a graph of the final pH versus the initial pH can be drawn. The PZC is given by the pH value at which a plateau appears on the graph (Schreier and Regalbuto, 2004).

Scanning electron microscopy (SEM) pictures were obtained on a

Table 1
Clay/TMOS and Clay/EDAS mass ratios.

Ratio Clay/TMOS (w/w)	Ratio Clay/EDAS (w/w)
3/3	3/3
10/3	10/3
3/10	–

TESCAN CLARA microscope operating at 15 keV.

The actual composition of the clay materials was determined by Inductively Coupled Plasma–Atomic Emission Spectroscopy (ICP–AES), equipped with an ICAP 6500 THERMO Scientific device. The mineralization is fully described in (Mahy et al., 2016) with HF used instead of HNO_3.

2.4. Adsorption experiments

The adsorption tests were evaluated on the raw clay material and on the TMOS and EDAS functionalized clay samples with the different mass ratios (6 samples in total). Three model pollutants and dyes used in the pesticide and textile industries, were tested: malachite green (MG, pKa 6.9), fluorescein (FL, pKa 6.4) and brilliant violet diamond (BVD, Remazol brilliant violet 5R, pKa not referenced in literature). Six vials containing sample powders of 5, 10, 15, 20, 25 and 30 mg with 20 mL of pollutant solution in water were prepared for adsorption experiment. Initial solution concentrations of pollutants were 20 mg/L for FL (pH = 5.3) and 4 mg/L for MG (pH = 6.2) and BVD (pH = 7.2), these pollutant concentrations are commonly found in adsorption studies on this kind of molecules (Shayesteh et al., 2015; Nodehi et al., 2020; Tchanang et al., 2021). The different samples were shaken continuously in the dark. Aliquots of pollutants were taken every 10, 20, 60 min up to 2 h. Residual concentrations of pollutants were assessed with a Genesis 150S UV–Vis spectrophotometer (Thermo Scientific) without filtration. Previously, calibration curves were made for each pollutant. The main adsorption peaks were located at 485 nm for fluorescein, 550 nm for brilliant violet diamond and 660 nm for malachite green.

3. Results and discussion

3.1. Composition of modified clays

Silica-clay nanocomposites were prepared at different ratios as described in the experimental section (section 2.2). Variable amounts of silicon alkoxysilanes (TMOS and EDAS) mixed with ethanol were slowly added to dispersions of clays acidified with hydrochloric acid. Each mixture was homogenized under continuous stirring at room temperature. HCl was added to allow TMOS or EDAS to be covalently bound to the surface of the clays so that it could react with other hydrolyzed molecules of the same type. Depending on the amount of TMOS or EDAS added, gelation of the system occurred. The gel formed in the Clay/TMOS 3/10 case does not have a high viscosity. TMOS contributes to a reaction gelation time between 30 min and 2 h for the 3/10 Clay/silane ratio. When EDAS is used, there is no gelation of the samples. The Clay/EDAS (3/10) sample did not yield any powder product after drying; the gel remained soft. The different capacities of silanes to insert themselves into the clay sheets could explain these observations. Diffusion is facilitated by the lower steric hindrance presented by TMOS (small molecular size) compared to EDAS. The condensation step is slower when the number of silanol groups on the alkoxysilane is smaller (He et al., 2005). The surfaces of the clays were fixed by silane arrays or silica nanoparticles depending on the Clay/TMOS or Clay/EDAS ratio (Qian et al., 2008).

The Al and Si composition measured by ICP-AES is given in Table 2.

Table 2
Al and Si compositions of all samples measured by ICP.

Sample	Al (wt%)	Si (wt%)	Si/Al
Raw clay	11.4	20.7	1.82
Clay/TMOS 3/10	9.74	21	2.16
Clay/TMOS 3/3	7.24	23.4	3.23
Clay/TMOS 10/3	10.2	22.7	2.23
Clay/EDAS 3/3	7.82	19.9	2.54
Clay/EDAS 10/3	10.5	22	2.10

The addition of silane increases the amount of silicon in the sample and the ratio Si/Al increases. TMOS/Clay samples contain more silicon than EDAS/Clay samples.

FTIR spectroscopy was applied to analyze possible differences in samples (Fig. 1). The FTIR spectrum of the raw Clay (Fig. 1a or 1b in blue) shows the following characteristic bands (Madejova'and et al., 2001): at 3650 cm^{-1}, stretching vibrations of the OH bonds that correspond to hydroxyl groups of the montmorillonite structure; at 3590 cm^{-1}, tension vibrations of the OH bonds of the chemisorbed and physisorbed water; and at 1610 cm^{-1}, the deformation vibration of the OH bonds. The band at 1020 cm^{-1} results from the stretching vibration of the Si–O bonds of the Montmorillonite (Mt) structure (Slaný et al., 2019). In addition, the band at 790 cm^{-1} corresponds to the deformation vibration of the Si–O bonds of silica, which is an associated phase. The bands at 909 cm^{-1}, result from the deformation vibrations of the Al–OH bonds of the AlAlOH structural groups. The band at 620 cm^{-1} is assigned to the coupling vibrations of the Al–O and Si–O groups of the Mt structure and the bands at 520 cm^{-1} and 490 cm^{-1} correspond to the deformation vibrations of the Al–O–Al and Si–O–Si groups, respectively.

The FTIR spectra of natural clay and modified ones are all presented in Fig. 1. Surface modification of montmorillonite with TMOS and EDAS was demonstrated by FTIR. Indeed, the asymmetric stretching modes of Si–O–Si were observed at 40 and 1020 cm^{-1} while the stretching vibrations of Al–O–Si were observed at 790 and 520 cm^{-1} for every TMOS and EDAS samples (Fig. 1a and b). The hydroxyl group bound to aluminum (Al(Al)OH) or magnesium (Al(Mg)OH) shows stretching vibrations at 3690 cm^{-1}. The stretching of the hydroxyl group and bending vibrations of the H–O–H bonds in the adsorbed water molecules intercalated in the clay mineral occur approximately at 3465 cm^{-1} and 1630 cm^{-1} respectively (Piscitelli et al., 2012). However, the latter was shifted to 1630 cm^{-1} in the amino-functionalized clay mineral (Fig. 1b). The new absorption band at 2950 cm^{-1} corresponds to the C–H stretching vibration of single bond CH_2 groups of EDAS (Fig. 1b). These FTIR bands indicate the surface modification of natural montmorillonite by silica alkoxides. New bands were observed at 1490 cm^{-1} and 1320 cm^{-1}, corresponding to single-bond NH_2 and Si–CH vibrations respectively, which also confirmed the presence of the silane (Fig. 1b).

3.2. Crystallinity

The XRD patterns of the different samples (Fig. 2) has allowed to estimate the crystalline structure of the samples. The raw cay is characterized by the following minerals: montmorillonite, talc, kaolinite, illite, feldspar, augite and cristobalite. The quantification of phases is presented in Table 3.

In the case of the Clay/TMOS sample series (Fig. 2), the intensity of the clay diffraction peaks decreases when the clay is modified with TMOS. It becomes practically nonexistent when the Clay/TMOS ratio is low (i.e. 3/10). This result suggests that the clay platelets were delaminated during the synthesis reaction (Qian et al., 2008) and that large amount of amorphous silica is introduced in the samples. Concerning the quantification of crystalline phases (Table 3), it is observed a decrease of three phases: kaolinite, illite and cristobalite. This modification of phases can be due to acid leaching during the modification of clay with the silane (Komadel and Madejová, 2006; Espínola et al., 2003). Indeed, it is made in acidic condition (HCl at pH of 1.5, see experimental section). For the sample Clay/TMOS 3/10, mainly montmorillonite is detected.

In the Clay/EDAS patterns (3/3) and (10/3) (Fig. 2), the peaks of the different minerals present in the raw material are still visible after the EDAS modification with similar intensities. This would mean that with the low proportion of EDAS used during the syntheses, its incorporation in the clay did not change the initial structure of the material. Concerning the quantification of crystalline phases (Table 3), it is also observed a decrease of three phases: kaolinite, illite and cristobalite. Similar explanation than samples modified with TMOS can be drawn

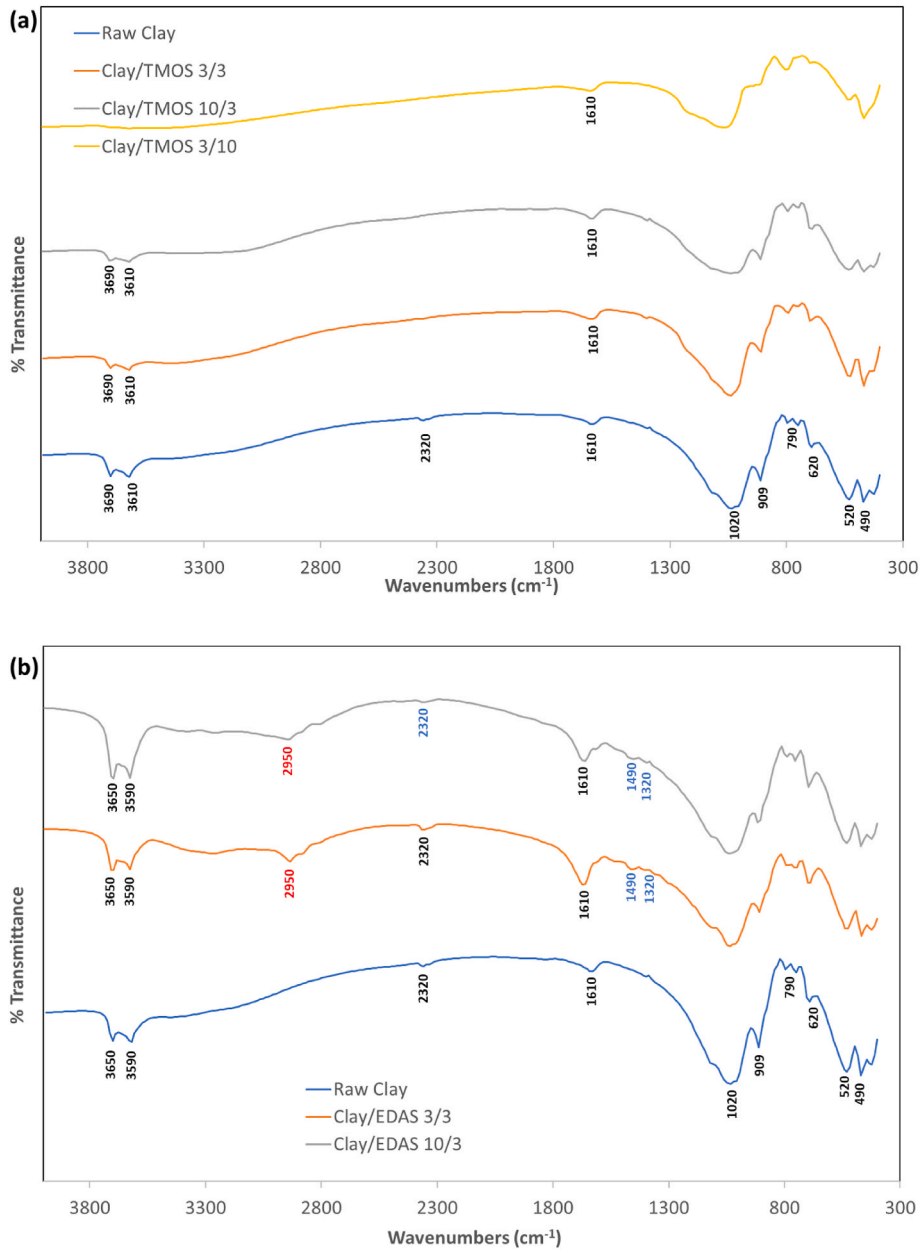

Fig. 1. FTIR spectra of the 6 samples: (a) TMOS series and (b) EDAS series.

due to the acidic treatment.

For all samples modified with silane (TMOS of EDAS), it is observed a modification of the pic located at 5.7° for the raw Clay. This peak corresponds to the basal spacing (001) and is related to the degree of intercalation of species in clay. According to (Asgari and Sundararaj, 2018), functionalization with silanes shifts the peak towards lower values of 2θ. The average value of (001) differs significantly depending on the medium used. This can be attributed to the high amounts of chemical grafting at the edges, which slightly separate the separated layers due to the richness of grafted species.

In (Piscitelli et al., 2010), X-ray diffraction patterns related to basal spacing (001), show that the introduction of any type of aminosilane into the Montmorillonite gallery shifts the peak to lower values compared to the bulk material. This increase in basal spacing is a clear signal that each aminosilane species has been grafted/intercalated into the Montmorillonite interplatelet space. In detail, pure MT sample shows a peak at 2 Θ equal to 7.5, while MT modified by aminosilane sample shows diffraction peaks at 2 Θ values between 5.3 and 5.9 (Piscitelli et al., 2010).

In the case of this study, the samples modified with EDAS have their basal peak modified from 5.7 for the raw Clay to 4.3 and 4.5 for the Clay/EDAS 3/3 and Clay/EDAS 3/10, respectively. It indicates an intercalation of the silane in the Montmorillonite structure.

Concerning the samples modified with TMOS, it is a displacement of the basal peak towards higher values (6.9, 7.1 and 6.6 for Clay/TMOS 3/10, Clay/TMOS 3/3, and Clay/TMOS 10/3, respectively). This indicates a different behavior with this silane (TMOS) compared to EDAS which leads to less spacing between the sheets of the Montmorillonite structure.

3.3. *Texture and surface aspect of samples*

The textural properties of samples were confirmed by nitrogen adsorption-desorption measurements. Table 4 shows the specific surface areas (S_{BET}), the microporous volume (V_{micro}) and the porous volume (V_P) of the different samples. The bare clay sample has a relatively low

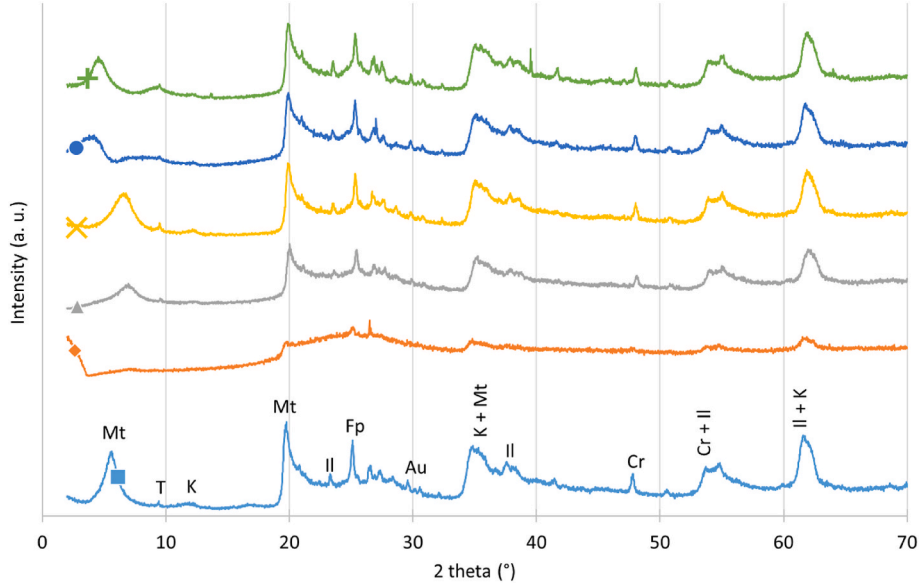

Fig. 2. XRD patterns of samples: (■) Raw Clay, (◆) Clay/TMOS 3/10, (▲) Clay/TMOS 3/3, (x) Clay/TMOS 10/3, (●) Clay/EDAS 3/3, and (+) Clay/EDAS 10/3. The positions of the reference peaks are indicated on the raw clay by the following letters: (Mt) montmorillonite, (T) talc, (K) kaolinite, (Il) illite, (Fp) feldspar, (Au) augite, and (Cr) cristobalite. The positions are not indicated on the composite materials to not overload the figure.

Table 3
XRD phase quantification with TOPAS software.

Samples	Montmorillonite (%)	Talc (%)	Kaolinite (%)	Illite (%)	Feldspar (%)	Augite (%)	Cristobalite (%)
Raw clay	80.22	2.01	4.19	7.58	0.52	0.85	4.64
Clay/TMOS 3/10	93.03	0.59	0	1.12	3.65	0.94	0.67
Clay/TMOS 3/3	83.87	0	1.1	2.24	5.13	3.13	4.54
Clay/TMOS 10/3	85.21	0	1.51	1.16	6.85	2.53	2.75
Clay/EDAS 3/3	84.1	0	1.02	3.23	5.78	3.1	2.78
Clay/EDAS 10/3	84.07	0	0.52	3.66	7.88	2.65	1.22

Table 4
Texture of samples.

Sample	S_{BET} (m^2/g) ±5	V_{micro} (cm^3/g) ±0.01	V_P (cm^3/g) ±0.01	Zeta potential (mV) ±0.01	pH of zeta potential (−)	PZC (−) ±0.1
Raw clay	45	0.03	0.07	−10.94	5.4	6
Clay/TMOS 3/10	660	0.30	0.39	−8.07	3.5	3.7
Clay/TMOS 3/3	285	0.14	0.20	+3.40	3.2	3.2
Clay/TMOS 10/3	135	0.07	0.12	+2.41	3.4	3.4
Clay/EDAS 3/3	55	0.02	0.03	+34.49	9.2	8.2
Clay/EDAS 10/3	55	0.02	0.04	+10.34	6.1	5.3

S_{BET}: specific surface area obtained by BET method; V_{micro}: microporous volume; V_p: specific liquid volume adsorbed at saturation pressure of nitrogen.

specific surface area (45 m^2/g), which increases highly when TMOS is used (between 135 and 660 m^2/g). This increase can be due to the production of micro-meso silica materials in the clay. In Fig. 2, the montmorillonite peak nearly disappears with the increase of TMOS amount used during the syntheses.

When EDAS is grafted, only a slight specific surface area increase is observed (around 55 m^2/g) and a reduction of the porous volume (Table 4). This increase is due to the intercalations of the silanes into the smectite lattice (Qian et al., 2008). This insertion is observed in the XRD diagrams (Fig. 2) with the change of position of the peak around 5°.

The isotherms corresponding to the Clay/TMOS and Clay/EDAS series are represented in Figs. 3 and 4, respectively. For the Clay/TMOS series, the isotherms evolve from a type IV isotherm (mesoporous solid for the raw clay) to a type I (microporous solid for the Clay/TMOS 3/10)

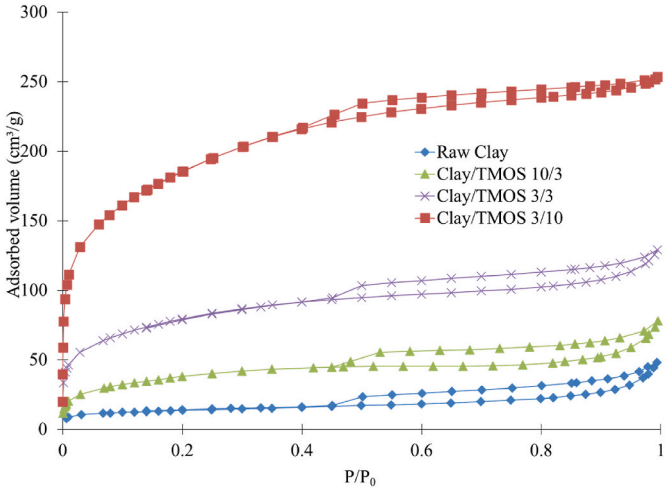

Fig. 3. Nitrogen adsorption–desorption isotherms for (◆) Raw Clay, (▲) Clay/TMOS 10/3, (x) Clay/TMOS 3/3 and (■) Clay/TMOS 3/10 samples.

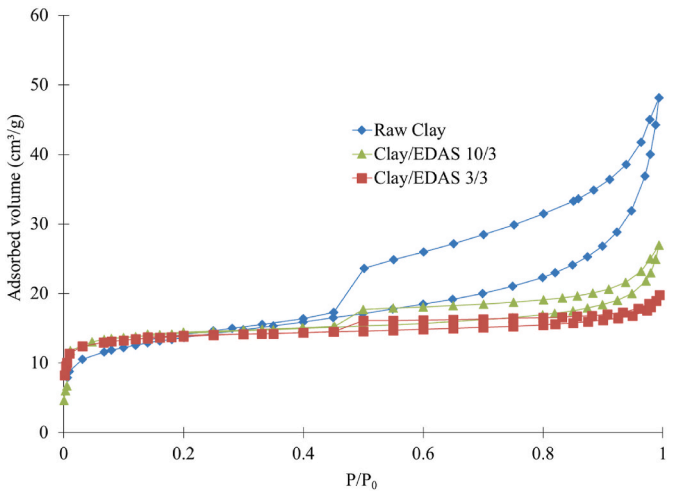

Fig. 4. Nitrogen adsorption–desorption isotherms for (◆) Raw Clay, (▲) Clay/EDAS 10/3 and (■) Clay/EDAS 3/3 samples.

when the amount of TMOS increases compared to the clay. In all samples, a hysteresis is noticed due the presence of mesopores. For the Clay/EDAS series, the shape of the isotherm stays the same, only the volume at saturation decreases due to less mesopores probably filled with EDAS molecules.

A more detailed study of the sample surface was carried out by SEM (Fig. 5). It is observed that the surface of the silica pillared clays by the sol-gel process is considerably affected on some samples as shown in the images in Fig. 5. On the raw material, the typical clay sheets are present; however, on the Clay/TMOS series, the surfaces of the samples are covered with large continuous silica networks giving a rougher aspect of the surface (Fig. 5b and c). These results are in agreement with the high specific surface areas found for the Clay/TMOS series. On the contrary the Clay/EDAS series does not show significant differences with the raw clay sample.

The differences observed in the SEM images, the gelation time during the grafting, XRD patterns and nitrogen adsorption-desorption isotherms in the TMOS and EDAS series can be explain by two different mechanisms in the two series: (i) in the Clay/TMOS series, the addition of TMOS produces amorphous silica network mixed with the clay (Fig. 2) leading to a porous hybrid material (Table 4) where porous silica particles cover the surface of the clay sheets (Fig. 5b, c and 5d); (ii) in the Clay/EDAS series, the EDAS molecules are probably grafted to the surface of the clay producing a continuous dense coating at the surface with similar aspect to the Raw Clay (Fig. 5e and f) reducing the porous volume of the Raw Clay (Table 4) and keeping the same crystallinity of the Raw Clay (Fig. 2) with a displacement of the basal peak.

The formation of both different structures leads to two series of hybrid materials with new surface properties, one with a high surface area containing a lot of silica surface groups and one with silane grafted at the surface containing amine groups. These materials can have interesting adsorption properties due to high porosity or specific amine groups at the surface, their adsorption capacities are explored in the next section.

3.4. Adsorption properties of hybrid samples

The adsorption efficiency of functionalized clays was tested on the removal of 3 model pollutants: fluorescein (FL), malachite green (MG), and brilliant violet diamond (BVD) which are represented in Fig. 6. These pollutants are listed among those generally used in the pesticide and textile industry (Mahy et al., 2019b; Lalonger, 1994; Alderman, 1985). For each pollutant, the evolution of the pollutant concentration over time is estimated with different concentrations of adsorbent materials between 5 and 30 mg of sample for 20 mL of pollutant solution. The initial pH for the three pollutant solutions is 5.3, 6.2, and 7.2 for FL, MG, and BVD, respectively.

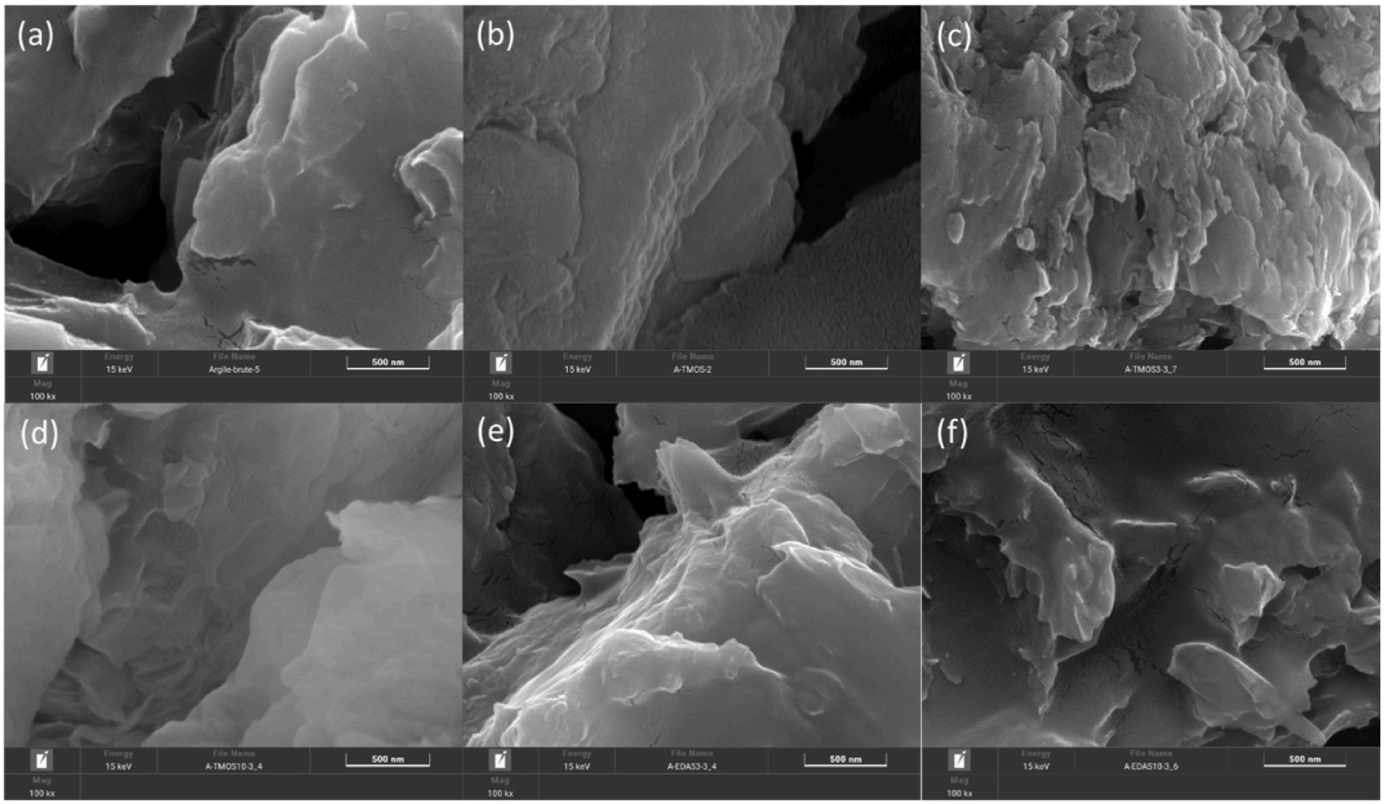

Fig. 5. SEM pictures of (a) Raw Clay, (b) Clay/TMOS 3/10, (c) Clay/TMOS 3/3, (d) Clay/TMOS 10/3, (e) Clay/EDAS 3/3, and (f) Clay/EDAS 10/3 samples.

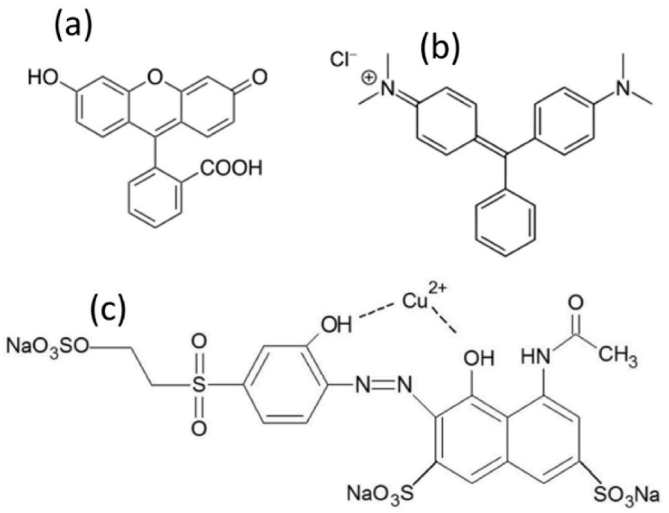

Fig. 6. Molecular structure of (a) fluorescein, (b) malachite green and (c) brilliant violet diamond.

For each sample, the zeta potential and the point of zero charge were measured (Table 4) for a concentration of 1 g/L of sample (it corresponds to the condition with 20 mg of sample). The pH with the different clays is also measured. It will allow to better understand the adsorption phenomenon.

For the fluorescein, Fig. 7 represents the evolution of the concentration (C/C_0) during 1 h for the 6 samples. With the Raw Clay, around 80% of FL are adsorbed during the experiment (Fig. 7a), the modifications with TMOS (Fig. 7b–d) allow to increase the adsorption capacity of the sample leading to a total FL adsorption during the experiments. This modification significantly increases the specific surface area (Table 4). However, the specific surface area is not the only parameter involved in the adsorption process, the nature of the surface groups of the adsorbent plays also a role. For the samples modified with EDAS (Fig. 7e), even if the specific surface area is slightly larger (Table 4), no adsorption occurs during the experiments. The insertion of the ethylenediamine groups of the EDAS have no affinity with FL. It is observed in Table 4, that the introduction of EDAS modifies the surface charge of the Clay/EDAS samples to a more positive value leading to less adsorption of FL.

Both samples modified with EDAS (Clay/EDAS 3/3 and Clay/EDAS 10/3) do not adsorb fluorescein whatever the adsorbent concentration. It is why only one set of point is represented on Fig. 7e.

For the malachite green, Fig. 8 represents the evolution of the concentration (C/C_0) during 1 h for the 6 samples. The raw clay and the

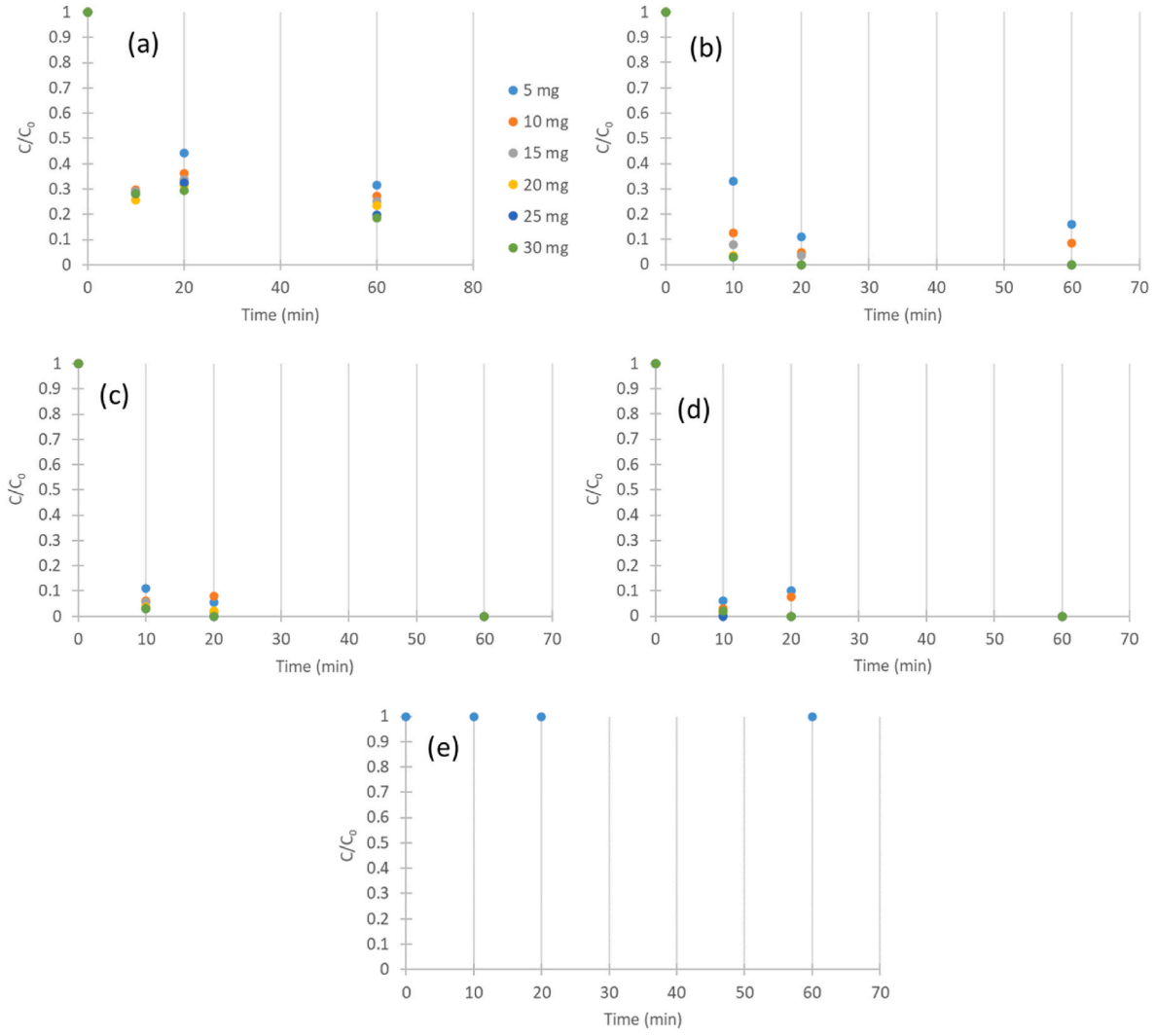

Fig. 7. C/C_0 fluorescein evolution with time for 5–30 mg concentration range for (a) raw clay, (b) Clay/TMOS 10/3, (c) Clay/TMOS 3/3, (d) Clay/TMOS 3/10, and (e) Clay/EDAS 3/3 samples.

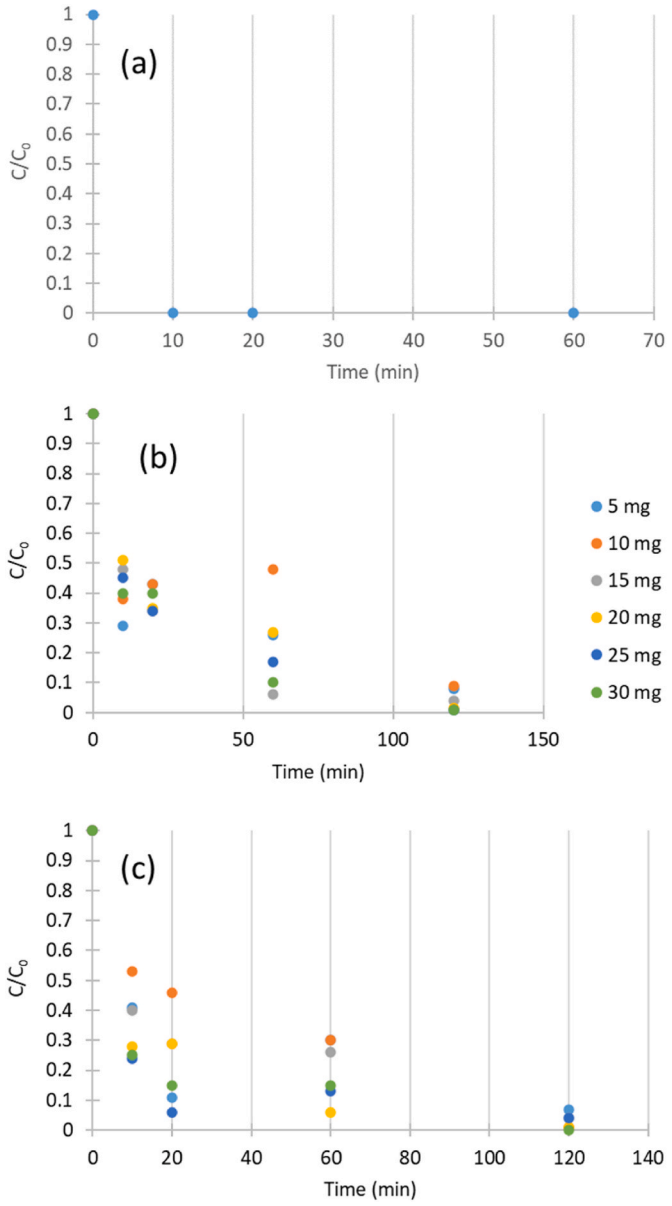

Fig. 8. C/C_0 malachite green evolution with time for 5–30 mg concentration range for (a) raw clay, (b) Clay/EDAS 10/3, and (c) Clay/EDAS 3/3.

samples modified with TMOS adsorb totally MG after 10 min, while the samples modified with EDAS take 2 h to adsorb it totally. The presence of the ethylenediamine groups slows the MG adsorption. The positive charges of the surface of the Clay/EDAS samples (Table 4) seem to slow down the adsorption process.

Raw Clay, and the 3 samples modified with TMOS have the same behavior as represented on Fig. 8a with a complete adsorption of MG after 10 min whatever the adsorbent concentration. It is why only one set of point is represented on Fig. 8a.

For the brilliant violet diamond, the same adsorption behavior is noticed for all samples (Fig. 9) with a fast adsorption of this pollutant in 10 min. For this pollutant, the modification of the clay is not necessary.

Throughout the adsorption of the 3 model pollutants, it is noticed that the surface obtained with samples modified with TMOS brings the most promising adsorbent materials. These materials present the highest specific surface area and a more acidic surface (Table 4). The Clays modified with EDAS results in a more basic surface (Table 4). Depending on the type of pollutant and the surface groups of the adsorbent, very different behaviors can be obtained.

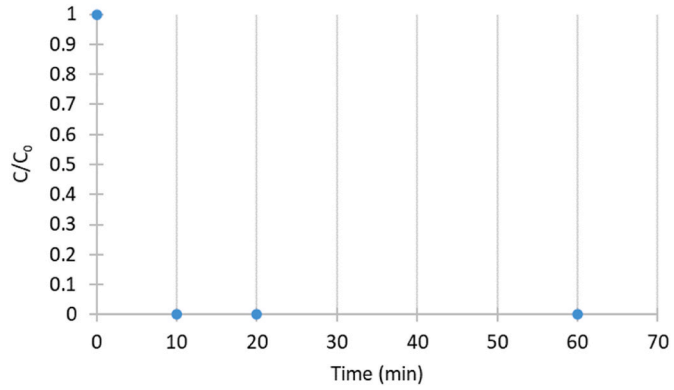

Fig. 9. C/C_0 brilliant violet diamond evolution with time for 5 mg concentration for Raw Clay.

When clay and modified clays are added, the pH of the solution is modified following these tendencies (Table 4): when Clay or Clay/TMOS is added, the pH becomes more acid (between 3.4 and 3.7, Table 4), while with Clay/EDAS, the pH becomes more basic (between 6.1 and 9.2, Table 4). So, the addition of raw Clay and Clay/TMOS samples will result in materials with more acidic sites and/or hydroxyl surface groups that will have more affinity to adsorb on the solid. Contrarily, the Clay/EDAS samples will induce materials with more basic adsorption sites with different adsorption affinity.

All other samples in any concentration have the same the same behavior as represented with a complete adsorption of BVD after 10 min whatever the adsorbent concentration it is why only one set of points is represented on Fig. 9.

3.5. *Comparison with literature*

In Table 5, a comparison of the main results of this study with literature is presented. It is observed that there are many different parameters for one study to another, so a direct comparison is difficult.

Indeed, the materials, the concentration of dye, the time of contact or the design of the adsorption study are different. Nevertheless, it is observed that the modified clays of this study are effective for the removal of three different dyes while usually only one is studied in the other papers. A complete removal of the three pollutants is obtained in a short time (100% in less than 1 h) compared to the other study where at least 2 h are needed. But the dye concentrations of this study (4–20 mg/L) are a bit lower than in other studies (10–240 mg/L). The adsorbent concentration used here (1 g/L) is a bit lower than in other studies (some at 2 (Zaoui et al., 2020), 4 (Ribeiro et al., 2017) or 30 g/L (Shayesteh et al., 2015)).

Zaoui et al. uses also a modified Montmorillonite clay for the removal of MG. 96% is removed after 300 min at a concentration of 2 g/L with an initial MG concentration of 27 mg/L.

4. Conclusion

In this paper, natural raw clay from Cameroon was modified with two silicon alkoxide molecules, tetramethoxysilane (TMOS) and [3-(2-aminoethylamino)propyl]trimethoxysilane (EDAS) in different proportions. The goals of these modifications are to produce hybrid materials with modified surface, higher specific surface area and different surface groups in order to increase their adsorption capacity. The aim is to use these modified clays as organic pollutant adsorbent for water depollution.

The XRD patterns show a dilution of the montmorillonite structure of the raw clay when it is modified with TMOS, while the modification with EDAS keeps its original crystalline structure. When EDAS is introduced, a displacement of the basal peak is observed due to the intercalation of

Table 5
Comparison with literature.

Reference	Materials	Pollutants	Main results
This study	Montmorillonite clay modified with EDAS or TMOS (from Cameroon)	FL (20 mg/L) MG (4 mg/L) BVD (4 mg/L)	100% of adsorption in less than 1 h with the best sample (660 m^2/g – TMOS modified – 1 g/L)
Shayesteh et al. (Shayesteh et al., 2015)	Pumice stone from Iran	MG (10–100 mg/L)	70% of adsorption with 30 g/L of adsorbent
Lesbani et al. (Lesbani et al., 2021)	Keggin Polyoxometalate Intercalated ZnAl Layered Double Hydroxide	MG (40–150 mg/L)	37 mg/g adsorbed on the best sample (2 m^2/g)
Tahir et al. (Tahir et al., 2010)	Montmorillonite clay from Pakistan	MG (10^{-6} to 10^{-3} M) Fast green	97% of removal after 120 min and a concentration of 1 g/L of adsorbent
Zaoui et al. (Zaoui et al., 2020)	natural clay modified with chitosan and thiosulfate (from Algeria)	MG (27 mg/L)	96% of removal after 300 min with 2 g/L of adsorbent
Ribeiro et al. (Ribeiro et al., 2017)	Rice hull from Brazil	BVD (100 mg/L)	73% of removal after 24 h with 4 g/L of adsorbent
Belbel et al. (Belbel et al., 2018)	Homoionic montmorillonite modified with ionic liquid from Wyoming, USA	FL (13–240 µmol/L)	Adsorption capacity of 70 mmol/100 g for the best sample
Pirillo et al. (Pirillo et al., 2009)	Iron oxides (obtained by precipitation method) and chitosan (commercial)	FL (2.5–125 mg/L)	No adsorption on chitosan and very weak on iron oxides
Li et al. (Li et al., 2023)	Anionic sulfonate-functionalized covalent organic framework (synthesized)	FL (10 mg/L)	10% after 120 min with a concentration of 0.25 g/L
Rosli et al. (Rosli et al., 2023)	pineapple peel–based activated carbon from Malaysia	BVD (25 mg/L)	72% after 24 h with a concentration of 0.25 g/L
Anthonysamy et al. (Izwan Anthonysamy et al., 2023)	MgAl/layered double hydroxide supported on rubber seed shell biochar	BVD (25 mg/L)	60% after 24 h with a concentration of 0.8 g/L

the silane. The SEM and BET measurements confirm that two types of materials are produced depending on the silane used: (i) with TMOS, highly porous materials are produced with the formation of silica particles at the surface of the clay with the porosity increasing with the amount of TMOS; (ii) with EDAS, a similar morphology as raw clay is obtained with only a small increase in porosity. In this case, EDAS molecules are grafted at the surface of the clay producing a layer at the surface with new surface ethylenediamine groups.

Both surfaces give different adsorption behaviors on the 3 model pollutants. For the raw clay and the TMOS modified clays, similar adsorption properties are obtained with a better adsorption when the specific surface increases (when TMOS contain increases). In all these samples, similar surface groups are present, the surface groups of the clay and the surface groups of the produced silica (mainly OH groups). A more acidic surface is produced. When clay is modified with EDAS, the adsorption properties change as the surface groups are different due to the grafting of EDAS and a large presence of ethylenediamine groups giving a basic surface. These EDAS modified samples have less affinity with fluorescein and malachite green reducing the adsorption capacity for this kind of pollutants.

The tuning of the raw clay with silane opens the way for the development of highly efficient adsorbent for pollutants in water from natural and inexpensive materials.

Ethical approval

The authors declare that they have no known competing financial interests or personal relationships that could have appeared to influence the work reported in this paper.

Consent to participate

All authors agreed to participate in this work.

Consent to publish

All authors agreed to this version for publication.

CRediT authorship contribution statement

Marlène Huguette Tsaffo Mbognou: Conceptualization, Formal analysis, Investigation, Methodology, Writing – review & editing. **Stéphanie D. Lambert:** Conceptualization, Funding acquisition, Methodology, Project administration, Writing – review & editing. **Ernestine Mimba Mumbfu:** Formal analysis, Investigation. **Joachim Caucheteux:** Funding acquisition, Investigation. **Antoine Farcy:** Formal analysis, Investigation. **Nathalie Fagel:** Funding acquisition, Project administration, Supervision. **Emmanuel Djoufac Woumfo:** Project administration, Supervision. **Julien G. Mahy:** Conceptualization, Formal analysis, Investigation, Methodology, Supervision, Validation, Writing – original draft, Writing – review & editing.

Declaration of competing interest

The authors declare that they have no known competing financial interests or personal relationships that could have appeared to influence the work reported in this paper.

Data availability

Data will be made available on request.

Acknowledgments

Julien G. Mahy and Stéphanie D. Lambert thank the F.R.S.-FNRS for their Postdoctoral Researcher position and Research Director position, respectively. J.G.M. is grateful to the Rotary for a District 2160 grant, to the University of Liège and the FNRS for financial support for a postdoctoral stay at INRS Centre Eau, Terre, Environnement in Québec, Canada. Marlène Huguette Tsaffo Mbognou thanks the PACODEL for her doctoral grant. The authors thank the CARPOR platform of the University of Liège and its manager, Dr. Alexandre Léonard, for the nitrogen adsorption–desorption measurements.

References

Akçay, G., Kilinç, E., Akçay, M., 2009. The equilibrium and kinetics studies of flurbiprofen adsorption onto tetrabutylammonium montmorillonite (TBAM). Colloids Surf. A Physicochem. Eng. Asp. 335, 189–193. https://doi.org/10.1016/j.colsurfa.2008.11.009.

Alderman, D.J., 1985. Malachite green: a review. J. Fish. Dis. 8, 289–298.

Asgari, M., Sundararaj, U., 2018. Silane functionalization of sodium montmorillonite nanoclay: the effect of dispersing media on intercalation and chemical grafting. Appl. Clay Sci. 153, 228–238. https://doi.org/10.1016/j.clay.2017.12.020.

Belbel, A., Kharroubi, M., Janot, J.M., Abdessamad, M., Haouzi, A., Lefkaier, I.K., Balme, S., 2018. Preparation and characterization of homoionic montmorillonite modified with ionic liquid: application in dye adsorption. Colloids Surf. A Physicochem. Eng. Asp. 558, 219–227. https://doi.org/10.1016/j.colsurfa.2018.08.080.

Brinker, G.W., Jeffrey, C., Scherer, 2013. Sol-gel Science: the Physics and Chemistry of Sol-Gel Processing. Academic press.

Carrado, K.A., 2000. Synthetic organo-and polymer-clays: preparation, characterization, and materials applications. Appl. Clay Sci. 17, 1–23. www.elsevier.nlrlocaterclay.

Celis, R., Carmen Hermosín, M., Cornejo, J., 2000. Heavy metal adsorption by functionalized clays. Environ. Sci. Technol. 34, 4593–4599. https://doi.org/10.1021/es000013c.

Claude, V., Mahy, J.G., Geens, J., Courson, C., Lambert, S.D., 2019. Synthesis of Ni/γ-Al2O3-SiO2 catalysts with different silicon precursors for the steam toluene reforming. Microporous Mesoporous Mater. 284, 304–315. https://doi.org/10.1016/j.micromeso.2019.04.027.

De Queiroga, L.N.F., França, D.B., Rodrigues, F., Santos, I.M.G., Fonseca, M.G., Jaber, M., 2019. Functionalized bentonites for dye adsorption: depollution and production of new pigments. J. Environ. Chem. Eng. 7 https://doi.org/10.1016/j.jece.2019.103333.

Dong, J., Zhang, J., 2018. Biomimetic super anti-wetting coatings from natural materials: superamphiphobic coatings based on nanoclays. Sci. Rep. 8 https://doi.org/10.1038/s41598-018-30586-4.

Espínola, J.G.P., Arakaki, L.N.H., De Oliveira, S.F., Da Fonseca, M.G., Campos Filho, J.A. A., Airoldi, C., 2003. Some thermodynamic data of the energetics of the interaction cation-piperazine immobilized on silica gel. Colloids Surf. A Physicochem. Eng. Asp. 221, 101–108. https://doi.org/10.1016/S0927-7757(03)00095-5.

He, H., Duchet, J., Galy, J., Gerard, J.F., 2005. Grafting of swelling clay materials with 3-aminopropyltriethoxysilane. J. Colloid Interface Sci. 288, 171–176. https://doi.org/10.1016/j.jcis.2005.02.092.

He, H., Tao, Q., Zhu, J., Yuan, P., Shen, W., Yang, S., 2013. Silylation of clay mineral surfaces. Appl. Clay Sci. 71, 15–20. https://doi.org/10.1016/j.clay.2012.09.028.

Izwan Anthonysamy, S., Ahmad, M.A., Nasehir, N.K., 2023. Insight the mechanism of MgAl/layered double hydroxide supported on rubber seed shell biochar for Remazol Brilliant Violet 5R removal. Arab. J. Chem. 16 https://doi.org/10.1016/j.arabjc.2023.104643.

Kemgang Lekomo, Y., Mwebi Ekengoue, C., Douola, A., Fotie Lele, R., Christian Suh, G., Obiri, S., Kagou Dongmo, A., 2021. Assessing impacts of sand mining on water quality in Toutsang locality and design of waste water purification system. Clean Eng Technol 2. https://doi.org/10.1016/j.clet.2021.100045.

Komadel, P., Madejová, J., 2006. Chapter 7.1 Acid Activation of Clay Minerals. Dev Clay Sci, pp. 263–287. https://doi.org/10.1016/S1572-4352(05)01008-1.

Lalonger, L., 1994. La transition des colorants naturels aux colorants synthétiques et ses répercussions. Material Culture Review 40.

Lambert, S., Tran, K.Y., Arrachart, G., Noville, F., Henrist, C., Bied, C., Moreau, J.J.E., Wong Chi Man, M., Heinrichs, B., 2008. Tailor-made morphologies for Pd/SiO2 catalysts through sol-gel process with various silylated ligands. Microporous Mesoporous Mater. 115, 609–617. https://doi.org/10.1016/j.micromeso.2008.03.003.

Lesbani, A., Taher, T., Palapa, N.R., Mohadi, R., Mardiyanto, Miksusanti, Arsyad, F.S., 2021. Removal of malachite green dye using keggin polyoxometalate intercalated ZnAl layered double hydroxide. Walailak J. Sci. Technol. 18 https://doi.org/10.48048/wjst.2021.9414.

Li, R., Tang, X., Wu, J., Zhang, K., Zhang, Q., Wang, J., Zheng, J., Zheng, S., Fan, J., Zhang, W., Li, X., Cai, S., 2023. A sulfonate-functionalized covalent organic framework for record-high adsorption and effective separation of organic dyes. Chem. Eng. J. 464 https://doi.org/10.1016/j.cej.2023.142706.

Madejovaʹand, J., Madejovaʹand, M., Komadel, P., 2001. Baseline studies of the clay minerals society source clays: infrared methods. Clay Clay Miner. 49, 410–432. http://pubs.geoscienceworld.org/ccm/article-pdf/49/5/410/3270398/clmn-49-05-0410.pdf?casa_token=bV0nWSPf4BYAAAAA:di3yNEPlB3LnqbzSLitCAQtyepbV1zBF5NSTpvMdV5jK7qQNG8kNGh9rBr2zeBVACfyw-g.

Mahy, J.G., Lambert, S.D., Léonard, G.L.M., Zubiaur, A., Olu, P.Y., Mahmoud, A., Boschini, F., Heinrichs, B., 2016. Towards a large scale aqueous sol-gel synthesis of doped TiO2: study of various metallic dopings for the photocatalytic degradation of p-nitrophenol. J. Photochem. Photobiol. Chem. 329, 189–202. https://doi.org/10.1016/j.jphotochem.2016.06.029.

Mahy, J.G., Claude, V., Sacco, L., Lambert, S.D., 2017. Ethylene polymerization and hydrodechlorination of 1,2-dichloroethane mediated by nickel(II) covalently anchored to silica xerogels. J. Sol. Gel Sci. Technol. 81, 59–68. https://doi.org/10.1007/s10971-016-4272-0.

Mahy, J.G., Paez, C.A., Carcel, C., Bied, C., Tatton, A.S., Damblon, C., Heinrichs, B., Wong Chi Man, M., Lambert, S.D., 2019a. Porphyrin-based hybrid silica-titania as a visible-light photocatalyst. J. Photochem. Photobiol. Chem. 373 https://doi.org/10.1016/j.jphotochem.2019.01.001.

Mahy, J.G., Lambert, S.D., Tilkin, R.G., Wolfs, C., Poelman, D., Devred, F., Gaigneaux, E. M., Douven, S., 2019b. Ambient temperature ZrO_2-doped TiO_2 crystalline photocatalysts: highly efficient powders and films for water depollution. Mater. Today Energy 13. https://doi.org/10.1016/j.mtener.2019.06.010.

Mahy, J.G., Mbognou, M.H.T., Léonard, C., Fagel, N., Woumfo, E.D., Lambert, S.D., 2022. Natural clay modified with ZnO/TiO2 to enhance pollutant removal from water. Catalysts 12. https://doi.org/10.3390/catal12020148.

Mahy, J.G., Carcel, C., Chi Man, M.W., 2023. Evonik P25 photoactivation in the visible range by surface grafting of modified porphyrins for p-nitrophenol elimination in water. AIMS Mater Sci 10, 437–452. https://doi.org/10.3934/matersci.2023024.

Mercier, L., Pinnavaia, T.J., 1998. Heavy metal ion adsorbents formed by the grafting of a thiol functionality to mesoporous silica molecular sieves: factors affecting Hg(II) uptake. Environ. Sci. Technol. 32, 2749–2754. https://pubs.acs.org/sharingguidelines.

Nodehi, R., Shayesteh, H., Kelishami, A.R., 2020. Enhanced adsorption of Congo red using cationic surfactant functionalized zeolite particles. Microchem. J. 153 https://doi.org/10.1016/j.microc.2019.104281.

Paredes-Quevedo, L.C., Castellanos, N.J., Carriazo, J.G., 2021. Influence of porosity and surface area of a modified kaolinite on the adsorption of basic red 46 (BR-46). Water Air Soil Pollut. 232 https://doi.org/10.1007/s11270-021-05450-3.

Park, A.Y., Kwon, H., Woo, A.J., Kim, S.J., 2005. Layered double hydroxide surface modified with (3-aminopropyl) triethoxysilane by covalent bonding. Adv. Mater. 17, 106–109. https://doi.org/10.1002/adma.200400135.

Pirillo, S., Pedroni, V., Rueda, E., Ferreira, M.L., 2009. Elimination of dyes from aqueous solutions using iron oxides and chitosan as adsorbents. Quim. Nova 32. A COMPARATIVE STUDY.

Piscitelli, F., Posocco, P., Toth, R., Fermeglia, M., Pricl, S., Mensitieri, G., Lavorgna, M., 2010. Sodium montmorillonite silylation: unexpected effect of the aminosilane chain length. J. Colloid Interface Sci. 351, 108–115. https://doi.org/10.1016/j.jcis.2010.07.059.

Piscitelli, F., Scamardella, A.M., Romeo, V., Lavorgna, M., Barra, G., Amendola, E., 2012. Epoxy composites based on amino-silylated MMT: the role of interfaces and clay morphology. J. Appl. Polym. Sci. 124, 616–628. https://doi.org/10.1002/app.35015.

Qian, Z., Hu, G., Zhang, S., Yang, M., 2008. Preparation and characterization of montmorillonite-silica nanocomposites: a sol-gel approach to modifying clay surfaces. Phys. B Condens. Matter 403, 3231–3238. https://doi.org/10.1016/j.physb.2008.04.008.

Queiroga, L.N.F., Pereira, M.B.B., Silva, L.S., Silva Filho, E.C., Santos, I.M.G., Fonseca, M. G., Georgelin, T., Jaber, M., 2019. Microwave bentonite silylation for dye removal: influence of the solvent. Appl. Clay Sci. 168, 478–487. https://doi.org/10.1016/j.clay.2018.11.027.

Queiroga, L.N.F., Nunes Filho, F.G., França, D.B., Rodrigues, F., Jaber, M., Fonseca, M.G., 2021. Aminopropyl bentonites obtained by microwave-assisted silylation for copper removal. Colloids Surf. A Physicochem. Eng. Asp. 630 https://doi.org/10.1016/j.colsurfa.2021.127557.

Ribeiro, G.A.C., Silva, D.S.A., Dos Santos, C.C., Vieira, A.P., Bezerra, C.W.B., Tanaka, A. A., Santana, S.A.A., 2017. Removal of Remazol brilliant violet textile dye by adsorption using rice hulls. Polimeros 27, 16–26. https://doi.org/10.1590/0104-1428.2386.

Rosli, N.A., Ahmad, M.A., Noh, T.U., 2023. Nature's waste turned savior: optimizing pineapple peel–based activated carbon for effective Remazol Brilliant Violet dye adsorption using response surface methodology. Inorg. Chem. Commun. 153 https://doi.org/10.1016/j.inoche.2023.110844.

Schreier, M., Regalbuto, J.R., 2004. A fundamental study of Pt tetraammine impregnation of silica: 1. The electrostatic nature of platinum adsorption. J. Catal. 225, 190–202. https://doi.org/10.1016/j.jcat.2004.03.034.

Shayesteh, H., Rahbar-Kelishami, A., Norouzbeigi, R., 2015. Adsorption of malachite green and crystal violet cationic dyes from aqueous solution using pumice stone as a low-cost adsorbent: kinetic, equilibrium, and thermodynamic studies. Desalination Water Treat. 57, 12822–12831. https://doi.org/10.1080/19443994.2015.1054315.

Slaný, M., Jankovič, Ľ., Madejová, J., 2019. Structural characterization of organo-montmorillonites prepared from a series of primary alkylamines salts: mid-IR and near-IR study. Appl. Clay Sci. 176, 11–20. https://doi.org/10.1016/j.clay.2019.04.016.

Song, K., Sandi, G., 2001. Characterization of montmorillonite surfaces after modification by organosilane. Clay Clay Miner. 49, 119–125.

Srivastava, R., Fujita, S., Arai, M., 2009. Synthesis and adsorption properties of smectite-like materials prepared using ionic liquids. Appl. Clay Sci. 43, 1–8. https://doi.org/10.1016/j.clay.2008.06.015.

Tahir, H., Hammed, U., Sultan, M., Jahanzeb, Q., 2010. Batch adsorption technique for the removal of malachite green and fast green dyes by using montmorillonite clay as adsorbent. Afr. J. Biotechnol. 9, 8206–8214. https://doi.org/10.5897/ajb10.911.

Tchanang, G., Djangang, C.N., Abi, C.F., Moukouri, D.L.M., Blanchart, P., 2021. Synthesis of reactive silica from kaolinitic clay: effect of process parameters. Appl. Clay Sci. 207 https://doi.org/10.1016/j.clay.2021.106087.

Tonle, I.K., Ngameni, E., Njopwouo, D., Carteret, C., Walcarius, A., 2003. Functionalization of natural smectite-type clays by grafting with organosilanes: physico-chemical characterization and application to mercury(II) uptake. Phys. Chem. Chem. Phys. 5, 4951–4961. https://doi.org/10.1039/b308787e.

Viville, P., Lazzaroni, R., Pollet, E., Alexandre, M., Dubois, P., 2004. Controlled polymer grafting on single clay nanoplatelets. J. Am. Chem. Soc. 126, 9007–9012. https://doi.org/10.1021/ja048657y.

Wheeler, P.A., Wang, J., Baker, J., Mathias, L.J., 2005. Synthesis and characterization of covalently functionalized laponite clay. Chem. Mater. 17, 3012–3018. https://doi.org/10.1021/cm050306a.

Zaoui, F., Choumane, F.Z., Hakem, A., 2020. Malachite green dye and its removal from aqueous solution by clay-chitosane modified. Mater. Today Proc. 49, 1105–1111. https://doi.org/10.1016/j.matpr.2021.09.487.

Zhou, C.H., Zhao, L.Z., Wang, A.Q., Chen, T.H., He, H.P., 2016. Current fundamental and applied research into clay minerals in China. Appl. Clay Sci. 119, 3–7. https://doi.org/10.1016/j.clay.2015.07.043.

Next Materials 9 (2025) 101290

Contents lists available at ScienceDirect

Next Materials

journal homepage: www.sciencedirect.com/journal/next-materials

Research article

Dual-function Cameroonian clay-supported ZnO and TiO_2 photocatalysts for ibuprofen mineralization and bacterial inactivation

Marlène Huguette Tsaffo Mbognou [a,b,c], Stéphanie D. Lambert [a], Antoine Farcy [a], Hela Rekik [d], Steven C.N. Wouamba [e,f], Emmanuel Djoufac Woumfo [b], Julien G. Mahy [a,*]

[a] Department of Chemical Engineering – Nanomaterials, Catalysis & Electrochemistry, University of Liège, B6a, Quartier Agora, Allée du six Août 11, Liège 4000, Belgium
[b] Laboratoire de Physico-chimie des matériaux minéraux, University of Yaounde, I, 337, Yaounde, Cameroon
[c] Institute of Geological and Mining Research (IRGM), Yaounde 4110, Cameroon
[d] Institut National de la Recherche Scientifique (INRS), Centre-Eau Terre Environnement, Université du Québec, 490, Rue de la Couronne, Québec, QC G1K 9A9, Canada
[e] Department of Chemistry, Higher Teacher Training College, University of Yaounde I, P.O. Box 47, SPO, Yaounde, Cameroon
[f] Université de Montpellier, INRAE, Montpellier SupAgro, Montpellier 34000, France

ARTICLE INFO

Keywords:
Ibuprofen
Photocatalysis
ZnO/TiO_2-doped clay
Mineralization
Antibacterial activity
Wastewater treatment

ABSTRACT

The increasing presence of pharmaceuticals, such as ibuprofen, in wastewater poses significant environmental and public health challenges, particularly in developing regions. In this study, we developed photocatalytic materials by doping natural Cameroonian clay with ZnO and TiO_2 to achieve efficient ibuprofen mineralization and bacterial inactivation under ultra-violet (UV) light. Characterization confirmed the successful integration of semiconductors into the clay matrix, which enhanced the surface area to 325 m^2/g for TiO_2-based composites. Under UVA irradiation (1.2 mW/cm^2), the Cu-doped TiO_2/clay composite achieved 48 % ibuprofen mineralization, measured by Total Organic Carbon (TOC) reduction, within 4 h, while ZnO-based composites reached up to 23 % under similar conditions. Antibacterial tests demonstrated complete inhibition of Shigella spp., total coliforms, and faecal streptococci at a catalyst dosage of 1 g/L under UVA, highlighting the dual functionality of the materials. These low-cost, locally sourced photocatalysts show promise for integrated pharmaceutical and microbial removal in decentralized wastewater treatment systems, offering a sustainable solution for water purification in resource-limited settings.

1. Introduction

Over the past two decades, numerous studies have reported the presence of harmful substances in environmental matrices such as sewage, surface and groundwater, and even drinking water [1–3]. According to the World Health Organization (WHO), approximately 10 % of the global population consumes food irrigated with untreated wastewater [4]. This widespread reuse of contaminated water contributes to the spread of waterborne diseases such as amoebiasis, affecting both industry workers and local populations, regardless of age, gender, or social status [1].

In many African countries, particularly in Cameroon, over 90 % of human waste is managed through non-centralized systems and is often discharged directly into the environment without proper treatment [3]. Such practices have severe implications for both human health and ecosystems, as fecal sludge is often rich in pathogenic indicator bacteria (E. coli, Shigella, fecal streptococci) and contains high levels of pharmaceutical residues.

Among these contaminants, ibuprofen, a widely used non-steroidal anti-inflammatory drug, has been frequently detected in the effluents of wastewater treatment plants and in surface waters at concentrations ranging from $ng{\cdot}L^{-1}$ to $\mu g{\cdot}L^{-1}$ [5,6]. It poses ecotoxicological risks to aquatic organisms and potential health concerns to humans [7–9]. Conventional wastewater treatment technologies often fail to remove such micropollutants effectively. Consequently, tertiary treatment approaches, particularly advanced oxidation processes (AOPs), have emerged as promising alternatives for degrading and mineralizing persistent organic pollutants, including pharmaceuticals and pathogenic microorganisms. AOPs operate through the generation of highly reactive and non-selective oxidizing species, primarily hydroxyl radicals ($^{\bullet}OH$), which can break down most organic compounds present in water [10–15].

* Corresponding author.
E-mail address: julien.mahy@uliege.be (J.G. Mahy).

https://doi.org/10.1016/j.nxmate.2025.101290
Received 5 August 2025; Received in revised form 27 September 2025; Accepted 30 September 2025
Available online 3 October 2025

Recent advancements in AOPs have emphasized the development of clay-supported semiconductor composites for enhanced degradation of pharmaceuticals and dyes, underscoring the potential for sustainable water treatment. For instance, Trigueiro et al. [16] synthesized a ZnO-alginate-hectorite nanocomposite achieving 65.55 % furosemide and 93 % ciprofloxacin removal under UV light within 120 min, with a band gap of 3.27 eV and predominant defects like zinc (V_{Zn} = 35.64 %) and oxygen vacancies (V_{O+} = 56.05 %, V_O = 8.31 %). Similarly, Y-doped ZnO on alginate-hectorite supports provided over 90 % degradation of direct blue 71 and 79 % of reactive black 5 in 120 min, driven by hydroxyl radicals [17]. Albuquerque et al. [18] reported a RuO_2@ZnO-alginate-halloysite composite with band gaps from 3.281 to 3.252 eV, degrading 82.53 % ciprofloxacin and 68.68 % eosin yellow under UV, with superoxide (•O_2^-) and hydroxyl (•OH) as key species. Trigueiro et al. [19] developed CuO-TiO_2-saponite nanocomposites achieving 83 % bromocresol green discoloration in 150 min via hydroxyl and superoxide radicals. Feitosa et al. [20] used Ce-doped TiO_2-sepiolite for 70.45 % tetracycline inactivation (35.11 % photocatalysis), primarily via holes (h^+). Hamarawf et al. [21] introduced a Fe^{2+}/Fe^{3+} mixed-valency porous coordination polymer with antibacterial activity (MIC 0.4 mg/mL against S. aureus, E. coli, P. aeruginosa) and 99.16 % rhodamine B degradation in 70 min via photo-Fenton, involving •OH (79.2 %), O_2•$^-$ (20.7 %), and h^+ (16.4 %). Specifically for ibuprofen, Aziz et al. [22] employed a TiO_2-coated falling film reactor under UVA, identifying low mineralization with by-products like formic and acetic acids. Soares et al. [23] showed pH-dependent Co-doped ZnO achieving up to 20 % ibuprofen degradation under UV with H_2O_2. These studies highlight the efficacy of hybrid materials but reveal gaps in using underexplored local clays like Cameroonian smectite for ibuprofen photodegradation, which this work addresses through low-cost, dual-functional ZnO/TiO_2-doped composites.

Photocatalysis, one of the most widely studied AOPs, relies on the activation of semiconductor materials such as titanium dioxide (TiO_2) or zinc oxide (ZnO) under UV irradiation [10,24,25]. These photocatalysts generate photo-induced electron-hole pairs (e^-/h^+), which in turn initiate the formation of reactive oxygen species. For instance, Méndez-Arriaga et al. [26] successfully demonstrated the photocatalytic degradation of highly concentrated ibuprofen (200 mg·L^{-1}) using TiO_2 in suspension under simulated solar light. Walczak et al. [5] showed the effective degradation of ibuprofen with TiO_2 doped with carbon nanotube up to 20 % in 1 h UV–visible exposition. While effective, the use of photocatalysts in suspension suffers from practical limitations such as aggregation, post-treatment recovery issues, and low adsorption capacity [5].

To overcome these limitations, research has increasingly focused on the development of hybrid materials combining photocatalysts with natural or engineered supports. In this context, clay minerals, particularly smectites, offer an attractive platform due to their low cost, chemical and mechanical stability, large surface area, high cation exchange capacity, and environmental compatibility [27–29]. In the African context, local clays, including those from Cameroon, remain largely underexplored despite their potential as adsorbents or catalysts. Promising results have been reported for the adsorption or degradation of dyes and volatile organic compounds, including green malachite and similar pollutants [30,31]. Nevertheless, applications targeting pharmaceuticals remain scarce and, to our knowledge, no published studies have yet investigated the photochemical degradation of ibuprofen using visible or UVA light on Cameroonian clays modified with photocatalysts.

Furthermore, in the search for multifunctional materials, the integration of antimicrobial activity into photocatalytic systems is gaining interest, especially in regions where waterborne pathogens pose a major health risk. The incorporation of metal ions (e.g., Cu^+, Zn^{2+}) into clay structures has been shown to enhance antibacterial effects, which could offer a dual action strategy: the degradation of pharmaceutical residues and the disinfection of contaminated water [32,33].

In this study, we synthesized and characterized composite photocatalysts based on natural Cameroonian smectite clay, doped with TiO_2 or ZnO nanoparticles, with or without ion-exchange modifications using Na^+, Zn^{2+}, or Cu^+ cations. Comprehensive analyses, including X-ray diffraction (XRD), scanning electron microscopy (SEM), and nitrogen adsorption-desorption, confirmed the successful integration of semiconductors into the clay matrix, enhancing surface area for composites and optimizing particle dispersion. We evaluated their performance for the photocatalytic degradation of ibuprofen under UVA (1.2 mW/cm^2) and UV-Visible (UV-Vis) irradiation, with mineralization efficiency quantified via Total Organic Carbon (TOC) analysis. This approach provides a rigorous assessment of complete pollutant breakdown into inorganic end-products, surpassing the limitations of UV-Vis spectroscopy alone and addressing a gap in similar studies where partial degradation is often reported.

In parallel, the antimicrobial properties of these materials were examined to assess their potential for simultaneous pharmaceutical removal and microbial disinfection. Antibacterial tests targeted waterborne pathogens, including Shigella spp., total coliforms, and faecal streptococci, under controlled UVA conditions. We hypothesize that the incorporation of TiO_2 or ZnO, combined with cationic modifications, will enhance ibuprofen mineralization by up to 50 % (based on preliminary TOC data) and achieve complete inhibition of these pathogens at a catalyst dosage of 1 g/L within 4 h, driven by improved surface charge, porosity, and reactive oxygen species (ROS) generation. This work proposes a multifunctional strategy, using locally sourced Cameroonian clay to develop low-cost, eco-compatible photocatalysts that integrate adsorption, photocatalysis, and antibacterial activity. By targeting this underexplored research niche, the study contributes to an innovative solution for sustainable water treatment technologies tailored to the needs of developing regions, particularly in the African context.

2. Materials and methods

2.1. Clay description and modification

A natural smectite clay was extracted from Bakotcha, in the western region of Cameroon (details in [13]). After drying to constant weight, the clay was modified via interlayer cation exchange with Cu^{2+} and Zn^{2+} ions, as well as homoionization with Na^+ ions.

2.1.1. Sodium Ion Insertion

The detailed protocol is given in [31] and summarized here. The following reagents were used: distilled water, sodium chloride (≥99.5 %, Fisher BioReagents), silver nitrate (99 %, ultrapure, Laboratorium Discounter), and clay powder (>160 μm). Sodium homoionization was performed to replace all exchangeable cations with Na^+: 100 g of clay was stirred in 1 M NaCl solution for 72 h. After drying at 100 °C for 24 h, the material was stirred again in NaCl for 4 h to promote cation exchange.

After settling, the supernatant was discarded and the solid was redispersed in a fresh NaCl solution. This step was repeated four times. The clay was then washed with distilled water until no chloride ions were detected via the silver nitrate test. A negative result (no precipitate) confirmed successful washing. The Na^+-homoionic clay was dried at 100 °C overnight.

2.1.2. Zinc ion insertion

The detailed protocol is given in [13] and summarized here. This treatment allowed incorporation of Zn^{2+} without altering the clay structure. The reagents used were zinc(II) chloride (≥97.0 %, Laboratorium Discounter), silver nitrate (99 %, ultrapure), clay powder (>160 μm), and distilled water. 50 g of clay was stirred in 0.1 M $ZnCl_2$ for 4 h. After settling for 2 h, the supernatant was discarded and replaced with fresh $ZnCl_2$ solution. The process was repeated twice. Washing continued until a negative silver nitrate test confirmed the removal of

excess Cl^-. The Zn^{2+}-homoionic clay was then dried overnight at 100 °C.

2.1.3. Copper ion insertion

The detailed protocol is given in [13] and summarized here. The reagents were copper(II) sulfate pentahydrate (≥98.0 %, Sigma-Aldrich), barium sulfate (99 %, Sigma-Aldrich), clay powder (>160 μm), and distilled water. 50 g of clay was stirred in 0.1 M $CuSO_4$ for 4 h, allowed to settle for 2 h and then treated with fresh $CuSO_4$ solution. This process was repeated twice. The material was washed with distilled water until no SO_4^{2-} ions were detected using the barium precipitation test. The Cu^{2+}-homoionic clay was then dried at 100 °C overnight.

2.2. Synthesis of pure TiO_2 and ZnO photocatalysts

2.2.1. ZnO powder

The sol-gel method by Benhebal et al. [34] was used. Reagents included absolute ethanol (ACS grade), oxalic acid dihydrate (99 %), and zinc acetate dihydrate (98 %) from BIOCHEM Chemopharma (France). 10.98 g of zinc acetate was dissolved in 300 mL ethanol at 60 °C. Separately, 12.6 g of oxalic acid was dissolved in 200 mL ethanol at the same temperature. The oxalic acid solution was slowly added to the zinc solution while stirring for 90 min at 50 °C. The gel was dried at 80 °C for 24 h and calcined at 400 °C for 4 h, resulting in a white ZnO powder.

2.2.2. TiO_2 powder

The sol-gel method by Mahy et al. [35] was followed. Reagents: isopropanol (99.5 %, Acros), nitric acid (65 %, Merck), titanium(IV) tetraisopropoxide (TTIP ≥ 97 %, Sigma-Aldrich), and distilled water.

250 mL of distilled water was acidified to pH 1 with HNO_3. Then, 15 mL TTIP and 15 mL isopropanol were mixed and stirred for 30 min at room temperature. This solution was added dropwise to the acidified water under continuous stirring and heated to 80 °C for 4 h. A blue sol formed. After drying under airflow for 10 h, the xerogel was obtained. It was then dried at 100 °C for 1 h, yielding a yellowish-white TiO_2 powder.

2.3. Synthesis of clay/photocatalyst composites

2.3.1. Clay/ZnO composites

Following the ZnO synthesis protocol, 10 g of clay was added during the oxalic acid addition step. The mixture was stirred for 90 min at 50 °C. After gelation and drying at 80 °C for 24 h, the composite was calcined at 400 °C for 4 h. The final material appeared light grey. The samples are called A-X/ZnO with X standing for a specific cation (Cu, Zn or Na). The raw clay modified with ZnO is called A/ZnO.

2.3.2. Clay/TiO_2 composites

Following the TiO_2 synthesis method, 10 g of clay was added to the blue sol and stirred for 2 h. The mixture was dried for 24 h to obtain the clay/TiO_2 hybrid material. The samples are named similarly to the ZnO series, replacing ZnO with TiO_2.

2.4. Characterization techniques

The apparent density was measured using a Micromeritics AccuPyc 1330 helium pycnometer at 20 °C and 18 psi. Three replicates per sample were performed and average values were reported with < 1 % standard deviation.

Specific surface area was determined by nitrogen adsorption–desorption isotherms at 77 K using a Micromeritics ASAP 2420 instrument.

SEM imaging (15 kV) was performed using a Bruker TESCAN CLARA. Samples were sonicated in acetone, deposited on slides, and gold-coated before observation.

Zeta potential and hydrodynamic diameter were measured by dynamic light scattering (DLS) using a Beckman Coulter DelsaNano C.

The point of zero charge (PZC) of each sample was determined using the method described by [36]. Eleven vials were prepared, each containing 10 mL of Milli-Q water. The initial pH of each vial was adjusted using diluted HCl or NaOH to cover a pH range from 2 to 10, with an increment of 1 pH unit between successive vials. An equal volume of the sample suspension was then added to each vial. The amount of sample added was calculated to achieve a surface concentration of 1000 $m^2 \cdot L^{-1}$, corresponding to a total surface area of 10 m^2 in 10 mL, depending on the specific surface area of the material. The vials were then shaken for 1 h to allow equilibration. After this time, the final pH of each solution was measured. A graph was plotted comparing the final and initial pH values, and the PZC was determined as the pH value at which the curve reaches a plateau, as described by [36]. All pH measurements were carried out using a Systronics μ 362 pHmeter (India).

ICP–AES (ICAP 6500 THERMO Scientific) was used to determine elemental composition [37]. HF digestion was used for mineralization [13,37].

XRD analysis was performed using a Bruker D8 Twin-Twin diffractometer with Cu-Kα radiation.

Similar comprehensive characterization approaches, including XRD, SEM-EDS, BET, and FTIR, have been employed in [38]. This reference underscores the importance of multi-technique analysis in validating catalyst efficacy for AOPs targeting pharmaceuticals.

2.5. Analytical methods

2.5.1. Photocatalytic activity

The photocatalytic activity of the synthesized materials was evaluated by monitoring the degradation of ibuprofen (IBU) under UV irradiation. The experiments were performed using 2 types of UV lamps: one emitting at 365 nm (Osram F18W/BLB-T8, 1.2 mW/cm^2) and one halogen lamp (with a continuous spectrum from 300 to 800 nm (300 W, 220 V), 78 mW/cm^2 with 77 mW/cm^2 in the visible range) placed in a irradiation chamber [39], maintaining a constant distance of 20 cm between the light source and the sample surface.

For each material, 50 mL of an aqueous ibuprofen solution (initial concentration: 52 mg/L) was placed in a flat Petri dish with a diameter of 8.5 cm. All tests were conducted under magnetic stirring in the dark for 30 min prior to irradiation, to ensure adsorption–desorption equilibrium. After this equilibration period, the samples were irradiated for up to 4 h. The reactor temperature was maintained at 25 ± 2 °C.

Three independent replicates were performed for each material. Control experiments were conducted under the same conditions and also in the dark using (i) raw clay, (ii) TiO_2 or ZnO alone, and (iii) the ibuprofen solution without any added material to distinguish between adsorption, photolysis, and photocatalytic degradation.

At regular time intervals (typically every 2 h), 20 mL aliquots were withdrawn, filtered through 0.45 μm membranes, and stored at 4 °C prior to analysis. The degradation of ibuprofen was monitored using Total Organic Carbon (TOC) analysis. TOC was performed using a Shimadzu TOC-L analyzer equipped with an autosampler and a high-sensitivity catalyst. TOC reduction was used to assess the mineralization efficiency of each material.

All measurements were conducted in triplicate, and the mean values are reported with standard deviations below 5 %.

For the two best composite samples, a kinetic study is performed under UVA light. From [40], IBU degradation can be described by the following equation:

$$C = C_0 e^{\left(-k\frac{m}{V_0}t\right)} \quad (1)$$

Where C is the concentration of the pollutant, C_0 is the initial concentration of the pollutant, k is the kinetic constant, m is the mass of the catalyst, V_0 is the initial solution volume, and t is the time.

By plotting -ln(C/C$_0$) as a function of time t, the constant reaction rate k, can be determined [41].

The amount of metal ion released during photocatalytic experiments under UVA after 4 h was also measured for TiO_2, A/TiO_2, ZnO and A-Cu/ZnO samples. After 4 h of photocatalytic experiments under UVA light, the water medium is filtered with syringe filter (polypropylene, 13 mm diameter, 0.2 µm pore size, Whatman™, VWR) and the metal ion (Ti, Zn, Cu) content in the filtrate is measured by ICP-AES.

2.5.2. Scavenger experiments

Ammonium oxalate (AO, 5 mM), isopropanol (ISOP, 5 mM), and p-benzoquinone (PB, 0.5 mM) are used as, respectively, hole, hydroxyl radical and superoxide scavenger in ibuprofen aqueous solution filled with the two best composite samples (A/ZnO and A-Cu/TiO_2) with a photocatalyst concentration of 1 g/L, inspired by [40,42,43]. Measurements are performed after 4 h (under UVA light) using TOC measurements previously calibrated with the scavengers.

2.5.3. Antibacterial assay

Wastewater was collected from the wastewater treatment plant « Cité verte » Yaoundé-Cameroun and used for the antibacterial experiments. 50 mL of this wastewater was stirred with the samples (with a concentration of 0.5, 1, or 10 g/L) under UVA illumination (365 nm) for 4 h at a control temperature of 25 °C. Then the bacterial content (3 types: total coliforms, faecal coliforms, and faecal streptococci) was evaluated with the protocol below. Control experiments were made without samples both with and without illumination to highlight the effect of the materials on the bacteria and also with the materials and no light.

a) Bacterial Strains analyzed

The culture media used were as follows:

XLD agar (Xylose-Lysine-Deoxycholate agar): a moderately selective and differential medium for the isolation and differentiation of Gram-negative enteric pathogens. It was specifically used for the identification of Salmonella and Shigella species.

Endo agar: a slightly selective and differential culture medium for the detection of coliforms and other enteric bacteria. It was primarily used to identify Escherichia coli and to enumerate total and faecal coliforms.

BEA agar (Bile Esculin Agar): a selective and differential medium used to detect group D Enterococci and Streptococcus. Only colonies forming black precipitates were counted.

b) Bacteriological Analysis

The bacteriological analysis focused on indicator organisms of microbial contamination, namely: total coliforms, faecal coliforms, and faecal streptococci.

Colonies were enumerated using two complementary techniques for data validation: surface plating and flooding on nutrient agar. Incubation was performed at 37 °C for 24 h for total and faecal coliforms, and 48 h for faecal streptococci.

Mueller-Hinton Dilution Method

The antibacterial activity of the hybrid materials was also assessed using the dilution method on Mueller–Hinton agar. In this assay, bacteria were cultured in the presence of increasing concentrations of the hybrid material (0.5 g·L^{-1}, 1 g·L^{-1}, and 10 g·L^{-1}). After incubation, the presence or absence of bacterial colonies was macroscopically examined to evaluate bacterial growth inhibition.

Sterilized distilled water (autoclaved at 121 °C for 15 min) was used as a diluent, with serial dilutions being performed up to 1:100,000 for highly contaminated samples. Three agar plates per dilution were inoculated using both surface plating and flooding methods. Colony counts were performed after incubation (37 °C for 24 h for total coliforms and Salmonella/Shigella; 37 °C for 48 h for faecal streptococci), and the results were corrected based on the dilution factors.

Results are expressed as log colony-forming units per milliliter (log (CFU·mL^{-1})) according to established procedures [44]. Colonies were counted only on plates with 15–300 colonies. If all plates contained fewer than 15 colonies, all observed colonies were counted, considering the total inoculated volume.

3. Results

3.1. Composition and crystallinity of samples

The elemental composition of the synthesized samples was determined by inductively coupled plasma atomic emission spectroscopy (ICP-AES) and is reported in Table 1. As expected, the raw clay is primarily composed of aluminum and silicon, with an Al/Si ratio close to 2, which is characteristic of smectite-type clays [13]. Upon incorporation of metal ions (Cu, Na, or Zn), a corresponding increase in the concentration of these elements is clearly observed, confirming the success of the ion-exchange process.

For the composite materials, the incorporation of 30 wt% photocatalyst (either TiO_2 or ZnO) was achieved as intended, according to the measured compositions. These values are consistent with similar materials reported in the literature [13], supporting the reproducibility and reliability of the synthesis route employed.

The crystalline structure of the samples was analyzed by X-ray diffraction (XRD), and representative diffractograms are presented in Fig. 1. The raw clay exhibits a complex mineralogical composition, including phases such as augite, cristobalite, montmorillonite, illite, kaolinite, feldspar, and talc. These phases remain identifiable in the ion-exchanged clays, indicating that the structural integrity of the clay matrix is largely preserved after modification.

The diffractograms of the pure ZnO and TiO_2 photocatalysts show diffraction peaks corresponding to the wurtzite structure for ZnO and a mixture of anatase and brookite for TiO_2. Accordingly, these crystalline phases are also observed in the composite samples, confirming the successful integration of the photocatalyst without significant alteration of its crystal structure. These findings are consistent with those reported in our previous study using similar preparation protocols [13].

Overall, the XRD and ICP-AES results jointly demonstrate that the synthesis procedure yields stable and well-defined clay-based composite materials with preserved crystalline properties and controlled photocatalyst loading.

3.2. Textures and morphology of samples

The textural properties and colloidal behavior of the prepared composites were assessed through BET surface area analysis, pore volume (V_p), apparent density (ρ_{app}), zeta potential measurements, and dynamic light scattering (DLS). These parameters are summarized in Table 2.

The pristine clay exhibited a modest surface area (45 m^2/g) and low

Table 1
Sample compositions by ICP-AES.

	Al	Si	Fe	Cu	TiO_2	ZnO
	wt%	wt%	wt%	wt%	wt%	wt%
Raw clay	10.1	20.9	3.7	< 0.1	< 0.1	< 0.1
A/ZnO	5.2	9.2	1.6	< 0.1	< 0.1	28.1
A-Cu/ZnO	6.4	11.6	1.8	0.4	< 0.1	30.3
A-Na/ZnO	5.9	11.7	1.7	< 0.1	< 0.1	29.6
A-Zn/ZnO	6.2	12.1	1.8	< 0.1	< 0.1	28.5
A/ TiO_2	5.7	10.2	1.6	< 0.01	28.8	< 0.1
A-Cu/ TiO_2	5.9	11.6	1.2	0.3	27.6	< 0.1
A-Na/ TiO_2	5.8	11.2	1.4	< 0.01	29.1	< 0.1
A-Zn/ TiO_2	6.1	11.6	1.5	< 0.01	28.6	0.4

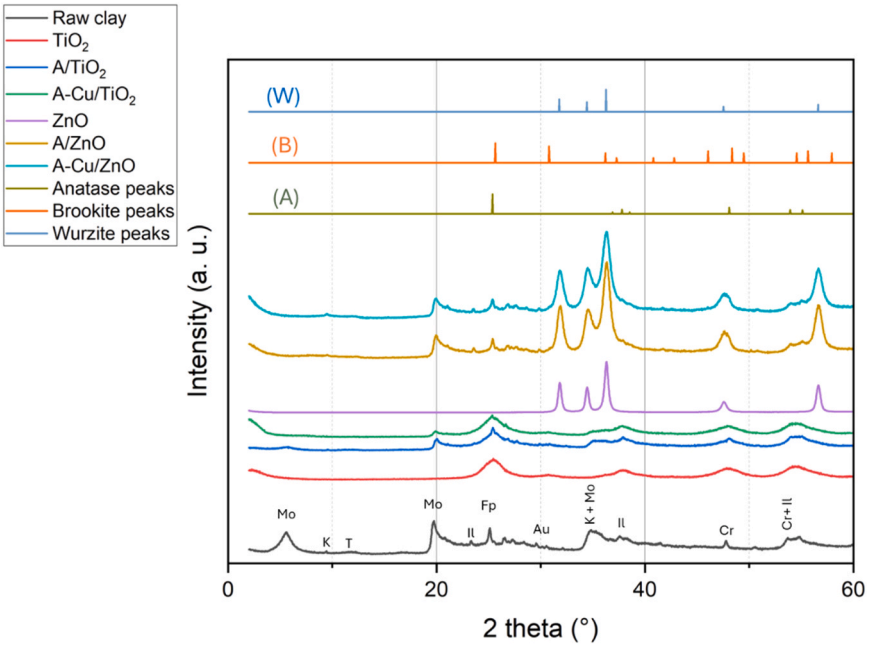

Fig. 1. XRD patterns of samples: raw clay, TiO_2, A/TiO_2, A-Cu/TiO_2, ZnO, A/ZnO, A-Cu/ZnO. Reference peak positions of the different phases of the raw clay are indicated directly on the diffractogram by the following letters: (A) anatase, (B) brookite, (Z) wurzite, (Mo) montmorillonite, (T) talc, (K) kaolinite, (Il) illite, (Fp) feldspar, (Au) augite, and (Cr) cristobalite. The positions are not indicated on the composite materials to avoid overloading the figure. The reference patterns of anatase ((A) from JCPDS 71–1167) [45], brookite ((B) from JCPDS 29–1360) [45] and wurzite ((W) from JCPDS 36–1451) [46] are represented in the range 2–60°.

Table 2
Physico-chemical properties of samples.

Sample	ρ_{app} (g/cm^3) ± 0.01	S_{BET} (m^2/g) ± 5	V_P (cm^3/g) ± 0.01	Zeta potential (mV) ± 0.01	pH of zeta potential (-) ± 0.1	DLS (nm) ± 10	PZC (-) ± 0.1
Raw clay	2.29	45	0.07	−10.94	5.4	4860	5.5
ZnO	6.23	30	0.14	14.61	7.1	6088	7.2
A-ZnO	2.64	125	0.44	2.20	5.3	2786	5.2
A-Cu-ZnO	3.09	50	0.21	12.22	7.2	4318	7.4
A-Na-ZnO	3.15	55	0.25	13.24	7.3	3503	7.4
A-Zn-ZnO	3.19	50	0.18	13.24	7.2	1612	7.1
TiO_2	2.98	180	0.12	24.51	2.7	1554	3
A-TiO_2	2.90	325	0.23	2.50	3.2	10648	3.1
A-Cu-TiO_2	2.56	240	0.15	−3.27	3.1	6451	3.3
A-Na-TiO_2	2.48	110	0.11	−12.99	4.0	3761	4.1
A-Zn-TiO_2	2.48	130	0.14	−4.15	4.3	1461	4.1

ρ_{app}: apparent density measured by helium pycnometry; S_{BET}: specific surface area determined by BET method; V_p: specific liquid volume adsorbed at saturation pressure of nitrogen; D_{DLS}: hydrodynamic diameter of TiO_2 particles aggregates measured by DLS; Zeta potential analysis and pH at different zeta potential; PZC: point of zero charge.

pore volume (0.07 cm^3/g), consistent with the compact structure of untreated layered silicates. Upon modification with ZnO or TiO_2, the surface area and porosity were significantly altered depending on the nature of the inserted ion and photocatalyst.

Among ZnO-based composites, the A/ZnO material showed a considerable increase in specific surface area (125 m^2/g) and pore volume (0.44 cm^3/g), suggesting that ZnO nanoparticles were well-dispersed within the clay matrix, creating additional porosity. In contrast, ion-inserted ZnO composites such as A-Cu/ZnO, A-Na/ZnO, and A-Zn/ZnO displayed reduced surface areas (50–55 m^2/g) and moderate pore volumes (0.18–0.25 cm^3/g), likely due to partial pore blocking or aggregation of ZnO particles in the presence of the inserted metal ions. Notably, the apparent density increased significantly in these doped samples (above 3.0 g/cm^3), indicating a more compact or denser composite structure.

The bare ZnO material had a low surface area (30 m^2/g), highlighting the beneficial role of the clay as a structuring and dispersing matrix for photocatalysts. Moreover, the DLS data suggest that ZnO formed relatively large aggregates (hydrodynamic diameters above 1600 nm), especially in A-Zn/ZnO, possibly limiting accessibility to active sites.

TiO_2-based composites exhibited distinct behavior. The A/TiO_2 sample demonstrated a remarkably high surface area (325 m^2/g), which is significantly higher than both the pristine clay and the pristine TiO_2 (180 m^2/g). This suggests that TiO_2 was homogeneously distributed over or within the clay layers, contributing to extensive mesoporous features. However, the inclusion of dopants (Cu, Na, Zn) generally led to surface area reductions (110–240 m^2/g), in line with a potential pore-blocking effect or formation of larger aggregates. For instance, A-Cu/TiO_2 and A-Zn/TiO_2 retained relatively high values (240 and 130 m^2/g, respectively), while A-Na/TiO_2 dropped to 110 m^2/g, possibly reflecting a higher degree of TiO_2 particle clustering or coverage by exchanged ions.

In terms of particle aggregation, the TiO_2-based composites presented larger DLS values than their ZnO counterparts, with A/TiO_2 reaching 10648 nm, suggesting the formation of large agglomerates in suspension. This behavior may stem from the higher surface energy and propensity for aggregation of anatase/brookite nanoparticles.

Overall, these results highlight that the presence of clay not only acts as a structural support but also significantly modifies the textural features of the photocatalysts. The ion-exchange step appears to modulate porosity and particle dispersion, impacting potential photocatalytic and antimicrobial performances.

Scanning Electron Microscopy (SEM) was employed to investigate the surface morphology of the prepared materials in greater detail (Fig. 2). The raw clay (Fig. 2a) displays the typical lamellar structure

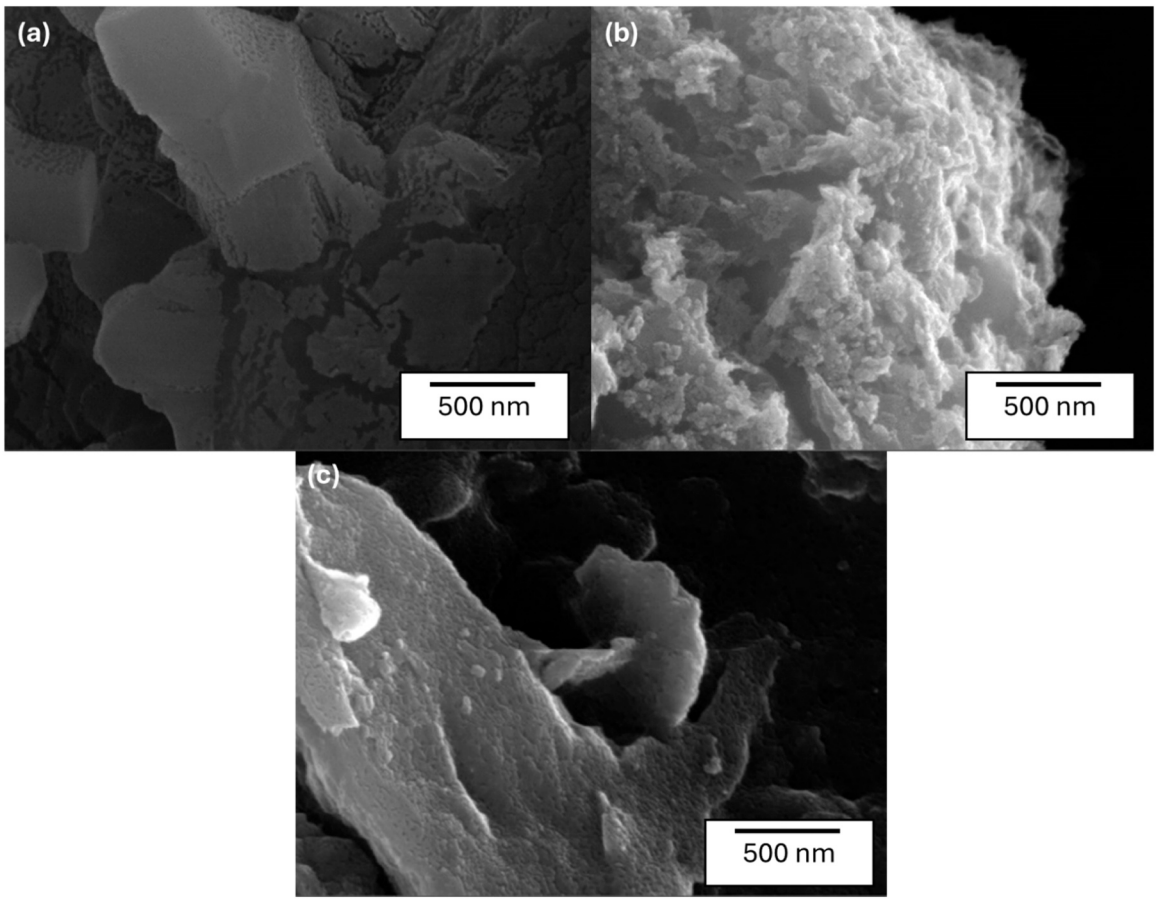

Fig. 2. SEM micrographs of (a) raw clay, (b) A/ZnO and (c) A/TiO_2 samples.

characteristic of montmorillonite-type clays, with stacked and slightly curved platelet-like layers. However, significant morphological transformations are observed after the sol-gel deposition of photocatalysts.

In both A/ZnO (Fig. 2b) and A/TiO_2 (Fig. 2c) samples, the clay surfaces appear to be homogeneously covered with granular particles, leading to a distinctly rougher and more textured surface. These particles correspond to ZnO or TiO_2 crystallites successfully deposited onto the clay layers. The absence of large aggregates and the relatively uniform distribution of the particles suggest an effective dispersion of the photocatalyst phase within the clay matrix.

This morphological evolution is consistent with the increase in specific surface area observed in the BET results (Table 2), particularly for A/TiO_2, which exhibits a highly porous structure. The intimate contact between the photocatalyst particles and the clay support is expected to enhance interfacial charge transfer and reduce recombination of photogenerated electron–hole pairs during photocatalytic processes.

Furthermore, the microstructural features observed by SEM support the role of the clay as a dispersing scaffold, preventing photocatalyst agglomeration and promoting a higher density of accessible active sites. This structural synergy between the clay and the metal oxide phase likely contributes to the improved photocatalytic and antibacterial performances observed in subsequent experiments.

3.3. Zeta potential and surface charge

Zeta potential measurements (Table 2) provide valuable insight into the surface charge properties and colloidal stability of the materials in aqueous suspension. These characteristics are crucial in governing particle aggregation, photocatalytic behavior, and interactions with charged pollutants or microbial membranes.

The raw clay exhibited a moderately negative zeta potential of –10.94 mV at pH 5.4, reflecting the natural surface charge of aluminosilicate layers due to isomorphic substitution and edge hydroxyl group ionization. Upon deposition of ZnO onto the clay (A/ZnO), a shift toward a slightly positive zeta potential (2.20 mV at pH 5.3) was observed. This indicates a successful surface modification and partial masking of the native clay charge by ZnO nanoparticles, which are typically amphoteric in character.

The ion-modified ZnO composites (A-Cu/ZnO, A-Na/ZnO, A-Zn/ZnO) all displayed increasingly positive zeta potentials, with values exceeding + 12 mV. This substantial shift confirms that the surface is dominated by the basic character of ZnO and/or the inserted metal ions. These positively charged surfaces may favor the adsorption of negatively charged pharmaceutical contaminants such as ibuprofen (predominantly anionic at neutral pH), as well as promote antibacterial effects through electrostatic interactions with bacterial cell walls.

Conversely, the TiO_2-based composites showed more variable zeta potential values, depending on the inserted ion. The undoped A/TiO_2 composite exhibited a mildly positive zeta potential (+2.50 mV at pH 3.2), whereas the Cu- and Zn-modified samples (A-Cu/TiO_2 and A-Zn/TiO_2) showed slightly negative values (–3.27 and –4.15 mV, respectively). Interestingly, A-Na/TiO_2 had a strongly negative zeta potential (–12.99 mV), even more so than the raw clay. This suggests that sodium ions enhance surface deprotonation or favor a more hydrated, negatively charged layer at the interface. Such surfaces may be less prone to aggregation but could exhibit reduced affinity for anionic molecules.

The point of zero charge (PZC) values, determined by electrokinetic measurements, further support these observations. ZnO-based composites showed PZCs ranging from 5.2 to 7.4, depending on the dopant, while TiO_2-based materials had lower PZCs (3.1–4.3), consistent with

their more acidic surface characteristics. Notably, A-Cu/ZnO and A-Na/ZnO had PZCs well above neutral pH, suggesting a strongly basic character, whereas A-Na/TiO_2 and A-Cu/TiO_2 had PZCs around 3.1–4.1, making them negatively charged under environmental pH conditions.

These findings demonstrate that the surface charge of the composites can be finely tuned by both the nature of the photocatalyst and the inserted cations. This tunability is key for optimizing adsorption and photocatalytic efficiency toward charged pharmaceutical compounds and for enhancing bactericidal action via electrostatic mechanisms.

3.4. Ibuprofen degradation

The photocatalytic activity of the synthesized materials was evaluated by monitoring the degradation of ibuprofen under UVA and UV-Vis irradiation, with results presented in Fig. 3. All experiments were performed in triplicate using a total catalyst concentration of 1 g/L, and mineralization was assessed via total organic carbon (TOC) analysis. Only ZnO and TiO_2 samples were also evaluated at 0.3 g/L. The kinetic study of IBU degradation under UVA light with A/ZnO and A-Cu/TiO_2 composite samples is shown in Fig. 4.

The raw clay exhibited no photocatalytic activity under either light condition, as expected due to the absence of photoactive components. In contrast, all composite materials demonstrated some degree of ibuprofen degradation, highlighting the contribution of the embedded photocatalyst phase.

Among the ZnO-based samples (Fig. 3), the pure ZnO reference (1 g/L) reached a maximum degradation efficiency of 30 % under both UVA and UV-Vis, whereas the A/ZnO composite reached 23 % under UVA and 10 % under UV-Vis. The lower activity of the A/ZnO composite relative to pure ZnO may be attributed to a partial coverage of active sites by the clay matrix or to reduced light absorption due to increased scattering. Additionally, ion-modified ZnO composites (A-Cu/ZnO, A-Na/ZnO, A-Zn/ZnO) exhibited significantly lower activities (8–10 %), suggesting that metal ion insertion may hinder charge separation or promote charge carrier recombination.

TiO_2-based materials exhibited overall superior performance (Fig. 3). The pure TiO_2 (1 g/L) achieved 45 % and 50 % degradation under UVA and UV-Vis, respectively. Notably, the A/TiO_2 composite also displayed high degradation rates, reaching 40 % under UVA and 35 % under UV-Vis, confirming efficient photocatalyst dispersion within the clay matrix.

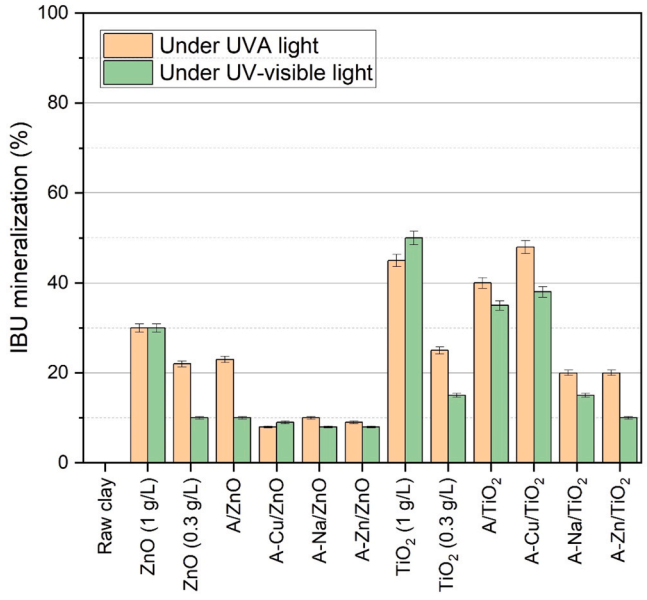

Fig. 3. Ibuprofen mineralization under UVA or UV–visible light after 4 h of illumination.

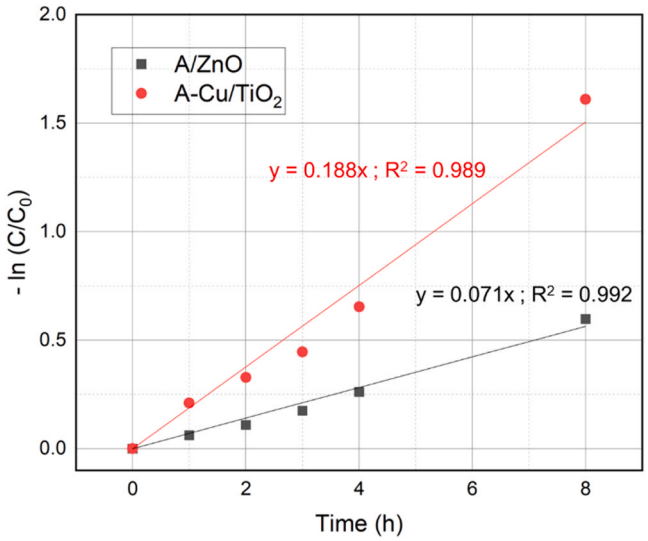

Fig. 4. Experimental determination of kinetic constant of IBU degradation for A/ZnO (black) and A-Cu/TiO_2 (red) samples under UVA light.

Among the doped TiO_2 composites, A-Cu/TiO_2 outperformed all others under UVA (48 %), while its performance dropped under UV-Vis (22 %), possibly due to limited visible-light absorption or dopant-induced recombination sites. In contrast, A-Na/TiO_2 and A-Zn/TiO_2 showed moderate activities (20 % or less), in line with their lower surface areas and less favorable textural and surface charge characteristics.

To better assess the intrinsic activity of the composites, control experiments were conducted using pure ZnO and TiO_2 at a lower dosage of 0.3 g/L, corresponding to the actual photocatalyst content in the composites (30 wt% in 1 g/L of material, as confirmed by ICP-AES, Table 1). Under these conditions, the degradation efficiency of ZnO decreased to 22 % (UVA) and 10 % (UV-Vis), closely matching that of A/ZnO. Similarly, TiO_2 at 0.3 g/L showed reduced degradation efficiencies (25 % UVA, 15 % UV-Vis), while A/TiO_2 still achieved significantly higher performance (40 % and 35 %, respectively).

These results clearly underline the beneficial role of the clay matrix in enhancing the effective utilization of the photocatalyst. The composite architecture, particularly in the case of A/TiO_2, appears to facilitate better dispersion of active sites, limit particle aggregation, and improve pollutant–catalyst interactions, leading to higher photocatalytic efficiency per unit mass of active material. Such features make these hybrid materials promising candidates for cost-effective water treatment applications where minimizing photocatalyst dosage is essential.

Fig. 4 shows that the kinetics of IBU degradation under UVA light are first order as the fitted curve of -ln(C/C_0) vs. time being linear for the 2 best composite samples, as previously observed in [40,41]. The kinetic constants can be calculated for each sample and are the slopes of the fitted curves in Fig. 4. The sample with the highest degradation (A-Cu/TiO_2) has the highest kinetic constant (Fig. 4).

To elucidate the reactive species involved in ibuprofen (IBU) degradation, scavenger experiments were conducted using the two most effective composite photocatalysts, A/ZnO and A-Cu/TiO_2, under UVA irradiation (1.2 mW/cm^2) for 4 h. The results, presented in Fig. 5, compare IBU degradation with and without the addition of three scavengers: ammonium oxalate (AO) for holes (h^+), isopropanol (ISOP) for hydroxyl radicals (•OH), and p-benzoquinone (PB) for superoxide radicals (O_2^-•). For both samples, the degradation trends were consistent. The addition of AO significantly reduced IBU degradation (by ~70–80 % based on preliminary data), as it scavenges photogenerated holes, thereby inhibiting the formation of •OH radicals via water oxidation, a key pathway in the process. Similarly, ISOP led to a

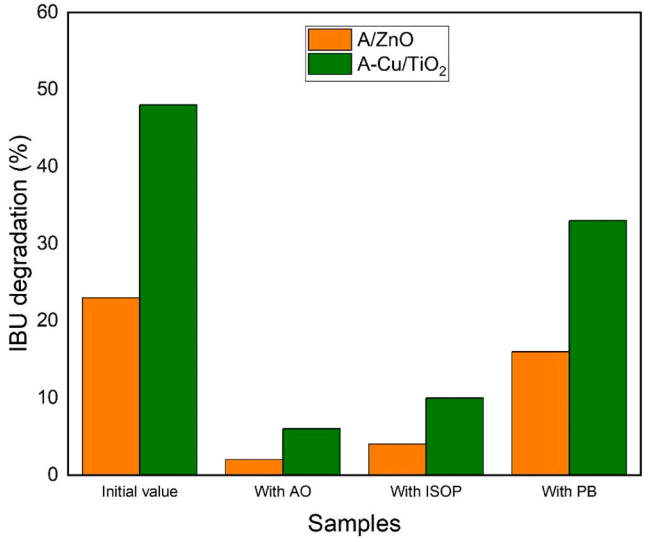

Fig. 5. IBU degradation with and without scavengers during 4 h under UVA light for (orange) A/ZnO and (green) A-Cu/TiO_2 samples. AO = ammonium oxalate, ISOP = isopropanol, PB = p-benzoquinone.

comparable decrease (~65–75 %), confirming the dominant role of •OH in IBU breakdown, consistent with the upstream inhibition observed with AO. In contrast, PB induced a moderate reduction (~20–30 %), suggesting that O_2^{-}• contributes less significantly to the degradation mechanism. These findings align with previous studies on photocatalytic systems, where hydroxyl radicals and holes were identified as the primary species for IBU degradation [40,42].

Metal leaching, particularly of zinc from ZnO-doped composites, is a critical factor to consider during photocatalytic degradation to prevent secondary pollution. In this study, ICP-AES analysis after 4 h under UVA (Table 3) revealed leaching levels of < 0.01 mg/L for Ti (TiO_2, A-Cu/TiO_2), 4 mg/L for Zn (ZnO), 0.1 mg/L for Zn (A/ZnO), and < 0.01 mg/L for Cu (A-Cu/TiO_2), indicating significant Zn release from unsupported ZnO compared to clay-supported A/ZnO, where leaching was reduced by 40-fold. These values remain below the WHO guideline of 3 mg/L for drinking water [47], suggesting acceptable environmental safety under tested conditions. Compared to Rahman et al. [48], who reported low copper leaching (<3 mg/L) with good reusability over five cycles in Fenton-like catalysts for ibuprofen degradation, our clay-supported composites demonstrate enhanced stability, particularly A/ZnO. However, the high Zn leaching from ZnO (4 mg/L) highlights the need for further optimization. Future studies should include extended cycle testing and ICP monitoring to ensure long-term stability and compliance with stricter environmental standards.

3.5. Bacteriological assay

The antibacterial properties of the synthesized materials were evaluated against several indicator microorganisms, including total coliforms, faecal coliforms, Escherichia coli, Salmonella/Shigella, and faecal streptococci. The tests were carried out using two complementary approaches: (i) culture on selective differential agars (XLD, Endo, and BEA) to monitor inhibition or reduction of target bacterial colonies, and (ii) a dilution-based viability assay on Mueller Hinton agar with various catalyst dosages (0.5, 1, and 10 g/L) to assess dose-dependent bactericidal effects. All tests were conducted under identical incubation conditions (37 °C, 24–48 h) and colony counts were expressed in log(CFU/mL).

Table 3
– ICP-AES measurement of metal leaching content after the photocatalytic experiment under UVA (4 h).

Samples	[Ti] after 4 h under UVA (mg/L)	[Zn] after 4 h under UVA (mg/L)	[Cu] after 4 h under UVA (mg/L)
TiO_2	< 0.01	-	-
A-Cu/TiO_2	< 0.01	-	< 0.01
ZnO	-	4	-
A/ZnO	-	0.1	-

- = not present in the sample initially

Control experiments were performed in the dark (with the materials, called Dark control in Fig. 6), under UVA alone (without materials, called Light control) and in the dark without the materials, all these conditions showed no reduction in bacteria populations. Light control and dark control without materials are not represented in Fig. 6 to avoid overloading it.

As shown in Fig. 6a, A/ZnO and A/TiO_2 composites led to a drastic reduction in the population of total and faecal coliforms, including E. coli, with complete inhibition observed at 1 g/L and above. This bactericidal effect was confirmed for enteric pathogens such as Salmonella and Shigella (Fig. 6b), as well as for Gram-positive faecal streptococci (Fig. 6c), demonstrating the broad-spectrum antimicrobial activity of these hybrid materials.

The raw clay already exhibited some antibacterial activity, especially against Salmonella/Shigella and faecal streptococci (Figs. 6b and 6c), while the ion-modified composites (A-Cu/ZnO, A-Na/ZnO, A-Zn/ZnO, and their TiO_2 analogues) showed moderate activity, generally requiring 10 g/L to achieve a significant reduction in CFU counts. This suggests that ion exchange alone is insufficient to induce bactericidal effects, and that the photocatalyst plays a central role. The bacterial activity of the raw clay suggests that the presence of ions in the raw clay (Table 1) can already inhibit the bacteria.

The strong antibacterial performance of A/ZnO and A/TiO_2, observed consistently across all tested strains and confirmed in Figs. 6a–6c, is likely related to the generation of reactive oxygen species (ROS) at the catalyst surface. These ROS, including hydroxyl radicals and superoxide anions, are known to damage bacterial membranes, proteins, and DNA [49,50]. Moreover, the surface charge of the composites may facilitate electrostatic interactions with negatively charged bacterial membranes, enhancing particle adhesion and subsequent membrane disruption.

Overall, these findings indicate that the developed hybrid materials, particularly A/ZnO and A/TiO_2, possess potent antibacterial activity, which complements their photocatalytic capabilities. This dual functionality is particularly advantageous for water treatment applications targeting both chemical micropollutants and microbial contamination.

3.6. From Material Design to Environmental Performance: A Comparative Perspective

The structure–function analysis of our hybrid materials reveals clear relationships between their physicochemical properties, such as specific surface area, zeta potential, and morphology, and their functional performance, including photocatalytic activity and antibacterial efficacy. These findings are consistent with recent literature on clay–photocatalyst composites.

Specific surface area plays a crucial role in pollutant degradation and antibacterial activity. For instance, the A/TiO_2 composite exhibits an exceptionally high specific surface area (325 m^2/g), while A/ZnO shows a respectable value (~125 m^2/g). These characteristics promote catalyst dispersion and access to active sites, as demonstrated by Adesina et al. [27], who reported approximately 84 % tetracycline removal after 2 h of exposure under UV and natural light with a kaolin–TiO_2–orange-peel biochar composite, attributing the performance to enhanced porosity and improved photocatalyst dispersion. Similarly, Yuan et al. [51] described montmorillonite/TiO_2 composites containing 30 wt% TiO_2 that achieved nearly complete dye degradation, correlating performance with superior dispersion and surface properties.

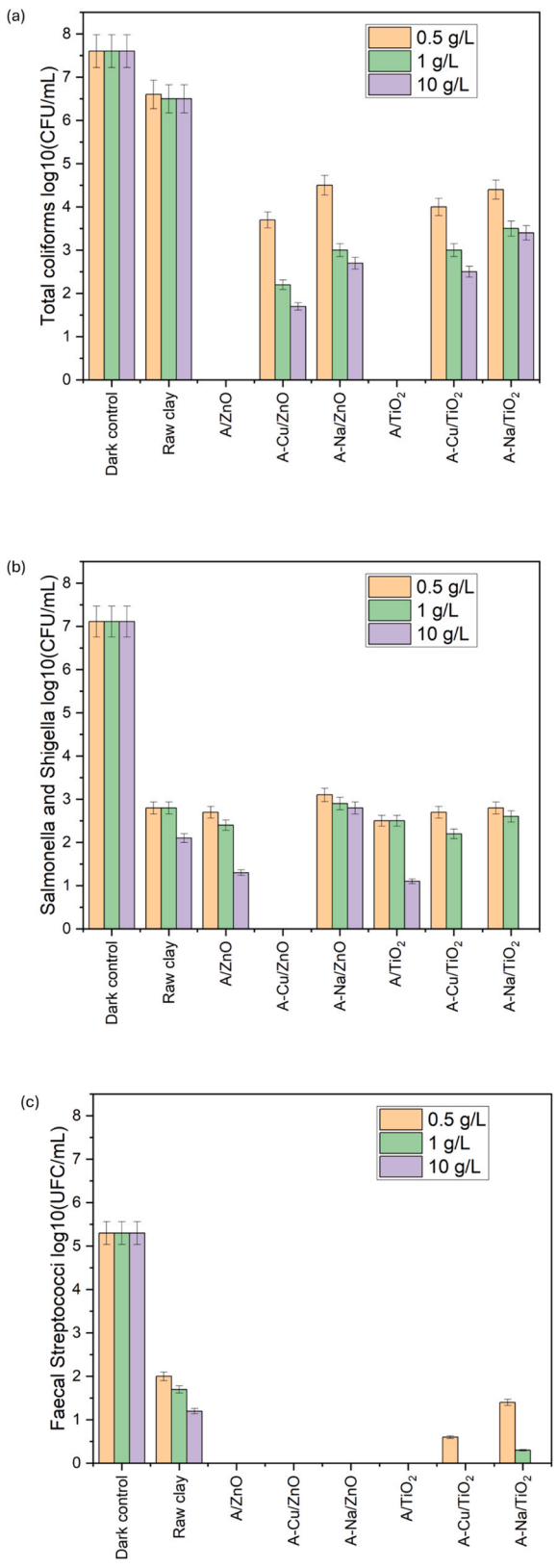

Fig. 6. Antibacterial activity on (a) total coliforms, (b) Salmonella/Shigella; and (c) faecal Strepotococci from the real wastewater. Previous to bacterial development the wastewater was stirred with the different samples under UVA illumination for 4 h. Light control and dark control without materials show no effect on any of the three bacteria (as Dark control) and so, are not represented on the figures to avoid overloading it.

Zeta potential is another key factor influencing pollutant adsorption and microbial interactions at the composite surface. Our ZnO-based composites acquire positive surface charge (up to +12 mV), favouring electrostatic attraction toward anionic contaminants, whereas TiO_2 variants have slightly negative to neutral charges, aligning with their distinct photoreactivity. Bai et al. [52] emphasized in their review that modulation of the zeta potential of clay-supported TiO_2/ZnO photocatalysts enhances affinity for anionic contaminants and improves photocatalytic efficiency.

When normalized to active-phase mass, our A/TiO_2 composites clearly outperform pure TiO_2 at equivalent loadings, highlighting the benefits of clay-supported systems. These results align with those of Karchiyappan et al. [53], who demonstrated that kaolin/TiO_2 composites synthesized via sol–gel methods deliver higher photocatalytic removal rates than pure TiO_2. Additionally, pillared montmorillonite (Ti-PILC) structures exhibit improved surface area and stability, further enhancing performance compared to unmodified oxide powders [28].

Regarding antibacterial activity, our A/ZnO and A/TiO_2 composites produced near-complete bacterial inhibition at concentrations $\geq$ 1 g/L. Wu et al. [50] reported similar outcomes for montmorillonite–Ag/TiO_2 composites under visible light, attributing bactericidal efficacy to reactive oxygen species (ROS)-induced membrane damage. Li et al. [49] also achieved remarkable antibacterial and pharmaceutical degradation performance using a kaolinite–TiO_2–g-C_3N_4 heterojunction, confirming the synergy between clay support and photocatalyst.

Overall, our hybrid materials offer performance comparable or superior to other clay–photocatalyst systems reported in the literature for dye removal, micropollutant degradation, or microbial decontamination. For example, orange-peel biochar/clay/TiO_2 composites demonstrated 89–92 % tetracycline degradation with 50 % of mineralization under UVB for 2 h and efficient E. coli inactivation without forming toxic intermediates [27]. In that study, the illumination was much more energetic than the present work. Similarly, a 3D-printed ZnO/clay architecture showed effective methylene blue degradation with 100 % degradation in 40 min under solar irradiation [54] but no mineralization was assessed.

Concerning the photocatalytic mineralization of ibuprofen, our study demonstrates a compelling 48 % Total Organic Carbon (TOC) reduction within 4 h using the A-Cu/TiO_2 composite under UVA irradiation with low intensity (1.2 mW/cm^2) [55], surpassing several literature benchmarks in terms of efficiency, practicality, and multifunctionality. For instance, Tanveer et al. [56] achieved 47 % TOC removal with UV/ZnO after only 15 min but required artificial UVC lamps (254 nm) and showed lower performance under solar conditions with quartz or borosilicate reactors, highlighting the limitations of non-supported catalysts in real-world applications, while at catalyst dosing of 1.5 g/L TiO_2 and 0.5 g/L ZnO, degradation rates were similar, with UV lamp-based photocatalysis yielding higher TOC and COD reduction than solar irradiation. Similarly, Loaiza-Ambuludi et al. [57] reported up to 90 % TOC abatement via UVC/H_2O_2/Fe photo-Fenton after 8 h, yet this homogeneous process necessitates high oxidant doses and lacks the catalyst recovery ease offered by our clay-supported system, with pseudo-second-order kinetics observed for TOC decay. Mendez-Arriaga et al. [58] attained 80 % Dissolved Organic Carbon (DOC) removal in 240 min through sonophoto-Fenton/TiO_2 hybrids under UV-Vis or visible light, but relied on energy-intensive ultrasound and extended reaction times without integrating antimicrobial properties, achieving up to 90 % mineralization with US/UV/TiO_2/H_2O_2/Fe. Jimenez-Salcedo et al. [59] focused on degradation pathways using TiO_2/UV and g-C_3N_4/visible light, identifying intermediates like 2-(4-acrylphenyl) acetic acid and 4-propenylbenzoic acid but not quantifying mineralization, highlighting incomplete breakdown and potential toxicity persistence absent in our approach, with degradation efficiencies varying by pH and light intensity. More recently, Pylarinou et al. [60] achieved efficient ibuprofen degradation with TiO_2/Mo-$BiVO_4$ bilayers under photoelectrocatalysis, yielding photocurrent densities up to

0.5 mA/cm^2 and 90 % removal in 120 min, yet mineralization data were not emphasized, and the complex electrode fabrication contrasts with our low-cost, natural smectite-derived composites. Across these studies and others, such as Braz et al. [61] with 50 % mineralization using pure TiO_2 under UV after 60 min, Candido et al. [33] reporting up to 78 % TOC reduction with TiO_2 in 60 min under UV lamp, Gong et al. [62] achieved higher mineralization rates (up to 60 % in 20 min) with a Fe^{2+}/Oxone/UV process, but required higher oxidant doses and showed toxicity evolution, and Feng et al. [63] using YMO-SO photocatalysts, reached 70–80 % degradation under visible light but reported lower mineralization (typically <40 % TOC removal) and relied on complex synthesis methods, typical mineralization ranges from 20 % to 80 % over 2–6 h with photocatalytic systems, often facing recovery challenges and higher costs.

Direct comparison between these studies is challenging due to significant variations in experimental conditions, such as the type and intensity of illumination (e.g., UVA vs. UVC lamps or solar simulators), pollutant and catalyst concentrations, and irradiation durations, which can range from 120 to 360 min across different setups. Moreover, not all articles provide comprehensive details on these parameters, including precise light power outputs or exact catalyst loadings, making quantitative benchmarking challenging. Despite these inconsistencies, our A-Cu/TiO_2 system stands out for its balanced efficiency under practical UVA conditions, highlighting its potential for scalable applications.

3.7. Limitations of this work

Despite the promising results, this study presents several limitations that warrant consideration. First, the photocatalytic performance under visible light remains suboptimal, with lower degradation rates compared to UVA conditions, indicating a need for further optimization to enhance visible-light responsiveness. Second, the long-term stability and reusability of the clay-supported composites were not fully assessed, as tests were limited to some cycles, potentially underestimating material degradation or leaching over extended use but giving first promising results. Third, the experiments were conducted under controlled laboratory conditions, which may not fully replicate the complex matrix of real wastewater, including varying pH, competing pollutants, and microbial loads. Finally, the scalability of the synthesis process and its economic viability in resource-limited settings require further investigation to ensure practical implementation in decentralized treatment systems.

4. Conclusion

In this study, a series of clay-based photocatalytic composites incorporating ZnO or TiO_2, with or without additional ion exchange (Cu, Na, Zn), were successfully synthesized and characterized. Elemental analysis and XRD confirmed the effective incorporation of photocatalyst phases without significant alteration of either their crystalline structure or clay matrix. Textural analysis revealed a substantial influence of both the photocatalyst type and the exchanged cations on surface area, porosity, and particle dispersion. TiO_2-based materials generally exhibited higher surface areas and more favorable morphologies than their ZnO-based counterparts, especially in undoped configurations.

Zeta potential and point of zero charge analyses showed that the surface charge of the composites could be finely tuned via cationic modification, influencing their colloidal stability and potential interaction with charged pollutants or microbial membranes. SEM imaging further confirmed the homogeneous dispersion of photocatalyst particles on the clay surface, contributing to the accessible active surface.

Photocatalytic degradation tests using ibuprofen as a model contaminant demonstrated that all composites exhibited measurable activity under UVA and UV-Vis irradiation, with TiO_2-based composites showing superior performance overall. Among these, the Cu-doped TiO_2 sample (A-Cu/TiO_2) achieved the highest degradation under UVA, suggesting a synergistic effect between copper doping and the clay support. However, performance under visible light was generally lower, indicating room for improvement in enhancing visible-light responsiveness.

Overall, the results highlight the potential of these hybrid materials as efficient and tunable photocatalytic platforms for water treatment applications. The structural, textural, and surface properties can be adjusted by choice of photocatalyst and exchanged ions, enabling the rational design of multifunctional materials for both pollutant degradation and antimicrobial applications. Future work will focus on optimizing the photocatalyst loading, improving visible-light activity, and assessing long-term stability and regeneration potential in real water matrices.

CRediT authorship contribution statement

Marlène Huguette Tsaffo Mbognou: Conceptualization, Writing – review & editing, Investigation, Formal analysis. **Stéphanie D. Lambert:** Conceptualization, Methodology, Writing – review & editing, Funding acquisition, Project administration. **Antoine Farcy:** Investigation, Formal analysis, Writing – review & editing. **Hela Rekik:** Investigation, Formal analysis, Writing – review & editing. **Steven C. N. Wouamba:** Investigation, Formal analysis, Writing – review & editing. **Emmanuel Djoufac Woumfo:** Supervision, Funding acquisition, Project administration, Writing – review & editing. **Julien G. Mahy:** Conceptualization, Methodology, Writing – original draft, Writing – review & editing, Investigation, Supervision, Formal analysis, Validation.

Declaration of Competing Interest

The authors declare that they have no known competing financial interests or personal relationships that could have appeared to influence the work reported in this paper.

Acknowledgements

Marlène Huguette Tsaffo Mbognou thanks the PACODEL for a doctoral grant. Stéphanie D. Lambert thanks the F.R.S.-FNRS for her Research Director position. The authors thank the CARPORVISU platform of the University of Liège and its manager, Dr. Alexandre Léonard, for the nitrogen adsorption–desorption measurements. The authors thank Bruno Correia for his carefully reading and corrections of the paper.

Data Availability

The raw/processed data required to reproduce these findings can be shared on demand.

References

[1] A.S. Adeleye, J. Xue, Y. Zhao, A.A. Taylor, J.E. Zenobio, Y. Sun, Z. Han, O. A. Salawu, Y. Zhu, Abundance, fate, and effects of pharmaceuticals and personal care products in aquatic environments, J. Hazard Mater. 424 (2022), https://doi.org/10.1016/j.jhazmat.2021.127284.

[2] M. Caban, E. Lis, J. Kumirska, P. Stepnowski, Determination of pharmaceutical residues in drinking water in Poland using a new SPE-GC-MS(SIM) method based on speedisk extraction disks and DIMETRIS derivatization, Sci. Total Environ. 538 (2015) 402–411, https://doi.org/10.1016/j.scitotenv.2015.08.076.

[3] G.R.K. Kenmogne, F. Rosillon, H.G. Mpakam, A. Nono, Enjeux sanitaires, socio-économiques et environnementaux liés à la réutilisation des eaux usées dans le maraîchage urbain: cas du bassin versant de l'Abiergué (Yaoundé-Cameroun), VertigOLa Rev. Électron. En. Sci. De. l'Environ. (2010).

[4] Organisation mondiale de la santé, NOTE D'ORIENTATION TECHNIQUE RELATIVE À L'EAU, L'ASSAINISSEMENT ET L'HYGIÈNE ET LA GESTION DES EAUX USÉES POUR PRÉVENIR LES INFECTIONS ET RÉDUIRE LA PROPAGATION DE LA RÉSISTANCE AUX ANTIMICROBIENS, 2020. ⟨https://iris.who.int/bitstream/handle/10665/336678/9789240014831-fre.pdf⟩ (accessed June 17, 2025).

[5] N. Walczak, A. Krzyszczak-Turczyn, B. Czech, Unveiling the effect of SWCNT as the dopants of TiO2 in pharmaceutical mixture photocatalytic removal from water and wastewater, J. Photochem. Photobio. A Chem. 467 (2025), https://doi.org/10.1016/j.jphotochem.2025.116437.
[6] N. Dammak, N. Fakhfakh, S. Fourmentin, M. Benzina, Natural clay as raw and modified material for efficient o-xylene abatement, J. Environ. Chem. Eng. 1 (2013) 667–675, https://doi.org/10.1016/j.jece.2013.07.001.
[7] M.R. Eskandarian, H. Choi, M. Fazli, M.H. Rasoulifard, Effect of UV-LED wavelengths on direct photolytic and TiO2 photocatalytic degradation of emerging contaminants in water, Chem. Eng. J. 300 (2016) 414–422, https://doi.org/10.1016/j.cej.2016.05.049.
[8] D.S. Villarreal-Lucio, V.S. Galván-Romero, C. López-Saldaña, B.V. Loera-García, K. X. Vargas-Berrones, R. Ocampo-Pérez, J.C. Serna-Carrizalez, R. Flores-Ramírez, Molecularly imprinted polymer with photocatalytic activity for ibuprofen adsorption, degradation, and detection in real water samples, J. Contam. Hydrol. 273 (2025), https://doi.org/10.1016/j.jconhyd.2025.104600.
[9] M. Gros, M. Petrović, A. Ginebreda, D. Barceló, Removal of pharmaceuticals during wastewater treatment and environmental risk assessment using hazard indexes, Environ. Int 36 (2010) 15–26, https://doi.org/10.1016/j.envint.2009.09.002.
[10] N. Bashir, T. Sawaira, A. Jamil, M. Awais, A. Habib, A. Afzal, Challenges and prospects of main-group metal-doped TiO2 photocatalysts for sustainable water remediation, Mater. Today Sustain. 27 (2024), https://doi.org/10.1016/j.mtsust.2024.100869.
[11] M.I. Din, R. Khalid, Photocatalysis of pharmaceuticals and organic dyes in the presence of silver-doped TiO2 photocatalyst–a critical review, Int J. Environ. Anal. Chem. 105 (2025) 276–300, https://doi.org/10.1080/03067319.2023.2258795.
[12] S. Douven, J.G. Mahy, C. Wolfs, C. Reyserhove, D. Poelman, F. Devred, E. M. Gaigneaux, S.D. Lambert, Efficient N, fe Co-Doped TiO2 active under Cost-Effective visible LED light: from powders to films, Catalysts 10 (2020) 547, https://doi.org/10.3390/catal10050547.
[13] J.G. Mahy, M.H.T. Mbognou, C. Léonard, N. Fagel, E.D. Woumfo, S.D. Lambert, Natural clay modified with ZnO/TiO2 to enhance pollutant removal from water, Catalysts 12 (2022), https://doi.org/10.3390/catal12020148.
[14] J.G. Mahy, C. Wolfs, C. Vreuls, S. Drot, S. Dircks, A. Boergers, J. Tuerk, S. Hermans, S.D. Lambert, Advanced oxidation processes for waste water treatment: from lab-scale model water to on-site real waste water, Environ. Technol. 42 (2021) 3974–3986, https://doi.org/10.1080/09593330.2020.1797894.
[15] H. Benhebal, C. Wolfs, S. Kadi, R.G. Tilkin, B. Allouche, D. Lambert, J.G. Mahy, Visible light sensitive SnO2/ZnCo2O4 material for the photocatalytic removal of organic pollutants in water, Inorganics 7 (2019) 77.
[16] P. Trigueiro, A.G. Jerônimo, W.A. Albuquerque, W.L. da Silva, J.A. Osajima, M. Jaber, R.R. Peña-Garcia, Shaping a ZnO-alginate-hectorite nanocomposite for improved photocatalytic drug removal, Appl. Mater. Today 44 (2025), https://doi.org/10.1016/j.apmt.2025.102680.
[17] P. Trigueiro, W.A. Albuquerque, A.G. Jerônimo, R. Barbosa, M. Jaber, R.R. Peña-Garcia, Tailoring Y-doped ZnO loaded onto eco-friendly support alginate-hectorite for azo dye removal, Appl. Surf. Sci. 704 (2025), https://doi.org/10.1016/j.apsusc.2025.163461.
[18] W. Albuquerque, P. Trigueiro, B.V. Silva, L. Neves, L.C. Almeida, R.R. Peña-Garcia, A novel RuO_2@ZnO-Alginate-Halloysite composite for the effective degradation of eosin yellow dye and ciprofloxacin drug, Mater. Res Bull. 182 (2025), https://doi.org/10.1016/j.materresbull.2024.113178.
[19] P. Trigueiro, W.A. Albuquerque, A.G. Jerônimo, M.S. Rodrigues, E.L.T. França, R. R. Peña-Garcia, CuO-TiO2–Saponite ternary nanocomposite for efficient removal of bromocresol Green dye, Minerals 14 (2024), https://doi.org/10.3390/min14121268.
[20] R.P. Feitosa, I.S. de Lima, Y. Guerra, E.C. da Silva-Filho, M.B. Furtini, L. Almeida, R.R. Peña-Garcia, I.B. Martín, J.A. Cecília, J.A. Osajima, Cerium-Doped TiO2 and sepiolite nanocomposites for tetracycline inactivation in water treatment, ACS Appl. Nano Mater. 8 (2025) 4324–4338, https://doi.org/10.1021/acsanm.4c01068.
[21] R.F. Hamarawf, D.I. Tofiq, K.H.H. Aziz, H.Q. Hassan, K.A. Abdalkarim, S. J. Mohammed, Antibacterial activity and photo-Fenton catalytic degradation of a novel FeII/FeIII mixed-valency porous coordination polymer, J. Environ. Chem. Eng. 13 (2025), https://doi.org/10.1016/j.jece.2025.116765.
[22] K.H.H. Aziz, K.M. Omer, A. Mahyar, H. Miessner, S. Mueller, D. Moeller, Application of photocatalytic falling film reactor to elucidate the degradation pathways of pharmaceutical diclofenac and ibuprofen in aqueous solutions, Coatings 9 (2019), https://doi.org/10.3390/coatings9080465.
[23] A.S. Soares, F.P. Araujo, R. França, J.A. Osajima, Y. Guerra, S. Castro-Lopes, E. C. Silva-Filho, F.E. Santos, L.C. Almeida, B.C. Viana, R.R. Peña-Garcia, Effect of ph on the growth and ibuprofen photocatalytic response of Zn1 − xCoxO compound synthesized by the co-precipitation method, J. Mater. Res 38 (2023) 2439–2452, https://doi.org/10.1557/s43578-023-00980-4.
[24] J.G. Mahy, L. Lejeune, T. Haynes, N. Body, S. De Kreijger, B. Elias, R.H.M. Marcilli, C.A. Fustin, S. Hermans, Crystalline ZnO photocatalysts prepared at ambient temperature: influence of morphology on p-nitrophenol degradation in water, Catalysts 11 (2021), https://doi.org/10.3390/catal11101182.
[25] J.G. Mahy, C.A. Paez, J. Hollevoet, L. Courard, E. Boonen, S.D. Lambert, Durable photocatalytic thin coatings for road applications, Constr. Build. Mater. 215 (2019) 422–434, https://doi.org/10.1016/j.conbuildmat.2019.04.222.
[26] F. Méndez-Arriaga, S. Esplugas, J. Giménez, Photocatalytic degradation of non-steroidal anti-inflammatory drugs with TiO2 and simulated solar irradiation, Water Res 42 (2008) 585–594, https://doi.org/10.1016/j.watres.2007.08.002.
[27] M.O. Adesina, M.O. Alfred, H. Seitz, K. Brennenstuhl, H.M. Rawel, P. Wessig, J. Kim, A. Wedel, W. Koopman, C. Günter, E.I. Unuabonah, A. Taubert, Orange peel biochar/clay/titania composites: low cost, high performance, and easy-to-reuse photocatalysts for the degradation of tetracycline in water, Environ. Sci. 10 (2024) 1432–1450, https://doi.org/10.1039/d4ew00037d.
[28] M. Chauhan, V.K. Saini, S. Suthar, Ti-pillared montmorillonite clay for adsorptive removal of amoxicillin, imipramine, diclofenac-sodium, and paracetamol from water, J. Hazard Mater. 399 (2020), https://doi.org/10.1016/j.jhazmat.2020.122832.
[29] E.G. Garrido-Ramírez, B.K.G. Theng, M.L. Mora, Clays and oxide minerals as catalysts and nanocatalysts in Fenton-like reactions - a review, Appl. Clay Sci. 47 (2010) 182–192, https://doi.org/10.1016/j.clay.2009.11.044.
[30] H. Bel Hadjltaief, P. Da Costa, M.E. Galvez, M. Ben Zina, Influence of operational parameters in the heterogeneous photo-fenton discoloration of wastewaters in the presence of an iron-pillared clay, Ind. Eng. Chem. Res 52 (2013) 16656–16665, https://doi.org/10.1021/ie4018258.
[31] M.H.T. Mbognou, S.D. Lambert, J. Caucheteux, A. Farcy, C. Alié, N. Fagel, E. D. Woumfo, J.G. Mahy, Hybrid clay-based materials for organic dyes and pesticides elimination in water, J. Solgel Sci. Technol. 105 (2023) 461–470, https://doi.org/10.1007/s10971-022-06005-6.
[32] K.H. Hama Aziz, H. Miessner, S. Mueller, D. Kalass, D. Moeller, I. Khorshid, M.A. M. Rashid, Degradation of pharmaceutical diclofenac and ibuprofen in aqueous solution, a direct comparison of ozonation, photocatalysis, and non-thermal plasma, Chem. Eng. J. 313 (2017) 1033–1041, https://doi.org/10.1016/j.cej.2016.10.137.
[33] J.P. Candido, S.J. Andrade, A.L. Fonseca, F.S. Silva, M.R.A. Silva, M.M. Kondo, Ibuprofen removal by heterogeneous photocatalysis and ecotoxicological evaluation of the treated solutions, Environ. Sci. Pollut. Res. 23 (2016) 19911–19920, https://doi.org/10.1007/s11356-016-6947-z.
[34] H. Benhebal, M. Chaib, A. Leonard, S.D. Lambert, M. Crine, Photodegradation of phenol and benzoic acid by sol-gel-synthesized alkali metal-doped ZnO, Mater. Sci. Semicond. Process 15 (2012) 264–269, https://doi.org/10.1016/j.mssp.2011.12.001.
[35] J.G. Mahy, G.L.-M. Léonard, S. Pirard, D. Wicky, A. Daniel, C. Archambeau, D. Liquet, B. Heinrichs, Aqueous sol-gel synthesis and film deposition methods for the large-scale manufacture of coated steel with self-cleaning properties, J. Solgel Sci. Technol. 81 (2017) 27–35, https://doi.org/10.1007/s10971-016-4020-5.
[36] M. Schreier, J.R. Regalbuto, a fundamental study of pt tetraammine impregnation of silica: 1. The electrostatic nature of platinum adsorption, J. Catal. 225 (2004) 190–202, https://doi.org/10.1016/j.jcat.2004.03.034.
[37] V. Claude, J.G. Mahy, T. Lohay, R.G. Tilkin, F. Micheli, S.D. Lambert, Sol – gel synthesis of Ni/Al2O3 catalysts for toluene reforming: support modification with alkali, alkaline earth or rare-earth dopant (Ca,K,Mg or Ce), Surf. Interfaces 20 (2020) 100511, https://doi.org/10.1016/j.surfin.2020.100511.
[38] F.S. Mustafa, K.H. Hama Aziz, Heterogeneous catalytic activation of persulfate for the removal of rhodamine b and diclofenac pollutants from water using iron-impregnated biochar derived from the waste of black seed pomace, Process Saf. Environ. Prot. 170 (2023) 436–448, https://doi.org/10.1016/j.psep.2022.12.030.
[39] C.M. Malengreaux, G.M.-L. Léonard, S.L. Pirard, I. Cimieri, S.D. Lambert, J. R. Bartlett, B. Heinrichs, How to modify the photocatalytic activity of TiO2 thin films through their roughness by using additives. A relation between kinetics, morphology and synthesis, Chem. Eng. J. 243 (2014) 537–548, https://doi.org/10.1016/j.cej.2013.11.031.
[40] A.S. Sá, R.P. Feitosa, L. Honório, R. Peña-Garcia, L.C. Almeida, J.S. Dias, L. P. Brazuna, T.G. Tabuti, E.R. Triboni, J.A. Osajima, E.C. da Silva-Filho, A brief photocatalytic study of zno containing cerium towards ibuprofen degradation, Materials 14 (2021), https://doi.org/10.3390/ma14195891.
[41] N. Shafeei, G. Asadollahfardi, G. Moussavi, M.M.Akbar Boojar, Degradation of ibuprofen in the photocatalytic process with doped TiO 2 as catalyst and UVA-LED as existing source, Desalin. Water Treat. 142 (2019) 341–352, https://doi.org/10.5004/dwt.2019.23214.
[42] C.B. Anucha, I. Altin, E. Bacaksiz, I. Degirmencioglu, T. Kucukomeroglu, S. Yılmaz, V.N. Stathopoulos, Immobilized tio2/zno sensitized copper (Ii) phthalocyanine heterostructure for the degradation of ibuprofen under uv irradiation, Separations 8 (2021) 1–21, https://doi.org/10.3390/separations8030024.
[43] A. Farcy, M. Mathy, L. Lejeune, P. Eloy, S. Hermans, P. Drogui, J.G. Mahy, Ce2O3 and TiO2 p-n heterojunction for enhanced degradation of p-nitrophenol under visible light, J. Photochem. Photobio. A Chem. 463 (2025), https://doi.org/10.1016/j.jphotochem.2025.116284.
[44] H.B. Saab, N. Nassif, A.G. El Samrani, R. Daoud, S. Medawar, N. Ouaïni, Survey of bacteriological surface water quality (Nahr Ibrahin River, Lebanon), Rev. Des. Sci. De. l'Eau 20 (2007) 341–352, https://doi.org/10.7202/016909ar.
[45] G. Zerjav, K. Zizek, J. Zavasnik, A. Pintar, Brookite vs. Rutile vs. Anatase: What's behind their various photocatalytic activities? J. Environ. Chem. Eng. 10 (2022) https://doi.org/10.1016/j.jece.2022.107722.
[46] W.A. Freitas, B.E.C.F. Soares, M.S. Rodrigues, P. Trigueiro, L.M.C. Honorio, R. Peña-Garcia, A.C.S. Alcântara, E.C. Silva-Filho, M.G. Fonseca, M.B. Furtini, J. A. Osajima, Facile synthesis of ZnO-clay minerals composites using an ultrasonic approach for photocatalytic performance, J. Photochem. Photobio. A Chem. 429 (2022), https://doi.org/10.1016/j.jphotochem.2022.113934.
[47] World Health Organization (WHO), Guidelines for Drinking-water Quality FOURTH EDITION INCORPORATING THE FIRST ADDENDUM, Geneva, 2017.
[48] K.O. Rahman, K.H.H. Aziz, Utilizing scrap printed circuit boards to fabricate efficient Fenton-like catalysts for the removal of pharmaceutical diclofenac and ibuprofen from water, J. Environ. Chem. Eng. 10 (2022), https://doi.org/10.1016/j.jece.2022.109015.
[49] C. Li, Z. Sun, W. Zhang, C. Yu, S. Zheng, Highly efficient g-C3N4/TiO2/kaolinite composite with novel three-dimensional structure and enhanced visible light

responding ability towards ciprofloxacin and S. Aureus, Appl. Catal. B 220 (2018) 272–282, https://doi.org/10.1016/j.apcatb.2017.08.044.
[50] T.S. Wu, K.X. Wang, G.D. Li, S.Y. Sun, J. Sun, J.S. Chen, Montmorillonite-Supported Ag/TiO2 nanoparticles: an efficient visible-Light bacteria photodegradation material, ACS Appl. Mater. Interfaces 2 (2010) 544–550, https://doi.org/10.1021/am900743d.
[51] L. Yuan, D. Huang, W. Guo, Q. Yang, J. Yu, TiO2/montmorillonite nanocomposite for removal of organic pollutant, Appl. Clay Sci. 53 (2011) 272–278, https://doi.org/10.1016/j.clay.2011.03.013.
[52] N. Bai, X. Liu, Z. Li, X. Ke, K. Zhang, Q. Wu, High-efficiency TiO2/ZnO nanocomposites photocatalysts by sol–gel and hydrothermal methods, J. Solgel Sci. Technol. 99 (2021) 92–100, https://doi.org/10.1007/s10971-021-05552-8.
[53] T. Karchiyappan, R. Rao, K. Mohammad, H. Dehghani, Water science and technology library industrial wastewater treatment emerging technologies for sustainability, Springer, 2022. ⟨https://www.springer.com/gp/⟩.
[54] S. Ali, M.T. Aljarrah, A. Al-Otoom, N. Abdelaziz, Development and testing of robust 3D printed ZnO/Clay photocatalysts for sustainable wastewater treatment, ACS Omega (2025), https://doi.org/10.1021/acsomega.4c09879.
[55] K.M. Reza, A. Kurny, F. Gulshan, Parameters affecting the photocatalytic degradation of dyes using TiO2: a review, Appl. Water Sci. 7 (2017) 1569–1578, https://doi.org/10.1007/s13201-015-0367-y.
[56] M. Tanveer, G.T. Guyer, G. Abbas, Photocatalytic degradation of ibuprofen in water using TiO2 and ZnO under artificial UV and solar irradiation, Water Environ. Res. 91 (2019) 822–829, https://doi.org/10.1002/wer.1104.
[57] S. Loaiza-Ambuludi, M. Panizza, N. Oturan, M.A. Oturan, Removal of the anti-inflammatory drug ibuprofen from water using homogeneous photocatalysis, Catal. Today 224 (2014) 29–33, https://doi.org/10.1016/j.cattod.2013.12.018.
[58] F. Méndez-Arriaga, R.A. Torres-Palma, C. Pétrier, S. Esplugas, J. Gimenez, C. Pulgarin, Mineralization enhancement of a recalcitrant pharmaceutical pollutant in water by advanced oxidation hybrid processes, Water Res 43 (2009) 3984–3991, https://doi.org/10.1016/j.watres.2009.06.059.
[59] M. Jiménez-Salcedo, M. Monge, M.T. Tena, Photocatalytic degradation of ibuprofen in water using TiO2/UV and g-C3N4/visible light: study of intermediate degradation products by liquid chromatography coupled to high-resolution mass spectrometry, Chemosphere 215 (2019) 605–618, https://doi.org/10.1016/j.chemosphere.2018.10.053.
[60] M. Pylarinou, E. Sakellis, S. Gardelis, V. Psycharis, M.G. Kostakis, N.S. Thomaidis, V. Likodimos, Bilayer TiO2/Mo-BiVO4 photoelectrocatalysts for ibuprofen degradation, Materials 18 (2025), https://doi.org/10.3390/ma18020344.
[61] F.S. Braz, M.R.A. Silva, F.S. Silva, S.J. Andrade, A.L. Fonseca, M.M. Kondo, Photocatalytic degradation of ibuprofen using TiO₂ and ecotoxicological assessment of degradation intermediates against <I>Daphnia similis</I&gt, J. Environ. Prot. 05 (2014) 620–626, https://doi.org/10.4236/jep.2014.57063.
[62] H. Gong, W. Chu, S.H. Lam, A.Y.C. Lin, Ibuprofen degradation and toxicity evolution during Fe2+/Oxone/UV process, Chemosphere 167 (2017) 415–421, https://doi.org/10.1016/j.chemosphere.2016.10.027.
[63] Z. Feng, Synthesis and full-spectrum-responsive photocatalytic activity from UV/Vis to near-infrared region of S-O decorated YMnO3 nanoparticles for photocatalytic degradation of ibuprofen, Front Chem. 12 (2024), https://doi.org/10.3389/fchem.2024.1424548.